The Journal of Fluids Engineering (USPS 278-480) is published quarterly for $72 per year by The American Society of Mechanical Engineers, 345 East 47th Street, New York, NY 10017. Second class postage paid at New York, NY and additional mailing offices. POSTMASTER: Send address changes to The Journal of Fluids Engineering, c/o THE AMERICAN SOCIETY OF MECHANICAL ENGINEERS, P.O. Box 3199, Grand Central Station, New York, NY 10163.
CHANGES OF ADDRESS must be received at Society headquarters seven weeks before they are to be effective. Please send old label and new address.
PRICES: To members, $36.00, annually: to nonmembers, $72.00. Single copies, $24.00 each. Add $6.00 for postage to countries outside the United States and Canada.
STATEMENT from By-Laws. The Society shall not be responsible for statements or opinions advanced in papers or . . . printed in its publications (B7.1, Par. 3).

INDEXED by the Engineering Index, Inc.

Journal of Fluids Engineering

Published Quarterly by The American Society of Mechanical Engineers

VOLUME 106 • NUMBER 1 • MARCH 1984

D. A. Johnson
Research Scientist.

D. Modarress
Professor, Mechanical Engineering,
California State University,
Long Beach, Calif. 90840

F. K. Owen
Consultant, Complere Inc.,
Palo Alto, Calif. 94302

NASA Ames Research Center,
Moffett Field, Calif. 94035

An Experimental Verification of Laser-Velocimeter Sampling Bias and Its Correction

The existence of "sampling bias" in individual-realization laser velocimeter measurements is experimentally verified and shown to be independent of sample rate. The experiments were performed in a simple two-stream mixing shear flow with the standard for comparison being laser-velocimeter results obtained under continuous-wave conditions. It is also demonstrated that the errors resulting from sampling bias can be removed by a proper interpretation of the sampling statistics. In addition, data obtained in a shock-induced separated flow and in the near-wake of airfoils are presented, both bias-corrected and uncorrected, to illustrate the effects of sampling bias in the extreme.

Introduction

The laser velocimeter makes it possible to measure the flow fields of extremely complex flows – measurements that would be impossible to make with any other technique. Of particular importance has been the application of the laser velocimeter to flows in which the turbulence exceeds that for which hot-wire anemometry can be expected to provide accurate measurements. Such flows are common in almost every engineering discipline concerned with the flow of fluids (e.g., aerodynamics, propulsion, and combustion).

As the ability to predict such complicated flow fields improves, it will become increasingly important that the experimental data used to assess and extend predictive methods be of the highest accuracy possible. Properly applied, the laser velocimeter technique can provide, in principle, accurate measurements of mean velocities and higher-order turbulence quantities even when the local turbulence level is infinite – a situation common to turbulent separated flows. There exists, however, considerable controversy whether corrections to the measurements must be made for a bias toward higher velocities when the measurements are obtained under conditions of relatively low particle concentration (i.e., conditions for which only one particle is present in the laser velocimeter sensing volume at any instant of time); these conditions usually prevail in airflow applications.

This bias toward higher velocities is commonly referred to as "sampling bias," and it is argued that it occurs because the particle arrival rate (hence, sampling rate) is dependent on the local instantaneous speed of the fluid at the sensing volume. The errors attributable to this form of biasing are only significant when the turbulence level becomes extremely high; however, it is precisely for these conditions that the potential utility of the laser velocimeter technique is the greatest.

The controversy is not so much about how to correct for sampling bias but whether a correction is warranted or not. This uncertainty has remained because of lack of conclusive experimental evidence to support or disprove the existence of this bias. As a consequence, some laser velocimetry data that are reported have been corrected for sampling bias and some have not; the latter is the most prevalent, possibly because correcting for sampling bias requires more effort in the experiment.

In this paper, experimental evidence is presented for a simple free-shear layer flow which clearly demonstrates the existence of sampling bias and how the data can be accurately corrected for this effect by a proper weighting of the velocity samples. The results are pertinent to the case in which signal processing is accomplished with a burst-period counter that uses a fixed number of fringe crossings to effect a measurement. The standard for comparison in assessing the presence of sampling bias was laser velocimeter measurements obtained at high seeding concentration levels, for which several particles were always present in the laser-velocimeter sensing volume. In addition, data obtained in a shock-induced separated flow and in the near-wake of a conventional and supercritical airfoil are presented bias-corrected and uncorrected to illustrate the effects of sampling bias in the extreme.

Background

In many practical applications of laser velocimetry in which air is the fluid media, the concentration of light-scattering particles is such that no more than one particle is present in the sensing volume at any instant. Under these conditions, the mode of operation is often referred to as individual-realization (IR) laser velocimetry to distinguish it from the continuous-wave (CW) mode, in which at least several particles are always present in the sensing volume. This latter mode of operation is prevalent in water-flow applications for which high seeding concentrations can easily be generated. At the other end of the spectrum are the applications in unseeded

Contributed by the Fluids Engineering Division and presented at the Winter Annual Meeting, Phoenix, Ariz., November 14–19, 1982, of THE AMERICAN SOCIETY OF MECHANICAL ENGINEERS. Manuscript received by the Fluids Engineering Division, March 1, 1983.

wind-tunnel environments in which the particle concentration is so sparse that the percentage of time that a particle exists in the sensing volume is extremely small relative to the percentage of time that the sensing volume is void of particles.

In the individual-realization mode, the collection of velocity information is statistical in nature, with the sampling being dependent on the occurrences of particles crossing the sensing volume. In early applications of individual-realization laser velocimetry, it was thought that the sampling of the local velocity field was random and unbiased. Consequently, statistical estimators for the mean and variances were used which assumed that the sampling was unbiased.

In 1973, well after the inception of individual-realization laser velocimetry, McLaughlin and Teiderman [1] postulated that the sampling was not totally random but biased in turbulent flows, with the probability of sampling high-velocity particles being greater than that of sampling low-velocity particles. Their arguments were based on the assumptions that the particles were homogeneously distributed in the fluid, that all particles crossing the sensing volume had an equal probability of producing a validated signal independent of speed or trajectory through the sensing volume, and that only one velocity sample was obtained for each particle transit. To show theoretically the dependence of particle arrival rate on the instantaneous speed of the flow at the sensing volume, and hence sampling bias, they also assumed that the concentration of particles was sufficiently high that the average time between particle occurrences was small compared to the time scale of the turbulence.

This assumption left open to question the sampling statistics for many applications in which the average time between particle realizations is large compared to the time scale of the turbulence. In reference [2], for example, it was suggested that the biased sampling situation discussed in reference [1] was not present at very sparse seeding conditions. It has also been proposed [3] that the sample biasing toward higher velocity particles proposed in reference [1] is either totally or partially eliminated by a compensating effect. This compensating effect is based on the argument that slower moving particles produce signals of higher amplitude than faster moving particles, as a result of the response characteristics of the detector, and hence a higher probability of producing a validated output. It has also been argued that the presence or absence of sampling bias is dependent on the type of signal processor used to extract the velocity information.

The number of papers cited in reference [4] that deal with laser velocimeter sampling bias indicates the degree of controversy that still remains on this subject.

Unfortunately, at the turbulence levels at which sampling bias becomes significant, the appropriateness of using either pitot pressure probe or hot-wire anemometer measurements as a standard for comparison must be questioned. This lack of another measurement technique that could provide a standard of comparison has been the primary reason sampling bias has not been experimentally confirmed. Moreover, there are many factors besides the sampling bias proposed in reference [1] that can affect the measurement accuracy of a laser velocimeter system. If extreme care is not taken, conclusions

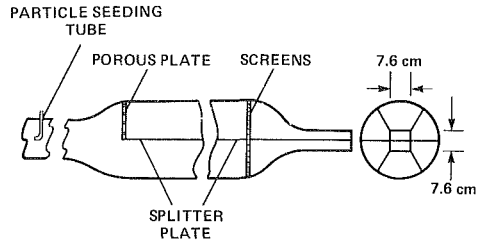

Fig. 1 Schematic of two-stream mixing flow model

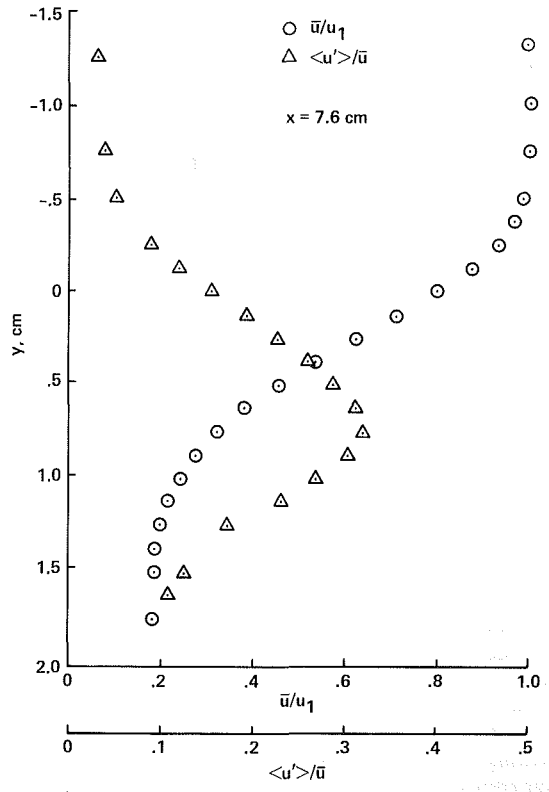

Fig. 2 Shear-layer mean velocity and turbulence intensity distributions

Nomenclature

c = chord of model
d = diameter of sensing volume
l = length of sensing volume
N = total number of velocity realizations
p = probability density function
P = probability distribution function
u = velocity component in streamwise direction
v = velocity component in normal direction
V = velocity vector, $u\hat{i} + v\hat{j} + w\hat{k}$
w = velocity component in cross-stream direction
x = streamwise distance from splitter plate
y = vertical distance from splitter plate
λ = mean particle occurrence rate
τ = interarrival time between velocity samples
τ_t = integral time scale of turbulence
ω = weighting factor for sampling bias

Subscripts

CW = continuous-wave quantity
e = boundary-layer edge conditions
i = ith velocity realization
UNW = unweighted quantity
1 = conditions at faster stream
1D = one-dimensional weighted quantity
2D = two-dimensional weighted quantity

Superscripts

$(\ )'$ = fluctuating quantity
$(\bar{\ })$ = averaged quantity
$\langle' \rangle$ = rms value of quantity

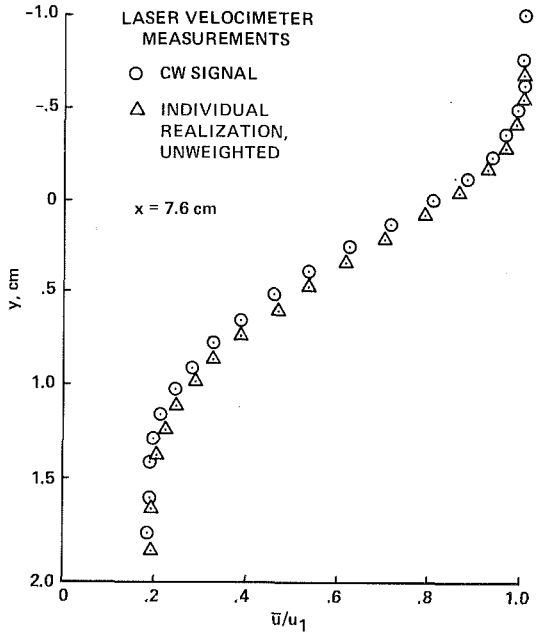

Fig. 3 Comparison of continuous-wave and individual-realization (unweighted) mean-velocity measurements

can be drawn regarding sampling bias that are really the results of some other elements of the experiment. For example, particle-concentration gradients, such as that present for a seeded air jet issuing into an environment of different particle concentration, can produce errors as large as that expected from sampling bias. The use of stationary fringes in a highly turbulent flow region also can result in measurement errors if the signal processor requires some minimum number of fringe crossings to produce a validated output. Velocity-gradient effects owing to insufficient spatial resolution, particle-lag effects, inadequate signal-to-noise ratio for accurate signal processing, and poor detector response are other sources of measurement error which can result in improper conclusions.

An apparent confirmation of sampling bias was reported by Quigley and Teidermann [5] for a two-dimensional (2D) channel flow in which the standard for comparison was the near-wall velocity gradient as inferred from the streamwise pressure gradient. However, in a later study of sampling-rate effects on sampling bias in the same facility, Bogard and Teidermann in reference [4] were unable to reproduce the earlier results of reference [5]. It would appear that the aspect ratio of the channel was insufficient for the assumption of a spanwise constant wall shear.

The approach in the present study was to use the laser velocimeter technique as its own standard for comparison. Theoretically, if particles are always present in the sensing volume, the sampling statistics are no longer dependent on particle arrival rate and sampling bias is absent. This concept was applied to obtain data free of sample bias for comparison with individual-realization results.

Experimental Approach

To experimentally assess the sampling-bias effect, a flow field was desired that had regions of high turbulence but for which a uniform concentration of seeding particles could be assured. Based on these requirements, a free-shear layer developed by two streams of unequal velocity was selected. By imposing a large difference in the velocities of the two streams, significant turbulence intensities could be generated. Contrary to a single-jet experiment, the realization of uniform seeding concentration across the shear layer was straightforward with this two-stream mixing model. Shown in Fig. 1 is a sketch of the flow model. A velocity ratio of 5:1 was generated by using a porous plate to impede the air flow in the upper stream. The mean velocity and turbulence intensity distributions for a measurement station 7.6 cm downstream of the splitter plate is shown in Fig. 2. As is conventionally done, the faster stream is shown as the upper stream in Fig. 2. As seen from Fig. 2, local turbulence levels approaching 35% are generated in this shear flow. The experiments were conducted with the faster stream traveling at 30 m/sec.

A two-color laser velocimeter system [6] designed for transonic boundary-layer studies in the Ames 2- by 2-ft Transonic Wind Tunnel was used in the study. This system uses a 40-MHz Bragg-cell shift in both colors to assure the minimum number of fringe crossings required for burst counters regardless of particle trajectory. To obtain a frequency offset more appropriate for the low speeds of the present experiment, the signals were mixed electronically. The same fringe spacing as that used in transonic testing – about 18 μm was used. Thus, the maximum Doppler frequency was only 1.7 MHz, whereas frequency offsets ranging between 2 and 4 MHz were used. With the 4-W argon-ion laser and off-axis forward light-scatter collection, the system can detect particles in the 1-μm range, even at transonic conditions. The present experiment with its low speeds (narrower bandwidth) and absence of flare sources, such as windows or solid surfaces, resulted in very high signal-to-noise ratios and high data rates when sufficient seed material was injected into the plenum.

The sensing volume diameter for this laser system is about 200 μm, well within the resolution requirements of the shear layer, which was nominally 1.25 cm thick. Because of the small angle ($\approx$2 deg) between incident beams used to establish a large fringe spacing for transonic testing, the sensing volume length was determined by the collection optics rather than by the transmitting optics. For the off-axis collection angle of 10 deg and the nominally large spatial filter of 1 mm at the detectors, the sensing volume was about 6 mm in length. Although this may appear excessive, the laser velocimeter's instantaneous spatial resolution in the individual-realization mode is determined by the particle's trajectory through the sensing volume, not by the total length of the sensing volume. Thus, fluctuations from turbulence scales much smaller than the sensing-volume length can be resolved. What must be insured is that the time-averaged quantities to be measured (e.g., $\bar{u}$, $\langle u' \rangle$, and $\overline{u'v'}$) not vary along the length of the sensing volume. For the two-dimensional shear layer of this experiment, the sensing-volume dimensions were more than adequate to meet this requirement.

The photodetector outputs were processed with burst-period counters that use eight fringe crossings to determine the period of the signal. The counters employ both a 5/8 comparison and a three-level validation circuit to minimize erroneous period readings. This latter circuit permits a validated output, only if for all eight fringe crossings the signal passes through a positive threshold, a zero level, and a negative threshold in the proper sequence.

The output from the two burst counters was recorded in two different ways. In one mode of operation, the digital output of the counters was fed directly to a desk-top computer via a multiplexer. The multiplexer could be operated in such a manner to insure that the validated data from the two velocity channels were from the same particle; it also provided interarrival times between particles. In this mode, the data rate was limited to 17 kHz. In the second mode of operation, the digital data were fed directly into a pulse-height analyzer, which sampled the output each time a validation pulse was detected from the counters. In this mode, data rates in excess

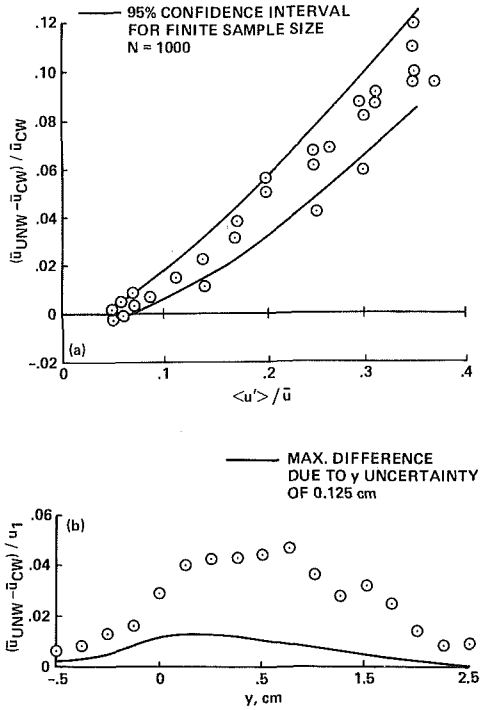

Fig. 4 Differences in continuous-wave and individual-realization (unweighted) mean-velocity measurements:
(a) As a function of turbulence level,
(b) Relative to the maximum shear-layer velocity, u_1

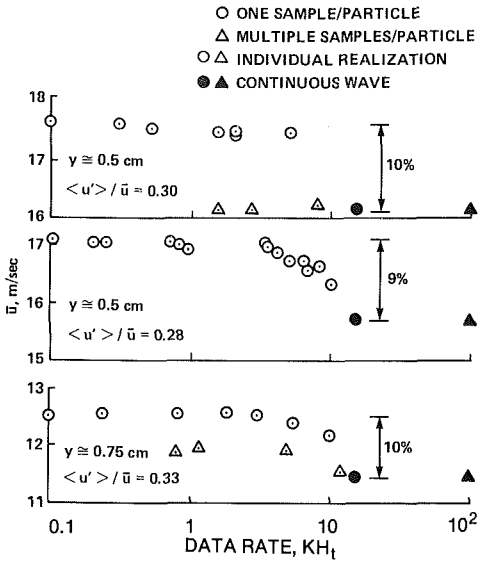

Fig. 5 Measured mean velocity as a function of data rate

of 100 kHz were achieved. The pulse-height analyzer was used to collect data in the CW mode. The primary advantage of the pulse-height analyzer was that it circumvented the problem of insufficient computer memory, allowing long averaging times even at data rates as high as 100 kHz. In this case, up to 500,000 velocity samples were accumulated at each measurement station. The other method of data acquisition via the multiplexer made possible the collection of data in a form which would allow for the correction of sampling bias at low particle concentration levels. In addition, with particle interarrival time measurements available, true time-averaged results could theoretically be obtained. As discussed later, however, the realization of sampling bias-free results at individual-realization conditions using the time-averaging approach is not nearly as straightforward as the approach of collecting data at CW conditions.

The source of air for the flow model was the 120-psig makeup air supply for the NASA Ames Unitary Wind Tunnel Plan. This air is dried to a very low specific humidity to allow supersonic testing without the formation of condensation shocks. Most of the naturally occurring particles are removed in the drying process; as a result, the air is very clean. With out artificially adding particles, data rates of only a few per second could be achieved, an ideal situation for the present experiment. It was easy to vary the concentration of particles from essentially no particles to many particles in the probe volume at any instant in time. To artificially seed the flow, an ultrasonic spray nozzle was used which generated mineral oil droplets with a mean diameter of 0.7 μm.

Equal particle concentrations in the two streams were confirmed in two ways. First, under conditions of heavy seeding (i.e., many particles in the proble volume at any instant) the dc output of the detectors was confirmed to be the same in both free streams. Assurance that the detectors were operating in the linear range was checked by varying the laser power. In the second case, the seeding level was lowered to insure single-particle occurrences. Oscilloscope sweeps of the unfiltered detector outputs were monitored for a constant threshold setting and confirmed to differ by the velocity ratio of the two streams, as it should for equal concentrations.

This latter check of the uniform seeding concentration was also a partial check on the detectors' frequency response. To confirm that there was little detector biasing, as described in reference [3], the validated signal rate of the burst counters was checked between the two streams and found to vary as the velocity ratio. This check was made with the counter cycle-time delayed to prevent multiple readings from the same particle.

Discussion

Sampling-Bias Results. Mean-velocity profiles obtained for the shear layer in both continuous wave and individual-realization modes are presented in Fig. 3. In the CW mode, the data rate was about 100 kHz, with 500,000 samples taken at each station. The individual-realization results were obtained at a particle concentration level that produced a validated data rate of only about 100 s^{-1}. In this case, between 1,000 and 4,000 samples were acquired at each measurement station. To prevent multiple readings from the same particle in the individual-realization mode, a 60-μs cycle-time between measurements was imposed on the data acquisition system. For both cases, the mean velocities were calculated from the expression

$$\bar{u} = \sum_{i=1}^{N} u_i / N, \qquad (1)$$

which assumes unbiased sampling. Under conditions of heavy seeding, the validated data rate remained essentially constant across the shear layer, and the mean-velocity results were independent of the cycle-time imposed between measurements. Both observations are consistent with CW-mode data collection. The differences in the two results follow the trends that would be expectd for sampling bias. The unweighted data indicate larger mean velocities, and the differences are greater where the turbulence levels are higher. The percent difference between the individual-realization and the CW results is shown in Fig. 4(*a*) as a function of turbulence intensity. Included in this figure is the 95 percent confidence interval for $\bar{u}$ when the sample size is limited to 1,000 readings (the minimum sample size for the individual-realization measurements). The difference in the individual-

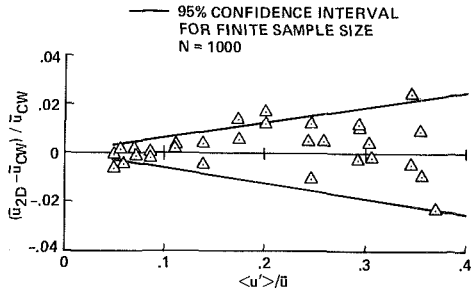

Fig. 6 Differences in continuous-wave and individual-realization (2D weighted) results as a function of turbulence level

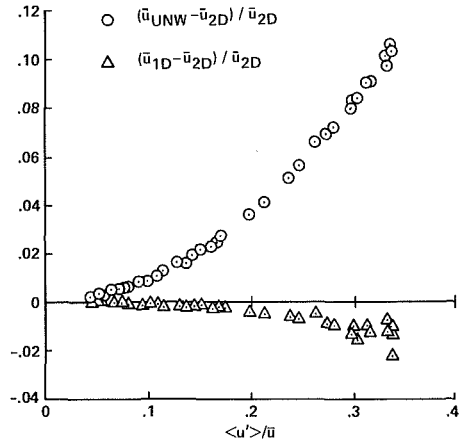

Fig. 7 Comparison of unweighted and 1D weighted mean velocities with 2D weighted mean velocities

realization and CW results are also shown in relation to the maximum velocity, u_1, in Fig. 4(*b*). This figure gives a perspective relative to overall measurement accuracy, because it is really u_1, not the local mean velocity, that dictates the precision of the measurements. The CW results are estimated to be accurate to within ± 1 percent of u_1. Included in Fig. 4(*b*) is the maximum error that could result from an estimated 0.125-mm uncertainty in y location.

The results presented in Figs. 3 and 4 clearly demonstrate that for the individual-realization mode of laser velocimetry, sampling bias exists and that it increases approximately with the square of the turbulence intensity. To investigate the dependency of this sampling error on data rate (or mean particle-arrival time), mean-velocity measurements were obtained in the region where the turbulence intensity was a maximum for a wide range of particle concentration levels. The measured mean velocities are presented in Fig. 5 as a function of data rate for three different runs in which the y location was fixed while the seeding concentration was varied. The data rates varied from 100 Hz to 100 kHz. In most of the measurements, the data acquisition cycle-time was set at 60 μs to prevent multiple readings on the same particle. With this cycle-time imposed, the CW data rate was limited to 17 kHz. The other results presented in Fig. 5 were obtained with a cycle-time of less than a few microseconds. In this mode, slower moving particles have a greater chance of being sampled more than once than do faster moving particles, thus resulting in an approximate "signal lifetime" weighting of the data.

Apparent from Fig. 5 is the independence of the sampling bias and data rate when the particle concentrations are sufficiently low for individual-realization measurements. A transition region between about 8 and 17 kHz is evident where the data acquisition system begins to control the sampling rate rather than the particle arrival rate. By allowing multiple readings on the same particle, the effect of sampling bias was totally or at least partially eliminated. This method of correcting for sampling bias can be effective, however, only if (1) the cycle-time of the data acquisition system is very short compared to the lifetime of the signals and (2) the frequency offset is large compared to the frequency shift due to velocity. In many laser velocimeter applications these conditions cannot be met.

Sampling-Bias Correction. To correct the data for sampling bias, each sample should be weighted inversely to the magnitude of the instantaneous velocity $V_i = (u_i^2 + v_i^2 + w_i^2)^{1/2}$ if the sensing volume is spherical [1]. The estimate for the mean velocity in which case is given by

$$\bar{u} = \sum_{i=1}^{N} \omega_i u_i / \sum_{i=1}^{N} \omega_i, \tag{2}$$

where the weighting factor ω_i is given by

$$\omega_i = 1/(u_i^2 + v_i^2 + w_i^2)^{1/2}. \tag{3}$$

When the sensing volume can be considered as a cylinder, the proper weighting factor can easily be shown to be given by

$$\omega_i = 1/\left[(u_i^2 + v_i^2)^{1/2} + \frac{\pi}{4}\frac{d}{l} w_i\right], \tag{4}$$

where d and l are the diameter and length of the cylinder, respectively.

In the present experiment, the sensing volume can be considered cylindrical with a length-to-diameter ratio of about 30. Thus, the particle arrival rate in the present study should depend little on the cross-stream velocity component w, and weighting the samples according to $1/(u_i^2 + v_i^2)^{1/2}$ (two-dimensional weighting model) should be quite accurate.

Instead of weighting the data with the 2D model, it has been proposed [7, 8] to weight the data according to the lifetime of the signal burst, which can theoretically treat ellipsoidal sensing volumes. The major disadvantages of this approach are that (1) signal lifetime measurements are inherently inaccurate and (2) the signal lifetime varies with particle size and the location the particle crosses the sensing volume. Since variations in signal lifetime as a result of these effects are uncorrelated with velocity, accurate unbiased results can in theory be obtained, but the sample size must be increased to average-out these contributions. To our knowledge there has been no attempt to quantify the degree to which the sample size would have to be increased. If the variances caused by these effects are large, as we suspect, the required sample sizes could be prohibitively large for many applications.

The effectiveness of the 2D weighting model in correcting the biased data is demonstrated in Fig. 6. The weighted data are compared with the CW data as a function of turbulence level. To within the data scatter, the 2D weighted results agree with the CW data. The scatter in the data is primarily a result of the limited sample sizes of the individual-realization results. Figure 7 shows the difference between the unweighted data and the 2D weighted data as a function of turbulence level. In this case, the scatter is reduced since the same data samples are involved. The amount of correction is approximately equal to the square of the intensity of turbulence. Included in Fig. 7 are results using the approximate one-dimensional correction, $\omega_i = 1/u_i$, proposed in reference [1]. For this particular flow, this correction of the mean velocity was quite effective, but obviously, it is inappropriate for turbulent separated flows because of the singularity at $u_i = 0$.

As in the calculation of the mean velocities, the presence of sampling bias requires that a weighting be applied in the calculation of the higher-order turbulence quantities $\langle u' \rangle$, $\langle v' \rangle$, and $u'v'$. The statistical estimators become

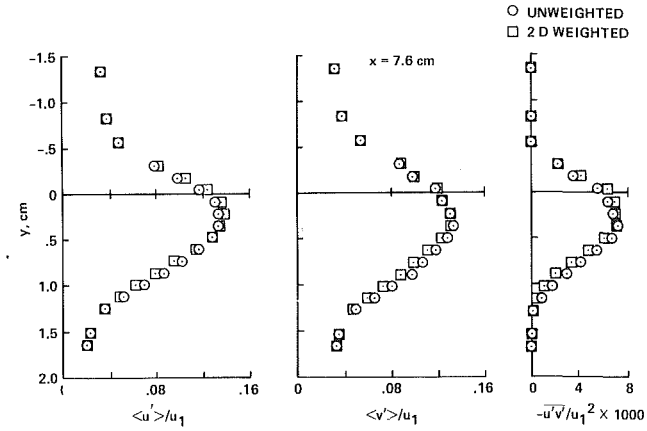

Fig. 8 Unweighted and 2D weighted turbulence intensity and Reynolds shear-stress results

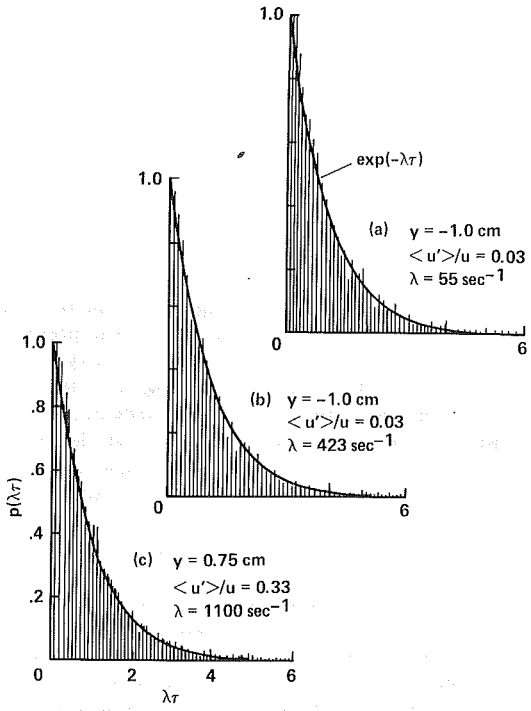

Fig. 9 Particle interarrival time distributions: (a) Outside shear layer; (b) Outside shear layer; (c) Within shear layer

$$\langle u' \rangle = \left[\frac{\sum_{i=1}^{N} \omega_i (u_i - \bar{u})^2}{\sum_{i=1}^{N} \omega_i} \right]^{1/2}, \tag{5}$$

$$\langle v' \rangle = \left[\frac{\sum_{i=1}^{N} \omega_i (v_i - \bar{v})^2}{\sum_{i=1}^{N} \omega_i} \right]^{1/2}, \tag{6}$$

and

$$\overline{u'v'} = \frac{\sum_{i=1}^{N} \omega_i (u_i - \bar{u})(v_i - \bar{v})}{\sum_{i=1}^{N} \omega_i}. \tag{7}$$

In Fig. 8, measurements of $\langle u' \rangle$, $\langle v' \rangle$, and $\overline{u'v'}$, obtained under individual-realization conditions, are presented for $\omega_i = 1$ (unweighted), and $1/(u_i^2 + v_i^2)^{1/2}$. As evident from this figure, the differences in the weighted and unweighted results are not large. Results for $\omega_i = 1/u_i$ were also obtained although not shown in this figure. These 1D model results were nearly identical to those for the 2D model. The effect of sampling bias for this flow is primarily a shift in the probability density function toward lower velocities, with the variances remaining nearly unchanged. It would be extremely difficult with these small differences to verify the effects of sampling bias on turbulence intensity and Reynolds shear-stress measurements. Moreover, theere is no standard available. Uncertainties in the measurements of these quantities in the CW mode arise from Doppler ambiguity effects [9] and spatial averaging if the sensing volume is relatively long. This latter effect in the present experiment resulted in $\overline{u'v'}$ dropping by a factor of 2 under CW conditions. Improvement of the cross-stream resolution by the insertion of a 0.3-mm pinhole in the collection optics raised the shear stress to about 80 percent of that obtained under individual-realization conditions.

Although the turbulence intensities and shear stress for the present flow were not markedly influenced by sampling bias, this is not necessarily the case for flows with a more extreme turbulence, as illustrated by the complex flow examples presented in a later section.

Interarrival Time Statistics. In the early phases of this work, the plan was to verify the existence of sampling bias by comparing mean velocities calculated by the two expressions

$$\tilde{u} = \sum_{i=1}^{N} u_i / N \tag{8}$$

and

$$\tilde{u} = \sum_{i=1}^{N} u_i \tau_i / \sum_{i=1}^{N} \tau_i \tag{9}$$

at individual-realization conditions but at very high sample rates. In equation (9), τ_i is the interarrival time between velocity samples. When τ_i is always sufficiently less than the integral time-scale of the turbulence, τ_t, equation (9) should be a good estimate of the desired time-averaged mean velocity [10]. This approach was generally unsuccessful, however, because in most cases either the data rate was too low for $\tau_i << \tau_t$ to be satisfied or the data rate was so high that τ_i was being controlled by the cycle-time of the data acquisition system (≈ 60 μs) rather than by the particle arrival rate.

In either of these situations, both expressions will give the same answer. At the lower data rate, both are affected by sampling bias and at the high data rate neither is affected. A positive result of this exercise, however, was the determination of particle interarrival time distributions. These distributions at first did not agree with our preconceived notions but were later shown to be consistent with Poisson statistics. It was expected that the most likely interarrival time would correspond to the average interarrival time (i.e., the reciprocal of the mean data rate); that this was not the case is shown in Fig. 9, where measured interarrival time distributions are presented. Instead, the likelihood monotonically increases as τ approaches zero; however, this behavior is what should be expected for a Poisson process, as shown in the next paragraph.

The probability of no particle occurrences, say in the time interval τ_a, is given by

$$P(0, \lambda\tau_a) = \int_{\lambda\tau_a}^{\infty} p(\lambda\tau) d\lambda\tau, \tag{10}$$

where λ is the mean particle occurrence rate and $p(\lambda\tau)$ is the

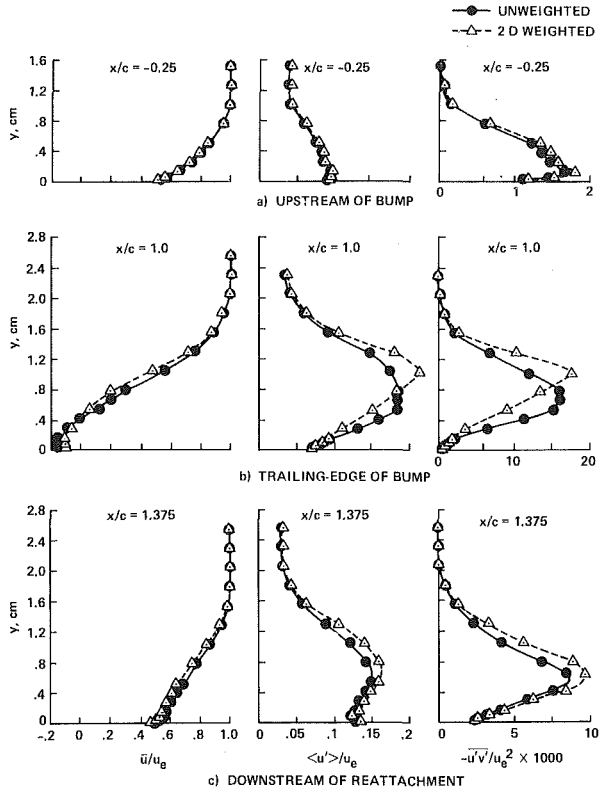

Fig. 10 Uncorrected and bias-corrected results; axisymmetric bump model ($M_\infty = 0.875$)

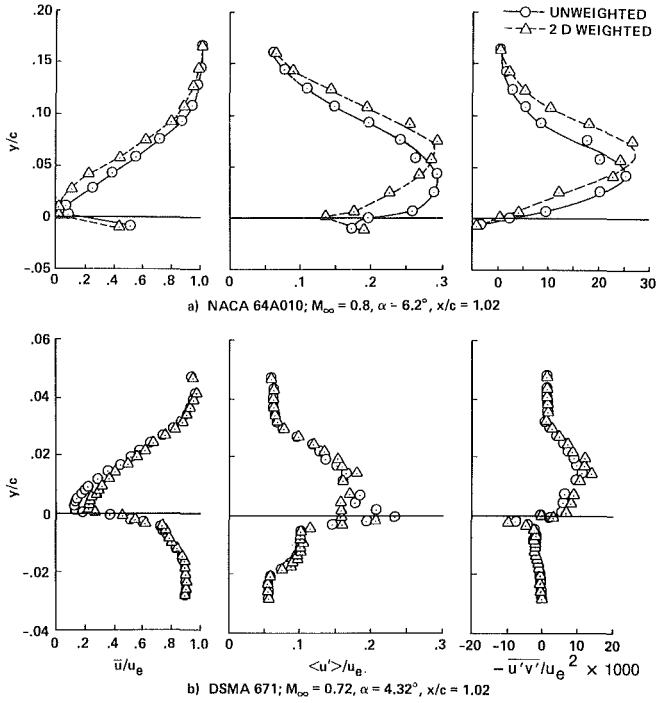

Fig. 11 Uncorrected and bias-corrected results; airfoil models

probability density function of the interarrival times [it is $p(\lambda\tau)$ which is presented in Fig. 9]. Equation (10) states that the probability of no particle in the time interval, τ_a, is given by the probability that the interarrival time τ_i is greater than or equal to τ_a. But if the particle arrivals obey Poisson statics, then the following must be true if the local velocity is invariant (e.g., steady laminar flow):

$$P(0,\lambda\tau_a) = \exp(-\lambda\tau_a). \tag{11}$$

It follows from equations (10) and (11) that $p(\lambda\tau)$ must be given by the following:

$$p(\lambda\tau) = \exp(-\lambda\tau). \tag{12}$$

Equation (12) is plotted in Fig. 9 and describes the measurements almost exactly. It is evident from Fig. 9 that for very small τ the probability of a particle occurrence is given by $\lambda\tau$, which must be true in a Poisson process.

Although equation (12) is strictly valid only when the local velocity is invariant, it was found to describe $p(\lambda\tau)$ quite well even where the turbulence intensity was a maximum, as seen in Fig. 9(*c*). This observation that the distribution of $\lambda\tau$ for even moderately high turbulence levels is primarily dependent on the spatial distribution of the particles rather than the local turbulence level can be theoretically shown. However, such an analysis would be beyond the scope of the present paper.

Complex Flows. The real concern of sampling-bias effects is not for the simple flow of the present experiment but for complex flows in which the turbulence levels are more extreme. For these flows, the effects of sampling bias can be considerably larger. In this section, uncorrected and sample-bias-corrected data are presented for several separated flow cases previously investigated [6, 11-13]. These data are presented to illustrate the levels of error that can result if no account of sampling bias is taken.

The first flow example is that generated on an axisymmetric model designed for study of interactions between transonic shock waves and turbulent boundary layers. The model consists of an axisymmetric circular bump affixed to a hollow 15-cm-diam cylinder aligned with the oncoming flow. The profile data shown in Fig. 10 were obtained at a free-stream Mach number of 0.875, which was sufficiently high to cause boundary-layer separation just downstream of the shock wave ($x/c = 0.7$). Data at three measurement stations are presented. The first station, $x/c = -0.25$, is just upstream of the bump, where a relatively mild adverse pressure gradient is present. The second station, $x/c = 1.0$, is at the trailing edge of the bump, where the separation bubble is the thickest. The remaining station, $x/c = 1.375$, was the farthermost downstream measurement station. Reattachment occurred at $x/c = 1.1$. The uncorrected and bias-corrected turbulent shear-stress distributions at $x/c = 1.0$ show a trend similar to that observed for the simple shear flow of the previous section (Fig. 8). At this streamwise station, the flow is basically a detached shear layer.

For separated flows, the situation where u_i and v_i are identically zero can arise, for which the two-dimensional weighting model is singular. In practice, however, these occurrences are so rare that they can be ignored without significantly affecting the statistical estimates. The condition where $u_i = v_i = 0$ can only occur if (1) the particle comes to rest in the sensing volume or (2) the particle enters the sensing volume from the side ($w_i \neq 0$). The likelihood of the former ($u_i = v_i = w_i = 0$) is very low, and, if the sensing volume is cylindrical with $l/d >> 1$, the latter also has a very low likelihood. For the data presented in this section, the number of samples with $u_i = v_i = 0$ never exceeded 0.3 percent of N, and most of these occurrences could have been the result of the finite clock frequency of the counters, which limited resolution of u_i and v_i to approximately $0.02u_e$.

The other two flow examples are for a NACA 64A010 and a supercritical (DSMA 671) airfoil section at transonic conditions. Profile data obtained just downstream of the trailing edges of these two airfoils are presented in Fig. 11. The data for the 64A010 section were obtained under conditions of shock-induced separation, whereas the supercritical section

data were obtained at near-cruise conditions (only a very small separation bubble was present at the trailing edge).

To some readers, the differences in the uncorrected and bias-corrected results in Figs. 10 and 11 may seem large. Others may consider them small in light of the difficulty of the measurements. The obvious question, and one that remains to be answered, is whether the differences are sufficiently large to cause erroneous conclusions pertaining to turbulence model formulations.

Concluding Remarks

The presence of sampling bias effects in individual-realization laser velocimeter mean-velocity measurements has been demonstrated in a free-shear layer flow by using laser-velocimeter results obtained under continuous-wave conditions as the *standard* for comparison. It has also been demonstrated that these bias effects are independent of sampling rate provided the seeding concentration is sufficiently low to insure individual-realization measurements. A two-dimensional weighting of the velocity samples was shown to be effective in correcting the individual-realization measurements for the sampling bias. This correction is valid provided the length of the laser velocimeter sensing volume is reasonably long in comparison to its cross section, as was the case in the present experiment (this generally is true for most laser-velocimeter systems). Although a confirmation of sampling-bias effects on higher-order turbulence quantities, such as the turbulence intensities and Reynolds shear-stress, could not be made since no standard is available in this case, it follows that the statistical estimators for these quantities must also include appropriate weighting for sampling bias.

Only at extreme levels of turbulence ($\langle u' \rangle / \bar{u} > 0.2$, approximately) do sampling-bias effects become important. At lower turbulence levels, the effects of sampling bias are generally less than the overall experimental uncertainty. However, in the case of turbulent separated flows, the effects can be significant, as illustrated in the transonic-flow cases presented in this paper, and the possibility of making erroneous conclusions regarding the physical aspects of a flow as a result of ignoring these effects cannot be ruled out.

References

1 McLaughlin, D. K., and Teiderman, W. G., "Biasing Correction for Individual Realization Laser Anemometer Measurements in Turbulent Flows," *Physics of Fluids*, Vol. 16, Dec. 1976, pp. 2082–2088.

2 Barnett, D. O., and Bentley, H. T. III, "Bias of Individual Realization Laser Velocimeters," *Proceedings of the Second International Workshop of Laser Velocimetry*, Purdue University, Vol. 1, Mar. 1974, pp. 438–442.

3 Durao, D. F. G., Laker, J., and Whitelaw, J. H., "Bias Effects in Laser Doppler Anemometry," *Journal of Physics E: Scientific Instruments*, Vol. 13, Apr. 1980, pp. 442–445.

4 Thompson, H. D., and Stevenson, W. H., eds., "Laser Velocimetry and Particle Sizing," *Proceedings of the Third International Workshop on Laser Velocimetry*, Purdue University, Hemisphere Publishing Corp., Washington, D.C., 1979.

5 Quigley, M. S., and Teiderman, W. G., "Experimental Evaluation of Sampling Bias in Individual Realization Laser Anemometry," *AIAA Journal*, Vol. 15, Feb. 1977, pp. 266–268.

6 Johnson, D. A., and Bachalo, W. D., "Transonic Flow about a Two-Dimensional Airfoil—Inviscid and Turbulent Flow Properties," *AIAA Journal*, Vol. 18, Jan. 1980, pp. 16–24.

7 George, W. K., "Limitations to Measuring Accuracy Inherent in the Laser Doppler Signal," *Proceedings of the LDA-Symposium Copenhagen*, Hemisphere Publishing Corp., Washington, D.C., 1975.

8 Hoesel, W., and Rodi, W., "New Biasing Elimination Method for Laser Doppler Velocimeter Counter Processing," *Review of Scientific Instruments*, Vol. 48, July 1977, pp. 910–919.

9 George, W. K., and Lumley, J. L., "The Laser-Doppler Velocimeter and Its Application to the Measurement of Turbulence," *Journal of Fluid Mechanics*, Vol. 60, 1973, pp. 321–362.

10 Dimotakis, P. E., "Single-Particle Laser Doppler Measurements of Turbulence," AGARD SP 193, Paper No. 10, AGARD Symposium on Non-Intrusive Instrumentation in Fluid Flow Research, St. Louis, France, 1976.

11 Bachalo, W. D., and Johnson, D. A., "An Investigation of Transonic Turbulent Boundary Layer Separation Generated on an Axisymmetric Flow Model," AIAA Paper 79-1479, Williamsburg, Va., July 23-24, 1979.

12 Johnson, D. A., Horstman, C. C., and Bachalo, W. D., "A Comprehensive Comparison Between Experiment and Prediction for a Transonic Turbulent Separated Flow," AIAA Paper 80-1407, Snowmass, Colo., July 14-16, 1980.

13 Johnson, D. A. and Spaid, F. W., "Measurements of the Boundary Layer and Near Wake of a Supercritical Airfoil at Cruise Conditions," AIAA Paper 81-1242, Palo Alto, Calif., June 23-25, 1981.

J. H. Lienhard V
Research Assistant,
Department of Chemical, Nuclear, and
Thermal Engineering,
University of California,
Los Angeles, Calif. 90024

J. H. Lienhard (IV)
Professor of Mechanical Engineering,
University of Houston,
Houston, Texas 77004,
Fellow ASME

Velocity Coefficients For Free Jets From Sharp-Edged Orifices

The viscosity-dependence of the velocity coefficient for a free liquid jet, issuing from a sharp-edged orifice, is predicted by computing the dissipation of energy in the boundary layer on the back of the orifice plate. The prediction is upheld by the only known direct measurements of velocity coefficients. The resulting coefficients are much closer to unity for large orifices than they are generally assumed to be. The influence of surface tension on small jets is also explained.

Objective

The common wisdom of the textbooks has it that the coefficient of velocity for a free jet leaving sharp-edged orifice is about 0.98 and that it is weakly dependent on viscosity. Nothing is normally said about the influence of surface tension. The issue has lain fallow in this state since before WW II.

An increasing use of miniature fluid flows in modern technologies gives us reason to re-examine this issue. Such applications as the IBM ink-jet printer (see e.g. [1]), the use of small free jets to achieve very high heat removal rates (see e.g., [2]), the use of colliding jets to create combustion sprays (see e.g. [3]), and many other configurations create a need to know more about the velocity of small jets.

Our aim is therefore to predict the velocity coefficient, C_v, chiefly for the most basic delivery system – a sharp-edged orifice. To do this we calculate the influence of viscosity, and question the role of surface tension as well.

On Measurements of C_v

Figure 1 shows the configuration of a sharp-edged orifice, and of a Borda mouthpiece. It also defines the terms we use. These include the coefficient of discharge, C_D; the coefficient of contraction, C_c; and the coefficient of velocity, C_v.

By 1908 many detailed measurements of C_D had been made for sharp-edged orifices, and it was well-known that for ideal flows:

$$C_c = \frac{\pi}{\pi+2} = 0.6110 \tag{1}$$

Some C_v's had been measured by the ballistic method or by measuring the rise of a vertically oriented jet (see e.g., [4].) Both methods underestimated C_v by including aerodynamic losses. Direct pitot tube measurements were not very accurate. Often C_v was reported as C_D/C_c, where C_c had been obtained with calipers or simply assumed to be 0.611. It was not uncommon to report the *assumption* that C_v was 0.97 or 0.98. This state of affairs is clearly reported in [4].

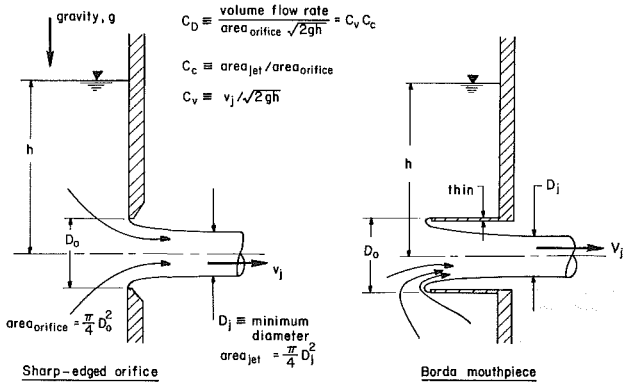

Fig. 1 Configuration and definition of terms

In 1908 Judd and King [5] conducted a remarkably accurate experiment in which they independently measured: C_D with a catch tank, C_c with a micrometer calipers, and C_v with a *differential* pitot tube – one that compared the dynamic pressure, in traverses across the jet, with static pressure upstream. The three measurements satisfied $C_D = C_c C_v$ very closely. For $D_o \geq 2$ in. and $h \geq 10$ ft they obtained $0.99995 \leq C_v \leq 0.99999$, and all their C_v values exceeded 0.9995.

Subsequent measurements of C_D culminated in the work of Medaugh and Johnson [6] who used a 1 in. orifice and found that C_D approached 0.595 at high heads. Unfortunately Judd and King measured C_D closer to 0.61 in their 1 in. orifice. Even though their largest orifice also gave $C_D \approx 0.595$, the comparison of their 1 in. orifice data with Medaugh and Johnson's results had the unfortunate effect of impugning their otherwise good work.

Medaugh and Johnson actually pointed out that C_c is highly susceptible to any minor malformation of an orifice. This explains why Judd and King's smaller orifice gave higher values of both C_c and C_D even though their measurements were accurate.

A careful reading of the literature up to 1940 thus shows

Contributed by the Fluids Engineering Division of THE AMERICAN SOCIETY OF MECHANICAL ENGINEERS and presented at the 7th Annual/Energy-Sources Technology Conference and Exhibition, New Orleans, La., Feb. 11-17, 1984. Manuscript received by the Fluids Engineering Division, August 2, 1983. Paper No. 84-FE-3.

that for large accurately-shaped sharp-edged orifices under high heads

$$C_c \leqslant 0.595 \quad \text{and} \quad C_v = 1.0000 \tag{2}$$

while the textbooks have reported

$$C_c = 0.611 \quad \text{and} \quad C_v \simeq 0.98$$

We next undertake to make a prediction of C_v that will reproduce Judd and King's data and apply to much smaller orifices as well. We presume that $C_v = fn(D_0, gh, \sigma, \rho, \mu)$, so the prediction should take the dimensionless form:

$$C_v = f(\text{Re}, \text{We}) \tag{3}$$

where we use the ideal jet velocity, $\sqrt{2gh}$, to define:

$$\text{Reynolds No., Re} \equiv \rho\sqrt{2gh}\, D_0/\mu = \sqrt{2gh}\, D_0/\nu$$

$$\text{Weber No., We} \equiv \rho(2gh)D_0/\sigma$$

and where it remains to be seen whether We really influences C_v.

Mechanical Energy Balance

Our analysis is based on conservation of mechanical energy. By constructing the balance among incoming, outgoing, and dissipated mechanical energy we are able to determine the roles of viscosity and surface tension in retarding a liquid jet issuing from a sharp-edged orifice.

We consider a control volume (C.V.) surrounding a sharp-edged orifice, with liquid entering far above the orifice and exiting at a downstream point in the jet, where contraction has been fully completed. Denoting the volume flowrate as Q and the ambient pressure as p_∞, we have:

rate of mech. energy in

= rate of mech. energy out + rate of visc. dis.

For the circular orifice this takes the form:

$$\underbrace{\rho ghQ}_{(1.)} + \underbrace{p_\infty Q}_{(2a.)} = \underbrace{p_\infty Q}_{(2b.)} + \underbrace{(\rho v_j^2/2)Q}_{(3.)} - \underbrace{\pi D_j \sigma v_j}_{(4a.)} + \underbrace{\pi D_j \sigma v_j}_{(4b.)} + \underbrace{\dot{E}_\mu}_{(5.)} \tag{4}$$

where the significance of the terms is as follows:

(1.) rate of potential energy into C.V.
(2*a*.) rate of work done on C.V. by atmosphere on top.
(2*b*.) rate of work done by C.V. on atmosphere at exit.
(3.) rate of outflow of kinetic energy
(4*a*.) rate of work done on C.V. by surface tension
(4*b*.) rate of outflow of surface energy
(5.) rate of viscous dissipation.

Terms (2*a*. and 4*a*.) cancel (2*b*.) and (4*b*.) so we are left with

$$\rho ghQ = (\rho v_j^2/2)Q + \dot{E}_\mu \tag{4}$$

Thus, no net pdV work is done, and there is also no net effect of surface tension. Using $v_j^2 = C_v^2(2gh)$, we can rearrange equation (4) as

$$C_v = \sqrt{1 - \frac{\dot{E}_\mu}{\dot{E}_f}} \tag{5}$$

where $\dot{E}_f = \rho ghQ$ is a characteristic kinetic energy associated with the liquid efflux (note that the square of the ideal jet velocity is $2gh$). This is the desired expression for C_v. However, before evaluating $\dot{E}_\mu$, we should consider more carefully the surprising disappearance of surface tension.

The Influence of Surface Tension

Our energy accounting shows the clean cancellation of the surface energy outflow and work done by surface tension in the contracted portion of the jet before Rayleigh breakup occurs. Yet net surface energy *is* carried away. We therefore look for the exchange between kinetic energy and surface energy to be made where Rayleigh breakup occurs, but not before.[1] The overall surface energy of the finite unbroken length of a jet stays more-or-less the same once the jet and its breakup length are established; and a continuous exchange of surface tension work with surface energy takes place within it.

However in the breakup portion, wavy segments are nipped off on the downstream side, creating an unbalanced force on the upstream side until it is too nipped off. The absence of the downstream surface tension force prevents the upstream transfer of surface tension work which allowed the surface energy to be smoothly transported downstream without affecting the jet. The only influence surface tension *can* have on the jet velocity, is that of retarding the droplets during breakup.

[1] We are most grateful to Lloyd M. Trefethen [7] for extremely helpful discussions in which he helped us to see through this paradoxical situation.

Nomenclature

C = constant in $U(r) = Cr^m$
C.V. = control volume
C_c, C_D, C_v = coefficients of contraction, discharge, and velocity defined in Fig. 1
C_{v_d} = coefficient of velocity based on droplet velocity, v_d
D_0, D_j = diameters of orifice and of contracted jet (see Fig. 1)
$\dot{E}_f$ = a characteristic rate of kinetic energy flow in a jet, ρghQ
$\dot{E}_\mu$ = rate of dissipation of energy as a result of the jet
$f(\eta)$ = dimensionless stream function (see equation (11))
g = gravitational body force per unit mass
h = head
k = constant which defines axisymmetric body shape: $r_0 \propto r^k$
K_1, K_2 = constants defined in equations (16) and (18)
m = constants in $U(r) = Cr^m$
p_∞ = ambient pressure
Q = flow rate (m^3/s in 3-dim case, m^2/s in 2-dim case)
r, y = coordinates along the surface of an axisymmetric body in the direction of flow, and normal to it
r_0 = radius of revolution of an axisymmetric body
Re = Reynolds number, $D_0\sqrt{2gh}/\nu$
$U(r)$ = velocity of flow just outside of a boundary layer
u, v = r and y velocity components
V = volume
v_j, v_d = actual velocity of jet; actual velocity of droplets after Rayleigh breakup
We = Weber number, $\rho D_0(2gh)/\sigma$
α = a positive constant in equations (11) and (12) which takes the form $2k+1$
η = similarity parameter defined by equation (12)
μ, ν = viscosity; kinematic viscosity $= \mu/\rho$
ρ = density of liquid
σ = surface tension

We can clarify this by balancing mechanical energy over a C.V. containing only the portion of the jet undergoing varicose instability. The net rate of energy inflow from upstream is $(\rho ghQ - \dot{E}_\mu)$, and (with the other end of the C.V. beyond the end of the jet) the net outflow is zero. The droplets then store kinetic and surface energies at the rate

$$\left(\frac{1}{2}\rho v_d^2 + \pi D_j v_d\right)Q,$$

where v_d is the droplet velocity. No net work is done and we neglect any viscous dissipation by the surface waves. If we let $C_{v_d} \equiv v_d/\sqrt{2gh}$, then some algebra gives

$$C_{v_d} \equiv \sqrt{1 - \frac{8}{\mathrm{We}\sqrt{C_c}} - \frac{\dot{E}_\mu}{\dot{E}_f}} \tag{6}$$

for a circular jet. The same logic gives

$$C_{v_d} = \sqrt{1 - \frac{4}{\mathrm{We}C_c} - \frac{\dot{E}_\mu}{\dot{E}_f}} \tag{7}$$

for a slot jet, where C_c for a slot is D_j/D_0 instead of $(D_j/D_0)^2$. As anticipated, the effect of surface formation is to retard the droplets formed at breakup.

This situation is quite evident when we view the breakup of water bells created by the coaxial collision of two equal jets at modest values of We. (See, e.g., the photographs in [8]). The resulting sheets (or water bells) spread out very thin but they suffer *no reduction* of velocity until surface forces exactly balance momentum. Then the large beads of liquid that form are observed to leave with a much reduced velocity.

Thus, while equations (6) and (7) apply to the drops formed when the jets break up, they do *not* apply to the unbroken jet, and $C_v \neq fn(\mathrm{We})$. Conversely, when the sum of the rates of creation of surface energy and of viscous loss exceed the rate of supply of potential energy, the radicals in equations (6) and (7) become imaginary, signifying that liquid can no longer escape from the orifice. As this condition approaches, the breakup region moves upstream toward the orifice, we lose the well-defined region of full contraction, the surface forces become increasingly dominant (We decreases), and C_{v_d} finally reaches zero when the jet can no longer flow freely.

To check this limiting behavior, Chen [9] ran the following experiment: He glued standard 0.65 mm, 0.749 mm, and 1.50 mm ASME sharp-edged brass orifices to the bottom of a 20 mm ID vertical graduated tube. Water inflow to the tube was regulated to give a very slowly falling head. When the vertically issuing jet stops flowing freely and starts chugging, we call $C_{v_d} = 0$. At that point, water can only escape by repeatedly wetting the metal outside the hole and oozing out. The only significant "error" in this experiment is that related to identifying the exact point which chugging begins. That uncertainty is about ± 10 percent.

The results of the experiments were as follows (we neglect $\dot{E}_\mu$ since there can be no dissipation when there is no flow.):

D_0(mm)	minimum h (mm) for steady flow	$\mathrm{We} = \frac{\rho D_0(2gh)}{\sigma}$	C_c if $\mathrm{We}\sqrt{C_c} = 8$
0.65	30	7.95	1.01
0.794	25	7.76	1.06
1.50	13	7.73	1.07

The results verify that surface tension throttles the flow as we would expect it to do. The fact that C_c is on the order of unity is consistent with our understanding that contraction is completely suppressed in small enough orifices and slow enough flow rates.

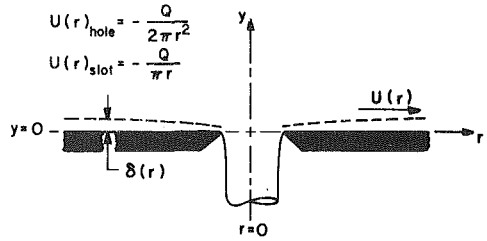

Fig. 2 Potential flows for boundary analyses

The Influence of Viscous Dissipation

We now return to the problem of evaluating $\dot{E}_\mu$, the rate of viscous dissipation of energy, which must be known in order to evaluate *either* C_v or C_{v_d}.

The viscous dissipation is obtained by integrating the incompressible dissipation function, $\mu(\partial u/\partial y)^2$, over and through the volume, V, of the boundary layer (see notation in Fig. 2.). Thus

$$\dot{E}_\mu = \mu \int_V (\partial u/\partial y)^2 dV \tag{8}$$

To evaluate this integral we must find $\partial u/\partial y$ in the boundary layer. The axisymmetric boundary layer equations are

$$\left.\begin{aligned} &\frac{\partial}{\partial r}(r_0 u) + r_0 \frac{\partial v}{\partial y} = 0 \\ &u\frac{\partial u}{\partial r} + v\frac{\partial u}{\partial y} = U\frac{dU(r)}{dr} + \nu\frac{\partial^2 u}{\partial y^2} \end{aligned}\right\} \tag{9}$$

where $r_0 = r_0(r)$ is the radius of revolution of body on which the boundary layer lies and r is the coordinate along the surface ($r_0 = r$ for the orifice plate). The pressure gradient term (see Fig. 2) becomes:

$$U\frac{dU}{dr} = \begin{cases} -\dfrac{Q}{2\pi^2}\dfrac{1}{r^5} \text{ for a hole where } Q = Q\dfrac{m^3}{s} \\ -\dfrac{Q}{\pi^2}\dfrac{1}{r^3} \text{ for a slot where } Q = Q\dfrac{m^2}{s} \end{cases} \tag{10}$$

if we use the far-field velocity distribution along the wall.

It is easy to show that the velocity potential at the wall for a two-dimensional slot flow (as given, for example, in [10]) has exactly the far-field form ($U(r) = Q/\pi r$) all the way up to the lip. We have *presumed* that this is also the case for flow through a circular hole.

Axisymmetric boundary layer flows for which $U(r) = Cr^m$ are self-similar under the transformation $(r,y) \rightarrow (r,\eta)$, with the stream function:

$$\Psi(r,\eta) = r_0(\pm \nu r U/\alpha)^{1/2} f(\eta) \tag{11}$$

and the similarity variable:

$$\eta = y(\pm \alpha U/\nu r)^{1/2} \tag{12}$$

where: α is an arbitrary constant, greater than zero; we consider $r_0 \propto r^k$ (where k is a constant); and the minus sign applies when the constant, C, is negative. If α is chosen as $2k+1$, we obtain the $f(\eta)$ appropriate to the Falkner-Skan flow for which $U \propto r^{m/\alpha}$ (see e.g., Batchelor [13], Sect. 5.9; White [11], Sect. 4-3, 4-9.)

Equation (8) now becomes

$$\dot{E}_\mu = \mu \int_V [U(r)]^2 \eta_y^2 (f''(\eta))^2 dV \tag{13}$$

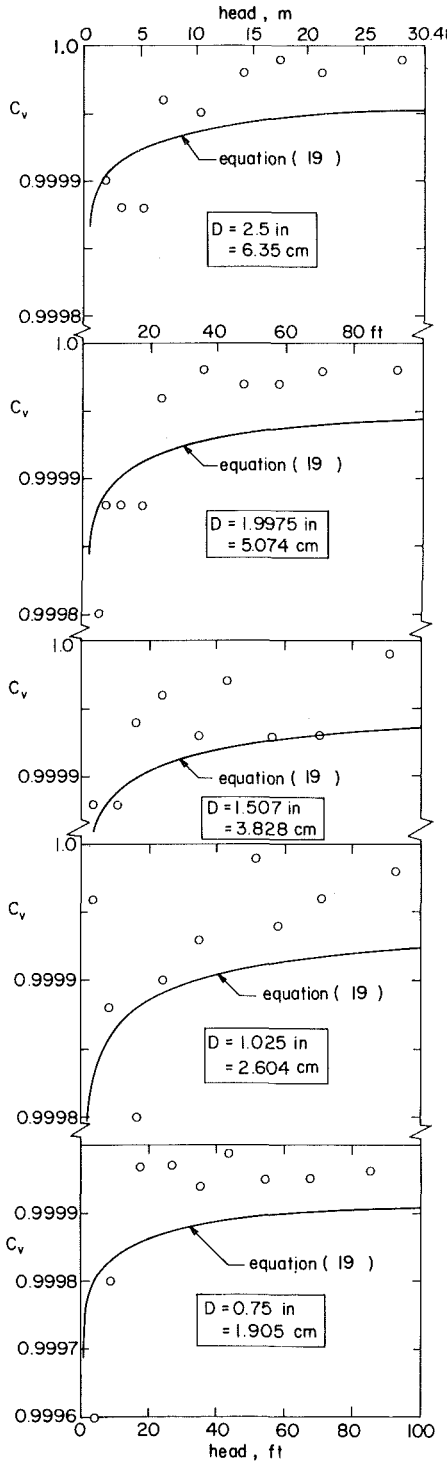

Fig. 3 Comparison of equation (19) with the data of Judd and King

and dV can be transformed with

$$\left.\begin{aligned} 2\pi r dr dy &= 2\pi |J(r,\eta)| r dr d\eta \quad \text{for the circular hole} \\ 1\, dr dy &= 1\, |J(r,\eta)|\, dr d\eta \quad \text{for the slot (per unit depth).} \end{aligned}\right\} \tag{14}$$

and the Jacobian is evaluated as

$$|J(r,\eta)| = |J(r,y)|^{-1} = \frac{1}{\eta_y} \tag{15}$$

Combining equations (13), (14), and (15), and using various preceding definitions, we get

$$\dot{E}_\mu = \dot{E}_f \frac{C_D{}^{3/2}}{\sqrt{\mathrm{Re}}} K_1 \int_0^\infty (f''(\eta))^2 d\eta \tag{16}$$

where

$$\left.\begin{aligned} K_1 &= 0.494872 \quad \text{for the circular hole} \\ K_1 &= 0.457316 \quad \text{for the slot} \end{aligned}\right\} \tag{17}$$

For the slot, $r_0 = \text{constant} \to \infty$ and we recover a well-known Jeffrey-Hamel wedge flow (see e.g., [11] Sect. 3-8.7). For the circular hole, $r_0 = r$ and we obtain a nonlinear ordinary *d.e.* in $f(\eta)$. (The latter case is included by Crabtree, Küchmann, and Sowerby [12].)

The dissipation integral was evaluated numerically for both cases, giving

$$K_2 \equiv K_1 \int_0^\infty (f''(\eta))^2 d\eta = \begin{cases} 0.242738 & \text{for the hole} \\ 0.284832 & \text{for the slot} \end{cases} \tag{18}$$

where the estimated accuracy of K_2 is at least 5 significant figures. Thus

$$C_v = \sqrt{1 - \frac{K_2 C_D{}^{3/2}}{\sqrt{\mathrm{Re}}}} \tag{19}$$

An easy calculation shows that 99 percent of the viscous loss occurs within 1.36 diameters of the edge of the circular hole (4.50 diameters for the slot), so that our infinite plate analysis is valid for fairly small plates if they have the appropriate potential flow.

Results

We thus advance equation (19) as the correct expression for C_v for jets leaving slots and orifices, before any air drag or droplet breakup has occurred. The expressions cannot be applied below

$$\mathrm{We} \simeq \begin{cases} 8 & \text{for a circular hole} \\ 4 & \text{for a slot} \end{cases} \tag{20}$$

Equation (19) requires knowledge of C_c, however its influence is secondary. At high values of Re it is adequate to guess $C_c \simeq 0.6$, and even to simplify the computation by taking $C_D = C_c$ under the radical, although we have made no such simplifications here.

Equation (19) is compared with Judd and King's data in Fig. 3. The comparison is good within the variability of the data but that variability is clearly large. We should be aware that Judd and King's C_v data depended on measurements of differential heads on the order of (1/20) in. of water, with manometer deflections on the order of (1/2) in. If we bear in mind that both the prediction and the data focus on $1 - C_v^2$, then we recognize that the prediction lies among the data while the conventional value of $(1 - 0.98^2)$ is high by a factor of 1000. Equation (19) is thus the surest prediction of C_v presently available, and probably is more accurate than any existing data.

It is worth noting that the Borda mouthpiece (see Fig. 1) offers very little way in which any viscous dissipation could occur, since very little of the liquid approaches the hole over a wall. It is well-known (see e.g., [4]) that for a Borda mouthpiece

$$C_c = \frac{1}{2C_v^2} \quad \text{or} \quad C_D = \frac{1}{2C_v} \tag{21}$$

Since C_v must be very close to unity for virtually any Borda flow, we anticipate that C_c and C_D will be equal to 1/2 for a perfectly shaped mouthpiece.

Unfortunately no existing data for the Borda Mouthpiece

have accuracy higher than about ± 2 percent thus we cannot verify this prediction. Furthermore C_D and C_c for Borda Mouthpieces, like those for sharp edged orifices, are vulnerable to minor machining defects in the vicinity of the lip.

Conclusions

1. Surface tension does not retard a liquid jet unless it completely stops it (see Conclusion 2). However it will retard the broken-up droplets approximately according to equation (5) or (6).
2. When $We \leqslant 8/\sqrt{C_c}$ any circular liquid jet flow will be choked off. When $We \leq 4/C_c$ a slot flow will be choked off.
3. C_v for a sharp-edged circular orifice or for a sharp-edged slot is given by equations (19) and (20).
4. C_v equals unity within 0.1 percent for almost any aperture for which $Re > 10{,}000$.

References

1 The entire issue of the January, 1977 *IBM Jour. Res. and Dev.* is devoted to the dynamics of small jets, Vol. 21, No. 1, 1977.

2 Monde, M., and Katto, Y., "Burnout in High Heat-Flux Boiling System with an Impinging Jet," *Int. J. Heat Mass Transfer*, Vol. 21, 1978, pp. 295–305.

3 Brodkey, R. S., *The Phenomena of Fluid Motions*, Addison-Wesley, Reading, Mass., 1967.

4 *Encyclopaedia Britannica*, 11th ed, Encyclopaedia Britannica Inc., New York, 1911, Article on "Hydraulics," pp. 38–56.

5 Judd, H., and King, R. S., "Some Experiments on the Frictionless Orifice," *Engr. News*, Vol. 56, No. 13, 1908, pp. 326–330.

6 Medaugh, F. W., and Johnson, G. D., "Investigation of the Discharge Coefficients of Small Circular Orifices," *Civil Engr.*, Vol. 7, No. 7, 1940, pp. 422–4.

7 Trefethen, Lloyd, M., private communications.

8 Huang, J. C. P., "The Breakup of Axisymmetric Liquid Sheets," *J. Fluid Mech.*, Vol. 43, Part 2, 1970, pp. 305–319.

9 Chen, Y., unpublished initiative project for course MECE 7397, Mech. Engr. Dept., Univ. of Houston, fall, 1981.

10 Birkhoff, G., and Zarantonello, E. H., *Jets, Wakes and Cavities*, Academic Press, New York, 1957, Section 11-5.

11 White, F. M., *Viscous Fluid Flow*, McGraw-Hill, New York, 1974.

12 Crabtree, L. F., Kuchemann, D., and Sowerby, L., "Three-Dimensional Boundary Layers," Chapter VIII, Sect. 9, *Laminar Boundary Layers* (L. Rosenhead, ed.) Oxford University Press, 1963.

13 Batchelor, G. K., *An Introduction to Fluid Dynamics*, Cambridge University Press, 1967.

Flow and Temperature Profile Independence of Flow Measurements Using Long Acoustic Waves

Baldwin Robertson
Chemical Process Metrology Division,
Center for Chemical Engineering,
National Bureau of Standards,
Washington, D.C. 20234

An expansion in powers of $\mathbf{V}/c$ is derived for the wave number of the fundamental sound mode in a flow conduit, where $\mathbf{V}$ is the velocity of fluid in the conduit and c is the local sound speed. Both $\mathbf{V}$ and c are assumed to be independent of the longitudinal coordinates and of the time, but may have arbitrary profiles. The calculation applies to frequencies well below the cutoff frequency of the conduit, which may have an arbitrary cross-sectional shape. To lowest order, the wave number depends only on the average of the longitudinal component of $\mathbf{V}$ and is independent of its profile.

Introduction

A long-wave acoustic technique has been used [1-2] for measuring the total mass flowrate and the total volume flowrate of gases in a conduit. This technique is superior to ultrasonic techniques because, with sufficiently long waves, the measurement is independent of the flow and temperature profiles. An ultrasonic beam, on the other hand, is bent and delayed in an uncontrollable and unpredictable way by the flow and temperature inhomogeneities that always occur in practice. This time delay is indistinguishable from the time delay caused by the mean velocity to be measured. Since the flow measurement is based on the time delay, the inhomogeneities lead to inaccuracy. The long-wave technique avoids this inaccuracy by using only frequencies well below the cutoff frequency of the conduit [3]. Then the sound consists of plane waves whose amplitude and phase are not affected by the shape of the profiles, but only by their average over the cross section of the flow conduit.

The purpose of this paper is to present a simpler and more general proof of the profile independence than has been given previously [4] and to calculate higher order corrections. The previous calculation used perturbation theory involving eigenfunctions for the zero-flow sound propagation. These eigenfunctions were themselves obtained from a perturbation calculation using eigenfunctions for the constant temperature limit. This requires a lot of algebra.

The new method does not involve eigenfunction expansions. The calculation is valid for flow in a rigid cylindrical conduit of arbitrary cross-sectional shape. The sound speed c and flow velocity $\mathbf{V}$ are assumed to be independent of the longitudinal coordinates and of the time, but may have arbitrary profiles. The calculation applies in the long-wave or low-frequency limit, with damping of the sound wave neglected. Dissipation in the unperturbed flow is taken fully into account for nonswirling flow, and approximately for swirling flow. Results to any order in $\mathbf{V}/c$ can readily be obtained by iterating a series expansion of a closed-form expression. No other assumptions or restrictions are made.

By analogy with optics, the profile independence is physically reasonable. It is well known that the minimum size of an object that can be seen with a microscope is, very roughly, the length of the light waves used. Also, the minimum angle of resolution of a telescope is proportional to the wavelength of the light detected. Only the location and apparent brightness of a distant star can be observed, not its diameter. Similarly, acoustic waves will not respond to the details of inhomogeneities that extend only over a distance much smaller than a wavelength. Only the average of the inhomogeneity over a wave length or so can be expected to be observed. Still a general proof of this effect is desirable in order to establish the specific limits of the profile independence and because the analogy with optics is not perfect.

Statement of the Problem

Consider a fluid with density R, velocity $\mathbf{V}$, pressure P, and entropy S per unit mass, each a function only of position in the cross section of the conduit and independent of time. We will analyze a sound wave propagating in this fluid with oscillating density ρ, velocity $\mathbf{v}$, pressure p, and entropy s. To do this, insert the total density $R+\rho$, velocity $\mathbf{V}+\mathbf{v}$, pressure $P+p$, and entropy $S+s$, into the equations of mass, momentum, and energy conservation in Eulerian form. Expand about the unperturbed flow, keep only the terms that are linear in the unknown oscillating quantities ρ, $\mathbf{v}$, p, and s, to get [5]

$$\partial\rho/\partial t+\nabla\cdot(\rho\mathbf{V}+R\mathbf{v})=0 \tag{1}$$

$$R\partial v/\partial t+R\mathbf{V}\cdot\nabla\mathbf{v}+(R\mathbf{v}+\rho\mathbf{V})\cdot\nabla\mathbf{V}=-\nabla p \tag{2}$$

Contributed by the Fluids Engineering Division for publication in the JOURNAL OF FLUIDS ENGINEERING. Manuscript received by the Fluids Engineering Division, March 22, 1983.

$$R\partial s/\partial t + R\mathbf{V}\cdot\nabla s + (R\mathbf{v}+\rho\mathbf{V})\cdot\nabla S = 0, \quad (3)$$

where we have neglected the dissipation of sound. Dissipation is of course taken fully into account in the unperturbed flow without the sound wave and will be expressed here in the functional form chosen for the R, $\mathbf{V}$, P, and S in equations (1)–(3).

These equations are closed by use of the equation of state to relate p to ρ and s. Consider the total pressure $P+p$ as a function of the total density $R+\rho$ and entropy $S+s$, expand about the unperturbed pressure P, and keep first order terms. The resulting acoustic (oscillating) pressure is [5]

$$p = c^2\rho + hs, \quad (4)$$

where

$$c^2 = (\partial P/\partial R)_S \quad (5)$$

is the square of the local sound speed and

$$h = (\partial P/\partial S)_R \quad (6)$$

is the change of pressure produced by a change in entropy. Since $\mathbf{v}$ is a vector, (2) is a vector equation, and thus we have six equations, (1)–(4), and six unknowns: ρ, $\mathbf{v}$, p, and s.

These equations are linear, so their solution can be written as a superposition of spatial modes for each frequency excited. To obtain one of these modes, separate each of ρ, $\mathbf{v}$, p, and s in the usual way into a product of a function of time t, a function of the longitudinal coordinate x, and a function of the transverse coordinates. Recall that R, $\mathbf{V}$, P, and S are independent of x and t. Then, without any loss of generality, the x and t dependence of each of ρ, $\mathbf{v}$, p, and s can be written as $\exp[i(\omega t - kx)]$, where $\omega/2\pi$ is the frequency of the sound, and k is a constant, the same constant for each. Since dissipation is small, the wave number k will turn out to be very nearly real. In this paper we will determine the value of k for the fundamental mode of sound propagating in the flow conduit.

To obtain the equations for a single spatial mode, replace ρ, $\mathbf{v}$, s, and p in equations (1)–(3) with $\exp[i(\omega t - kx)]$ times those quantities, and factor out the $\exp[i(\omega t - kx)]$ to get

$$i(\omega - kV_x)\rho - ikRv_x + \nabla_t\cdot(R\mathbf{v}_t + \rho\mathbf{V}_t) = 0 \quad (7)$$

$$i(\omega - kV_x)Rv_x + R\mathbf{V}_t\cdot\nabla_t v_x + (R\mathbf{v}_t + \rho\mathbf{V}_t)\cdot\nabla_t V_x = ikp \quad (8)$$

$$i(\omega - kV_x)R\mathbf{v}_t + R\mathbf{V}_t\cdot\nabla_t\mathbf{v}_t + (R\mathbf{v}_t + \rho\mathbf{V}_t)\cdot\nabla_t\mathbf{V}_t = -\nabla_t p \quad (9)$$

$$i(\omega - kV_x)Rs + R\mathbf{V}_t\cdot\nabla_t s + (R\mathbf{v}_t + \rho\mathbf{V}_t)\cdot\nabla_t S = 0. \quad (10)$$

Here we have separated equation (2) into its longitudinal component (8) and a transverse vector component (9), where v_x is the longitudinal component of $\mathbf{v}$, and $\mathbf{v}_t$ is the transverse vector component of $\mathbf{v}$, and ∇_t denotes the two-dimensional gradient operator for the transverse coordinates. Equation (4) contains no derivative and so is unchanged.

The unknowns ρ, v_x, $\mathbf{v}_t$, p, and s in equations (7)–(10) and (4) are functions of the transverse coordinates only. We seek the value of k for which there is a solution to these equations for an arbitrary shape of the cross section of the conduit.

Equation for k

Some progress in solving equations (7)–(10) and (4) simultaneously can be made be combining equations (7) and (8) to eliminate v_x. First solve equation (7) for kv_x:

$$kv_x = R^{-1}(\omega - kV_x)\rho - iR^{-1}\nabla_t\cdot(R\mathbf{v}_t + \rho\mathbf{V}_t). \quad (11)$$

Insert this into $-ik$ times equation (8) to get

$$(\omega - kV_x)^2\rho - i(\omega - kV_x)\nabla_t\cdot(R\mathbf{v}_t + \rho\mathbf{V}_t) - iR\mathbf{V}_t\cdot\nabla_t[R^{-1}(\omega - kV_x)\rho - iR^{-1}\nabla_t\cdot(R\mathbf{V}_t + \rho\mathbf{V}_t)] - i(R\mathbf{v}_t + \rho\mathbf{V}_t)\cdot\nabla_t kV_x = k^2 p.$$

Divide this by $(\omega - kV_x)^2$, note that $\nabla_t\omega = 0$, and rearrange:

$$-i\frac{\nabla_t\cdot(R\mathbf{v}_t + \rho\mathbf{V}_t)}{\omega - kV_x} + i(R\mathbf{v}_t + \rho\mathbf{V}_t)\cdot\frac{\nabla_t(\omega - kV_x)}{(\omega - kV_x)^2} - \frac{iR\mathbf{V}_t}{(\omega - kV_x)^2}\cdot\nabla_t\left(\frac{\omega - kV_x}{R}\rho - i\frac{\nabla_t\cdot(R\mathbf{v}_t + \rho\mathbf{V}_t)}{R}\right) + \rho = k^2 p/(\omega - kV_x)^2.$$

Recall that for the unperturbed flow we have assumed that R, $\mathbf{V}$, and P are independent of x and t. Hence the mass conservation equation reduces to

$$\nabla_t\cdot(R\mathbf{V}_t) = 0, \quad (12)$$

and the x component of the momentum conservation equation reduces to

$$\mathbf{V}_t\cdot\nabla_t V_x = 0, \quad (13)$$

where in the latter we have neglected dissipation. This neglect involves an additional approximation, which, however, is unimportant if $\mathbf{V}_t$ is not large. Equation (13) is not needed at all if $\mathbf{V}_t$ is negligible. To continue, combine the first two terms of equation (11) and use equations (12) and (13) on the third term to get

$$-i\nabla_t\cdot\left(\frac{R\mathbf{v}_t + \rho\mathbf{V}_t}{\omega - kV_x}\right) - \nabla_t\cdot\frac{iR\mathbf{V}_t}{(\omega - kV_x}\left(\frac{\omega - kV_x}{R}\rho - i\frac{\nabla_t\cdot(R\mathbf{v}_t + \rho\mathbf{V}_t)}{R}\right) + \rho = k^2 p/(\omega - kV_x)^2.$$

Finally combine the second term in the first divergence with the first term in the second divergence to get

$$-\nabla_t\cdot\left(i\frac{R\mathbf{V}_t + 2\rho\mathbf{V}_t}{\omega - kV_x} + \frac{\mathbf{V}_t}{(\omega - kV_x^2}\nabla_t\cdot(R\mathbf{V}_t + \rho\mathbf{V}_t)\right) + \rho = k^2 p/(\omega - kV_x)^2. \quad (14)$$

This is to be solved simultaneously with equations (9), (10), and (4) for the unknowns ρ, $\mathbf{v}_t$, p, and s.

The short cut comes here by observing that the first term of equation (14) vanishes when integrated over the cross section of the flow conduit. The two-dimensional Gauss theorem converts the integral of the divergence into an integral of its

Nomenclature

- R = unperturbed density
- $\mathbf{V}$ = unperturbed velocity vector
- P = unperturbed pressure
- S = unperturbed entropy per unit mass
- ρ = acoustic (oscillating) density
- $\mathbf{v}$ = acoustic (oscillating) velocity vector
- p = acoustic (oscillating) pressure
- s = acoustic (oscillating) entropy per unit mass
- c = adiabatic sound speed
- h = change of pressure with entropy at constant density
- t = time
- x = longitudinal coordinate
- ∇ = vector differential operator del
- ω = 2π times frequency
- k = wave number
- $\langle\ \rangle$ = average over cross-sectional plane

Subscripts

- x = longitudinal component
- t = transverse component (in the cross-sectional plane)
- 0 = average defined by equations (19) or (21)

argument over the boundary, which is a path around the cross section just inside the wall. Since the normal components of $\mathbf{v}_t$ and $\mathbf{V}_t$ are both zero at the wall, the integral is zero. This is true regardless of the shape of the cross section. The result is that only the second and third terms of equation (14) survive when integrated over the cross section so that

$$\langle k^2 p/(\omega - kV_x)^2 \rangle = \langle \rho \rangle. \tag{15}$$

Here the angular brackets denote the average over the cross section of the flow conduit. To use this result, we need to know the dependence of the pressure p on the transverse coordinates. Then equation (15) will be an algebraic equation for the eigenvalue k.

Expression for k

In order to get an explicit expression for k we must first show that p is a constant in the limit $\omega \to 0$ and $k \to 0$. In that limit, equations (7)–(9) become

$$\nabla_t \cdot (R\mathbf{v}_t + \rho \mathbf{V}_t) = 0 \tag{16}$$

$$R\mathbf{V}_t \cdot \nabla_t v_x + (R\mathbf{v}_t + \rho \mathbf{V}_t) \cdot \nabla_t V_x = 0 \tag{17}$$

$$R\mathbf{V}_t \cdot \nabla_t \mathbf{v}_t + (R\mathbf{v}_t + \rho \mathbf{V}_t) \cdot \nabla_t \mathbf{V}_t = -\nabla_t p. \tag{18}$$

It is easier to work with these equations than trying to take the limit in equation (14). Note from equations (16) and (17) that $\mathbf{v}_t \to 0$ linearly with $\mathbf{V}_t$. Now $\mathbf{V}_t$ is generally not so large that second order terms are significant. So we neglect second order terms in $\mathbf{V}_t$ and $\mathbf{v}_t$ in equation (18), and conclude that p is a constant $= p_0$. Regardless of the value of $\mathbf{V}_t$, this result is exact for a circular pipe when there is axial symmetry, which can be true even when $\mathbf{V}_t$ is large.

It is convenient at this point to introduce two definitions. First define the effective mean sound speed c_0 by

$$c_0^{-2} = \langle \rho \rangle / p_0. \tag{19}$$

This reduces to the average of $1/c^2$:

$$c_0^{-2} = \langle c^{-2} \rangle \quad \text{when } s = 0, \tag{20}$$

since equation (4) then gives $p_0 = c^2 \rho$. This will be true when S is constant, as can be seen from equation (10). In general, however, s is not zero, and equation (20) is not valid. In the following we will use the more general expression (19).

The second expression we find convenient to introduce is the effective mean flow velocity V_0, which is defined by

$$(\omega - kV_0)^{-2} = \langle (\omega - kV_x)^{-2} \rangle. \tag{21}$$

Clearly V_0 reduces to V_x when the latter is constant. We will examine the dependence of V_0 on V_x shortly.

When these definitions are used in equation (15), the result is

$$k^2/(\omega - kV_0)^2 = c_0^{-2}. \tag{22}$$

$$k = \pm \omega/(c_0 \mp V_0), \tag{23}$$

where the upper sign is for an upstream traveling wave, and the lower sign is for a downstream traveling wave. This expression is identical in form to the elementary result for the wave number, except that equation (23) involves the effective mean flow velocity V_0. The result shows that k/ω is of order $1/c_0$. This suggests solving equation (21) for V_0:

$$V_0 = (\omega/k)[1 - \langle (1 - kV_x/\omega)^{-2} \rangle^{-1/2}] \tag{24}$$

and expanding in powers of k/ω:

$$\begin{aligned} V_0 &= (\omega/k)[1 - \langle 1 + 2kV_x/\omega + 3k^2 V_x^2/\omega^2 \\ &\quad + 4k^3 V_x^3/\omega^3 + \ldots \rangle^{-1/2}] \\ &= (\omega/k)\left[1 - \frac{1}{2}\langle 2kV_x/\omega + 3k^2 V_x^2/\omega^2 + 4k^3 V_x^3/\omega^3 + \ldots \rangle \right. \\ &\quad + \frac{3}{8}\langle 2kV_x/\omega + 3k^2 V_x^2/\omega^2 + \ldots \rangle^2 \\ &\quad \left. - \frac{5}{16}\langle 2kV_x/\omega + \ldots \rangle^3 + \ldots \right]. \end{aligned}$$

Gather terms:

$$\begin{aligned} V_0 &= \langle V_x \rangle + \frac{3}{2}\frac{k}{\omega}(\langle V_x^2 \rangle - \langle V_x \rangle^2) \\ &\quad + \frac{k^2}{\omega^2}(2\langle V_x^3 \rangle - \frac{9}{2}\langle V_x \rangle \langle V_x^2 \rangle + \frac{5}{2}\langle V_x^3 \rangle) \ldots \end{aligned} \tag{25}$$

This can be iterated with equation (23) to get

$$k = \frac{\pm \omega}{c_0 \mp \langle V_x \rangle - \frac{3}{2}\dfrac{\langle V_x^2 \rangle - \langle V_x \rangle^2}{c_0 \mp \langle V_x \rangle}} \tag{26}$$

correct to second order in $\mathbf{V}/c_0$. Here, as before, the upper sign is for an upstream traveling wave, and the lower sign is for a downstream traveling wave.

Discussion

We have obtained an expression for the wave number k of the fundamental sound mode in a flow conduit. This is given by equation (23), where c_0 is the effective mean sound speed and V_0 is the effective mean flow velocity, which is given by equation (24) or (25). These can be iterated to get an explicit expression for k as a continued fraction involving c_0 and the moments of V_0. The result to second order in $\mathbf{V}/c_0$ is given in equation (26). When restricted to first order, this equation establishes that k depends on the mean velocity $\langle V_x \rangle$ and not on the profile of V_x. The second order terms in equation (26) serve as error estimates for this profile independence. Note that in all these equations, k is independent of the transverse velocity $\mathbf{V}_t$. The results are valid in the low-frequency or long-wave limit.

References

1 Potzick, J. E., and Robertson, B., "Long-Wave Acoustic Flowmeter," ISA-82 International Conference, Philadelphia, October 18–21, 1982, Paper CI 82-701.

2 Potzick, J. E., and Robertson, B., "Long Wavelength Acoustic Flowmeter," U.S. Patent Application SN 300830, 1981, Canadian and European patent applications filed.

3 Morse, P. M., and Ingard, K. V., *Theoretical Acoustics*, McGraw-Hill, 1968, pp. 494, 497, 504, and 511.

4 Robertson, B., "Effect of Arbitrary Temperature and Flow Profiles on the Speed of Sound in a Pipe," *J. Acoust. Soc. Am.*, Vol. 62, 1977, pp. 813–818.

5 Blokhintsev, D., "The Acoustics of an Inhomogeneous Moving Medium," 1946, NACA Translation TM 1399, 1952, p. 17, equations (1.70)–(1.73).

Visualization Studies of a Shear Driven Three-Dimensional Recirculating Flow

J. R. Koseff
Acting Assistant Professor.

R. L. Street
Professor of Fluid Mechanics and Applied Mathematics. Mem. ASME

Department of Civil Engineering, Stanford University, Stanford, Calif. 94305

A facility has been constructed to study shear-driven, recirculating flows. In this particular study, the circulation cell structure in the lid-driven cavity is studied as a function of the speed of the lid which provides the shearing force to a constant and uniform density fluid. The flow is three-dimensional and exhibits regions where Taylor-type instabilities and Taylor-Görtler-like vortices are present. One main circulation cell and three secondary cells are present for the Reynolds number (based on cavity width and lid speed) range considered, viz., 1000–10000. The flows becomes turbulent at Reynolds numbers between 6000 to 8000. The transverse fluid motions (in the direction perpendicular to the lid motion) are significant. In spite of this, some key results from two-dimensional numerical simulations agree well with the results of the present cavity experiments.

Introduction

Recirculating flows take varied forms and have relevance to many different aspects of engineering, including heat transfer. Important among the flows in this domain are natural and forced convection in rectangular spaces and flow over cut-outs, cavities and repeated ribs on walls. The lid-driven flow in a rectangular cavity is an ideal representation of such a flow because the lid-driven flow can be studied systematically by both numerical methods and by experiments.

A study of the literature concerning numerical simulations of lid-driven cavities reveals good agreement among the various solutions at low Reynolds numbers, but very little agreement at higher Reynolds numbers. Reynolds number is defined as VB/ν: where V is the velocity of the lid; B is the width of the cavity; and ν is the kinematic viscosity of the fluid. Most of these studies were for a two-dimensional cavity and did not contain any turbulence modelling. As a rule the laminar flow equations were solved over the entire Reynolds number range considered, even though, as it now appears, parts of the flow are turbulent at the higher Reynolds numbers. Exceptions to the general pattern are the three-dimensional simulations of de Vahl Davis and Mallinson [1] and Gresho et al. [2] for low Reynolds number (i.e., truly laminar) flows and the two-dimensional simulations incorporating turbulence models by Findikakis [3], Young et al. [4], Gosman et al. [5], and Ideriah [6].

Relatively few experiments have been done with lid-driven cavities, and all would be classified as three-dimensional. Most of the experiments have been performed with cavities located at the wall of a channel, the circulation being driven by the shear stress imposed at the top of the cavity by the velocity gradient in the channel. High Reynolds number experiments were performed in wind tunnels by Roshko [7], Fox [8], Maull and East [9], and Haugen and Dhanak [10]. Low Reynolds number experiments were made in water channels by Reiman and Sabersky [11], Johnson and Dhanak [12], and Orlandi and Ianetta [13].

The flow in a totally enclosed lid-driven cavity constitutes a more controlled problem with fewer external factors affecting the state of the flow. Thus, we have focused on this flow. Mills [14, 15], Chashechkin [16], and Pan and Acrivos [17] performed experiments in wall-driven cavity flows. (Pan and Acrivos used a cylinder as the driving force.) Building on this work, we have constructed a facility which allows systematic studies of many aspects of this type of flow.

To date our work has focused on qualitative measurements by flow visualization. Subsequent sections of this paper describe the experimental apparatus and instrumentation and the visualization technique used in this initial phase of the work. The main body of the paper highlights the observations and evaluations made to date. In particular we have studied the following aspects of the lid-driven flow in a square cavity with constant density fluid: (1) the presence of turbulence in the flow; (2) the three-dimensionality of the flow and associated flow structures; (3) the size of the downstream secondary eddy as a function of Reynolds number; and (4) the formation of Taylor-type instabilities during the first 30 seconds or so after the lid is started. (The lid achieves final velocity instantaneously, but the fluid is initially at rest so that a finite transient period occurs.) We chose to concentrate on the downstream secondary eddy in this paper as it has been the traditional focus of cavity flow studies and its charac-

Contributed by the Fluids Engineering Division and presented at the AIAA/ASME Joint Fluids, Plasma, Hormophysics and Heat Transfer Conference, St. Lewis, MO, June 7-11, 1982, of The American Society of Mechanical Engineers. Manuscript received by the Fluids Enginering Division, June 28, 1982.

teristics serve as a useful benchmark when comparing numerical results with each other and experiments.

Experimental Facility and Instrumentation

The central component of the facility is a cavity upon which the system supplying the driving force rests (see Fig. 1(*a*)). The cavity has a width B of 150 mm in the direction of lid motion, a maximum vertical depth D of 925 mm and a span L of 450 mm transverse to the direction of lid motion. It is fabricated from 12.5 mm plexiglas. Figure 1(*b*) gives a schematic cross section of the cavity.

The facility is shown in assembled form in Fig. 2. It could be described as consisting of two attached "shoe boxes." The lower box is the cavity area of interest, while the upper box houses the drive system. It consists of a variable speed motor connected by a chain drive to one of a pair of rollers. The "lid" is a thermally conductive copper belt which drives the flow, is 0.08 mm thick, and is supported on and driven by the two rollers shown.

The cavity area of interest (area KTMN in Fig. 1(*b*)) is bounded at the top by the "UPPER PLATE" and at the bottom by the "LOWER PLATE." The upper plate which guides the belt running beneath it can be heated (or cooled) while the lower plate may be similarly cooled (or heated). However, these features are not relevant to this study and are not discussed further. Reynolds numbers (as defined previously) in the range from 1000 to 35,000 can be obtained, with water as the medium, by varying the speed of the belt from 7 mm/s to 230 mm/s. Aspect ratios (D/B) of 1:1 to 5:1 are obtained by adjusting the position of the lower plate. The spanwise aspect ratio (SAR) is 3:1.

The copper belt rests on the cavity lip (KTQP in Fig. 1(*a*)) and is restrained from lifting off the lip by the "UPPER PLATE" (see Fig. 1(*b*)) which overlaps the lip edge and whose vertical position is adjustable to ensure continuous contact between the plate and the belt. The tension in the belt is controlled by adjusting the position of the rollers. This arrangement facilitates the smooth tracking of the belt over the lip and minimizes undulations in the belt. The belt speed is checked by a tachometer and is constant to within 2 percent. During belt installation the apparatus is run at low speed, and the belt is adjusted so that the transverse motions (along the spanwise direction) in the flow are completely unbiased. The inner edge (i.e., the edge inside the cavity itself) of the 12.5 mm wide lip is sharp and forms a 90 deg angle with the belt. The apparatus is filled such that the water level is about 5 cm above the belt (see Fig. 3). Thus, no air is entrained by the belt into the cavity.

Flow Visualization Technique

The visualization method used for flows in the Reynolds number range of 1000 to 10000 is the thymol blue pH-indicator technique. This technique requires the preparation of a working fluid by the addition of the indicator to distilled water and titrating the resulting solution to its end point. Details about preparation of the fluid are given by Baker [18]. If two electrodes are placed in the fluid and a DC voltage of

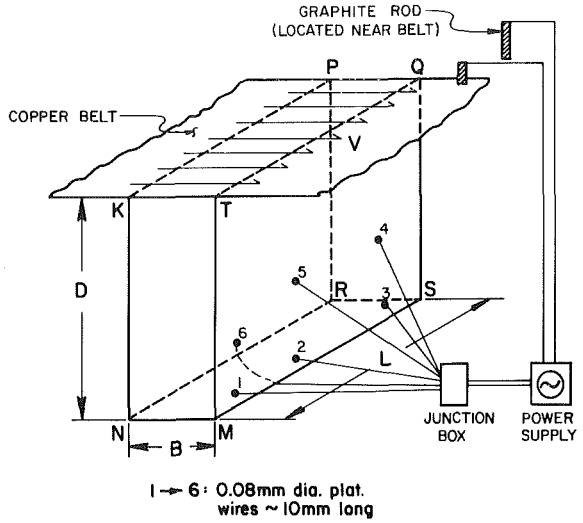

Fig. 1(*a*) Schematic of turbulence modelling facility showing location of flow visualization electrodes on walls of lid-driven cavity

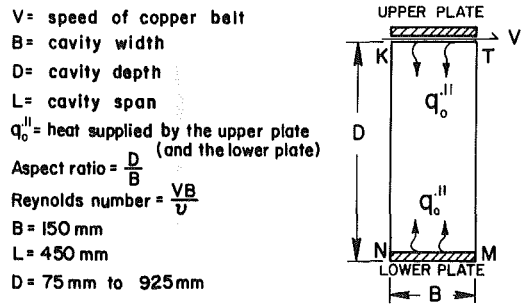

Fig. 1(*b*) Schematic cross section of turbulence modeling facility

about 10 volts is applied across them, a proton transfer and subsequent pH change at the negative electrode (cathode) is induced. Thus, the color of the solution changes from yellow (acidic form of thymol blue) to blue (basic form) in the region of the cathode, and a neutrally buoyant marker is formed.

The electrodes used were 0.08 mm diameter platinum wires mounted along the vertical walls of the cavity (see Fig. 1(*a*)). The wires were connected such that each could serve as a positive or negative electrode. As seen in Fig. 1(*a*) wires 1 through 5 are located in wall TMQS, while wire 6 is located in wall KNRP.

The "start-up" or initial transient period was visualized by using the copper belt itself as the cathode and a graphite rod placed near it as the anode. When this system is activated by placing a potential of 30V across the electrodes, blue dye is formed along the length of belt in the cavity itself. When the belt is started up, the dye on its surface is stripped off by the downstream cavity lip. This occurs because the belt is forced by the "UPPER PLATE" to move against the sharp inner lip of the cavity, and fluid in contact with the belt is prevented

Nomenclature

B = width of the cavity
D = depth of the cavity
L = span of the cavity
D_3^* = dimensionless vertical extent of downstream secondary eddy
D_3 = depthwise dimension of downstream secondary eddy
D_{HP}^* = horizontal extent of upper secondary eddy
D_{US}^* = vertical extent of upper secondary eddy
q_0'' = heat flux through upper and lower plates
Re = Reynolds number based on speed of cavity lid, VB/ν
SAR = spanwise aspect ratio, L/B
V = velocity of cavity lid
ν = kinematic viscosity of fluid
ψ_{max} = maximum value of stream function in two-dimensional numerical simulation

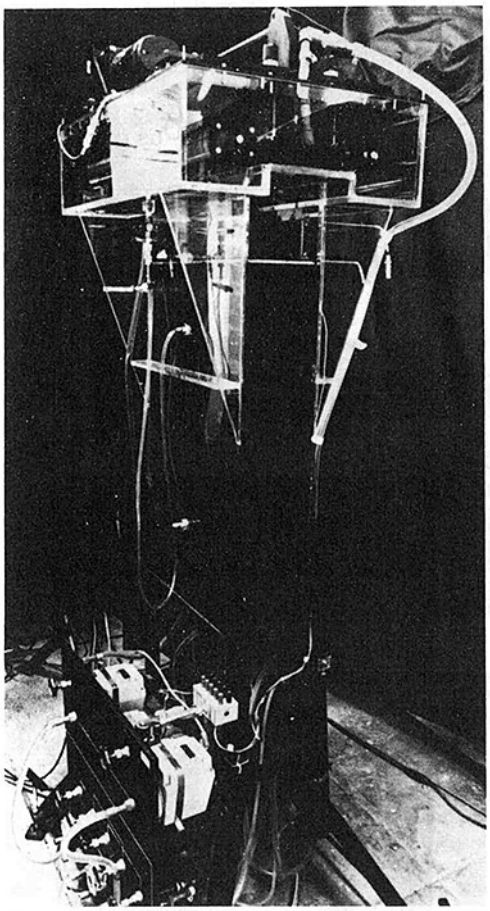

Fig. 2 Complete view of turbulence modeling facility

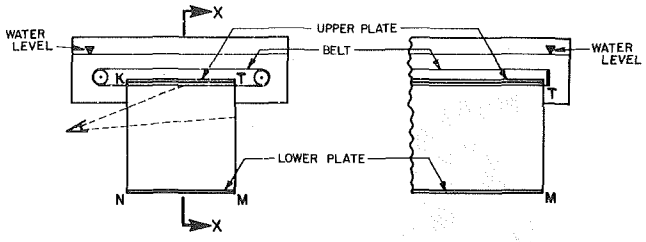

Fig. 3 Schematic of cavity planes depicted in photographs

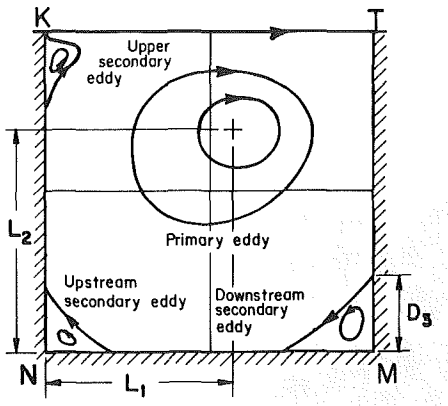

Fig. 4 Lid-driven cavity flow definition sketch

from leaving the cavity by this contact; to be precise, no dyed fluid is observed leaving the cavity between the belt and the lip. If the fluid is dyed blue (in the manner described above), then its path may be traced as the fluid moves into the corner formed by the belt and the lip and then out into the cavity. Thus the high vorticity region near this lip, as well as the time development of the circulation, is easily visualized.

The belt was used in a similar fashion at later stages in each experiment to visualize the flow along the downstream wall and the lower plate. Since flows with velocities higher than 5 cm/s sweep the colored fluid from the electrode faster than it can be formed in visible amounts, the thymol blue technique can only be used for Reynolds numbers up to 10000.

Experimental Observations

In this section the observations and evaluations mentioned in the introduction are presented and discussed. The evaluations were made from real-time observation of the flow and the resultinig photographs. To make the photographs more understandable, Fig. 3 is included to show the plane of the cavity depicted in each photograph. View A is an end view of the cavity, while View B is a side view. Since the flow is symmetric about the center plane, only half of the side view was photographed. In the side view the region near the belt is obscured by the upper box overhang, and hence it was necessary to view this region at an angle. This is shown by the "eye" in View A.

The basic time-averaged flow structure is sketched in Fig. 4. The fluid in the region of the lid (KT) is dragged by the lid to the corner T where a region of high pressure develops. The fluid is driven down TM but decelerates due to the effects of friction and the stagnation induced by the corner M. This results in an increase in pressure. The flow cannot overcome this "pressure hill," and separation occurs resulting in the formation of a secondary eddy in the vicinity of M. A similar phenomenon is found in the regions N and K, although the upper secondary eddy was not observed at our lower Reynolds number limit (Re = 1000). However, region K is very difficult to visualize, and the occurrence of a secondary eddy there at a Reynolds number of 1000 is a distinct possibility.

(*a*) Presence of Turbulence. The Reynolds number at which the flow first exhibits turbulent features appears to be in the range from 6000 to 8000. The technique used for this determination involves the observation of the instability and diffusivity of dye streaks, as was first described by Osborne Reynolds in 1883. Figure 5 (View A as shown in Fig. 3) shows a dye streak (generated by wire no. 5) for Reynolds numbers from 3000 to 8000. This dye streak visualizes the interface between the primary eddy and the downstream secondary eddy. At Re = 3000 (5*a*) the streak is clearly part of a laminar flow. At Re = 5000 (5*b*) the first signs of instability are present, though at times the streak showed the same characteristics as the Re = 3000 case. At Re = 6000 (5*c*) the increase in flow instability and the beginning of lateral dispersion of the dye can be seen. According to Tennekes and Lumley [19] the marked increase (several orders of magnitude) in diffusivity is one of the "outstanding characteristics of turbulence." This accounts for the reduced amount of dye visible as the dye production was maintained at a constant level for the entire range. At Re = 8000 (5*d*) the trend continues and the increased level of diffusion can be seen.

The flow in this region does not always display turbulent characteristics in the Reynolds number range of 6000-8000. Rather, there are intermittent turbulent "bursts" during which the dye streaks diffuse rapidly. At the higher Reynolds numbers, such as 10000, these bursts occur more frequently than at Re = 6000. Clearly, while a "steady" time-averaged flow exists, the presence of the Taylor-Görtler-like vortices

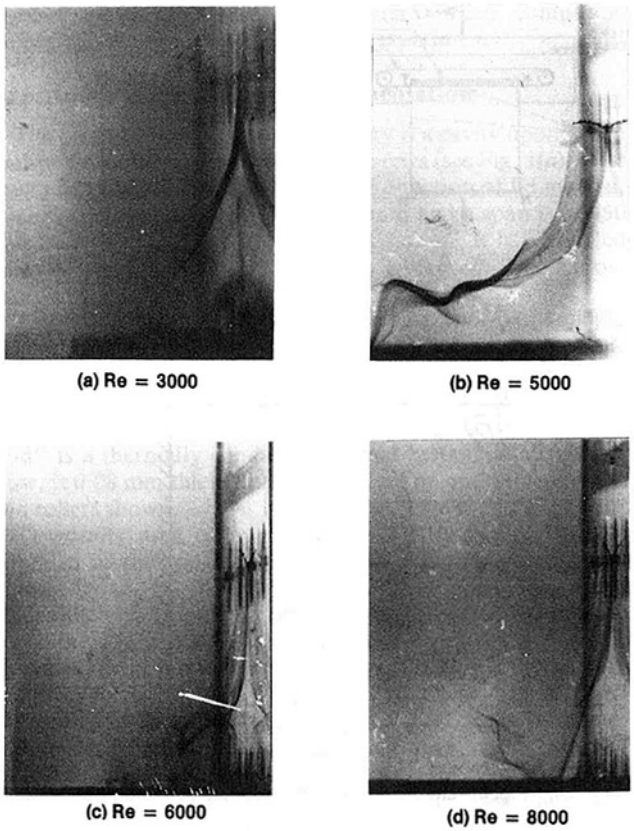

Fig. 5 Dye streaks showing transition from laminar to turbulent flow. (Right side of view A shown only.)

described below indicates that the instantaneous flow is not steady. However, the diffusive property of turbulence makes it possible to distinguish turbulent behavior from simple unsteadiness.

Is it possible that the flow exhibits turbulent characteristics in other regions of the flow before they are present in the region of the downstream secondary eddy? Görtler [20] showed that, at a critical Reynolds number, a concave curved boundary would promote instability in the flow leading to turbulence, whereas flow over a flat plate would be stable for the same Reynolds number. In the region of the downstream secondary eddy the nature of the separation is such that a curved boundary for the primary eddy is formed. Thus, it is logical that turbulence is observed in this region. The separation surface in the region of the upstream secondary eddy is also concave and therefore one might expect a similar instability in this region leading to turbulent flow. Ghia et al. [21] showed, however, that in a numerical simulation the strength (as indicated by the maximum value of the stream-function, ψ_{max}) of the downstream secondary eddy is more than twice that of the upstream secondary eddy. Thus, because the velocity of the flow is higher in downstream secondary eddy region, it is likely that the flow will become turbulent here first.

It is also possible that the flow in the region of the belt may become turbulent before it does in the downstream secondary eddy region. From Fig. 6(*b*), however, it seems that the flow in the region of the upper secondary eddy is quite laminar at a Re = 8000. This is not entirely unexpected even though the flow is somewhat turbulent in the region of the downstream secondary eddy at this Re. Investigators, including Clauser and Clauser [22], have shown that convex surfaces tend to stabilize the flow over them, thereby delaying the transition to turbulence. Since the shape of the "surface" separating the upper secondary eddy from the main eddy is convex (when

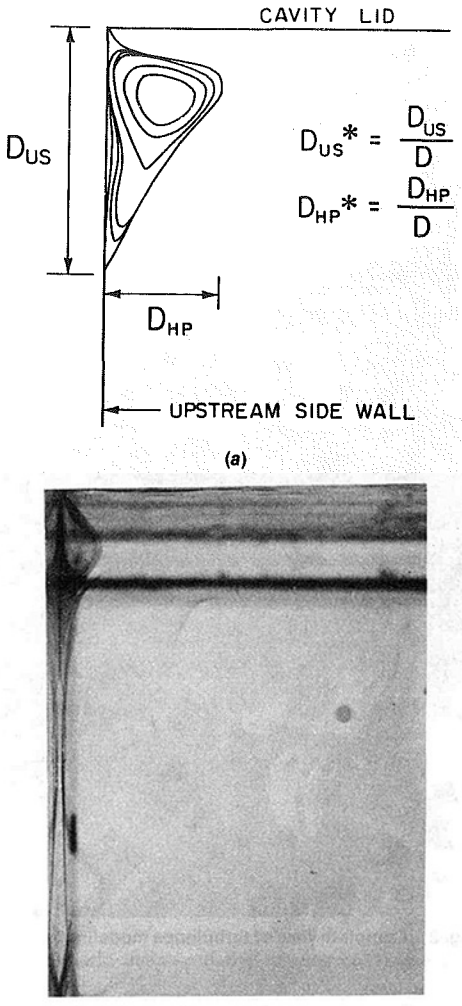

Fig. 6 (*a*) Schematic detail of upper secondary eddy. (*b*) Upper secondary eddy shows laminar flow characteristics at Re = 8000. (Left side of view A shown only.)

viewed from the cavity center), it is likely that the flow is stabilized in this region.

(*b*) Flow Start-Up. The "start-up" of the flow (defined above) was visualized by generating dye on the belt just before it was started and then watching the progress of the dye as it was stripped off the belt by the downstream cavity lip. This shows the high vorticity region developing near the lip and the penetration of the rotating fluid into the quiescent cavity. Figure 7 (View B as shown in Fig. 3) shows the flow development near the downstream lip for a Reynolds number of 3000 during the first 30 seconds of flow. Similar results are obtained for the entire Reynolds number range considered, the major difference being the time scaled involved.

The sequence of pictures in Fig. 7 shows a "cylinder" of high vorticity fluid becoming unstable and developing a set of toroidal vortices which also become unstable and begin to interact with one another. This process, which is a Taylor-type instability, is very similar to that observed by Kirchner and Chen [23], Chen and Christensen [24], and Taneda [25] for an impulsively-started, rotating cylinder. The number of toroidal vortices formed varied in a similar manner to that in the case of the rotating cylinder observed by Kirchner and Chen [23]. At the higher Reynolds numbers there are more, smaller, closely spaced vortices present. Thus, the high vorticity "cylinder" of fluid formed by the stripping action of the cavity lip produces the same effect as a solid cylinder.

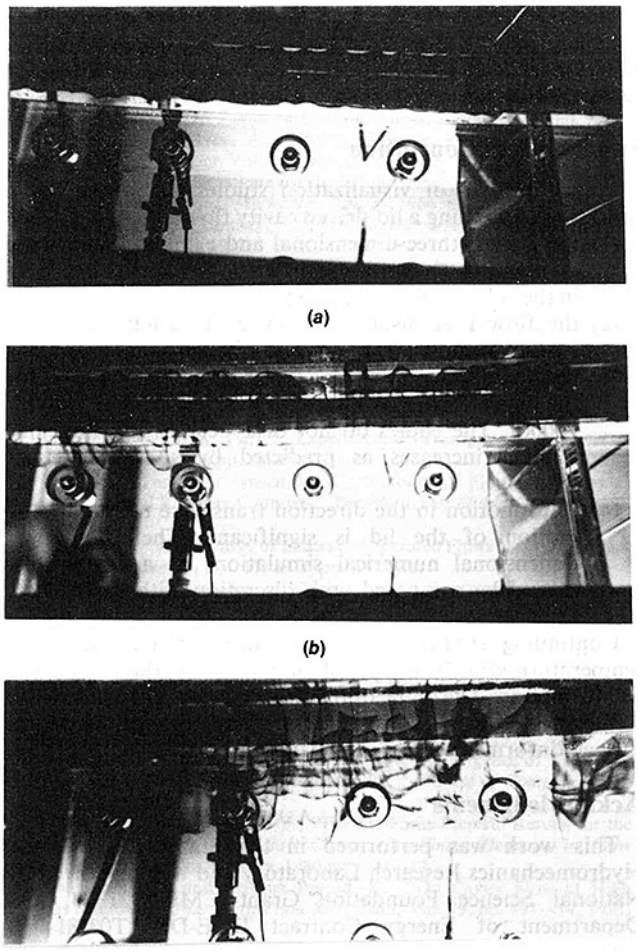

(a)

(b)

(c)

Fig. 7 Development of the flow during the first 30 seconds after start up for Re = 3000. (View B.)

Further instability and breakdown of the toroidal vortices is caused by the influence of the end walls. As can be seen in Fig. 7(*c*) the penetration of the rotating fluid is greatest near the end wall, and the dye is moving to the left toward the center of the cavity.

(*c*) Three Dimensional Features. The end-walls appear to cause significant motions in the direction perpendicular to the plane of the main circulation system, shown in Fig. 4, and also seem to influence the strength of the flow in this plane. The latter effect is shown by the following evidence. At Re = 8000 the normalized dimensions of the upstream secondary eddy (see Fig. 6(*a*)), obtained in the experiments, are $D_{US}{}^{*}$ = 0.3 and $D_{HP}{}^{*}$ = 0.1. For a Re = 7500, Ghia et al. [21] obtained dimensions of 0.3 and 0.15, respectively. They also showed that this eddy became smaller with decreasing Re. Because the size of this eddy in the experiment is smaller than that predicted by a numerical solution at a lower Re we can deduce that the flow in the experiment at a particular Re is weaker than that obtained from a 2-d solution. The result of this comparison is consistent with that obtained for the downstream secondary eddy (see below). Another significant three-dimensional feature is the presence of Taylor-Görtler-like vortices.

The presence of a "box-like distribution of sharply defined vortices" was shown theoretically to exist by Görtler [20] for flow over a concave wall. The existence of these vortices was shown experimentally by Taylor [26]. When, in the case of our cavity, dye was generated from the upper belt, it was found that a sheet of dye formed on the downstream vertical wall. However, at the point of separation, the dye formed

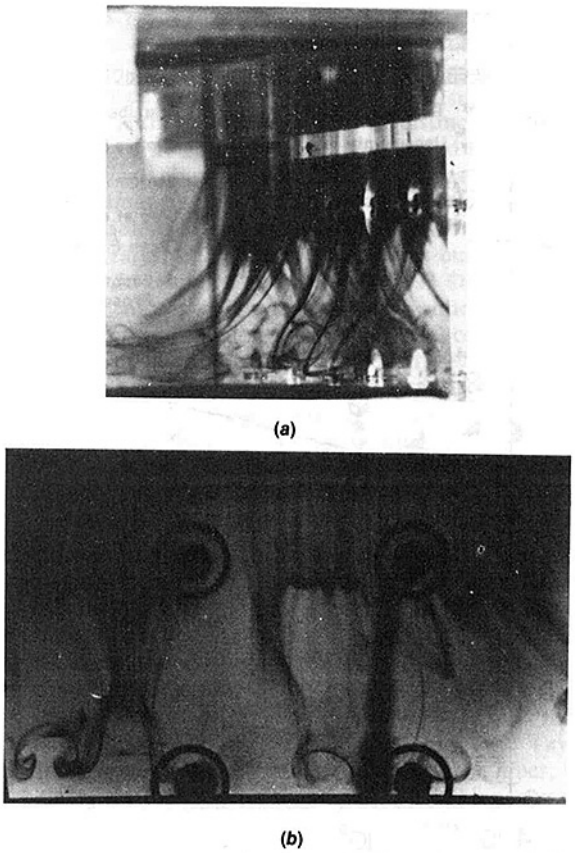

(a)

(b)

Fig. 8 Dye sheet and streaks along the downstream vertical wall (photograph taken slightly oblique to view A (*a*) and from view B (*b*), respectively). Streaks are Taylor-Görtler like vortices at Re = 3000.

discrete spirals at fairly regular intervals. This is shown in Fig. 8. Figure 8(*a*) (view slightly oblique to view A) shows the dye sheet above the separation point and the discrete streaks below it. (All apparent streaks which go to the right from the separation point are reflections!) The downstream secondary eddy can also be clearly seen in this picture. Figure 8(*b*) (View B in Fig. 3) shows the same phenomena as well as the spiralling nature of the dye streaks. The formation of the horseshoe structure in the lower left corner of the picture is a good example. These pictures were taken for a Reynolds number of 3000, but the behavior is similar over the entire Reynods number range considered.

The structures in these pictures bear strong resemblance to Taylor-Görtler vortices. They are formed because the surface of separation between the primary eddy and the secondary eddy is effectively a concave "wall." The vortices, which occur in pairs, cause the dye to form the discrete streaks. Thus, each streak forms the boundary for a pair of vortices. The number of vortex pairs varies with Reynolds number; at Re = 3000 there are 8 pairs and at Re = 6000 there are 11 pairs. The end walls appear to affect the distribution of the vortices. Thus the picture in Fig. 8(*b*) shows irregularly spaced dye streaks as opposed to the "box-like" distribution shown by Taylor [26]. The existence of these vortices is a further indication of the three dimensionality of the flow.

In the high Reynolds number range, the Taylor-Görtler-like vortices become progressively less like the structures Görtler [20] describes in his paper. This occurs because, with the onset of turbulence, other structures form and interfere with the integrity of the Taylor-Görtler-like vortices. The spiralling features in the direction of flow are, however, evident for the entire flow range considered.

(*d*) Downstream Secondary Eddy Size. One of the largest discrepencies in the results of two-dimensional numerical

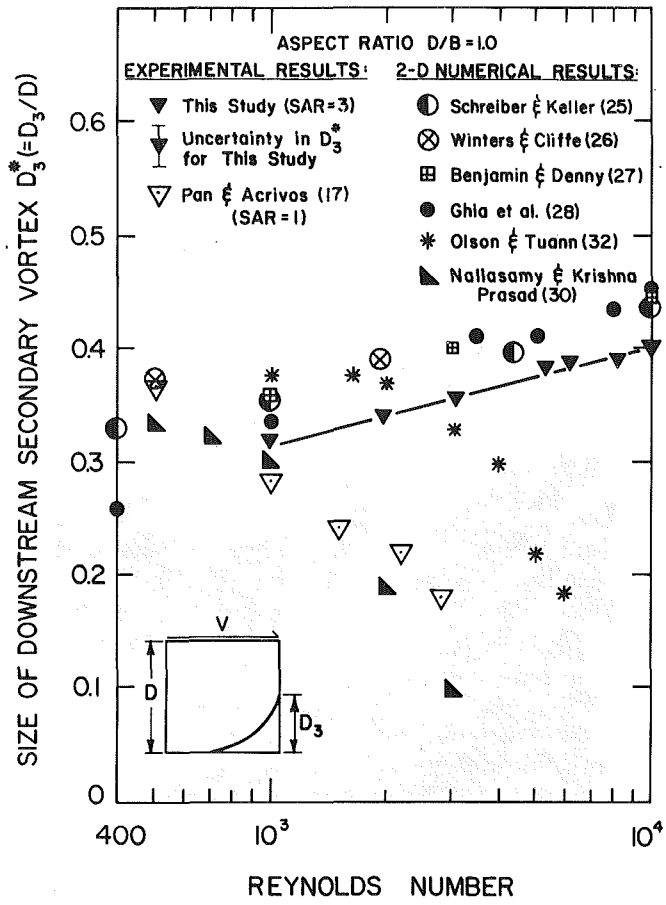

Fig. 9 Downstream secondary eddy size as a function of Reynolds number

simulations is in the predicted size D_3 (see Fig. 4) of the downstream secondary eddy as a function of Reynolds number. As can be seen in Fig. 9, some solutions predicted the disappearance of this eddy at a Reynolds number of about 5000. The observations in the present study reveal that the eddy grows quite rapidly in size up to a Reynolds number of 5000 and then remains roughly constant in size. The referenced size is the distance D_3 from the point of separation to the lower boundary, measured at the cavity center-plane. This dimension is normalized by the cavity depth D and plotted in Fig. 9 as D_3^* $(=D_3/D)$. The size of this eddy was determined by scaling the distances from the corner to the dye separation point on the visualization photographs. This value does not vary significantly with time, but the point of reattachment does. Our experimental results show the same trend as the numerical results of Schreiber and Keller [27], Winters and Cliffe [28], Benjamin and Denny [29] and Ghia et al. [21]. However, the experimental points lie about 5 percent of the cavity depth closer to the lower boundary for Reynolds numbers up to 10000. This occurs because the numerical simulations are two- dimensional and the cavity flow is three-dimensional. In addition the cited numerical simulations are all for laminar flow and, therefore, may not adequately represent the flow physics for the higher Reynolds numbers where parts of the flow are thought to be turbulent.

Pan and Acrivos [17] show a trend (with Re) which is opposite to that of the present results. However, their cavity was a cube (SAR = 1), while the present facility's SAR = 3. Additional experiments in our facility (to be reported later) at SAR = 2 and 1 confirm that their results are consistent and that spanwise-aspect-ratio (SAR) is an important factor. Also, they did not use a flat lid to drive the flow, but rather used a cylinder which penetrated into the cavity. This penetration, which reaches a maximum of about 10 percent of the cavity depth, appears to accentuate this opposing trend. Mills (14) showed that the downstream secondary eddy was in fact present at a Reynolds number of 100,000.

Summary and Conclusion

This initial set of visualization studies has revealed the following concerning a lid-driven cavity flow:

(1) the flow is three-dimensional and exhibits Taylor-type instabilities at start up and Taylor-Görtler-like vortices in the fully-established state;
(2) the flow first displays evidence of turbulence in the Reynolds number range of 6000-8000;
(3) there are apparently three secondary eddies present for the entire Reynolds number range considered (1000 – 10000). The eddies do not disappear as the Reynolds number increases as predicted by some numerical studies;
(4) fluid motion in the direction transverse to the driving motion of the lid is significant. Therefore, two-dimensional numerical simulations of a cavity flow should be compared with discretion with cavity flow experiments.

Continuing studies are concentrating on the effects of temperature stratification and buoyancy on the circulation cell formation. The scope of this work has been expanded also to include velocity and temperature measurements, as well as the very informative flow visualization.

Acknowledgments

This work was performed in the Stanford University Hydromechanics Research Laboratory and was supported by National Science Foundation Grant CME-7921324, and Department of Energy Contract DOE-DE-AT03-81-ER-10867.

References

1 Davis, G. De Vahl, and Mallinson, G. D., "An Evaluation of Upwind and Central Difference Approximations by a Study of Recirculating Flow," *Computers and Fluids*, Vol. 4, 1976, pp. 29–43.

2 Gresho, P. M., Chan, S. T. K., Lee, R. L. and Upson, C. D., "Solution of the Time-Dependent, Three-Dimensional Incompressible Navier-Stokes Equations via FEM," *Proc. Int. Conference on Num. Meth. for Laminar and Turbulent Flow*, Venice, Italy, July 13–16, 1981, pp. 27–39.

3 Findikakis, A. N., "Finite Element Simulation of Turbulent Stratified Flows," Ph.D. dissertation, Department of Civil Engineering, Stanford University, 1980.

4 Young, D. L., Liggett, J. A., and Gallagher, R. H., "Unsteady Stratified Circulation in a Cavity," *Journal of Engineering Mech. Div.* ASCE 102, EM6, 1976, pp. 1009–1023.

5 Gosman, A. D., Pan, W. M., Runchal, A. K., Spalding, D. B. and Wolfshtein, M., *Heat and Mass Transfer in Recirculating Flows*, Academic Press, London, 1969.

6 Ideriah, F. J. K., "On Turbulent Forced Convection in a Square Cavity," *Numerical Methods in Laminar/Turbulent Flow, Proc. 1st Int'l. Confer.*, 1978, pp. 257–269.

7 Roshko, A., "Some Measurements of Flow in Rectangular Cut-Out," NASA Technical Report 3488, 1955.

8 Fox, J., "Flow Regimes in Transverse Rectangular Cavities," *Heat Transfer and Fluid Mechanics*, Stanford University Press, 1965, pp. 230–247.

9 Maull, D. J. and East, L. F., "Three-Dimensional Flow in Cavities," *Journal of Fluid Mechanics*, Vol. 16, 1963, pp. 620–632.

10 Haugen, R. L., and Dhanak, A. M., "Momentum Transfer in Turbulent Separated Flow Past a Rectangular Cavity," ASME *Journal of Applied Mechanics*, 1966, pp. 641–646.

11 Reiman, T. C. and Sabersky, R. H., "Laminar Flow Over Rectangular Cavities," *Int'l. Journal of Heat and Mass Transfer*, Vol. 11, 1968, pp. 1083–1085.

12 Johnson, R. W., and Dhanak, A. M., "Heat Transfer in Laminar Flow Past a Rectangular Cavity with Fluid Injection," ASME *Journal of Heat Transfer*, 1976, pp. 226–231.

13 Orlandi, P., and Ianetta, S., "Laser Doppler Anemometer Flow Measurements in a Channel with a Wall Cutout," 13th Biennial Fluid Dynamics Symposium, Kortowo, 1977.

14 Mills, R. D., "Numerical Solutions of the Viscous Flow Equations for a

Class of Closed Flows," *Journal of Royal Aero. Soc.*, Vol. 69, 1965, pp. 714–718.

15 Mills, R. D., "On the Closed Motion of a Fluid in a Square Cavity," *Journal of Royal Aero. Soc.*, Vol. 69, 1965, pp. 116–120.

16 Chashechkin, J. D., "Experimental Studies of the Mixed Layer in Stratified Liquids," *IAHR Symp. on Stratified Flows*, Trondheim, 1980.

17 Pan, F., and Acrivos, A., "Steady Flows in Rectangular Cavities," *Journal of Fluid Mechanics*, Vol. 28, 1967, pp. 643–655.

18 Baker, D. J., "A Technique for the Precise Measurement of Small Fluid Velocities," *Journal of Fluid Mechanics*, Vol. 26, 1966, pp. 573–575.

19 Tennekes, H. and Lumley, J. L., *A First Course in Turbulence*, MIT Press, Cambridge, Mass., 1972.

20 Görtler, H., "On the Three-Dimensional Instability of Laminar Boundary Layers on Concave Walls," NACA Technical Mem, 1375, 1954.

21 Ghia, U., Ghia, K. N., and Shin, C. T., "Solution of Incompressible Navier-Stokes Equations by Coupled Strongly Implicit Multi-Grid Method," *J. Comp. Phys.*, Vol. 48, 1982, pp. 387–411.

22 Clauser, M., and Clauser, F., "The Effect of Curvature on the Transition from Laminar to Turbulent Boundary Layer," NACA-TN613, 1937.

23 Kirchner, R. P., and Chen, C. F., "Stability of Time-Dependent Rotational Couette FLow. Part 1. Experimental Investigation," *Journal of Fluid Mechanics*, 40, 1970, pp. 39–47.

24 Chen, C. F., and Christensen, D. K., "Stability of Flow Induced by an Impulsively Started Rotating Cylinder," *The Physics of Fluids*, Vol. 10, 1967, pp. 1845–1846.

25 Taneda, S., "Visual Study of Unsteady Separated Flows around Bodies," *Prog. Aerospace Science*, Vol. 17, 1977, pp. 287–348.

26 Taylor, G. I., "Stability of Viscous Liquid Contained between Two Rotating Cylinders," *Phil. Trans. Roy. Soc. (London)*, Vol. 223, 1923, pp. 289–343.

27 Schreiber, R., and Keller, H. B., "Driven Cavity Flows by Efficient Numerical Techniques," *Journal of Computational Physics*, Vol. 49, 1983, pp. 310–333.

28 Winters, K. H., and Cliffe, K. A., "A Finite Element Study of Laminar Flow in a Square Cavity," UKAERE Harwell Report R-9444, 1979.

29 Benjamin, A. S., and Denny, V. E., "On the Convergence of Numerical Solutions for 2-D Flows in a Cavity at Large Re," *Journal of Comp. Physics*, Vol. 33, 1979, pp. 340–358.

30 Olson, M. D., and Tuann, S-Y., "Further Finite Element Results for the Square Cavity," *Proc. Third Int'l Confer. on Finite Elements in Flow Problems*, Banff, Alberta, Canada, 1980, pp. 143–152.

31 Nallasamy, M., and Krishna Prasad, K., "On Cavity Flow at High Reynolds Numbers," *Journal of Fluid Mechanics*, Vol. 79, pp. 391–414, 1977, pp. 391–414.

Class of Closed Flows," *Journal of Royal Aero. Soc.*, Vol. 69, 1965, pp. 714–718.

15 Mills, R. D., "On the Closed Motion of a Fluid in a Square Cavity," *Journal of Royal Aero. Soc.*, Vol. 69, 1965, pp. 116–120.

16 Chashechkin, J. D., "Experimental Studies of the Mixed Layer in Stratified Liquids," *IAHR Symp. on Stratified Flows*, Trondheim, 1980.

17 Pan, F., and Acrivos, A., "Steady Flows in Rectangular Cavities," *Journal of Fluid Mechanics*, Vol. 28, 1967, pp. 643–655.

18 Baker, D. J., "A Technique for the Precise Measurement of Small Fluid Velocities," *Journal of Fluid Mechanics*, Vol. 26, 1966, pp. 573–575.

19 Tennekes, H. and Lumley, J. L., *A First Course in Turbulence*, MIT Press, Cambridge, Mass., 1972.

20 Görtler, H., "On the Three-Dimensional Instability of Laminar Boundary Layers on Concave Walls," NACA Technical Mem, 1375, 1954.

21 Ghia, U., Ghia, K. N., and Shin, C. T., "Solution of Incompressible Navier-Stokes Equations by Coupled Strongly Implicit Multi-Grid Method," *J. Comp. Phys.*, Vol. 48, 1982, pp. 387–411.

22 Clauser, M., and Clauser, F., "The Effect of Curvature on the Transition from Laminar to Turbulent Boundary Layer," NACA-TN613, 1937.

23 Kirchner, R. P., and Chen, C. F., "Stability of Time-Dependent Rotational Couette FLow. Part 1. Experimental Investigation," *Journal of Fluid Mechanics*, 40, 1970, pp. 39–47.

24 Chen, C. F., and Christensen, D. K., "Stability of Flow Induced by an Impulsively Started Rotating Cylinder," *The Physics of Fluids*, Vol. 10, 1967, pp. 1845–1846.

25 Taneda, S., "Visual Study of Unsteady Separated Flows around Bodies," *Prog. Aerospace Science*, Vol. 17, 1977, pp. 287–348.

26 Taylor, G. I., "Stability of Viscous Liquid Contained between Two Rotating Cylinders," *Phil. Trans. Roy. Soc. (London)*, Vol. 223, 1923, pp. 289–343.

27 Schreiber, R., and Keller, H. B., "Driven Cavity Flows by Efficient Numerical Techniques," *Journal of Computational Physics*, Vol. 49, 1983, pp. 310–333.

28 Winters, K. H., and Cliffe, K. A., "A Finite Element Study of Laminar Flow in a Square Cavity," UKAERE Harwell Report R-9444, 1979.

29 Benjamin, A. S., and Denny, V. E., "On the Convergence of Numerical Solutions for 2-D Flows in a Cavity at Large Re," *Journal of Comp. Physics*, Vol. 33, 1979, pp. 340–358.

30 Olson, M. D., and Tuann, S-Y., "Further Finite Element Results for the Square Cavity," *Proc. Third Int'l Confer. on Finite Elements in Flow Problems*, Banff, Alberta, Canada, 1980, pp. 143–152.

31 Nallasamy, M., and Krishna Prasad, K., "On Cavity Flow at High Reynolds Numbers," *Journal of Fluid Mechanics*, Vol. 79, pp. 391–414, 1977, pp. 391–414.

DISCUSSION

J. A. C. Humphrey[1]

This is indeed an eye-opening flow visualization study, illustrating especially the importance of critically conducted experimentation for the development and testing of computational fluid mechanic models. The authors are to be complimented for their fine work in revealing several new and very interesting findings in a shear-driven, isothermal, enclosure flow. Since it is not mentioned in the paper, the reader should be aware that there is also a wealth of similar information relating to the case of thermally stratified flow in the Ph.D. thesis of Koseff [32], the basis for the present study.

With their results, the authors have dispelled conclusively the myth of "two-dimensional," shear-driven, cavity flow. While such a hypothetical flow will probably continue to serve as a useful test case for the evaluation of numerical calculation procedures, it is in the prediction of the transient and steady state three-dimensional structures discovered by the authors wherein the real challenge now lies. Thus, recent efforts [33] to predict the cross-stream vortices they observed were unsuccessful due, most likely, to insufficient grid refinement. In this regard, Han et al. [34] have demonstrated the importance of higher order finite difference schemes for resolving all three of the corner-eddies arising in two-dimensional, shear-driven, turbulent, cavity flow.

Taylor and Taylor-Görtler vortices are manifestations of the same type of physical instability, albeit in different flow configurations. They are cross-stream secondary flows, driven by pressure gradient-centrifugal force imbalances acting upon fluid elements moving along curved paths in the vicinity of concave surfaces [35]. In spite of their commonality, the authors appear to draw a distinction between the "Taylor" vortices observed at start-up and the "Taylor-Görtler" vortices observed near the downstream secondary eddy at later times. Is there a sound basis for this distinction? Is it not possible that the authors have, in fact, visualized *evolving* structures; i.e., the same structures but at different points in the flow and at subsequent times? Of course, the appearance of the vortical structures begs the question of their origin. Working by analogy with Taylor's celebrated investigation [36], the authors postulate that a "cylinder" of high vorticity fluid near the downstream lip of the cavity is the source of the vortices during start-up. A calculation of the possible range spanned by the Taylor number

$$\left(\mathrm{Ta} \equiv \frac{U_i d}{\nu}\left(\frac{d}{R_i}\right)^{1/2}\right)$$

of the flow contained in the gap between such a "cylinder" and the enclosure walls can be made using the experimental data given in Figs. 5.2.2, 5.2.3, and 5.5.3 in [32]. From the data, estimates of the cylinder radius, peripheral velocity and gap width in the region where the vortices initially appear are, respectively, given by $R_i \simeq B/8$, $U_i \simeq 0.8\ V$ and $d \simeq B/20$. Using these values yields $76 \lesssim \mathrm{Ta} \lesssim 250$ for the range $3000 \lesssim \mathrm{Re} \lesssim 10{,}000$. On the basis of this result the Taylor instability is favored for this range of Reynolds number, but not the turbulent flow regime for which $\mathrm{Ta} \gtrsim 400$ is necessary. This contrasts with the observation reported by the authors, that "the flow first displays evidence of turbulence in the Reynolds number range of $6{,}000 \lesssim \mathrm{Re} \lesssim 8{,}000$", corresponding to $152 \lesssim \mathrm{Ta} \lesssim 202$.

There is only a tenuous relation between the conditions of Taylor's experiment, for which the Taylor number is precisely defined, and the authors' postulated rotating cylinder. Therefore, the above numerical estimates should be viewed mainly as providing additional support for referring to the observed cross-stream structures as Taylor (or Taylor-Görtler) vortices and not, necessarily, for supporting the correctness of a "rotating cylinder" model. Thus, in fact, in the downstream lip region of the cavity, where the shear-driven flow impacts on the vertical side wall, the flow is also similar in some respects to that arising near the forward stagnation point of a bluff body in a stream. According to Schlichting [35], Görtler has noted that this type of flow is prone likewise to the cross-stream flow instability of interest here.

Given the fragility of arguments based on imperfect analogies, like the one pursued here, it is clear that further in-depth theoretical analysis of the authors' findings is still necessary. Here is a fresh and stimulating new opportunity for the fluid mechanics community!

Additional References

32 Koseff, J. R., "Momentum Transfer in a Complex Recirculating Flow," Ph.D. thesis, Department of Civil Engineering, Stanford University, Stanford, Calif. 94305.

33 Koseff, J. R., Street, R. L., Gresho, P. M., Upson, C. D., Humphrey, J. A. C. and To, W.-M. "A Three-Dimensional Lid-Driven Cavity Flow: Experiment and Simulation," *Proc. of Third Int'l Conf. on Numerical Methods in Laminar and Turbulent Flow*, Univ. Washington, Aug. 8-11, 1983, pp. 564–581.

34 Han, T., Humphrey, J. A. C., and Launder, B. E., "A Comparison of Hybrid and Quadratic-Upstream Differencing in High Reynolds Number Elliptic Flows," *Computer Methods in Applied Mechanics and Engineering*, Vol. 29, 1981, pp. 81–95.

35 Schlichting, H., *Boundary-Layer Theory*, McGraw-Hill Book Company, 6th edition, pp. 500–508, 1968.

36 Taylor, G. I., "Stability of A Viscous Liquid Contained Between Two Rotating Cylinders," Phil. Trans. A*223*, pp. 289–343, 1923.

[1] Department of Mechanical Engineering, University of California, Berkeley, Calif. 94720.

A. Pollard[2]

I would first like to congratulate the authors on constructing such a well conceived and delightfully simple experimental rig. Not only does it permit the illustration of the three-dimensional complexity of this flow, often taken by numerical analysts as two-dimensional, but the potential for detailed studies that include the structures of turbulence, heat transfer, and transients is considered by this discusser to be most exciting.

The results presented in this paper I find most intriguing; particularly the formation of what the authors refer to as Taylor-Gortler-like vortices on the downstream wall. While it can be readily seen that such structures exist, I question their origins. The author's note that they are formed because the downstream eddy provides a concave surface. I wonder, however, if something upstream of this surface is providing a preferential mode of instability such that the curved surface downstream is just acting to amplify this basic instability.

The basic instability seems to originate with the vortex as it is formed at the corner T (Fig. 4); for, in Fig. 7 it is clear that the vortex possesses a wave like surface structure. Although calculations have not been done, perhaps the driving belt, that is but 0.08 mm thick, is buckling and setting up a series of waves parallel to the belt's motion; or, possibly, the dye sheet, originally "on" the belt's under-surface, develops instabilities as it is forced into forming the vortex. This latter instability could be, I suppose, likened to Taylor-Gortler instabilities. Perhaps the authors could comment upon these speculations.

However the wave-like structure is precipitated, there is developed a series of toroidal vortices. Can the authors discuss the correlation between the number of these vortices and the number of pairs of Taylor-Görtler-like vortices observed on the surface of the downstream eddy including the effect of Reynolds number?

P. Orlandi[3]

The Authors of this paper considered a flow-field which in the last twenty years has been the subject of study by many scholars using numerical methods to solve Navier-Stokes equations. This preliminary study, although limited to visualizing the flow-field, allows a good understanding of the complex behavior of this flow-field. To my knowledge this is the first study to show clearly that below Re = 5000 the flow is laminar. The experimental evidence is very useful in developing new numerical methods to solve Navier-Stokes equations. In my opinion a numerical method for recirculating flows is worth being considered only if it can give accurate solutions at high Re numbers. From the computational point of view the case of Re = 5000 can be considered a very high Re number case and can be taken as a good test case in checking the qualities of a numerical method. I hope that the authors will publish velocity profiles, in particular vertical velocity profiles along the horizontal center line, as soon as possible. From my unpublished numerical experience in solving this flow-field, I feel the necessity to have experimental velocity data in the vertical boundary layers, becaue good numerical solutions in the central regions can be easily obtained in spite of a poor representation of the vertical boundary layers.

[2]Department of Mechanical Engineering, Queen's University at Kingston, Kingston, Ontario, Canada

[3]Universita Degli Studi Di Roma, Dipartimento de Meccanica E Aeronautica, Rome, Italy

The authors emphasize the rapid penetration of the initial vorticity sheet into the core region. This aspect is very interesting to "computors" which prefer to use unsteady codes. It is difficult to have a clear image of the flow "start up," by reading the paper, but better description was given at the meeting where the authors showed a movie. The authors, from the movie, could draw the time evolution of the vortex center and plot it in a form which could be easily used for comparison with numerical results.

The most important conclusion is that flow-field obtained by an experimental apparatus with a high aspect ratio still shows a three-dimensional character, due to the Taylor-Görtler vortices formation on the concave surfaces of the two bottom secondary eddies. Since today's computers allow three-dimensional calculations, the observed periodicity of the Taylor-Görtler vortices suggests to the "computors" the use of periodical boundary conditions in the direction transverse to the driving motion. This visualization study does not give a description of the dimensions and spacing of the Taylor-Görtler vortices of benefit to the "computors." A more quantitative analysis would allow three-dimensional calculation by using a limited number of grid points in the "spanwise" direction and leaving at disposal a larger number of points in the other two directions, where more complex structures appear. The investigation of the Taylor-Görtler vortices formation allows a better knowledge of the formation of the small scale eddies which, in the full turbulent regime, will extract turbulent energy from the two-dimensional mean motion. An analysis similar to the one suggested by Hussain[4] (topological features of coherent structures) could be appropriate in giving a better understanding of the flow due to the interaction between the primary and secondary eddies.

Authors' Closure

We share the enthusiasm of all three discussers for the facility and our visualization study and appreciate their thoughtful questions regarding the formation and presence of the Taylor-Görtler-like (TGL) vortices and their relationship with the toroidal vortices formed near the downstream lip of the cavity. We treat the questions and comments in turn.

First, the possibility exists (as Professor Pollard suggests) that an instability is generated upstream of the concave surface in the region of the downstream secondary eddy (DSE). During start-up, the toroidal vortices formed in the region of the downstream lip of the cavity (corner T; Fig. 4) are one possible source. However, these vortices are present only during the start-up (the initial transient) period. There is no vortex in corner T once the flow is established. Clearly, as Professor Humphrey suggests, we have visualized evolving structures; the transient toroidal vortices may contribute to the initial establishment of the TGL vortices, but are not a factor in the continued presence of the TGL vortices. It was for this reason that we choose to distinguish between the phenomena.

Second, Professor Pollard notes that the vortex formed in the region of corner T at start-up "possesses a wave like surface structure." He asks if buckling of the belt may trigger an instability leading to the formation of the toroidal vortices and hence the TGL vortices. We think not for three reasons:

(*a*) The very same toroidal structure was observed by Kirchner and Chen (23), among others, during their experiments with impulsively started cylinders. The wave like structure is the first phase of the boundary layer instability

[4]Hussain, A. K. M. F., "Coherent Structures—Reality and Myth," *The Physics of Fluids*, Vol. 26, No. 10, 1983, pp. 2816–2850.

leading to the formation of the toroidal vortices. They form in the corner T at startup in an analogous fashion.

(*b*) Visual observations made during our experiments indicated no significant deformations of the belt. Great care was taken to ensure that the belt tracked smoothly. It is under tension as it passes over the cavity and so buckling is unlikely. Also, the belt is forced to move against the upper heat exchanger plate which aids in keeping the belt smooth as it passes over the cavity.

(*c*) The dye generated by the belt (once the flow is established) flows down the downstream side wall (out of corner T; see TM in Fig. 4) in a uniform sheet. There are no wavy structures present in this sheet or any indication of other instabilities (see Fig. 8). This strongly suggests that the belt is not generating instabilities. Also, the dye is neutrally buoyant and so plays no role in the flow dynamics. Additional flow visualization studies [see Rhee, et al. (37)] with rheoscopic liquid show the same flow features which are therefore unrelated to the flow visualization method.

With regard to Professor Pollard's last point, we have not found a useful correlation between the number of pairs of TGL vortices and the number of toroidal vortices, although, as Professor Humphrey points out, the Taylor and Taylor-Görtler vortices are manifestations of the same type of physical instability. The number of each type observed is a function of the Reynolds number (Re). At higher Re an increased number of smaller toroidal vortices form [a result consistent with that of Kirchner and Chen (23)] and the number of pairs of TGL vortices increases. In general, more toroidal vortices are observed for a given Re than TGL vortices. The former interact with each other after forming during start-up (due partially to the presence of the end-walls). Thus, the number of toroidal vortices is a function of time and decreases to zero when the flow is fully established.

We turn now to the thought-provoking calculations made by Professor Humphrey with regard to the Taylor number (Ta) of the flow. In spite of (as Humphrey puts it) the fragility of the relationship between our experiments and those of Taylor [26], it is satisfying to know that Humphrey's analysis shows that the formation of the toroidal vortices is favored for the Ta range calculated. However, he poses his analysis for the start-up conditions. Our observation that the flow first displays evidence of turbulence in the Re range of 6000 to 8000 is related to the later conditions when the TGL vortices are fully formed. Thus, the Ta calculations are no longer relevant as a criterion for the onset of turbulence. Unlike the experiments of Taylor [26] in which solid cylinders were used, our concave surface (the DSE) varies not only with spanwise location but also with time. In addition, strong spanwise motions in this region are caused by the presence of the end-walls. The criteria for the appearance of turbulence in each flow are therefore likely to be quite different.

Professor Orlandi posed questions about the numerical aspects of this flow. With regard to his question concerning grid requirements for the adequate resolution of all the flow features it appears that in order to resolve the TGL vortices ". . . greater numbers of grid or node points, especially in the spanwise direction, will be required. . ." (33). Dr. John Kim of NASA-AMES recently performed a three-dimensional calculation (private communication) for a "slice" of the flow (of span equal to 1/6 that of our cavity) for Re = 1000, using periodic boundary conditions in the spanwise direction. He was able to resolve the TGL vortices with 31 node points in the spanwise direction. It is, however, most important to include the end-walls in future calculations as they are a very significant influence on the flow.

Last, we have measured velocity profiles for the extant case at Reynolds numbers of 3200 and 10,000 (38). We hope to publish more detailed data on the TGL vortices in the near future.

Additional References

37 Rhee, H., Koseff, J. R., and Street, R. L., "Flow Visualization of a Recirculating Flow by Rheoscopic Liquid and Liquid Crystal Techniques," *Experiments in Fluids*, 1983, in press.

38 Koseff, J. R., Street, R. L., and Rhee, H., "Velocity Measurements in a Lid-Driven Cavity Flow," ASME Symposium on Numerical and Experimental Investigations of Confined Recirculating Flows, preprint No. 83-FE-12, Houston, June 20–22, 1983.

Flow Structure and Pressure Loss for Two Phase Flow in Return Bends

K. Hoang
Professional Officer.

M. R. Davis
Associate Professor.

School of Mechanical and Industrial Engineering,
University of New South Wales,
Kensington, Australia

Experimental observations of flow structure and pressure loss have been made for froth flow within 180 deg circular pipe bends. Within the bend the distributions of pressure observed reflected the onset of rotation and phase separation effects, whilst secondary flow effects were apparent in the voidage distributions at outlet. Significant components of the overall pressure drop were found both within the bend itself and in the pipe immediately downstream of the bend. Velocity slip between gas and liquid was found to increase observed loss coefficients by approximately 10 percent. The overall loss coefficients were substantially larger than in single phase flow, particularly for bends with larger radius of centerline curvature where they increased by as much as five times the single phase value. The overall pressure loss coefficients were highest for the sharper radius bends, and it was deduced that flow separation and remixing contributed mainly to the increase over single phase loss coefficients.

Introduction

It is the purpose of the present work to consider the influence of flow structure on pressure loss and pressure distribution for two phase bubbly or froth flow in a pipe bend. While Pigott [1, 2] and Ito [3] have investigated the influence of bend geometry on the pressure loss for single phase flow, no comparable investigation has been carried out for two phase flows. Banerjee et al. [4] observed these effects for gas-liquid flow in a coiled helical tube and were able to relate their observations to the Lockart-Martinelli correlation [5] for frictional pipe flow. However, in the present work much smaller values of the ratio R_c/r_0 are to be investigated, R_c being the radius of curvature of the pipe centerline and r_0 the radius of the pipe cross section. For these relatively sharp bends the pressure drop is very much larger than that which would occur in a pipe of equivalent length to the bend (e.g., by a factor of approximately 20) and the losses are mainly dependent on the sharpness of the bend as described by Ito [3] but with the additional complications due to the interfacial structure of the two phase flow.

Consideration of the pressure loss in two phase flow is somewhat more complicated than in single phase flow. Firstly, slip or relative motion between the two phases has a direct effect on the momentum of the flow. The average velocity of flow determined from volumetric flow rate is not an adequate basis for momentum determination, and detailed voidage and velocity distributions at the pressure measurement positions are required. Secondly, as pressure reduces the mixture accelerates and it is necessary to consider this acceleration in the momentum balance. In this paper an analysis for isothermal gas/liquid mixture flow is introduced to provide a means of correctly allowing for mixture momentum in the determination of pressure loss in the bend from actual pressure data.

Two phase flow through a curved bend in a circular pipe will be influenced by the secondary flow effects which are well known in single phase flows (Zanker and Brock [6], Lacey [7]) and also by separation of the phases due to centrifugal forces which will tend to concentrate the liquid toward the outside of the bend. Separation of phases in this way is likely to give rise to significant slip or relative motion effects between the phases. Further insight on the actual flow within the bend can be obtained from pressure data at the bend wall. In the present paper such pressure data are analyzed to show how the phases separate in the bend and also to show how rotation of the flow within the bend develops due to the radial velocity shear gradients.

Observations of the Flow Structure

Experiments were carried out in two 180 deg pipe bends, with pipe radius 2.54 cm and centerline radii 5.08 cm and 7.62 cm, carrying flows of air water mixture which entered the bend through a vertical 1.02 m length of pipe from a nozzle mixer (see Herringe and Davis [8]). The flow discharged downwards from the bend through a 1.23 m length of circular pipe. The inlet flow conditions to the bend were similar to those of Herringe and Davis [8], and are specified in Table 1. The mass flows of the two phases were recorded by standard orifice plates ahead of the mixer unit, and mean volumetric

Contributed by the Fluids Engineering Division of THE AMERICAN SOCIETY OF MECHANICAL ENGINEERS and presented at the 7th Annual/Energy-Sources Technology Conference and Exhibition, New Orleans, La., February 11–17, 1984. Manuscript received by the Fluids Engineering Division, January 8, 1980. Paper No. 84-FE-1.

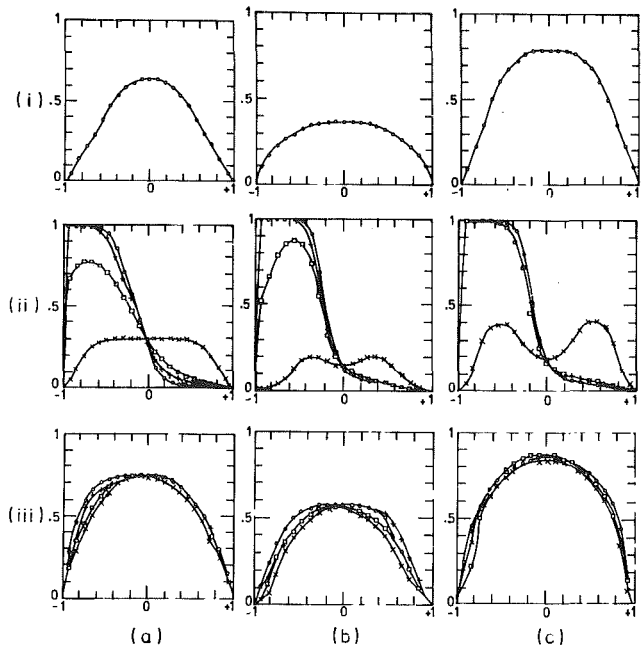

Fig. 1 Void distributions in vicinity of the 180 deg bend ($R_c/r_0 = 2.0$)
(i) At inlet plane
(ii) At outlet plane
(iii) In outlet pipe, 9 diameters downstream of outlet
(a) U_m = 4.0 m/s, $\beta = 0.30$
(b) U_m = 6.0 m/s, $\beta = 0.20$
(c) U_m = 10.6 m/s, $\beta = 0.42$
Vertical scale = void fraction (α)
Horizontal scale = radial position (r/r_0) (−1 is inside wall of bend)
○: ϕ = 0 deg; +: ϕ = 30 deg
□: ϕ = 60 deg; ×: ϕ = 90 deg

flows and speeds were thus calculated on the basis of the observed pressures at the test section. High speed ciné film records at 2000 frames/s and flash photographs showed the inlet flows to be well mixed and froth-like at inlet. Within the bend, separation of phases was observed, the liquid concentrating to the outer wall. Downstream of the bend the flow remixed in an intermittent manner, large gas slugs appearing irregularly, interspersed with clouds of finer bubbles. At higher mean mixture speeds it appeared from these external observations that the remixing occurred more rapidly.

Detailed observations of the internal flow structure were

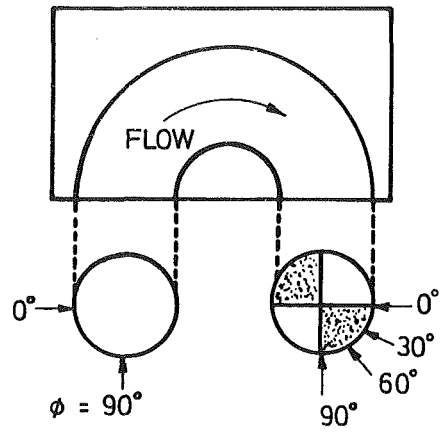

Fig. 2 Definition of angular coordinate ϕ

made using very sharp needle probes to record the time history of void fluctuations at the sensing point (Herringe and Davis [9]). Analysis of the unsteady two state signals from these probes allows determination of time average void fraction at the point of convection velocity of the gas bubbles by correlation between two needles displaced axially by a small distance and also of size distributions of the bubbles passing the point by analysis of the durations for each bubble to pass the probe. Herringe and Davis [9] have shown that these methods are reliable for the flow conditions used. The local voidage can be determined to within 3 percent after checking against the known total gas volumetric flow rate by integration of the observed local voidage distribution across the cross section of the pipe.

In addition, the Froude number is considered in the present work because the test bend is located in a vertical plane so that the flow passes from vertical up-flow to vertical down-flow. The velocities in the tests were such that the Froude number based on the bend radius was of order 5-50, and thus gravitational forces can play a significant part in the motion of the mixture as it passes up and over through the bend.

Figure 1 shows distributions of local void fraction for three flow conditions. The local void fraction is defined as the fraction of total time for which the probe is immersed in the gas phase. At inlet the distribution is symmetrical and has a maximum voidage at the centerline showing the flow to be well mixed but with higher liquid concentration toward the

Nomenclature

A = pipe cross-section area
A_g = inlet mean dimensionless dynamic head ($\rho m_0 U_0^2/2p_0$)
D = bubble diameter
d = pipe diameter ($d = 2r_0$)
E = energy
Fr = Froude number (u_m^2/gd)
g = gravitational acceleration
h = vertical position
K = bend loss coefficient
$\dot{m}$ = mass flow rate
n = compression index of polytropic relation
N_d = detected bubble frequency
p = absolute wall static pressure
$\tilde{p}$ = dimensionless pressure $= p/p_0$
Q = volumetric flow rate
R_c = bend centerline radius of curvature
r = radial coordinate in pipe
S = slip ratio $= [U_g]/[U_l]$, based on cross-sectional average values
U_0 = mixture mean velocity at bend inlet
u = streamwise velocity
u_{mr} = mean mixture velocity at mid section of the bend $((Q_g + Q_l)/A)$
α = void fraction
β = volumetric flow fraction $(Q_g/(Q_g + Q_l))$
θ = angle from bend inlet plane
η = dimensionless radial coordinate $= r/R_c$
μ = absolute viscosity
ρ = density
σ = liquid surface tension
ϕ = angle between the plane passing through the bend's centerline and the vertical plane in which the probe traverses
ω = angular velocity of fluid mixture

Subscripts

b = bend inlet to outlet plane
bd = bend inlet to plane nine diameters beyond outlet plane
m,g,l = mixture, gas and liquid
n = component perpendicular to bend plane of symmetry
0 = upstream reference point (bend inlet plane)
t = value obtained from single phase correlation of Ito [3]
[ ] = area averaged property

wall. At the bend outlet it is clear that centrifugal effects have produced a nearly stratified flow condition, with mainly liquid on the outer 40 percent of the diameter in the plane of symmetry ($\phi = 0$ deg, ϕ is illustrated in Fig. 2) and only gas on the inner 30 percent of this diameter along the diameter at right angles to the plane of symmetry ($\phi = 90$ deg) there is evidence of a secondary flow effect at the two higher Froude number conditions (Fr = 60, 160, where $\mathrm{Fr} = u_m^2/2gr_0$, u_m being the mean mixture speed equal to total volumetric flow/cross-sectional area). Two maxima in voidage occur at the mid radius to each side of a central minimum on the plane of symmetry, corresponding to an outward entrainment of gas by the outward secondary flow at the mid radius position, and an inward entrainment of liquid on the plane of symmetry by the secondary inflow in that plane. At a distance of 9 diameters downstream of the bend exit the distribution of voidage has almost returned to a symmetrical form, particularly at the highest velocity condition tested. At the bend exit plane the centroid of voidage was found to lie at between 37 and 43 percent of the pipe radius towards the inside of the bend. However, at the 9 diameter downstream position it lay on average at 3 percent of the radius from the centerline for all flows observed. However, it is clear that strong mixing of the flow induced by the bend has eliminated the variations in the shape of the void profiles for different flows evident at the bend inlet. Thus it might be expected that even beyond the 9 diameter position where observations were made some further but relatively small adjustment of the flow structure would occur towards the fully developed condition which existed at inlet as discussed by Herringe and Davis [8]. However, it would be a much smaller adjustment than occurs within the bend and the 9 diameter length of outlet pipe. The 9 diameter downstream location was selected for detailed measurements on the basis that the strong stratification caused by the bend was virtually eliminated at that position. As discussed by Herringe and Davis [8] quite long distances (e.g., over 100 diameters of tube length) are required for development of symmetrical flows to the fully developed void profiles which they identified for these flow conditions.

Velocity profiles at the same positions in the flow near the bend are shown in Fig. 3. Conditions at inlet were again found to correspond to those observed by Herringe and Davis [8] for a flow following a long length of vertical tube. At the bend exit there was a tendency for higher velocities to occur in the low voidage outer region on the plane passing through the bend's centerline, and also in the vicinity of the high voidage regions on the diameter perpendicular to this plane. For the higher velocity condition a larger proportionate variation of velocity occurred. At the position 9 diameters downstream of the bend exit quite significant nonuniformities of velocity persisted, especially at the higher mean velocity flow condition, the flow on the outside of the bend largely retaining its higher velocity at the bend exit.

From the observed mean flow distributions the mean slip (S) was calculated

$$S = \frac{(1/[\alpha]) - 1}{(1/\beta) - 1} \tag{1}$$

where $[\alpha]$ is the average voidage over the flow cross section and β the ratio of gas to total volumetric flow rates (Zuber and Findlay [10]). Owing to the need to determine slip from voidage observations over the complete cross section as discussed for symmetrical flow conditions, it was only possible to make a limited number of determinations of S as shown in Table 1. The distribution of slip in the region of the bend is most strongly influenced by the Froude number ($\mathrm{Fr} = u_m^2/gd$) in these observations as the bend turns the flow from vertically upwards to downwards. At Fr = 24, the slip at bend exit was much higher than at inlet, and a slight reduction subsequently occurred at the 9 diameter downstream position.

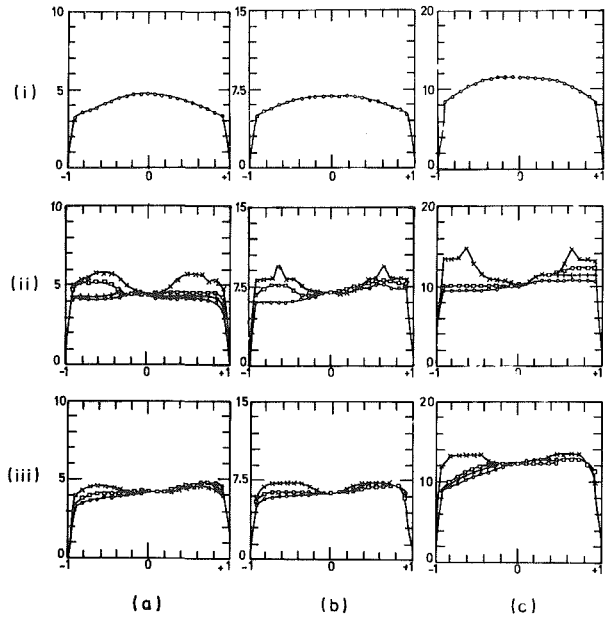

Fig. 3 Velocity profile in vicinity of the 180 deg bend ($R_c/r_0 = 2.0$)
(i) At inlet plane
(ii) At outlet plane
(iii) In outlet pipe, 9 diameters downstream of outlet
(a) U_m = 4.0 m/s, $\beta = 0.30$
(b) U_m = 6.0 m/s, $\beta = 0.20$
(c) U_m = 10.6 m/s, $\beta = 0.42$
Vertical scale = local mean convection velocity (m/s)
Horizontal scale = radial position (r/r_0) (−1 is inside wall of bend)

At the highest Froude number (Fr = 160), the slip at bend outlet was lower than at inlet and then increased in the downstream pipe. At the intermediate Froude number (Fr = 60), the slip in the sharper bend ($R_c/r_0 = 2$) followed the behavior observed at the lower Froude number, whilst that in the larger bend ($R_c/r_0 = 3$) followed the higher Froude number behavior. As can be seen quite significant variations in slip occur ($1.10 < S < 1.65$) and could influence the estimation of flow momentum and kinetic energy significantly (see following section).

Owing to the size of the void probe mountings and the need for streamwise displacement of the two sensing needles for velocity observations, it was not possible to insert the probe at all positions inside the bend itself, and wall pressure observations were therefore made. An example of these is shown in Fig. 4. The wall pressures were observed using bourdon type pressure gauges, ensuring (by short duration purging with air flow) that the lines were clear of water. In the first part of the bend the pressure curve $p(r)$ appears in a concave downwards form ($d^2p/dr^2 < 0$, $\theta = 30$ deg) and follows quite closely the pressure distribution corresponding to a free vortex formed from a homogeneous flow

$$\frac{\partial p}{\partial r} = \rho_m \frac{{U_0}^2 {R_c}^2}{(r + R_c)^3} \tag{2}$$

Putting the mixture density $\rho_m = \rho_{m0}/(1 - \alpha_0 + \alpha_0 \bar{p}^{-1})$, where α_0 is the inlet void fraction, $\bar{p} = p/p_0$ and suffix zero denotes a reference inlet condition (see Davis [11]), the integrates to give the equation for the free vortex pressure distribution shown in Fig. 3 which is of concave downwards form

$$A_g(1/\eta^2 - 1) = (1 - \alpha_0)[\bar{p}(1) - \bar{p}(\eta)] + \alpha_0 \log_e \left(\frac{\bar{p}(1)}{\rho(\eta)} \right) \tag{3}$$

where $A_g = \rho_{m0} U_0^2/2p_0$ and $\eta = r/R_c$. Gravitational effects were estimated to be less than 0.5 percent of the variations in pressure observed and have been neglected. Further into the

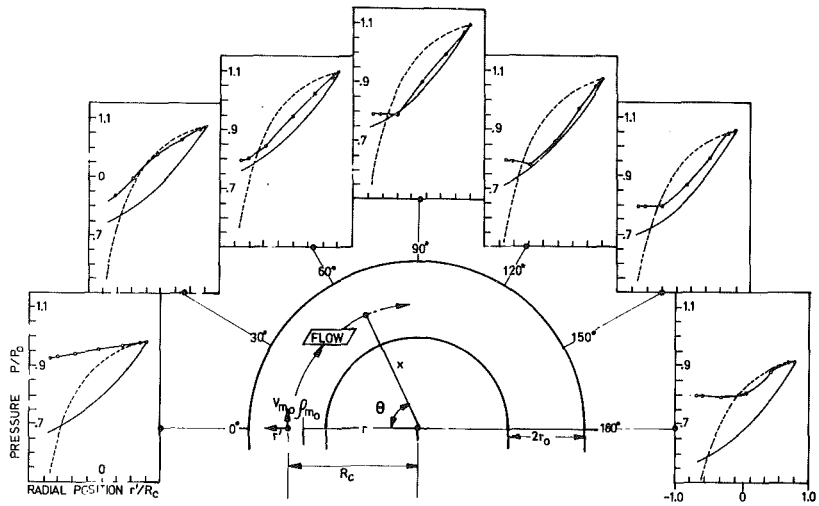

Fig. 4 Radial static pressure distributions within the bend ($R_c/r_0 = 2$; $U_m = 10.6$ m/s; $\beta = 0.42$)
o _ o _ : observed values
——— : pressure distribution for homogeneous forced vortex (equation (5))
..... : pressure distribution for homogeneous free vortex (equation (3))

bend ($\theta = 60$ deg) the pressure distribution alters to a concave upwards form ($\partial^2 p/\partial r^2 > 0$) and thus follows more closely the distribution for a forced vortex motion, rotating about the axis of the radius of curvature of the bend centerline. This may be determined by integrating in the plane of symmetry for a homogenous flow

$$\frac{\partial p}{\partial r} = \rho_m \left(\frac{U_0}{R_c}\right)^2 (r + R_c) \tag{4}$$

which becomes the concave upwards distribution shown in Fig. 4

$$A_g(1-\eta^2) = (1-\alpha_0)(\bar{p}(1) - \bar{p}(\eta)) + \alpha_0 \log_e \left(\frac{\bar{p}(1)}{\bar{p}(\eta)}\right) \tag{5}$$

Thus we see that the change in form of the pressure distribution corresponds to the establishment of rotation (ω_n) within the flow about axes perpendicular to the plane of symmetry of the bend. However, the internal flow is further complicated by the subsequent introduction of significant phase separation for $\theta = 90$ deg and beyond, as evidenced by the flat inner portions of the observed pressure profiles due to the high concentration of gas in this region. The outer portions of the pressure profiles retain the concave upwards form and thus the flow retains the rotation established in the first half of the bend (at $\theta = 60$ deg in this case). In the absence of detailed profiles of $\rho_m(r)$ within the bend, a precise prediction of the expected pressure profile is not possible. However, the results show clearly the onset of rotation and stratification in the bend, and are summarized in Table 1, where the angle θ_t at which rotation appeared to develop is indicated. For the sharper radius bend ($R_c/r_0 = 2$) and at lower mean flow speed, the rotation begins at a further angular displacement (θ_t) into the bend from inlet. The vorticity generation principle for a turbulent fluid relates the rate of increase of vorticity ($D\omega_n/D_t$) to the product of turbulent viscosity (μ_t) and the second derivative of the vorticity ($\nabla^2 \omega_n$). Since these three terms scale respectively in proportion to

$$\left(\frac{U_0 \partial \omega_n}{R_c \partial \theta}\right), \left(\frac{\rho U_0^2}{U_0/R_c}\right) \text{ and } \left(\frac{\omega_n}{{r_0}^2}\right)$$

we expect

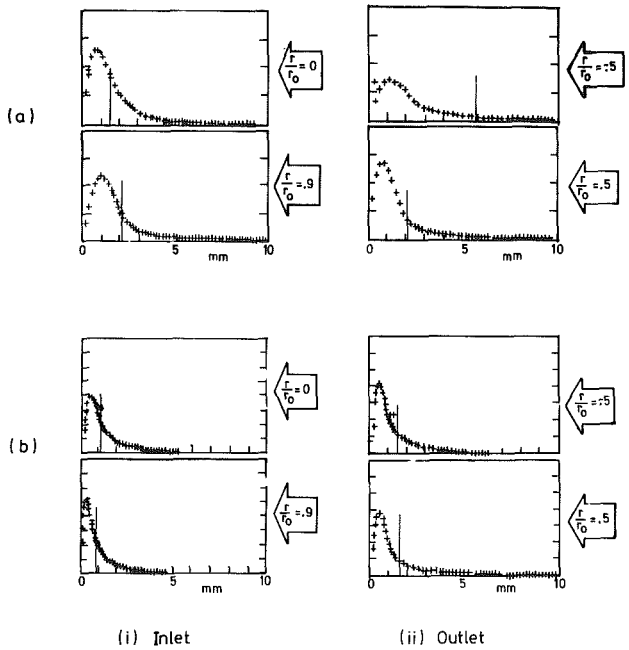

Fig. 5 Changes in bubble size distribution caused by the bend ($R_c/r_0 = 2.0$)
(i) At inlet plane
(ii) At outlet pipe, 9 diameters downstream of outlet
(a) U_m = 4.0 m/s, $\beta = 0.30$
(b) U_m = 10.6 m/s, $\beta = 0.42$
Vertical scale = probability density function for detected bubble chords
Horizontal scale = size (mm)
Vertical lines show mean size

$$\frac{\partial \omega_n}{\partial \theta} \sim \left(\frac{R_c}{r_0}\right)^2 \tag{6}$$

(The component of vorticity perpendicular to the plane of symmetry of the bend is denoted by ω_n). Thus the increase of flow rotation with angular displacement from the bend entry would be faster for larger values of (R_c/r_0), as has been observed. The decrease of θ_t at higher flow speeds suggests in addition that the finer sized bubble structures which occur at

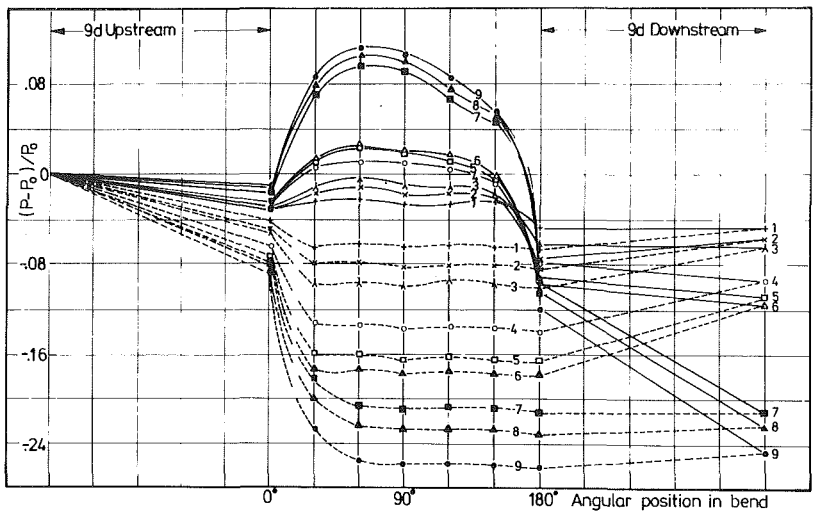

Fig. 6(*a*)

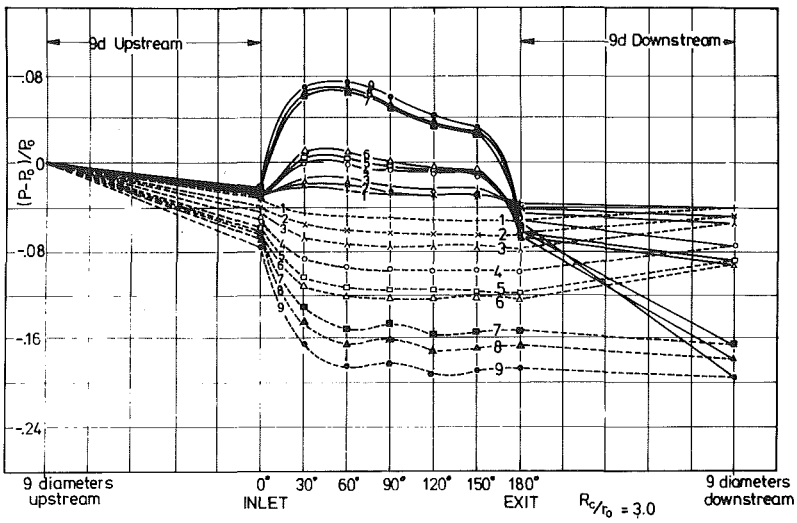

Fig. 6(*b*)

Fig. 6 Axial static pressure distributions
(*a*) $R_c/r_0 = 2.0$
——: outer wall pressure
-----: inner wall pressure
Numbers denote flow conditions (Table 1)
(*b*) $R_c/r_0 = 3.0$

higher speeds (see subsequent discussion) increase the turbulent shear stresses and promote more rapid development of flow rotation ω_n as the flow passes through the bend.

The size distributions of gas voids in the flow were measured using the needle probe and signal analysis method of Herringe and Davis [8]. The individual fixed amplitude voltage pulses produced by the needle probe for each gas void are converted to fixed, short duration impulses of amplitude corresponding to the passages of time of the gas void. The probability distribution of the short duration variable amplitude impulses was determined using a Hewlett Packard 3721A Probability Analyzer, and used to form bubble size distribution on the basis of the known local velocity. Fig. 5 shows selected results at the bend inlet and in the flow downstream of the bend. It is seen that significantly smaller bubbles are formed at the higher velocity conditions, and that quite large voids occur on the inside of the bend at outlet at the lower velocity (Fig. 5(*a*)(ii)). At the higher velocity condition it is seen that flow re-mixing after the bend has been much more effective as there is little difference between size distributions on the inside and outside observation positions (Fig. 5(*b*)(ii)). In general, for a much larger set of observations it was found that most probable bubble sizes lay in the 1–3 mm range, whilst the mean size lay in the 1–15 mm range at inlet and 1–25 mm range at outlet, owing to the contribution of small numbers of large gas voids at some flow conditions. The mean sizes were determined from void fraction and total bubble count rate data, as the distribution curve could not be sufficiently accurately determined to allow for the very small numbers of larger bubbles occurring. From these results we see that finer sized bubbles exist under higher speed flow conditions, and would increase the resistance of the mixture to mean shear deformation thus increasing the generation of flow rotation (ω_n) in the bend as observed.

In summary the detailed observations of flow structure show the development of rotation and then stratification effects within the bend and that these have largely been eliminated after the flow has remixed in the 9 diameter length

of outlet tube. It thus appears that the inlet and 9 diameter observation positions are appropriate as reference points for determination of pressure loss effects associated with the bend. In particular, the values of slip observed for a limited number of flows provide a basis for estimating the influence of slip on the bend pressure loss coefficients to be discussed in the following section. While we have only presented here observations for selected flow conditions, these are selected to indicate as much variety (e.g., in void profile) as was observed over all our tests. Full data are given by Hoang [12].

Streamwise Pressure Loss Due to the Bend

Observations of pressure were made in the inlet and outlet pipes in order to investigate the overall pressure drop associated with the bend. Upstream of the bend inlet it was found that the pressure drop was closely consistent with that observed by Davis [11] for developed frictional two phase pipe flow, and values of the friction factor were found to be only slightly higher (by 10 percent on average) than those of Davis. Thus the inlet plane of the bend was taken as the reference position from which the bend pressure loss was observed experimentally. All pressures were observed using bourdon pressure gauges of ±2 percent accuracy, and care was taken to purge all water from the connecting leads with an air flow temporarily introduced to the connecting leads.

Figure 6 shows the streamwise distribution of pressure. In the first part of the bend, the variation of the pressure (rising on outer wall and falling on inner wall of the bend) is expected for the nonseparate flow of a mixture in a curved path. In both bends ($R_c/r_0 = 2, 3$), from $\theta = 30$ deg or 60 deg onward, the pressures at the inner wall are almost constant and much lower than that at the outer wall. This is due to the separation of phases and the relatively small variations of pressure which occur in the region of high gas concentration. Thus the outer wall pressure must, from the highest pressure point, reduce to this value at the bend exit as there is then no curvature of flow. Thus we see that separation of phases combined with the radial pressure variation plays an important role in the overall pressure loss. The overall bend loss coefficient can be defined as

$$K = \Delta E/(\rho u^2)_{mr}/2) \tag{7}$$

where ΔE is the overall energy drop attributable to the bend and u_{mr} is the average mixture velocity at the midpoint of the bend chosen as a characteristic velocity. u_{mr} is calculated simply from the total volumetric flow rate at that position and the pipe cross sectional area.

For a moving mixture without appreciable wall friction a fair assumption as the bend losses exceeded that of an equivalent length of tube by a factor of 20, the momentum equation is

$$\left[[u_m]\frac{d[u_m]}{dx}\right] + \left[\frac{1}{[\rho_m]}\frac{dp}{dx}\right] + g\sin\theta = 0 \tag{8}$$

which upon integration between two sections (suffix 1 and 2) becomes:

$$\Delta E/[\rho_m] + \left[\{[u_{m2}]^2 - [u_{m1}]^2\}/2\right] + \Big[1/[\rho_{m0}]\{(p_2 - p_1)(1-\alpha_0) + p_0\alpha_0\log_e(p_2/p_1)\}\Big] + g\int_1^2 \sin\theta dx = 0 \tag{9}$$

The gravitational term is retained because the length of vertical outlet tube is not negligible and the term $\Delta E/[\rho_m]$ is introduced to represent the overall losses. Once again, the expression $\rho_m = \rho_{m0}/(1-\alpha_0+\alpha_0\bar{p}^{-1/n})$ is used. Using the definition of the loss coefficient, equations (7) and (9) become with the insertion of a loss term

$$\{K[u_{mr}]^2\}/2 + \{[u_{m2}]^2 - [u_{m1}]^2\}/2 + \{1/[\rho_{m0}]\}\{(p_2-p_1)(1-\alpha_0) + p_0\alpha_0\log_e(p_2/p_1)\} + g\Delta h = 0 \tag{10}$$

where $\Delta h = \int_1^2 \sin\theta dx$ is the vertical separation between an upstream section 1 and a downstream section 2. If the momentum equation (8) is rearranged, its integration for isothermal flow leads to

$$K = -(2/[u_{mr}]^2)(\dot{m}_g/A)\int_1^2 (1/[\rho_m])(d[u_g]/dx)dx - (2/[u_{mr}]^2)(\dot{m}_l/A)\int_1^2 (1/[\rho_m])(d[u_l]/dx)dx - (2/[u_{mr}]^2)\int_1^2 (1/[\rho_m])(dp/dx)\,dx - (2/[u_{mr}]^2)g\Delta h \tag{11}$$

where $\dot{m}_g = [\alpha]\,[\rho_g]\,[u_g]A$

and $\dot{m}_l = [1-\alpha]\rho_l[u_l]A$

are gas and liquid mass flow rates, respectively. If slip in the flow is neglected, equation (11) would become

Table 1 Observed flow structure and pressure loss results

		Inlet Conditions							Observed Slip Ratios S					
R_c/r_0	Flow	$\dot{\beta}$	u_m (m/sec)	Re $\times 10^{-3}$	Fr (u_m^2/gd)	θ_t	K_b*	K_{bd}*	Inlet†	Outlet†	Downstream†	K_b†	K_{bd}†	K_t (Ito[5])
	1	0.35	2.96	95	17.6	90°	0.82	1.49	–	–	–	–	–	0.67
	2	0.30	3.44	119	23.4	75°	0.82	1.23	1.29	1.54	1.40	0.91	1.27	0.64
	3	0.26	3.84	139	29.6	60°	0.86	1.09	–	–	–	–	–	0.62
	4	0.25	4.81	178	46.4	50°	0.85	0.99	–	–	–	–	–	0.60
2	5	0.23	5.27	201	55.7	45°	0.87	0.94	–	–	–	–	–	0.59
	6	0.22	5.48	212	60.3	40°	0.88	0.92	1.13	1.37	1.38	0.97	1.00	0.58
	7	0.42	8.92	251	160.0	35°	0.58	0.91	1.33	1.19	1.65	0.53	1.11	0.56
	8	0.40	9.25	270	171.7	35°	0.61	0.91	–	–	–	–	–	0.56
	9	0.37	9.75	299	190.8	30°	0.64	0.90	–	–	–	–	–	0.55
	1	0.35	2.96	95	17.6	50°	0.55	1.38	–	–	–	–	–	0.28
	2	0.30	3.44	119	23.4	40°	0.48	1.08	1.13	1.36	1.31	0.58	1.15	0.27
	3	0.26	3.84	139	29.6	30°	0.49	0.93	–	–	–	–	–	0.26
	4	0.25	4.81	178	46.4	25°	0.48	0.79	–	–	–	–	–	0.25
3	5	0.23	5.27	201	55.7	25°	0.50	0.75	–	–	–	–	–	0.24
	6	0.22	5.48	212	60.4	25°	0.50	0.72	1.15	1.10	1.24	0.49	0.75	0.24
	7	0.42	8.92	251	160.0	20°	0.32	0.65	1.23	1.10	1.44	0.21	0.77	0.24
	8	0.40	9.25	270	171.7	15°	0.33	0.65	–	–	–	–	–	0.23
	9	0.37	9.75	299	190.8	15°	0.34	0.68	–	–	–	–	–	0.23
Est. Errors		±0.01	±0.10	±5	±0.3	±5°	±0.02	±0.02	±0.02	±0.02	±0.02	±0.02	±0.02	±0.01

* Measured two-phase flow values on basis of mean mixture velocity (Equation 12)
† Measured two-phase values allowing for observed slip (Equation 14)

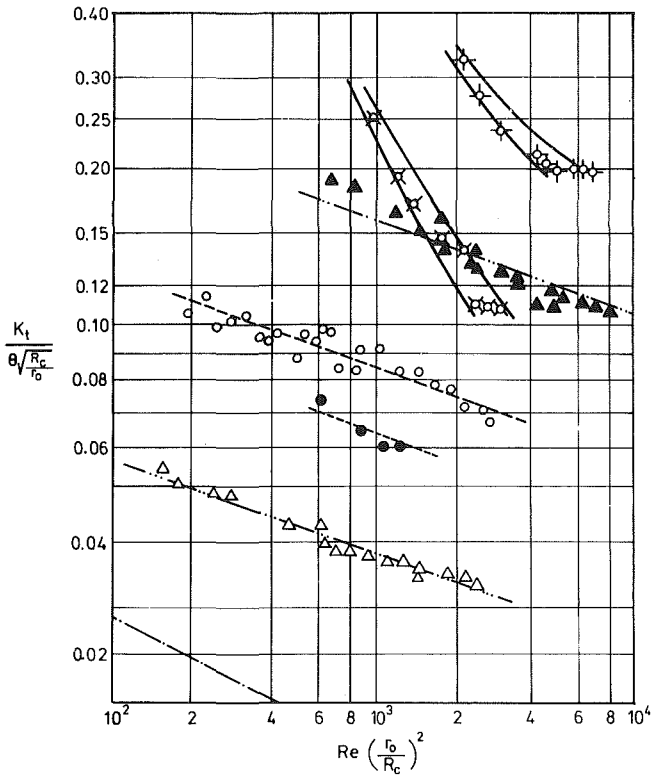

Fig. 7 Total bend-loss coefficient as a function of dimensionless number $\mathrm{Re}(r_0/R_c)^2$
(Data based on homogeneous flow equation (12) and experimental observations)
——: limits of present data
—o—: loss for equivalent straight lengths of pipe
·····: Hoffman ($\theta = 90$ deg, $R_c/r_0 = 4.0$)
– – –: Ito ($\theta = 180$ deg, $R_c/r_0 = 3.68$)
–·–·–: Ito ($\theta = 90$ deg, $R_c/r_0 = 2.01$)
–·–·–: Ito ($\theta = 45$ deg, $R_c/r_0 = 3.68$)

$$K = -\{[u_{m2}]^2 - [u_{m1}]^2\}/[u_{mr}]^2 - \{2/(\rho_{m0}[u_{mr}]^2\} \{(p_2 - p_1)(1-\alpha_0) + p_0\alpha_0 \log_e(p_2/p_1)\} - 2g\Delta h/[u_{mr}]^2 \quad (12)$$

Values of the two phase loss coefficient K calculated from equation (12) using the experimental data for pressure change and mean flow speeds are given in Table 1 and Fig. 7. The coefficients in Table 1 are given for the bend (i.e., entry plane to exit plane, K_b) and bend plus downstream re-mixing zone (from inlet to the position 9 diameters after the bend, K_{bd}). Equation (12) can be used also to determine pressure drop for design purposes when flow conditions are known using these values of K_{bd}, provided that the flow has a similar structure. This depends of course upon its Froude number, void fraction and Reynolds number, and inevitably the data could only be applied to a limited range of flows in such a complicated type of flow.

If we introduce the velocity ratio (slip ratio), $S = [u_g]/[u_l]$ where $[u_g]$ and $[u_l]$ are the average gas and liquid velocities at a section, we can make the assumption that S varies only slightly in the flow so that a linear relationship becomes a good approximation of the actual slip variation

$$S = S_1 + \{(S_2 - S_1)/(p_2 - p_1)\}(p - p_1) \quad (13)$$

then an explicit derivation of the equation for the loss coefficient may be made. The linear assumption of the slip variation as the flow pressure reduces will not be critical as only limited changes in S occur. The loss coefficient can now be written as:

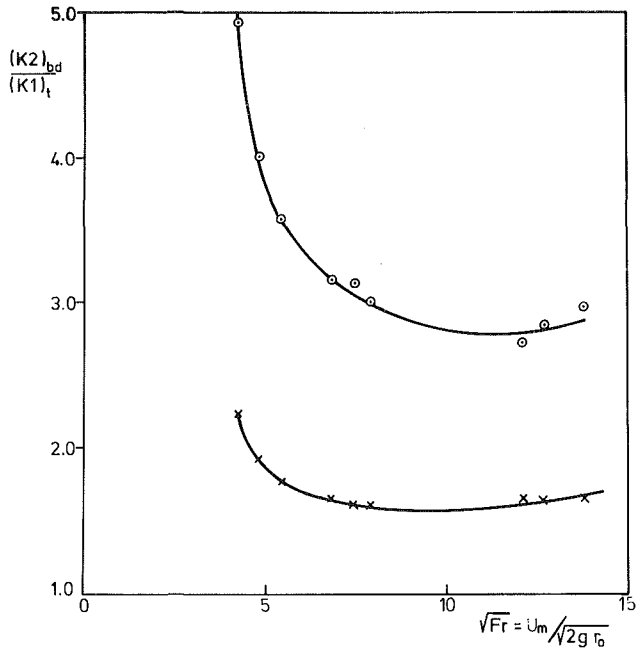

Fig. 8 Ratio of two phase to single phase loss coefficients $(K_2)_{bd}$ based on experimental data and equation (12)
⊙ $R_c/r_0 = 3.0$
× $R_c/r_0 = 2.0$

$$K = -\frac{2}{[u_{mr}]^2}\left(\frac{\dot{m}_g}{[\rho_{m0}]A^2}\int_1^2\left(\frac{A_1p^3 + B_1p^2 + C_1p + D_1}{(ap^2+bp)^2p} + K_1\frac{A_2p^3 + B_2p^2 + C_2p + D_2}{(ap^2+bp)p}\right)dp + \frac{\dot{m}_l}{[\rho_{m0}]A^2}\int_1^2\frac{A_3p^2 + B_3p + C_3}{(ap^2+bp)^2p}\,dp + \int_1^2\frac{(1-\alpha_0)p + \alpha_0p_0}{[\rho_{m0}]p}\,dp + g\Delta h\right) \quad (14)$$

where the constants introduced are

$$A_1 = -2\alpha_0p_0S_1(1-\alpha_0)^2(\dot{m}_l/\rho_l)\{(S_2 - S_1)/p_2 - p_1)\}^2$$

$$B_1 = -\{\alpha_0p_0S_1(1-\alpha_0)(\dot{m}_l/\rho l)(S_2 - S_1)/(p_2 - p_1)\}\{2\alpha_0p_0(S_2 - S_1)/(p_2 - p_1) + 3(1-\alpha_0)(S_1 - (S_2 - S_1)p_1/(p_2 - p_1))\}$$

$$C_1 = -\{\alpha_0p_0S_1(1-\alpha_0)(\dot{m}_l/\rho_l)(S_1 - (S_2 - S_1)/(p_2 - p_1))\}\{3\alpha_0p_0(S_2 - S_1)/(p_2 - p_1) + (1-\alpha_0)(S_1 - (S_2 - S_1)p_1 - (p_2 - p_1))\}$$

$$D_1 = -\alpha_0^2p_0^2S_1(1-\alpha_0)(\dot{m}_l/\rho_l)\{S_1 - (S_2 - S_1)p_1/(p_2 - p_1)\}^2$$

$$A_2 = (1-\alpha_0)^2(S_2 - S_1)/(p_2 - p_1)$$

$$B_2 = (1-\alpha_0)\{\alpha_0p_0(S_2 - S_1)/(p_2 - p_1) + (1-\alpha_0)(S_1 - (S_2 - S_1)p_1/(p_2 - p_1))\}$$

$$C_2 = \alpha_0p_0(1-\alpha_0)\{2S_1 - (S_2 - S_1)p_1/(p_2 - p_1)\}$$

$$D_2 = \alpha_0^2p_0^2S_1$$

$$A_3 = -2\alpha_0p_0S_1(1-\alpha_0)^2(\dot{m}_l/\rho_l)(S_2 - S_1)/(p_2 - p_1)$$

$$B_3 = -\alpha_0p_0S_1(1-\alpha_0)(\dot{m}_l/\rho_l)\{2\alpha_0p_0(S_2 - S_1)/(p_2 - p_1) + (1-\alpha_0)(S_1 - (S_2 - S_1)p_1/(p_2 - p_1))\}$$

$$C_3 = -\alpha_0^2p_0^2S_1(1-\alpha_0)(\dot{m}_l/\rho_l)\{S_1 - (S_2 - S_1)p_1/(p_2 - p_1)\}$$

$$K_1 = (\dot{m}_l/\rho_l)\,(S_2 - S_1)/(p_2 - p_1)$$
$$a = (1-\alpha_0)(S_2 - S_1)/(p_2 - p_1)$$
$$b = (1-\alpha_0)\{S_1 - (S_2 - S_1)p_1/(p_2 - p_1)\}$$

For a limited range of flows for which slip values were available (Hoang and Davis [13]), loss coefficients taking account of slip between phases are given in the table on the basis of equation (14) into which observed pressures, slip values and speeds are substituted to determine K_2 from the data. For the present measurements the loss coefficients have again been calculated for the bend K_b and for the combination loss of bend and downstream flow K_{bd} to the 9 diameter position from the bend exit.

The results of Table 1 show that where high exit slip values occur the calculated loss coefficient is increased by the slip corrections. This is due to the over-estimate of the flow kinetic energy which arises in the flow speed from the total volumetric flow rate. Under conditions of large slip the liquid phase, which conveys most of the kinetic energy, moves at a higher velocity than this mean flow velocity. Thus the largest increase in calculated loss coefficient occurs where the largest exit slip ratio was observed ($S = 1.65$ for these results).

The loss coefficient between bend inlet and exit planes K_b showed on average only a 1 percent increase due to the slip corrections. However, at low flow speeds where higher slip existed at the exit plane of the bend a positive slip correction on K_b occurred, whilst the reverse occurred at high flow speeds. A more consistently high slip was observed at the reference exit position 9 diameters downstream of the bend, and the overall loss coefficient K_{bd} was increased on average by 10 percent due to slip corrections; rather larger increases in K_{bd} due to slip were then observed at the highest flow velocity where the larger slip values were determined. It is interesting to note that large slip in the vicinity of the bend is not directly associated with the flow stratification which occurs at the bend exit plane. The largest slip ratio was in fact observed 9 diameters downstream of the bend exit, while the higher flow velocities reduced the slip at the bend exit plane.

In order to make a comparison between the overall bend loss coefficients observed here with those observed in single phase flow, Table 1 gives values of the results K_l obtained using the correlation of Ito [5] for single phase flow. Figure 7 shows also the variation of loss coefficient as a function of the dimensionless parameter $\mathrm{Re}(r_0/R_c)^2$ following the form of correlation used by Ito [3]. Ito's correlation is in terms of the total bend loss coefficient K_l, and refers to the loss between bend inlet and a section downstream of the bend where the flow is effectively not influenced by the bend. Thus the single phase coefficient K_l corresponds closely to the overall loss coefficient K_{bd} for the two phase data. We see that substantially larger loss coefficients occur in two phase flow, the values of K_{bd} being on average larger than K_l by a factor of 1.7 for the sharper bend ($R_c/r_0 = 2$) and 3.4 for the larger bend ($R_c/r_0 = 3$). In addition there is a consistent trend for the two phase losses to be relatively larger at the lower flow velocities as shown in Fig. 8. It should be noted that Figs. 7 and 8 show results calculated without slip corrections, as more values of loss coefficient were obtained. However, as discussed above, allowance for slip would increase K_{bd} by a further 10 percent on average.

The substantially higher losses which occur in two phase flow cannot directly be attributed to interfacial surface tension energy of the interphase surfaces. As discussed by Herringe and Davis [8] the energy of the interfacial surface tension is $6\sigma\alpha/\bar{d}\rho_m$, where $\bar{d}$ is the mean bubble diameter and σ the surface tension. Estimates of this energy on the basis of the mean bubble sizes observed showed it to be approximately three orders of magnitude less than the overall energy loss in the bend. Further, Herringe and Davis [9] showed that the turbulent kinetic energy in a turbulent two phase mixture was of closely comparable magnitude to the interfacial surface tension energy. Thus it appears that the mechanism for the relatively very high losses that occur in two phase flows must be the dissipation associated with separating and subsequently re-mixing the two phases in the bend and downstream of it. This is consistent with the observation of a higher loss relative to single phase flow (Fig. 8) for the larger bend ($R_c/r_0 = 3$) and the onset of rotation and separation more rapidly in this bend as discussed. However, as in single phase flow, the radius ratio (R_c/r_0) has the predominant overall effect, the sharper bend exhibiting the highest overall losses (Fig. 7).

Conclusions

Detailed observations of the flow structure in the froth flow regime have shown that rotational and separation effects develop in the first half of the 180 deg pipe bends. The flow becomes relatively well mixed, although somewhat modified in structure compared with the inlet flow, at a position 9 diameters downstream of the bend. Slip was deduced from the voidage distributions, and it was found to be substantially increased at the bend exit for lower velocity conditions, after which it reduced slightly in the downstream pipe. At higher velocity, the slip reduced in the bend, and then increased considerably in the downstream pipe. The effect of the slip was to increase estimates of the overall bend loss coefficient by approximately 10 percent on average but by more at higher flow speeds.

Significant pressure loss was associated with the remixing process downstream of the bend, and it was found from detailed bubble size observations that the corresponding energy loss was very much greater than the energy associated with the interfacial surface tension effect. The overall loss coefficients were substantially larger than in single phase flow, by up to a factor of 5, and it was deduced that this was caused by the separation and remixing of the phases within the downstream of the bend. The pressure losses were larger for the sharper bend, as in single phase flow. However, relative to the single phase losses for a bend, a larger proportionate increase in loss coefficient was observed in the two phase flow for a larger bend radius.

References

1 Pigott, R. J. S., "Pressure Losses in Tubing, Pipe and Fittings," *Trans. ASME*, Vol. 72, 1950, pp. 679–688.

2 Pigott, R. J. S., "Losses in Pipe and Fittings," *Trans. ASME*, Vol. 79, 1957, pp. 1767–1783.

3 Ito, H., "Pressure Losses in Smooth Pipe Bends," *Trans. ASME*, Vol. 82, 1960, pp. 131–143.

4 Banerjee, S., Rhodes, E., and Scott, D. S., "Studies on Cocurrent Gas-Liquid Flow in Helically Coiled Tube, Part I: Flow Patterns, Pressure Drop and Hold Up," *Can. J. Chem. Eng'ng.*, Vol. 47, 1969, pp. 445–453.

5 Lockhart, R. W., and Martinelli, R. C., "Proposed Correlation of Data for Isothermal Two-Phase Two-Component Flow in Pipes," *Chem. Eng. Prog.*, Vol. 45, 1949, pp. 39–48.

6 Zanker, K. J., and Brock, T. E., "A Review of the Literature on Fluid Flow Through Closed Conduit Bends," British Hydromechanics Research Association, TN 901, 1067.

7 Lacey, P. M. C., "Two-Phase Flow in Curved Ducts," Annual meeting 1970 of DECHEMA, Frankfurt/Main Che. Eng. Dept., University of Exeter, 1970.

8 Herringe, R. A., and Davis, M. R., "Structural Development of Gas-Liquid Mixture Flows," *J. Fluid Mechanics*, Vol. 73, Part I, 1976, pp. 97–123.

9 Herringe, R. A., and Davis, M. R., "Detection of Instantaneous Phase Changes in Gas-Liquid Mixtures," *J. of Physics E: Scientific Instruments*, Vol. 7, 1974, pp. 807–812.

10 Zuber, N., and Findlay, J. A., "Average Volumetric Concentration in Two Phase Flow Systems," ASME *Journal of Heat Transfer*, Vol. 87, No. 2, 1965, pp. 453–468.

11 Davis, M. R., "The Determination of Wall Friction for Vertical and Horizontal Two-Phase Bubbly Flows," *Trans. ASME*, 1974, pp. 173–179.

12 Hoang, K., "A Study of Gas-Liquid Flow in Return Bend," Ph.D. thesis, University of New South Wales, Australia, 1976.

13 Hoang, K., and Davis, M. R., "The Influence of Return Bends on Velocity Ratio in Gas-Liquid Pipe Flow," *Int. Journal of Multiphase Flow*, Vol. 6, No. 3, 1980, pp. 267–272.

Mark D. Hoover
Inhalation Toxicology Research Institute,
Lovelace Biomedical and Environmental
Research Institute,
Albuquerque, N. Mex. 87185

Werner Stöber

Gerd Morawietz
Fraunhofer-Institut fUr Toxikologie
Und Aerosolforschung,
Nottulner Landweg 102,
D-4400 Münster-Roxel,
Federal Republic of Germany

Experiment on Laminar Flow in a Rotating, Curved Duct of Rectangular Cross Section

Experimental results are presented here for laminar flow in a rotating, curved duct of rectangular cross section. The duct geometry is that of the spiral duct aerosol centrifuge designed by Stöber and Flachsbart (1969). Primary velocity was measured by laser Doppler anemometry. Secondary flow velocity was characterized by dye injection. The experiment was done in a dynamically similar Plexiglas mock-up of the centrifuge. Water flow in the mock-up simulated air flow in the aerosol centrifuge. The Reynolds number based on hydraulic diameter was 500. The Rossby number was 0.16. The duct aspect ratio was 3.3. Results are compared for flow in a straight stationary duct, the curved duct with no rotation, the curved duct with rotation in the direction of flow and the curved duct with rotation in the direction opposite of flow. There is agreement between the observed flow and the boundary layer theory of Ludwieg (1951).

Introduction

Aerosol centrifuges [1–5] apply curved, rotating ducts (e.g., Fig. 1) to the problem of separating airborne particles according to aerodynamic size. Particles are drawn into a centrifuge at the center of rotation as a thin layer of dusty air along the inner wall of the duct. Clean winnowing air is introduced between the dusty air and the outer wall of the channel. Typical conditions are an aerosol sampling rate of 0.3 L/min, a total flow rate of 10 L/min in a 1.0 cm wide, 3.3 cm deep duct and a rotation rate of 314 rad/s. As particles are carried along the duct by the laminar air flow, they are subjected to Coriolis and centrifugal accelerations. The particles with larger aerodynamic diameters penetrate the clean air layer quickly and are collected early on the outer wall of the channel. Particles with smaller aerodynamic diameters are carried further through the duct before reaching a site of deposition. After collection is complete, a removable foil which covers the outer wall is examined for information about the collected particles. The collection foil in the centrifuge of Stöber and Flachsbart [1] is 180 cm long. Sampling results are very good for particles having aerodynamic diameters between about 0.1 and 3.0 μm.

Due to the complexity of the fluid flow and the accelerations influencing particle motion in spinning duct aerosol centrifuges, there was no complete theoretical model for centrifuge performance. We wanted to develop such a model to help explain and perhaps improve centrifuge performance. As a first step to developing a valid model we needed to determine the actual fluid flow pattern in the curved, rotating centrifuge duct. The information we needed included (1) the fully developed primary velocity profile, (2) the ratio of secondary velocity to primary velocity, (3) the thickness of the secondary flow boundary layer, and (4) an estimate of the length of the duct required for development of the flow. This paper describes how we characterized the flow experimentally and compares the experimental results to the boundary theory of Ludwieg [6] for flow in a curved, rotating duct.

Methods

Previous Theory. Relatively little has been published on laminar flow in rotating ducts. Barua [7] studied flow in a straight, rotating duct. He showed that a secondary flow is set up in the cross section of the duct and that this secondary flow

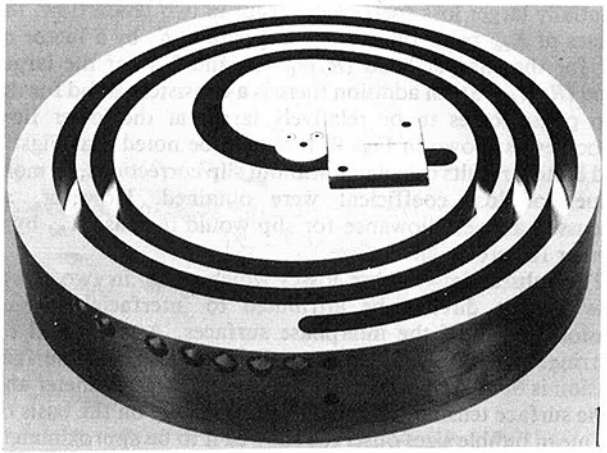

Fig. 1 The spiral duct aerosol centrifuge of Stöber and Flachsbart [1] with its cover removed. The width of the duct is 1 cm and the overall diameter of the device is 26 cm.

Contributed by the Fluids Engineering Division for publication in the JOURNAL OF FLUIDS ENGINEERING. Manuscript received by the Fluids Engineering Division, February 8, 1983.

is similar to that described by Dean [8, 9] in a stationary curved pipe. Secondary flow in the core region is directed toward the outer wall and continuity is maintained by a return flow at the top and bottom walls. Speziale [10] used finite difference techniques to solve the full time-dependent nonlinear equations of motion for laminar flow of an incompressible viscous fluid in straight, rotating ducts of rectangular cross section. He predicted that the secondary flow at high rotation rates will be stable in a slightly asymmetric double-vortex configuration with the axial velocity assuming a Taylor-Proudman configuration in the interior of the duct.

Ludwieg [6] proposed a boundary layer solution for fully developed laminar flow in a square duct which is both curved and rotating and he made pressure drop measurements in such a duct. He predicted that secondary flow in the core region is quite uniform and that secondary return flow is confined to narrow boundary layers at the top and bottom walls (Fig. 2). He predicted that the primary velocity profile is very flat in the direction, y, parallel to the axis of rotation with peaks near the boundary layers and that it is skewed toward the outer wall in the radial direction, x, when the direction of rotation is the same as the direction of flow. He predicted the profile is skewed toward the inner wall as a mirror image of the above case when the direction of rotation is opposite the direction of flow.

He described the dependence of the primary velocity in the core region, $V_{\phi 0}$, on the dimensionless radial position, r, as:

$$\frac{1}{\sqrt{\mathrm{Re}\xi}} V_{\phi 0} \frac{\partial V_{\phi 0}}{\partial r} = \frac{\lambda}{2} + \frac{1}{\mathrm{Re}} \frac{\partial^2 V_{\phi 0}}{\partial r^2} - 2\left(\frac{\xi}{\sqrt{\mathrm{Re}}}\right)^{1/2} V_{\phi 0} \quad (1)$$

where λ is the coefficient of friction. The boundary conditions are that $V_{\phi 0} = 0$ at the inner and outer duct walls. The assumptions of Ludwieg's theory are that the radius of curvature of the duct is large compared to the length, A, of a side of his square duct; the Reynolds number, $\mathrm{Re} = AV/\nu$, is much greater than 100; and the inverse of the Rossby number, $\xi = \omega A/V$, is much greater than 1; where V is the average primary velocity in the duct, ν is the kinematic viscosity of the fluid, and ω is the rotation of the duct in radians per second.

Present Theory. Ludwieg's conditions are met for the normal operation of spinning duct aerosol centrifuges. In the Stöber and Flachsbart aerosol centrifuge [1] the minimum radius of curvature is 8.0 cm and the radial dimension, A, of the duct is 1.0 cm. While Ludwieg considered a duct of square cross section, the centrifuge duct is rectangular with a depth, B, of 3.3 cm. At a flow rate of 10 L/min the Reynolds number AV/ν is 350 and the Reynolds number based on the hydraulic diameter of the duct $2AB/(A + B)$ is 540. The value of ξ is 6.25 at the standard rotation rate of 314 rad/s.

We used Ludwieg's boundary layer approach [6] to derive expressions [11] for the thickness of the boundary layer, the ratio of secondary flow velocity to primary flow velocity in the core region and the shape of the primary velocity profile. Whereas, Ludwieg had nondimensionalized with respect to the length, A, of a side of his square duct, we nondimensionalized with respect to the length, A, of the radial dimension of our rectangular duct. In this way the dimensionless boundary layer thickness, δ, was:

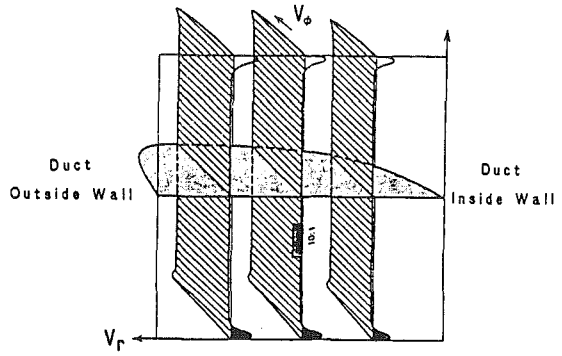

Fig. 2 Primary and secondary flow profiles in a curved, rotating duct according to the boundary layer theory of Ludwieg [6]

$$\delta = \frac{\pi}{\sqrt{\mathrm{Re}\xi}} \quad (2)$$

or $d = A\delta$, where d was the actual thickness of the boundary layer. By substituting the definitions for Re and ξ into the expression for δ, we obtained a simple expression for d:

$$d = \pi\left(\frac{\nu}{\omega}\right)^{1/2} \quad (3)$$

Relation (3) is of course an expression for the Ekman boundary layer thickness which is a classical result in geophysical fluid dynamics [12]. Thus, under conditions in which equation (3) applies, the boundary layer thickness was predicted to increase with viscosity, decrease with rotation and be independent of duct dimensions.

Ludwieg [6] also gave an expression for the secondary flow velocity in the core region as a function of the average primary velocity (see the expression for V_{r0} following his equation (6*b*)). We rearranged his expression into a dimensional form and substituted in the definitions of δ, ξ, and Re to obtain a relationship in our rectangular duct between the secondary flow in the core region, V_{r0}, and the primary flow in the core region, $V_{\phi 0}$ [11]:

$$V_{r0} = \frac{V_{\phi 0}}{B\left(\frac{\omega}{\nu}\right)^{1/2} - 2\pi} \quad (4)$$

Thus, for the flows which satisfy the conditions of Ludwieg's

Nomenclature

A = width or radial dimension of the curved duct
B = depth or axial dimension of the curved duct
b = dimensionless depth of duct, B/A
d = boundary layer thickness
N = Dean number divided by the curvature ratio, $N_{\mathrm{De}}/(R/A)$
N_{De} = Dean number, $\mathrm{Re}/(R/A)^{1/2}$
R = radius of curvature of the duct
r = dimensionless, (radial position in the duct)/A
Re = Reynolds number, AV/ν
V = average primary velocity in the duct
V_{r0} = radial secondary flow in the core region
$V_{\phi 0}$ = primary flow in the core region
x = radial coordinate for the duct on the interval $[-1, 1]$
y = depth coordinate for the duct in the direction parallel to the axis of rotation, on the interval $[-1, 1]$
δ = dimensionless, (thickness of the boundary layer)/A
λ = coefficient of friction
ν = kinematic viscosity
ξ = inverse of the Rossby number, $\xi = \omega A/V$
ϕ = angular coordinate in the curved duct measured from the inlet plane
ω = duct rotation rate

boundary layer theory as given above following equation (1), the secondary flow in the core region was predicted to be linearly related to primary flow and to decrease in ducts of equal cross sectional area as the ratio of duct height to duct width decreases. The secondary flow which returns in the boundary layers at the top and bottom walls of the duct must be distributed over the entire depth of the core region.

We expected the major development of the flow to occur within the first semicircular turn of the duct. This estimate was based on Austin's [13] empirical correlation in which the number of degrees required for fully developed flow in a stationary helically coiled tube is equal to $49.0\ N^{2/3}$ where N is the Dean number, N_{De}, divided by the curvature ratio. This correlation predicted development of the flow within the first 170° of our curved duct. We anticipated only minor changes in the flow as it passed through the second 180° of the duct. As can be seen in Fig. 1, the first 180 deg of the duct carries the fluid from the center of rotation to a region of the duct which has its center of curvature coincident with the center of rotation.

Experiments. We wanted to experimentally evaluate the applicability of the boundary layer theory to the flow in the aerosol centrifuge of Stöber and Flachsbart [1]. Even if the theory were found to be invalid, direct measurements of the velocity profiles would be sufficient for a model of centrifuge performance. Direct observation of flow in working centrifuges would be extremely difficult since they are made of high strength metals and generally rotate at high rates. Our experiments were done in a dynamically similar mock-up of the Stöber centrifuge (Fig. 3). Because flow in the Stöber centrifuge is incompressible [11], dynamic similarity could be achieved with water. Ludwieg's nondimensionalization of the equation of motion for flow in a curved rotating tube (Equation 1) revealed that the dynamic similarity criteria are duplication of the Reynolds and Rossby numbers. Martonen [14] used a similar nondimensionalization approach as well as the Buckingham Pi theorem to demonstrate that pertinent dimensionless groups for dynamic similarity are the Rossby and Ekman numbers. (The Ekman number is the Rossby number divided by the Reynolds number.)

Our mock-up was three times larger than the Stöber centrifuge. It was made of Plexiglas to allow studies by potassium permanganate dye injection and laser Doppler anemometry. The duct in the mock-up had a constant width of 3 cm and a depth of 10 cm. The normal aerosol centrifuge operating condition of 10 L/min airflow and 314 rad/s rotation rate for a 1.0 cm wide and 3.3 cm deep duct yields Reynolds number 540 based on hydraulic diameter and Rossby number 0.16. For our experiments the Reynolds number was duplicated at value 500. This gave a water flow rate of 2 L/min in the mock-up. Duplication of the Rossby number, $1/\xi$, at value 0.16 gave similarity at a mock-up rotation rate of 2.4 rad/s.

The Plexiglas centrifuge was mounted on a pedestal with a bearing, seal and shaft design that allowed water to flow in and out during rotation. The centrifuge was driven by a mechanical adjustable speed gearmotor. The rotation range was 0.6 to 6 rad/s. The pedestal and motor were on separate vibration isolation pads. Rotation period was measured by a timer connected to an optical sensor. The timer output was shown on an LED display and also passed to a PDP-11/45 data acquisition computer. Rotation period was stable to ± 1 percent. A constant head tank provided uniform feed water pressure. Flow rate was continuously monitored on a digital voltmeter using the output of a Mini-Major water meter with a model SS2000 frequency to DC rate of flow transmitter (Kent, Ocala, FL). Flow was stable to ± 1 percent.

Qualitative information on the primary and secondary flow in the centrifuge mock-up was obtained in dye injection

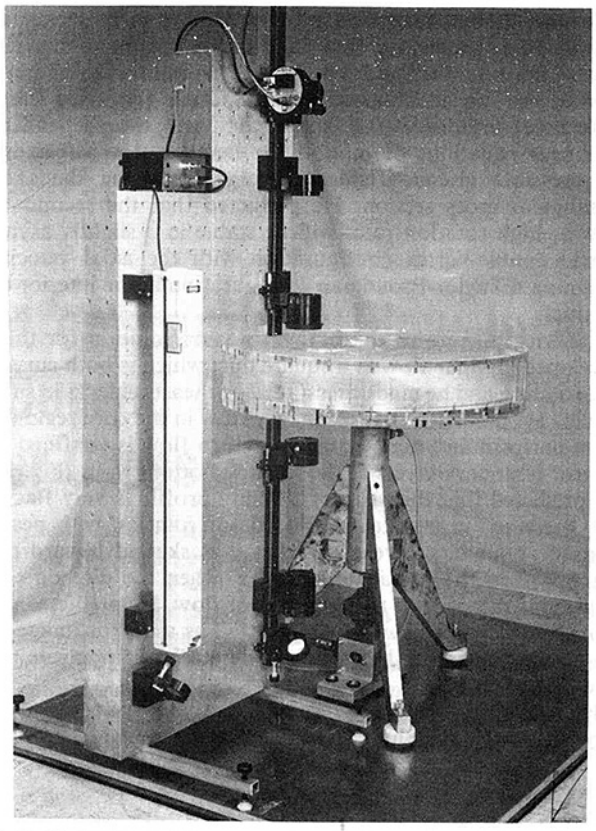

Fig. 3 Hydrodynamic mock-up of the Stöber and Flachsbart [1] spiral duct aerosol centrifuge with laser Doppler anemometer, vibration isolation and drive system

studies. These were done with potassium permanganate ($KMnO_4$) and videotaped for repeated viewing. The Reynolds number was maintained at 500. The rotation conditions were 1.2 rad/s, 2.4 rad/s, and 4.8 rad/s. Rotation was in the direction of primary flow. The 2.4 rad/s study was also run with rotation in the direction opposite to primary flow. Dye injected into the duct inlet as a liquid bolus revealed the time integrated shape of the leading edge of the flow profile in the entire duct and the thickness of the boundary layer. Large crystals of $KMnO_4$ placed on the floor of the duct next to the outer wall released streaks of the red dye and revealed the magnitude of the secondary flow in the boundary layer. Exhaust water containing the dye was not returned to the constant head tank. Make-up water was provided from a house line.

Quantitative information on the primary flow velocity was obtained by laser Doppler anemometry (LDA). The secondary flow velocity was too small in comparison to the net primary flow and rotation velocity to be resolved by LDA. We used a model 1990 LDA counter-type signal processor and model 900 series optics (Thermo Systems, St. Paul, MN) in the forward scatter mode. The resolution of the signal processor was 2 ns. The measuring volume was approximately ellipsoidal in shape with major axis 2 mm and minor axis 0.5 mm for our 120 mm lens. We wrote [11] software to control the LDA data collection and to calculate, on-line, the mean velocity, standard deviation and two other higher order moments for an ensemble of 50,000 measurements at each location of interest in the centrifuge duct.

The coefficient of variation within a single data ensemble was on the order of 0.03. The coefficient of variation for repeated measurements was 0.001. Very clean water for the laser Doppler anemometry (LDA) study was provided from a Milli-Q Filter System (Millipore, Bedford, MA). The clean water still retained some of its natural content of particles in

the micron size range. These particles are small enough to move with the flow of water and large enough to be detected by LDA. The water was recirculated through the constant head tank.

Primary velocity profiles were measured in the mock-up at Reynolds number 500 for conditions of no rotation, rotation at 2.4 rad/s in the direction of flow and rotation at 2.4 rad/s in the direction opposite of flow. Considering the x-y cross section of the duct to be bounded by $x = -1$ at the inner wall, $x = 1$ at the outer wall, $y = -1$ at the bottom wall and $y = 1$ at the top wall, measurements of the primary velocity were made at $x = -0.67$, $x = -0.33$, $x = 0$, $x = 0.33$ and $x = 0.67$ for $y = 0$, $y = 0.5$, $y = 0.7$, and $y = 0.9$. This pattern of measurements was made in the stationary mock-up at a location 630 deg from the start of the spiral. This was well into the region predicted to have fully developed flow. It was also far from the exhaust port located 450 deg further in the duct. The first 180 deg of the duct, where flow was expected to develop, was inacessable to LDA because of the presence of the rotor support plate.

During rotation, measurements could not be made in a cross sectional plane of the duct but had to be made over a finite arc. The duct made three 360 deg turns from inlet port to exhaust port. The first 180 deg of each turn had a center of curvature which was offset from the center of rotation of the centrifuge. The second 180 deg of each turn had a center of curvature which was coincident with the center of rotation of the centrifuge. It was in these coincident center arcs that velocity measurements at constant radial locations could be made during rotation. Such measurements would not be possible in centrifuge ducts having designs such as an Archimedean spiral [4]. The portion of the duct between 540 and 720 deg from the inlet port had its center of curvature coincident with the center of rotation. We took the bulk of our measurements over a 90 deg arc centered on 630 deg from the start of the spiral. As a verification that flow was fully developed in this region, we compared measurements taken in 5 deg intervals at the beginning and end of this portion of the duct. They were statistically the same. The data validation rate was on the order of 1000 measurements per second during rotation. Approximately 20 revolutions of the mock-up occurred during the collection of 50,000 individual LDA measurements. We placed a light shield over the centrifuge so that LDA signals generated outside the region of interest could not reach the photomultiplier tube.

We compared the flow rates measured by the rate of flow water meter to those calculated by numerically integrating the individual LDA velocity measurements. They agreed within 1 percent. For comparing the actual flow in the curved, rotating duct to the theoretical flow in a straight stationary duct, we used the approximation of Stöber and Zessack [15] for Poiseuille flow in a straight rectangular duct:

$$V(x,y) = \frac{9}{4} V\left(1 - \left(\frac{2x}{A}\right)^2\right)\left(1 - \left(\frac{2y}{B}\right)^2\right) \quad (5)$$

We used a spline-collocation method [16] to solve the boundary value problem (equation (1)) of the dependence of the primary velocity on the dimensionless radial position in the duct. This was to provide a comparison between our measured radial primary velocity profiles and the profile predicted by the theory.

Results

Injection of dye as a bolus qualitatively revealed that a boundary layer flow occurred in the curved, rotating duct. The initial view of the dye bolus was the same for both the forward and reverse rotations. The dye entered the duct as a fairly compact bolus with its center extending into the clear fluid ahead of it and its edges lagging behind due to the no slip conditions at the duct walls. The leading edge had a quasi-parabolic shape in the radial direction and was rather flat in the depth or y-direction.

While viewing the videotapes in the stop frame mode, the radial position of the bolus was observed to change as a function of distance along the duct. When rotation was in the direction of fluid flow, the shift of flow in the core region of the duct was toward the outer wall. When rotation was in the direction opposite of fluid flow, the shift of flow was toward the inner wall. This shift to the inner wall provided the observer a clear view of the duct cross section. Initially the most intense coloration was in the central region of the duct cross section. The shift of this color band appeared to commence immediately after the fluid entered the duct. After 180 deg, narrow boundary regions at the top and bottom of the duct were depleted of dye.

Under reverse rotation at 2.4 rad/s the central portion of the bolus appeared to reach the inner wall by 540 deg and coloration was very intense in the narrow boundary layers at the top and bottom walls. We measured the image of the dye in the boundary layer on the video tape replay of the experiments and the edge of the boundary layer was assumed to occur where the dye intensity fell to background level. The thickness of these layers was estimated from the video tapes to be about 1.5 mm to 2.5 mm. By 720 deg the core region of the duct was depleted of dye and the intense dye bands at the top and bottom walls were visibly moving down the outer wall in the top half of the duct and up the outer wall in the bottom half of the duct.

We had difficulty estimating the thickness of the vertical boundary layers at the inner and outer walls. It would be predicted [10] that the vertical or Stewardson boundary layer would be substantially thicker than the horizontal or Ekman boundary layers. In our observations, the boundary layer at the outer wall appeared to be at least as thick as the boundary layer at the top and bottom walls, but dye was moving radially from the outer wall back into the core region, making any estimate of thickness uncertain. Qualitatively similar estimates of the boundary layer thickness and motion of the dye in the core region were obtained in forward rotation, although the motion of the bolus toward the outer wall partially obscured the observer's view.

The estimated length of the duct required for the center of the bolus to move to a wall was used to crudely estimate the ratio of secondary to primary flow velocities. At rotation 2.4 rad/s the radial motion of 1.5 cm occurred within 540 deg or 225 cm of the duct inlet. The ratio of these distances covered in the same amount of time was 0.007 and agreed with the boundary layer theory prediction (equation (4)) of 0.0067. The center of the bolus reached the wall in about 360 deg or 133 cm at rotation 1.2 rad/s. This gave a ratio of secondary to primary flow of 0.011 as compared to 0.0097 predicted by equation (4). The center of the bolus reached the wall in about 720 deg or 320 cm at rotation 4.8 rad/s. This gave a ratio of secondary to primary flow of 0.005 as compared to 0.0047 predicted by equation (4).

There was also good agreement between the boundary layer thicknesses predicted for the three cases by equation (3) and those estimated in the video replay of the experiments. At 1.2 rad/s a thickness of 2.85 mm was predicted and a thickness of 2 mm to 3 mm was observed. At 2.4 rad/s a thickness of 2.0 mm was predicted and a thickness of 1.5 mm to 2.5 mm was observed. At 4.8 rad/s the predicted thickness was 1.41 mm and the observed thickness was 1 mm to 2 mm.

The trajectories of dye streams from potassium permanganate crystals placed on the duct floor provide a basis for estimating the average or integrated transport of fluid in the Ekman boundary layer. It appeared that the cross channel flow in the Ekman boundary layer increased to a steady state

well within the first two semicircles of the duct. At the laminator block exit during rotation 2.4 rad/s, the dye crossed the 3 cm duct width in about 6 cm of downstream movement. After the second and greater semicircles, it crossed the 3 cm in about 4.5 cm of downstream movement. Thus, when the flow is fully developed, the average cross channel velocity in the Ekman boundary layer is estimated to be 0.67 of the average primary velocity in the boundary layer. This compared very well to an expected ratio at this location of 0.64, computed in the following way: The secondary flow in the core region was 0.0067 of the average primary flow in the duct (equation (4)). All the secondary flow that crossed the duct in the 48 mm thick lower half of the duct core had to return in the opposite direction through the 2 mm thick boundary layer. Therefore, the average cross channel velocity in the Ekman boundary layer was 48/2 times stronger than the average cross channel velocity in the core region. This made the average cross channel velocity in the Ekman boundary layer equal to 0.161 of the average primary velocity in the duct. The average primary velocity in the Ekman boundary layer (with the measuring volume centered 1 mm from the duct top or bottom wall) was measured by laser Doppler anemometry to be 0.25 of the average primary velocity in the duct. Thus, the expected ratio of average cross channel velocity to average primary velocity at the location of the crystals was 0.64.

The dimensionless axial primary velocity profiles measured by LDA are shown in Fig. 4. The theoretical profile [15] for flow in a stationary straight duct (*a*) is compared to the profiles in the stationary curved duct (*b*), the curved duct rotating at 2.4 rad/s in the direction of flow (*c*), and the curved duct rotating at 2.4 rad/s in the direction opposite to flow (*d*). The same data are plotted as dimensionless radial primary velocity profiles at various axial positions in Fig. 5. Table 1 shows the average dimensionless primary flow velocity as a function of height in the duct for the four cases. This is the average primary velocity that a particle would have if it moved at a uniform speed from the duct inner wall to the duct outer wall. It is near but not equal to 1.0 for the curved duct in forward and reverse rotations.

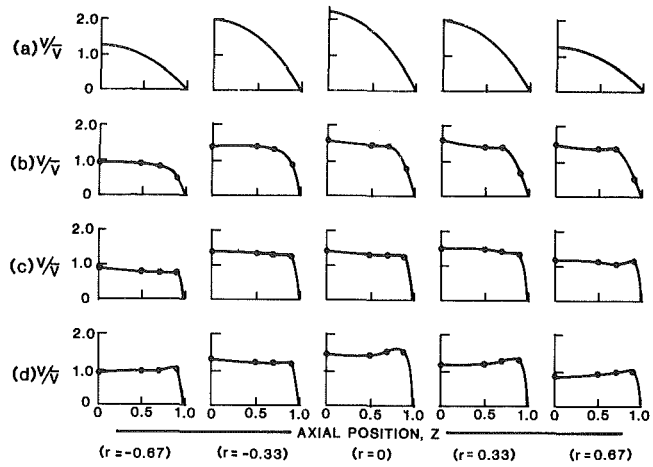

Fig. 4 Dimensionless axial velocity profiles at Reynolds number 500 for (*a*) theoretical flow in a straight stationary duct and for measured flows in the mock-up at (*b*) no rotation and at (*c*) forward rotation and (*d*) reverse rotation of 2.4 rad/s. (Coefficient of variation of *V* is 0.001.)

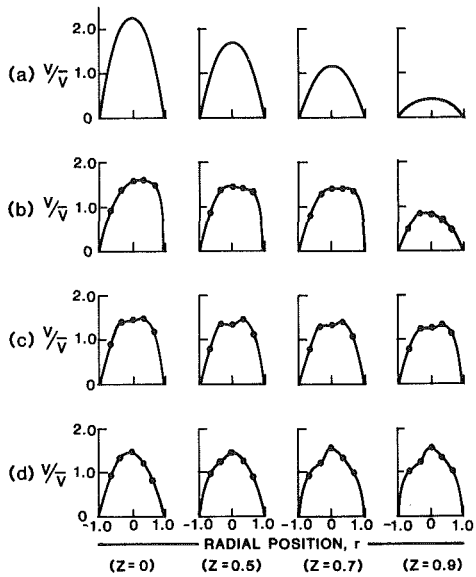

Fig. 5 Dimensionless radial velocity profiles at Reynolds number 500 for (*a*) theoretical flow in a straight stationary duct and for measured flows in the mock-up at (*b*) no rotation and at (*c*) forward rotation and (*d*) reverse rotation of 2.4 rad/s. (Coefficient of variation of *V* is 0.001.)

Discussion

There is a consistent pattern of the influence of curvature and secondary flow on the primary velocity profile in the rectangular duct. Curvature alone shifts the region of maximum velocity toward the outer wall and flattens the axial velocity profile by shifting faster moving fluid from the core region into the top and bottom regions of the duct. Rotation

Table 1 Average dimensionless primary velocity at Reynolds number 500 as a function of axial position in the duct

Dimensionless height, *y*	Stationary straight duct[(a)]	Stationary curved duct[(b)]	Curved duct at +2.4 rad/s[(b)]	Curved duct at −2.4 rad/s[(b)]
0.00	1.50	1.20	1.10	1.00
0.10	1.49	1.18	1.08	1.00
0.20	1.44	1.16	1.07	1.00
0.30	1.37	1.14	1.06	1.01
0.40	1.26	1.12	1.05	1.01
0.50	1.13	1.11	1.03	1.02
0.60	0.96	1.10	1.01	1.04
0.70	0.77	1.07	1.00	1.07
0.80	0.54	0.92	1.00	1.08
0.90	0.29	0.55	0.99	1.08
1.00	0.00	0.00	0.00	0.00

[(a)] Based on theory of Stöber and Zessack [15] for Poiseuille flow in a rectangular duct.
[(b)] Based on laser Doppler anemometry data in the mock-up of the Stöber and Flachsbart [1] spiral duct centrifuge.

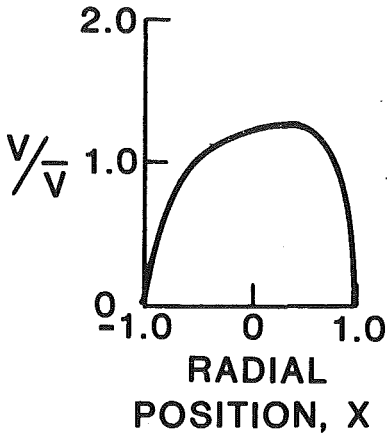

Fig. 6 Dimensionless radial velocity profiles in the core predicted by the boundary layer theory (equation (1))

in the forward direction further shifts the regions of maximum velocity toward the outer wall and introduces an asymmetry to the radial profile as slower moving fluid from the inner wall region is shifted into the central part of the duct. There is an indication of peaking of the primary velocity near the boundary layer regions at the top and bottom walls. The peaking results because the boundary layer is being fed by high velocity fluid from near the outer wall, but the core is being fed by lower velocity fluid from near the inner wall.

When the rotation is counter to the direction of fluid flow, the region of maximum velocity is shifted back toward the inner wall. The radial velocity profile in the reverse rotation case is not the mirror image of the forward rotation case because of the influence of curvature. Both profiles are more complex than the profile (Fig. 6) described by equation (1) (following Ludwieg [6]) for the same Reynolds and Rossby numbers. In addition, the axial velocity profiles are not flat.

The inflection points in the radial and axial primary velocity profiles are qualitatively similar to those predicted in the numerical calculations of Speziale [10] (see his Fig. 10) in a straight rotating duct of aspect ratio 2 with Reynolds number 279 and Rossby number 0.6. They are also similar to numerical calculations of Cheng, Lin, and Ou [17] for a stationary curved duct of aspect ratio 2 and Dean numbers between 100 and 200 (see their Fig. 8). These calculations [10, 17] revealed the appearance of a second pair of counter-rotating vortices which are near the horizontal centerline of the duct but are not symmetric to the vertical centerline of the duct.

Although a four vortex flow pattern may exist in our duct, our flow visualization results and our results for the modelling of centrifuge performance [18] were consistent with a pattern resulting from a single pair of symmetric, counter-rotating vortices. Better agreement between the bondary layer theory and the experiments might be obtained if a more complete theory including the influence of curvature were developed. The centrifuge operating conditions are near the lower limit for meeting Ludwieg's assumptions allowing curvature to be neglected. The qualitative results of his theory do explain the good performance of aerosol centrifuges.

The near uniformity of primary velocity in curved, rotating ducts allows aerosol centrifuges to function as true particle spectrometers [18]. Particles introduced at all heights in the core region are carried downstream at essentially the same rate. Particles of the same aerodynamic diameter deposit in compact bands on the outer wall of the duct. If the axial velocity profile were parabolic rather than blunt, particles introduced at the duct center plane would be carried to deposit sites far from the inlet in the same amount of time it would take particles of similar size introduced near the top or bottom of the duct to reach deposit sites very near the inlet. Particles of the same size would be deposited over long distances on the collection foil. With a boundary layer type of secondary flow in force, however, only particles introduced in the boundary layer regions at the top and bottom walls are deposited at locations outside the compact deposits. Particles crossing the duct in these boundary layer regions encounter a secondary flow opposite that in the core. Their deposition is retarded if rotation is in the direction of the flow and it is enhanced if rotation is opposite the direction of flow.

Under normal operating conditions of forward rotation, the secondary flow in an aerosol centrifuge carries particles in the core region toward the other wall where collection on the removable foil occurs. The usuable length of an aerosol centrifuge is therefore the distance required for the secondary flow to displace an element of fluid from the inner to the outer wall. Within this usuable length even very small particles which achieve no appreciable radial velocities under centrifugal acceleration will reach the outer wall by secondary flow alone. We can use the results of the dye injection studies to estimate the usuable length for the Stöber and Flachsbart centrifuge [1] under those standard conditions equivalent to 2.4 rad/s in the mock-up. The dye bolus moved radially from the middle of the duct to the side wall in the first 540 deg of the spiral. If we assume that development of the flow was linear over the first 180 deg of the sprial then the secondary flow will cross the other half of the duct width in an additional 450 deg. Thus, the usuable length of the centrifuge is the first 990 deg of the 1080 deg spiral. This corresponds to a region over which deposition of particles of all sizes is predicted to occur by our centrifuge model [18] and does occur in experiment [1]. Our model of centrifuge performance [18] uses equation (3) to predict the thickness of the secondary flow boundary layer, equation (4) to predict the ratio of the secondary to primary flow velocity in the core region, and the empirical formula of Austin [13] to estimate the flow development length. The model further uses the dimensionless velocity data from the Plexiglas mock-up as the primary velocity profile. The model moves particles under cenrifugal and Coriolis accelerations through the assumed flow fields.

We obtained only qualitatively correct results [18] when we applied our model to a centrifuge which does not have a constant duct width. The Lovelace Aerosol Particle Separator [3] has a duct which is 1.54 cm wide at the inlet and gradually expands to 3.9 cm width at the exhaust port. Quantitative prediction of particle deposition in such a duct would require detailed information on the flow profiles in an expanding duct. The model predictions for the Stöber and Flachsbart centrifuge [1] and other centrifuges of similar duct geometry [2, 4, 5], however, agreed with the instrument calibrations. This substantiated the applicability of the boundary layer theory to flow in the curved, rotating ducts of aerosol centrifuges.

Conclusion

Secondary return flow in a curved, rotating duct similar to that of an aerosol centrifuge was confined to a narrow boundary layer. The thickness of the boundary layer and the ratio of secondary to primary flow velocities in the core region could be approximated by applying the boundary layer theory approach of Ludwieg [6]. The radial primary velocity profile in the reverse rotation case was not the mirror image of the radial primary velocity profile in the case where rotation was in the direction of fluid flow. The axial velocity profile was quite blunt as a result of both curvature and rotation but was not entirely flat. The good performance of spinning duct aerosol centrifuges appears to be due in large part to

secondary flow and the resulting uniformity of primary fluid velocity.

Acknowledgments

This research was performed under U.S. Department of Energy Contract Number DE-AC04-76EV01013. Mr. Gerd Morawietz participated in the experimental work reported here while he was a visiting scientist at the Inhalation Toxicology Research institute. Dr. Colin E. Hackett of Sandia National Laboratories advised on laser anemometry and Dr. Franz Durst of the University of Karlsruhe, West Germany provided very useful discussion and advice at the time the study was being conceived. Walter H. Vandevender of Sandia National Laboratories assisted with the COLSYS program. The advice, review, and criticism of our colleagues are gratefully acknowledged.

References

1 Stöber, W., and Flachsbart, H., "Size-Separating Precipitation of Aerosols in a Spinning Spiral Duct," *Environmental Science and Technology*, Vol. 3, 1969, pp. 1280–1296.

2 Hochrainer, D., "A New Centrifuge to Measure the Aerodynamic Diameter of Aerosol Particles in the Submicron Range," *Journal of Colloid and Interface Science*, Vol. 36, 1971, pp. 191–194.

3 Kotrappa, P., and Light, M. E., "Design and Performance of the Lovelace Aerosol Particle Separator," *Review of Scientific Instruments*, Vol. 43, 1972, pp. 1106–1112.

4 Moss, O. R., Ettinger, H. J., and Coulter, J. R., "Aerosol Density Measurements Using a Modified Spiral Centrifuge Aerosol Spectrometer," *Environmental Science and Technology*, Vol. 6, 1971, pp. 614–617.

5 Tillery, M. I., "A Concentric Aerosol Spectrometer," *American Industrial Hygiene Association Journal*, Vol. 35, 1974, pp. 62–74.

6 Ludwieg, H., "Die ausgebildete Kanalströmung in einem rotierenden System," *Ingenieur-Archiv*, Vol. 19, 1951, pp. 296–308.

7 Barua, S. N., "Secondary Flow in a Rotating Straight Pipe," *Proceedings of the Royal Society of London*, Vol. A227, 1954, pp. 133–139.

8 Dean, W. R., "Note on the Motion of Fluid in a Curved Pipe," *Philosophical Magazine*, Vol. 4, 1927, pp. 208–223.

9 Dean, W. R., "The Stream-Line Motion of Fluid in a Curved Pipe," *Philosophical Magazine*, Vol. 5, 1928, pp. 673–695.

10 Speziale, C. G., "Numerical Study of Viscous Flow in Rotating Rectangular Ducts," *Journal of Fluid Mechanics*, Vol. 122, 1982, pp. 251–271.

11 Hoover, M. D., "Particle Deposition in Spinning Duct Aerosol Centrifuges," PhD dissertation, University of New Mexico, 1980.

12 Pedlosky, J., *Geophysical Fluid Dynamics*, Springer-Verlag, New York, 1979.

13 Austin, L. R., "The Development of Viscous Flow Within Helical Coils," PhD dissertation, University of Utah, 1971.

14 Martonen, T. B., "Aerosol Sedimentation in a Spinning Spiral Duct Centrifuge," PhD dissertation, University of Rochester, New York, 1976.

15 Stöber, W., and Zessack, U., "Zur Theorie einer konischen Aerosolzentrifuge," *Staub*, Vol. 24, 1964, pp. 295–305.

16 Ascher, U., Christiansen, J., and Russell, R. D., "COLSYS-Collocation Software for Boundary-Value ODES," *ACM Transactions on Mathematical Software*, Vol. 7, 1981, pp. 209–229.

17 Cheng, K. C., Lin, R. C., and Ou, J. W., "Fully Developed Flow in Curved Rectangular Channels," ASME JOURNAL OF FLUIDS ENGINEERING, Vol. 98, 1976, pp. 41–48.

18 Hoover, M. D., and Stöber, W., "Model of Particle Deposition in Spinning Duct Aerosol Centrifuges," *Journal of Aerosol Science*, Vol. 12, 1981, pp. 223–232.

Dynamics of Vertical Annular Liquid Jets

P. D. Esser

S. I. Abdel-Khalik

Nuclear Engineering Department,
University of Wisconsin-Madison,
Madison, Wis. 53706

A theoretical model is developed to determine the flow characteristics for vertical liquid jets of annular cross section. The fully implicit numerical marching integration procedure is based on the parabolic flow theory of Patankar and Spalding. The method is more accurate and general than previous analytical models, since it accounts for all significant forces acting upon the jet and for complex boundary conditions, such as an ambient pressure difference across the jet or a non-uniform velocity profile at the inlet. Comparison of the results with existing experimental data indicates reasonable agreement, and the predictions correspond closely to those of the earlier theories for simplified flow cases.

Introduction

Interest in the flow characteristics of annular liquid jets has grown recently in connection with a proposed design for an inertial confinement fusion (ICF) reactor brought forth by the Lawrence Livermore National Laboratory (LLNL) [1-3]. ICF devices produce pulsed fusion power by focusing lasers or charged particle beams at intervals of approximately 1 Hz onto a small pellet composed of deuterium and tritium. The rapid heating and compression of the pellet compels it to explode, with an attendant release of high-energy alpha particles, neutrons, electrons, X-rays, and other ionic debris. The particles, radiation, and shock waves produced would subject a solid reactor chamber, or "first wall," to intolerable cyclical loadings and stresses. To alleviate this problem, the LLNL concept utilizes a thick, recirculating annular jet, or "waterfall," of liquid lithium that flows between the fuel pellets and the reactor chamber wall. The lithium jet thus serves the triple purpose of first wall shield, heat transfer medium and tritium fuel breeder. A typical design for a commercial-sized fusion power plant envisions a lithium fall with an average inner radius of about 4 m, a 0.6 m thickness at the midplane, and an inlet velocity of about 8 m/s.

Several parameters of interest are associated with the waterfall concept. These include the following:

1. The "convergence length" of the annular lithium jet. This is defined as the distance from the inlet at which the inner radius vanishes and the jet assumes a cylindrical form. Convergence clearly must be avoided for distances on the order of the reactor chamber height.
2. The minimum thickness of the jet. This criterion is established by analyzing the attenuation of fusion pellet debris and radiation by the lithium curtain. The limiting thickness must be maintained through the entire fall distance in order to provide adequate protection for the first solid structural wall.
3. The variation of the inner and outer jet radii with axial distance. The geometry of the waterfall must be accurately known when designing the fusion reactor chamber, including the beam ports and auxiliary equipment.
4. The total exposed surface area of the jet. This parameter is required for determining the effectiveness of the lithium liquid in condensing the vaporized lithium that is formed after each fuel pellet explosion.
5. The stability of the annular lithium waterfall. Disturbances caused by external perturbations or internal turbulent motion may cause the jet to break up and disperse before it reaches the bottom of the reactor chamber. (The waterfall is expected to vaporize and disintegrate shortly after each explosion. However, recirculating flow to the reactor chamber inlet renews the continuous annular jet before the next fusion reaction is triggered.)

Stability considerations in laminar and turbulent annular jets require a separate analysis and are treated by the authors in another paper [4]. The first four parameters listed above may be evaluated accurately by the numerical procedure described below.

Background

Before outlining the main features of the present model, it is useful to review existing theories of annular jet flow and to assess their strengths and weaknesses. The first known papers devoted to the dynamics of annular jets are those of Binnie and Squire [5] and Baird and Davidson [6]. Both analyses employ the basic equations of fluid flow to derive nonlinear differential equations that describe the behavior of the jet flow as it proceeds downward from an annular orifice or nozzle. The differential equations are simplified to obtain closed-form solutions for idealized flow situations. The theory of Baird and Davidson accounts for the presence of an

Contributed by the Fluids Engineering Division of THE AMERICAN SOCIETY OF MECHANICAL ENGINEERS and presented at the 7th Annual Energy-Sources Technology Conference and Exhibition, New Orleans, La., February 11-17, 1984. Manuscript received by the Fluids Engineering Division, December 28, 1981. Paper No. 84-FE-9.

Table 1 Physical parameters accounted for in annular jet models

Authors	A	B	C	D	E	F	G	H	I
Binnie and Squire [5]	x	x							
Baird and Davidson [6]	x	x	x						
Hovingh [7]	x			x					
Hoffman et al. [8]	x	x		x	x	x			
Paul [9]	x	x			x	x	x		
ANNJET	x	x	x	x	x	x	x	x	x

Key: A curvature in horizontal plane
B curvature in vertical plane
C ambient pressure difference
D gravitational acceleration
E initial radial velocity component
F finite jet radius at convergence
G separation of inner and outer jet radii
H effective viscosity
I nonuniform velocity profile

ambient pressure difference across the jet, but for equal pressures the result for the jet profile as a function of distance reduces to that of Binnie and Squire. Both papers also describe experiments that were conducted to validate the theoretical predictions. In general, the analyses overestimate the observed convergence lengths, with the differences being most pronounced at low flow velocities. The authors attribute the disparities to "meniscus effects" as the jet approaches the convergence point.

Recent theories on annular jet convergence have been proposed by Hovingh [7] and Hoffman et al. [8]. Unlike the simplified versions of the theories described above, Hovingh's analysis accounts for the influence of gravity and gives the time and distance to convergence as the solution to a cubic algebraic equation. Hoffman et al. use the theory of "water bells," which resemble annular jets, to generalize Hovingh's analysis by improving the treatment of surface tension forces and allowing for the existence of a radial component of flow at the inlet to the jet. The results of both theories express convergence time (or length) as a function of a nondimensional convergence parameter N_c:

$$N_c = \frac{\rho g^2 \bar{r}_0^2 b_0}{2 u_0^2 \sigma} \tag{1}$$

The derivation of Hoffman et al. is also backed by experimental data. Agreement between theory and experiment is generally very good, except at high flow velocities where marked reductions in the observed convergence length are thought to be caused by a flow-induced pressure decrease inside the jet. Based on the three data points at the highest values of N_c, there are also indications of a drop-off in measured convergence lengths at very low flow velocities.

Another recent analysis is that of Paul [9], whose model includes horizontal and vertical curvature on both surfaces of the jet and the presence of a radial velocity component at the inlet, although it neglects the effect of gravity. Paul's theory gives good agreement with experimentally measured surface profiles of annular jets with significant inward radial velocities. However, his flow equations are rather cumbersome and, as discussed later, do not correctly account for the effects of continuity.

The main features of the annular jet theories proposed to date are summarized and compared in Table 1. It is seen that while successive analyses have been improved and generalized, no single model incorporates *all* of the physical factors discussed so far. None of the models is able to treat the influence of laminar viscosity (or effective turbulent viscosity) or the presence of a nonuniform axial velocity profile at the jet inlet. In addition, the analytical theories cannot be conveniently solved for some of the parameters of interest outlined in the previous section, such as the surface area of a jet or its complete geometrical profile. However, the numerical procedure developed in this paper, referred to as ANNJET (ANNular JET), includes all of the features listed in Table 1 and provides a detailed representation of the flow characteristics for vertical annular jets.

The development of the numerical procedure described below was motivated by the recognition that no purely analytical model can simultaneously account for all of the flow parameters of interest. Closed-form solutions are available only for simplified cases that do not accurately represent actual engineering situations. Since the more general algebraic or differential equations developed in the previous analyses must be solved numerically in any event, it seems logical to develop a computer code that accounts for all important physical factors and tabulates the solutions in a convenient form. Attention is now turned to the development of such a code.

Analysis

Consider a cross section of a vertical annular liquid jet as sketched in Fig. 1. In general, the jet is acted upon by at least four primary forces: Inertia; gravity; surface tension; and

Nomenclature

b_0 = jet thickness at inlet
g = acceleration of gravity
l = Prandtl mixing length
N_c = dimensionless convergence parameter
p = static pressure of jet
p_1 = boundary pressure at inner jet surface
p_2 = boundary pressure at outer jet surface
P_1 = ambient pressure on inner jet surface
P_2 = ambient pressure on outer jet surface
r = radial coordinate
δr = change in radial coordinate
$\bar{r}_0$ = mean jet radius at inlet
r_{10} = inner jet radius at inlet
r_{20} = outer jet radius at inlet
r_1 = inner jet radius
r_2 = outer jet radius
r_{max} = radius of maximum velocity in annular duct
u = axial velocity
u_0 = axial velocity at inlet
U = average axial velocity in annular duct
v = radial velocity
v_0 = radial velocity at inlet
z = axial coordinate
Δz = axial increment size
α = aspect ratio
ν_{eff} = effective kinematic viscosity
ρ = density
σ = surface tension

Subscripts

0 = parameter evaluated at jet inlet
1 = parameter evaluated at inner jet surface
2 = parameter evaluated at outer jet surface

viscosity. The flow pattern is also influenced by the boundary conditions, which may include a nonuniform axial velocity profile at the inlet or an ambient pressure difference between the inner and outer jet surfaces. These forces and boundary conditions may be incorporated into the Navier-Stokes equations of fluid flow, whose solutions would yield a complete description of the flow characteristics. Unfortunately, the general Navier-Stokes equations are elliptical in nature and usually require excessive computer time or space for their numerical solution. The equations can be cast into parabolic form, however, if shear stresses and diffusive momentum fluxes acting on the horizontal (r-θ) plane are ignored. The flow equations can then be solved efficiently by the well-known numerical technique of Patankar and Spalding [10, 11].

In order to make the present problem amenable to this procedure, the following assumptions and restrictions are established:

1. The jet consists of a steady, vertical, annular flow of an incompressible Newtonian liquid without surface shear.
2. At any point in the flow field, the axial velocity is large compared to the radial velocity.
3. The fluid should not have a high laminar viscosity (or effective turbulent viscosity).
4. The flow is two-dimensional with no angular (swirl) velocity component.
5. Gravity is the only body force.
6. The axial pressure gradient is negligible compared to the gravitational force.
7. There is no heat transfer or viscous dissipation.

The second and third criteria permit the transformation of the Navier-Stokes equations to parabolic form. The remaining assumptions are not essential to the procedure, but represent reasonable simplifications for most applications. Since heat transfer and viscous dissipation are ignored, the energy conservation equation is not required.

Therefore, the velocity components and pressure distribution in the flow field are found from the continuity equation and momentum balances in the axial and radial directions. With the positive z-coordinate in the downward vertical direction, and $r = 0$ at the center of the annulus, the parabolic Navier-Stokes equations are written out below in cylindrical coordinates for an incompressible liquid [12]:

$$\frac{\partial u}{\partial z} + \frac{1}{r}\frac{\partial}{\partial r}(rv) = 0 \tag{2}$$

$$\frac{\partial}{\partial z}(u^2) + \frac{1}{r}\frac{\partial}{\partial r}(ruv) = \nu_{\text{eff}}\left[\frac{\partial^2 u}{\partial r^2} + \frac{1}{r}\frac{\partial u}{\partial r}\right] + g \tag{3}$$

$$\frac{\partial}{\partial z}(uv) + \frac{1}{r}\frac{\partial}{\partial r}(rv^2) = \nu_{\text{eff}}\left[\frac{\partial^2 v}{\partial r^2} + \frac{\partial}{\partial r}\left(\frac{v}{r}\right)\right] - \frac{1}{\rho}\frac{\partial p}{\partial r} \tag{4}$$

The quantity ν_{eff} refers to the kinematic fluid viscosity for laminar jets, or an effective kinematic viscosity for turbulent jets. The Prandtl mixing length hypothesis or other suitable turbulent shear stress model [13] can be readily adapted to the solution procedure.

Eight boundary conditions (three for each of the velocity components, and two for the pressure field) are required to complete the formulation of the problem. At the jet inlet, the velocity distributions are assumed to be known, and the pressure field is taken to be uniform. (The latter criterion is a reasonable assumption in most cases of interest. If the nonuniform radial pressure distributions accompanying fully-developed flow emerging from a long annular nozzle are known, they may be readily incorporated into the initial boundary specifications.) As explained below, the axial and

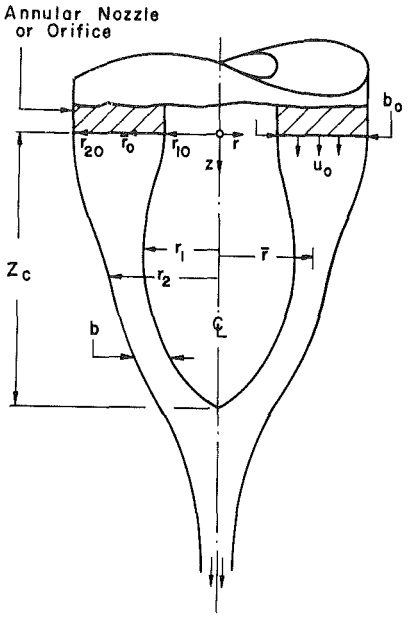

Fig. 1 Geometry and key parameters of a vertical annular liquid jet

radial velocity distributions at the top boundary of a given axial location are known from the calculation for the preceding incremental step in the marching integration procedure. Since the jet flow is assumed to be free, the components of axial shear stress and radial normal stress at the boundaries must vanish. Applying this requirement to the inner and outer jet surfaces, four additional boundary conditions are obtained:

$$\frac{\partial u}{\partial r} = \frac{\partial v}{\partial r} = 0 \quad \text{at} \quad r = r_1 \quad \text{and} \quad r = r_2 \tag{5}$$

The interior and exterior ambient pressures, which are specified input parameters, are combined with surface tension stresses to establish the pressure boundary conditions for the annular jet. The inner and outer surface pressures are evaluated at each axial location by the following equations [14]:

$$p_1 = P_1 + \sigma\left\{-\frac{1}{r_1} + \left(\frac{\partial^2 r_1}{\partial z^2}\right)\left[1 + \left(\frac{\partial r_1}{\partial z}\right)^2\right]^{-3/2}\right\} \tag{6}$$

$$p_2 = P_2 + \sigma\left\{\frac{1}{r_2} - \left(\frac{\partial^2 r_2}{\partial z^2}\right)\left[1 + \left(\frac{\partial r_2}{\partial z}\right)^2\right]^{-3/2}\right\} \tag{7}$$

In these formulas, the first term inside the braces represents the surface tension component resulting from curvature in the horizontal plane, while the second term represents the component produced by curvature in the vertical plane.

Equations (2)-(7), together with appropriate boundary conditions, are solved by the finite-difference computer code ANNJET. The code is based on the fully-implicit, non-iterative marching integration procedures developed by Patankar and Spalding for two-dimensional [10] and three-dimensional [11] flows. Complete details on the formulation of the finite-difference equations and the execution of the solution procedure are furnished in reference [15]. This reference also contains a FORTRAN source listing of the ANNJET program.

At each axial node in the flow field, the jet is divided into a number of concentric annular rings. ANNJET uses a set of 100 evenly spaced rings at each axial location, but this number may be varied depending on the accuracy required, and the code could be adapted to utilize unequal radial increments. (This would be especially useful for jets with steep axial

velocity gradients.) After the grid geometry is established at the axial node, the finite-difference equations for axial and radial momentum are solved implicitly for each annular ring. The pressure distribution is adjusted so that the continuity equation is satisfied for each increment, and the radial velocity components are recalculated from the corrected pressures.

The resulting velocity distributions are used to determine the location of the physical boundaries (surfaces) of the jet and to set up the difference grid at the downstream location. The change in position of a radial node is given by the following expression:

$$\delta r = \frac{v}{u} \Delta z \tag{8}$$

Three tridiagonal matrix systems, containing the coefficients for the axial and radial velocity components and the pressure field, must be solved at each axial location. The matrix dimensions are approximately equal to the number of radial increments. This solution procedure is repeated along the axial distance of interest, or until the computed value of the inner radius attains a negative value, at which point the annular jet physically converges into a solid circular jet.

The axial increment size must be chosen sufficiently small so that numerical instabilities do not develop. Such instabilities manifest themselves by the appearance of physically unrealistic results, such as negative pressures or excessively large radial velocities. However, test runs indicate that if numerical stability is maintained, the results are not sensitive to the size of the axial nodal spacing. For a finite-difference array with 100 radial increments, approximately 0.09 s of CPU time is required per axial increment on a Univac 1180 computer. The location of output edits and the detail of information listed are designated by the user.

ANNJET requires the following information to be input: physical properties of the liquid; inner and outer radii of the orifice or nozzle; axial and radial velocity distributions at the inlet; and the interior and exterior ambient pressures. For turbulent jets, a suitable model for evaluating effective shear viscosities must also be included. The basic version of ANNJET incorporates the Prandtl mixing length hypothesis, which may be expressed as:

$$\nu_{\text{eff}} = l^2 \left| \frac{\partial u}{\partial r} \right| \tag{9}$$

The mixing length l is taken to be proportional to the jet thickness. The constant of proportionality depends on the flow situation, but a value of approximately 0.075 is representative [10, 13].

The inlet velocity distributions must be found by experiment or analysis. It has been observed [9] that jets emanating from annular orifices have nearly uniform velocity profiles with a significant inward radial component, while jets issuing from annular nozzles have partially or fully developed axial profiles with little radial flow. For the latter case, if the flow in the nozzle is laminar the axial velocity distribution is given by the following equations [16]:

$$u = 2U \frac{r_{20}^2 - r^2 - 2r_{\max}^2 \ln(r_{20}/r)}{r_{20}^2 - r_{10}^2 - 2r_{\max}^2} \tag{10}$$

where

$$r_{\max} = \left[\frac{r_{20}^2 - r_{10}^2}{2\ln(r_{20}/r_{10})} \right]^{1/2} \tag{11}$$

A number of experimental and semiempirical methods have been proposed to determine the velocity profiles for turbulent flows in annular ducts or nozzles [16–22]. For Reynolds numbers less than about 100,000 the results of Rao and Sarma [21], which are derived from boundary layer theory, are convenient to use with ANNJET since they can be expressed in closed form. The analysis of Wilson and Medwell [19] appears to be suitable for computing the velocity distribution in highly turbulent annular flows. The iterative solution procedure is based on the Prandtl mixing length hypothesis, which conforms to the turbulence model employed in the basic version of ANNJET. However, further investigation is needed to assess the validity of these turbulent flow models over various ranges of the Reynolds number. In addition, the effects on the velocity distribution resulting from the transition of confined flow in the annular nozzle to the inlet of the free jet must be addressed.

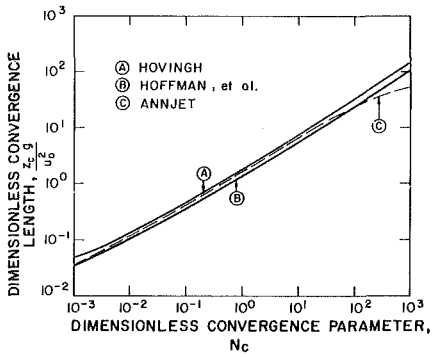

Fig. 2 Comparison of ANNJET convergence length predictions with previous theoretical results

Results

Comparison of ANNJET Convergence Length Predictions With Previous Theories. Figure 2 compares the convergence length predictions of the ANNJET code with the previous theoretical results of Hovingh [7] and Hoffman et al. [8]. The graph is a replica of the nondimensional convergence length plot included in reference [8]. It is based on a vertical annular jet of water at 20°C produced by a nozzle with inner and outer radii of 1.91 cm and 2.54 cm, respectively. The ordinate is the dimensionless convergence length $z_c g/u_0^2$, while the abscissa is the dimensionless convergence parameter N_c defined by equation (1). The average flow velocity at the inlet of the jet is taken as the independent variable. In executing the ANNJET program, it is assumed that there is no initial radial velocity component or contraction of the flow. The inlet velocity distribution is assumed to be uniform since this is required by the other analytical methods. (The effect of a fully developed velocity profile is investigated below.) The size of the axial increment Δz is chosen to be about 0.1 percent of the actual convergence length for each run. (However, in the runs for $N_c = 10^2$ and $N_c = 10^3$ smaller step sizes are used to preserve numerical stability.) The jet flow is assumed to be turbulent in all cases, although the computed convergence length is not sensitive to the flow regime when the inlet velocity is uniform.

Examination of Fig. 2 indicates that ANNJET agrees well with the previous theories. As explained by Hoffman et al., the results of Hovingh represent an upper bound for convergence length since that theory ignores the finite size of the jet at the convergence point. All of the ANNJET predictions fall below this limit. The curve due to Hoffman et al. accounts for the nonzero jet size at convergence in an approximate manner and represents a more realistic prediction. The ANNJET results, which do not require assumptions or approximations concerning the jet size at convergence, generally lie between the two theories, but closer to that of Hoffman et al.

It should be noted that the ANNJET results begin to drop off perceptibly compared to the other theories at values of N_c

Table 2 Effect of flow regime and inlet velocity profile on annular jet convergence*

Inlet velocity profile: Jet flow regime:	uniform turbulent	fully developed turbulent	fuily developed laminar
$N_c = 10^{-3}$	0.0368	0.0352	0.0342
$= 10^{-2}$	0.1201	0.1181	0.1115
$= 10^{-1}$	0.415	0.408	0.385
$= 10^{0}$	1.590	1.542	1.469
$= 10^{1}$	6.67	6.43	6.19

* Table gives dimensionless convergence length $z_c g/u_0^2$ for the nozzle described in reference [8]: 1.91 cm i.r., 2.54 o.r., water at 20°C.

greater than about 10^1. Since jet velocity decreases with increasing N_c, the effects of gravity, which are not fully accounted for by the two previous theories, become more pronounced. Therefore, it is concluded that the ANNJET predictions are more accurate in this range. This is corroborated by the experimental results of Hoffman et al., which exhibit a similar deviation from the previous theories at low flow velocities.

Dependence of Convergence Length on Flow Regime and Inlet Velocity Profile. ANNJET can be used to examine the effects of laminar and turbulent flow regimes and the inlet velocity profile on the convergence length of a vertical annular jet. The following example is based on the physical characteristics of the nozzle used in the experimental studies of Hoffman et al. [8], and described in the previous section. For values of N_c between 10^{-3} and 10^1 the flow in the nozzle is turbulent, and the fully developed velocity distribution at the exit is calculated by the method of Rao and Sarma [21]. The flow in the jet itself may be either laminar or turbulent. Hoffman et al. do not report the flow regimes in their experimental results, so separate runs of the ANNJET code assuming laminar and turbulent flow are made.

The results are listed in Table 2. The dimensionless convergence lengths for a uniform inlet velocity profile match the ANNJET results plotted in Fig. 2. For a fully developed velocity distribution at the nozzle exit and turbulent flow in the jet, the predicted convergence lengths are several percent lower than for the case of uniform flow. If the jet is laminar, the convergence lengths decrease even further.

The fact that a fully developed velocity profile at the inlet of an annular jet tends to hasten its convergence can be explained on a theoretical basis. Before surface tension effects become important, the increased contraction is due to the relaxation, or flattening, of the velocity distribution after the flow leaves the nozzle. The fluid near the boundaries of the jet accelerates as the surface shear vanishes, while the fluid in the interior decelerates. In order to satisfy continuity of the flow, the jet must contract more rapidly than it would under the influence of gravity alone. These effects can be analyzed by means of macroscopic balances. Bird [23] presents a theory that is valid for cylindrical jets of both Newtonian and non-Newtonian fluids. In the case of an annular jet, the faster contraction of a fully developed flow implies a shorter convergence length.

The results in Table 2 reveal that the effect of a fully developed inlet velocity distribution is much more pronounced in a laminar jet than in a turbulent one. This is explained by the fact that the greater effective viscosities in turbulent flow cause more rapid relaxation of the velocity profile, and the jet assumes a nearly uniform velocity much sooner than in the corresponding laminar case. Since the nonuniform profile persists for a longer time in the laminar jet, its contraction is enhanced and the convergence length is reduced.

Dependence of Convergence Length on Ambient Pressure Difference. In this section, predictions of the ANNJET code

Table 3 Effect of ambient pressure difference on annular jet convergence*

$(P_1 - P_2)$ (dynes/cm^2)	Baird and Davidson theory	Baird and Davidson experiment	ANNJET
0	2.8	2.5	3.50
+180	5.2	5.2	5.93
−180	---	---	2.76

* Table gives convergence length z_c in cm for the orifice described in reference [6]: 0.606 cm i.r, 0.653 cm o.r., u_0 = 268 cm/s, water at 20°C.

are compared to the theoretical and experimental results of Baird and Davidson [6] for the convergence length of vertical annular jets with and without an ambient pressure difference between the jet surfaces. The calculations and experiments of Baird and Davidson are based on a long, concentric annular duct with a 0.606 cm inner radius and 0.635 cm outer radius. The working fluid is again water at 20°C. The experimental apparatus maintains the exterior of the jet at atmospheric pressure, but the interior pressure can be varied by inert gas injection.

In applying the ANNJET program, the jet flow is assumed to be laminar and to have a uniform inlet velocity. In all cases, the axial step size is 10^{-3} cm. All computations are made for an inlet flow velocity of 268 cm/s, which represents the upper limit of Baird and Davidson's data. At lower velocities, numerical instabilities are encountered with ANNJET, and the required axial step size becomes prohibitively small for economical computations.

The results are compared in Table 3. It is seen that for the cases of zero pressure difference and $P_1 - P_2 = 180$ dyne/cm^2 (i.e., higher pressure on the inner boundary of the jet), ANNJET predicts larger convergence lengths than those found theoretically and experimentally by Baird and Davidson, with the differences ranging from 14 to 40 percent. There are three possible reasons for this discrepancy in the results. First, Baird and Davidson define the convergence length as the distance to the point at which the outer jet radius decreases to a value of 0.2 cm, instead of the distance at which the inner radius vanishes. The ANNJET results in Table 3 are adjusted to reflect this change, but discrepancies may still exist in comparing the results directly with those of Baird and Davidson.

Second, Baird and Davidson state that their annular duct has a discharge coefficient of 0.75, but do not explain how this experimental parameter is incorporated into their theory. Undoubtedly this also affects the inlet conditions that are supplied as input to the ANNJET program. However, modifications have not been made since the exact influence of the discharge coefficient is not known. If one of the effects is a reduction in the flow area at the inlet of the jet, then ANNJET can be expected to overpredict the convergence lengths, which is the case in Table 3.

The third explanation for the discrepancy between theory and experiment relates to the somewhat vague concept of "meniscus effects." This phenomenon was originally postulated by Baird and Davidson to account for the con-

Table 4 Experimental data for annular jet profile measurements in Figure 3

Figure	Orifice i.r. (cm)	Orifice o.r (cm)	α	u_0(cm/s)	v_0(cm/s)
3(*a*)	0.889	1.270	0.7	171.4	−60.0
3(*b*)	1.016	1.270	0.8	339.9	−119.0
3(*c*)	1.143	1.270	0.9	383.4	−134.2

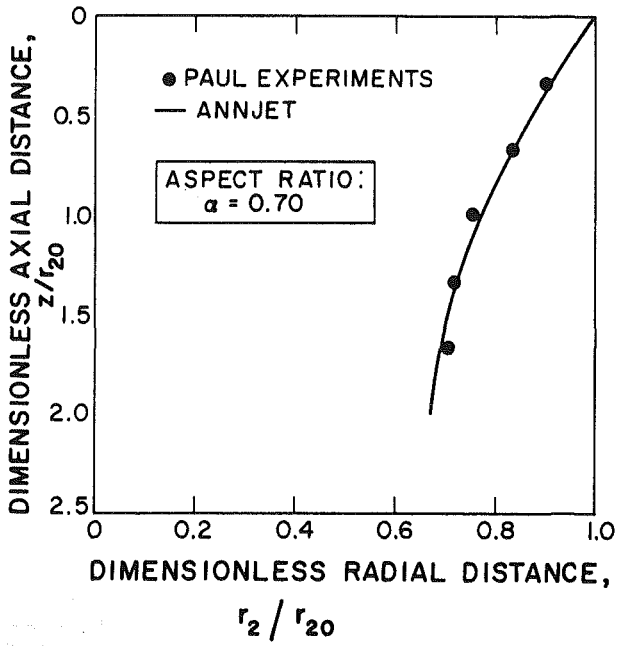

Fig. 3(*a*) Comparison of ANNJET geometrical profiles with experimental results (α = 0.70)

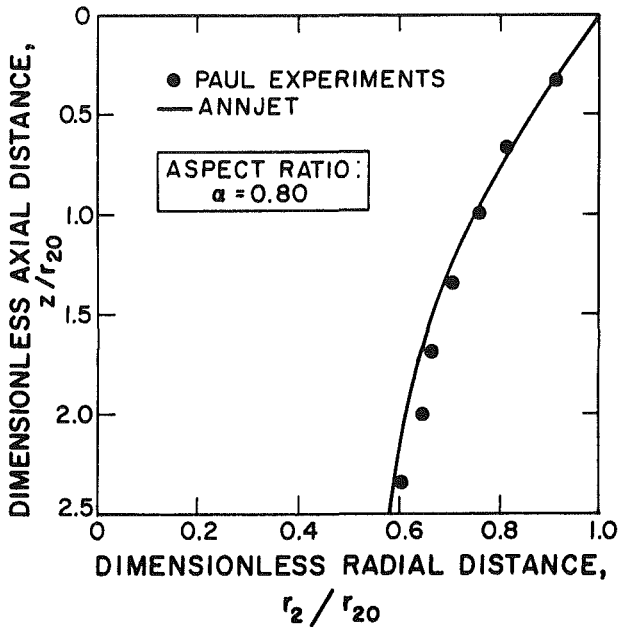

Fig. 3(*b*) Comparison of ANNJET geometrical profiles with experimental results (α = 0.80)

vergence length overpredictions in their analytical results. As applied to free-falling annular jets near the point of convergence, there are two possible manifestations of meniscus effects arising from surface tension. The fact that the radius of the inner boundary gradually becomes much smaller than the outer radius leads to an imbalance of the surface tension forces acting on the two free surfaces. This difference is not considered in the theory of Baird and Davidson, which bases surface tension forces only on a single arithmetic mean radius. However, it is accounted for explicitly in the ANNJET code, in which the inner and outer boundary treatments are completely separated.

Alternatively, meniscus phenomena may relate to the axial pressure gradient that develops in the inner portion of the jet as convergence is approached. This adverse pressure gradient also results from surface tension forces arising from strong radial curvatures. Since ANNJET is based on a parabolic formulation of the flow equations, whereas the axial pressure variation is an elliptical influence, this phenomenon is not modeled in the predicted results. The principal effect of the adverse pressure gradient would, of course, be to retard the axial acceleration, which would lead in turn to a reduced convergence length.

Table 3 also gives the ANNJET results for the case of an opposite pressure difference, $P_1 - P_2 = -180$ dyne/cm^2 (i.e., higher pressure on the outer boundary of the jet). This situation is not analyzed by Baird and Davidson, but the effect is a reduction in the convergence length of about 20 percent from the case of equal ambient pressures. Note, however, that for a given magnitude of $(P_1 - P_2)$ the increase in convergence length produced by a higher interior pressure is considerably greater than the reduction caused by a higher exterior pressure.

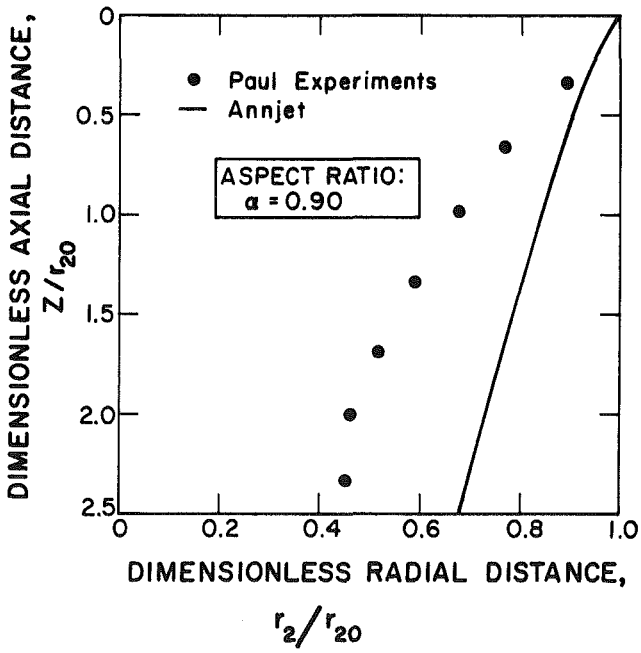

Fig. 3(*c*) Comparison of ANNJET geometrical profiles with experimental results (α = 0.90)

Comparison of ANNJET Geometrical Profile Predictions With Experiment. Paul [9] presents theoretical and experimental investigations of the geometrical profiles of annular jet surfaces. Three orifices, with aspect ratios of 0.7, 0.8, and 0.9, are used in his studies. The aspect ratio is defined as the ratio of the inner and outer radii of the orifice:

$$\alpha = \frac{r_{10}}{r_{20}} \tag{12}$$

For each orifice it is found experimentally that the magnitude of the (negative) radial velocity at the exit is a constant fraction of the axial velocity. The factor, which also equals the slope of the fluid streamlines at the exit, has a value of 0.35. The working fluid is water at 13°C. Additional experimental data for the three orifices are summarized in Table 4. The profile measurements are restricted to the outer jet surface, since the inner surface is usually obscured from view.

The comparisons of the ANNJET predictions with Paul's experiments are shown in Fig. 3. The ANNJET profiles for aspect ratios of 0.7 and 0.8 fit the experimental data well. However, the results for the orifice with an aspect ratio of 0.9 deviate significantly from Paul's measurements. Although it was originally speculated that this discrepancy may be caused by numerical instabilities in the ANNJET calculation [15], a detailed review indicates that the code predictions are valid. The differences are apparently due to inaccuracies in the values of experimental parameters cited by Paul. In particular, the assumption that the slope of the exit streamlines has a constant value of 0.35 for all three orifices is not physically realistic. Furthermore, the streamlines are not parallel over the entire cross section of the orifice opening. For orifices of the design used by Paul, the sensitivity of the geometrical profiles to these effects increases rapidly as the aspect ratio approaches unity. Accordingly, reasonable agreement may be achieved for orifices with moderate aspect ratios using approximate experimental parameters, but for very thin jets the inlet flow distribution must be specified more completely.

Paul also provides theoretical predictions for the geometrical profiles and convergence lengths of his experimental jets. The main features of the theory are noted in Table 1. Paul's theoretical profiles show good agreement with an aspect ratio of 0.9. However, the apparent success of his theory is actually coincidental. The equations of motion for the inner and outer jet surfaces are not treated consistently, and the theory neglects to apply the continuity equation to the inner surface. According to Paul's analysis, if surface tension and gravitational forces are neglected the slope of the inner jet surface remains constant, and is equal to the original streamline slope at the orifice. This, of course, is not physically true, and Paul's theory cannot be expected to yield accurate predictions in general. On the other hand, if the experimental or design parameters (including boundary conditions) are specified completely and accurately, the ANNJET code can be expected to give reliable results.

Conclusions

The ANNJET computer code offers a more general and accurate solution procedure for the flow characteristics of vertical annular jets than previous analytical models. Comparison of ANNJET predictions with published experimental results indicates variable agreement. However, the differences are attributed to incomplete or inaccurate specification of the experimental parameters or boundary conditions. Further validation of the ANNJET program with well-defined experimental comparisons would be beneficial. Also meriting additional investigation are the numerical instabilities encountered in certain flow situations, the calculations of the inlet velocity distributions, and the treatment of turbulent jets.

Practical applications of vertical annular jets can be analyzed with ANNJET. For example, the code is used to obtain detailed information on the flow behavior of the LLNL lithium "waterfall" scheme for ICF reactors. For typical values of the fluid properties and inlet flow conditions ($N_c \simeq 10^4$), the predicted convergence length is approximately 1000 m. While this result is quite large, it appears to be significantly less than the value of "several thousand meters" quoted by Hoffman et al. [8]. Accordingly, jet convergence is not a limiting criterion in this design concept. Additional results for the flow behavior of the annular lithium waterfall design are discussed in reference [15].

References

1 Maniscalco, J. A., and Meier, W. R., "Liquid-Lithium 'Waterfall' Inertial Confinement Fusion Reactor Concept," *Transactions of the American Nuclear Society*, Vol. 26, June 1977, pp. 62–63.

2 Maniscalco, J. A., Meier, W. R., and Monsler, M. J., "Conceptual Design of a Laser Fusion Power Plant," UCRL-79652, Lawrence Livermore National Laboratory, July 1977.

3 Maniscalco, J. A., and Meier, W. R., "Reactor Concepts for Laser Fusion," UCRL-79654, Lawrence Livermore National Laboratory, July 1977.

4 Esser, P. D., Paul, D. D., and Abdel-Khalik, S. I., "Stability of the Lithium 'Waterfall' First Wall Protection Concept for Inertial Confinement Fusion Reactors," *Nuclear Technology/Fusion*, Vol. 1, Apr. 1981, pp. 285–294.

5 Binnie, A. M., and Squire, H. B., "Liquid Jets of Annular Cross Section," *The Engineer*, Vol. 171, Apr. 1941, pp. 236–238.

6 Baird, M. H. I., and Davidson, J. F., "Annular Jets - I (Fluid Dynamics)," *Chemical Engineering Science*, Vol. 17, June 1962, pp. 467–472.

7 Hovingh, J., "Stability of a Flowing Circular Annular Liquid Curtain with a Vertical Axis Subjected to Surface Tension Forces," Internal Memo SS&A-77-108, Lawrence Livermore National Laboratory, Aug. 1977.

8 Hoffman, M. A., Takahashi, R. K., and Monson, R. D., "Annular Liquid Jet Experiments," ASME JOURNAL OF FLUIDS ENGINEERING, Vol. 102, Sept. 1980, pp. 344–349.

9 Paul, D. D., "Dynamics of Newtonian Annular Jets," M.S. thesis, Nuclear Engineering Department, University of Wisconsin-Madison, Dec. 1978.

10 Patankar, S. V., and Spalding, D. B., *Heat and Mass Transfer in Boundary Layers*, Second Edition, Intertext, London, 1970.

11 Patankar, S. V., and Spalding, D. B., "A Calculation Procedure for Heat, Mass and Momentum Transfer in Three-Dimensional Parabolic Flows," *International Journal of Heat and Mass Transfer*, Vol. 15, Oct. 1972, pp. 1787–1806.

12 Schlichting, H., *Boundary-Layer Theory*, Seventh Edition, McGraw-Hill, New York, 1979.

13 Launder, B. E., and Spalding, D. B., *Lectures in Mathematical Models of Turbulence*, Academic Press, London, 1972.

14 Anno, J. N., *The Mechanics of Liquid Jets*, D. C. Heath, Lexington, MA, 1977.

15 Esser, P. D., "Theory of Annular Liquid Jet Flow," M.S. thesis, Nuclear Engineering Department, University of Wisconsin-Madison, May 1980.

16 Knudsen, J. G., and Katz, D. L., *Fluid Dynamics and Heat Transfer*, McGraw-Hill, New York, 1958.

17 Barrow, H., Lee, Y., and Roberts, A., "The Similarity Hypothesis Applied to Turbulent Flow in an Annulus," *International Journal of Heat and Mass Transfer*, Vol. 8, Dec. 1965, pp. 1499–1504.

18 Levy, S., "Turbulent Flow in an Annulus," ASME *Journal of Heat Transfer*, Vol. 89, Feb. 1967, pp. 25–31.

19 Wilson, N. W., and Medwell, J. O., "An Analysis of Heat Transfer for Fully Developed Turbulent Flow in Concentric Annuli," ASME *Journal of Heat Transfer*, Vol. 90, Feb. 1968, pp. 43–50.

20 Quarmby, A., "An Analysis of Turbulent Flow in Concentric Annuli," *Applied Scientific Research*, Vol. 19, July 1968, pp. 250–273.

21 Rao, P. S. V. K., and Sarma, P. K., "Turbulent Flow in Concentric Annuli," *Indian Journal of Technology*, Vol. 14, Feb. 1976, pp. 59–62.

22 Malik, M. R., and Pletcher, R. H., "A Study of Some Turbulence Models for Flow and Heat Transfer in Ducts of Annular Cross-Section," ASME *Journal of Heat Transfer*, Vol. 103, Feb. 1981, pp. 146–152.

23 Bird, R. B., "The Change in Cross-Sectional Areas of Jets as Analyzed by Macroscopic Balances," RRC 23, University of Wisconsin Rheology Research Center, Feb. 1974.

J. O. Cruickshank
Research Division,
Carrier Corporation,
Subsidiary of United Technologies Corp.,
Syracuse, N.Y. 13221

A Similarity Between Plane and Axisymmetric Viscous-Gravity Jets

The equations governing the flow of plane and axisymmetic viscous-gravity jets are shown to have solutions which can be derived from one generalized equation. Solutions for the plane jet for various boundary and flow conditions are given here. Similar solutions for the axisymmetric jet are already in the literature.

The viscous-gravity jet is defined as a fluid jet that is influenced only by viscous and gravitational forces. It has been the subject of various studies over the years [1-3].

Recently, a paper [3] was published concerning the axisymmetric jet in stagnation flow. The plane, as distinct from the axisymmetric jet, is of importance in certain industrial processes [4], and has been the subject of one study, but no analytical solutions were given in that study.

It is interesting to note that both plane and axisymmetric viscous-gravity jets may be considered sub-sets of a more general equation such that solutions for the velocities in both types of jets can be obtained from the one solution.

Taylor [5] has shown that, for a one-dimensional plane jet, the axial velocity is governed by the equation

$$\frac{\partial u}{\partial x} = 4\nu \frac{\partial}{\partial x}\left(\frac{1}{u}\frac{\partial u}{\partial x}\right) + \frac{g}{u} \tag{1}$$

In this equation, u is the axial velocity, x is the axial direction, ν is the kinematic viscosity, g is the acceleration due to gravity, and surface tension effects are considered negligible.

If we let the jet thickness at the slot (orifice) be t_0 and the corresponding velocity be U_0, then equation (1) can be cast in nondimensional form:

$$\mathrm{Re}\left(u^2\frac{\partial u}{\partial x}\right) - 4u\frac{\partial^2 u}{\partial x^2} + 4\left(\frac{\partial u}{\partial x}\right)^2 - \frac{g{t_0}^2}{\nu U_0}u = 0 \tag{2}$$

where u and x are now nondimensionalized and $\mathrm{Re} = U_0 t_0/\nu$. Hence for very low Reynolds numbers equation (2) reduces to

$$uu'' - (u')^2 + \frac{u}{{K_1}^2} = 0 \tag{3}$$

with

$$ {K_1}^2 = \frac{4\nu U_0}{g{t_0}^2} \quad \text{and} \quad (') = \frac{d}{dx}. \tag{4}$$

This equation is best written in terms of the thickness of the jet, t, using continuity considerations. Thus the nondimensional thickness of the jet is governed by the equation

$$tt'' - (t')^2 = \frac{t^3}{2{K_2}^2} \tag{5}$$

where

$$ {K_2}^2 = \frac{2\nu U_0}{g{t_0}^2}. $$

For the axisymmetic viscous-gravity jet, it has been shown [3] that the jet radius is governed by the equation

$$aa'' - (a')^2 = \frac{a^4}{2K^2} \tag{6}$$

where

$$K^2 = \frac{3\nu U_0}{g{a_0}^2} \quad \text{and} \quad a_0$$

is the orifice radius. Experimental studies reported in [3] show that this one-dimensional model is a good approximation of the viscous-gravity jet. The similarity between equations (5) and (6) is very clear and both equations are seen to be sub-sets of the general class of nonlinear second order ordinary differential equations:

$$tt'' - (t')^2 = \frac{t^n}{2A^2},\ A = \text{constant}. \tag{7}$$

There are three solutions to this nonlinear ordinary differential equation; depending on the constant of integration, e_1, obtained from the transformations needed to solve (7).

We consider these cases separately:

(*a*) Let

$$\alpha^2 = \frac{1}{A^2(n-2)} \quad \text{and} \quad -\beta^{2-n} = \frac{e_1}{\alpha^2},\ e_1 < 0.$$

Then

$$t = \left[\frac{1}{\beta^{2-n}}\left\{\cos\left[\tfrac{1}{2}(\pm x + e_2)(2-n)\alpha\sqrt{\beta^{2-n}}\right]\right\}^2\right]^{\frac{1}{2-n}} \tag{8}$$

where e_2 is a constant of integration.

(*b*) For the case $e_1 > 0$, let

$$\beta^{2-n} = \frac{e_1}{\alpha^2}$$

and the corresponding solution is given by

$$t = \left\{\frac{2\beta^{2-n}}{\cosh[(\pm x + e_3)(n-2)\alpha\sqrt{\beta^{2-n}}] - 1}\right\}^{\frac{1}{n-2}} \tag{9}$$

where e_3 is a constant of integration.

(*c*) The third and final case is $e_1 = 0$. For this case we have

Contributed by the Fluids Engineering Division for publication in the JOURNAL OF FLUIDS ENGINEERING. Manuscript received by the Fluids Engineering Division, November 29, 1982.

$$t=\left[\frac{(n-2)\alpha}{2}(\pm x+e_4)\right]^{\frac{2}{2-n}} \tag{10}$$

where e_4 is also a constant of integration.

The axisymmetric jet discussed in [3] thus results when $n = 4$. We can thus obtain the velocity along the plane viscous-gravity jet as the solution of the above equations for $n = 3$. Hence, (using $t = 1, x = 0, t \to \infty, x = H$ for the stagnation flow, and $t = 1, x = 0, t \to 0, x \to \infty$ for the semi-infinite jet) we have for a plane viscous-gravity jet

$u=\left(1+\frac{x}{2K_2}\right)^2$ for the semi-infinite jet;

$u=\left(1-\frac{x}{2K_2}\right)^2$ for plane stagnation flow if $\frac{H}{K_2}=2$.

(H is the axial distance of the surface of stagnation);

$$u=\frac{\cosh\left[\sqrt{e_1}\,(H-x)\right]-1}{2e_1K_1{}^2} \quad \text{if} \quad \frac{H}{K_2}<2$$

where e_1 is obtained from the transcendental equation

$$\cosh H\sqrt{e_1}=1+2e_1K_2{}^2$$

and

$$u=\frac{\cos\left[\sqrt{-e_1}\,(H-x)\right]-1}{2e_1K_2{}^2}, \quad \text{if} \quad \frac{H}{K_2}>2$$

with e_1 given by another transcendental equation

$$\cos\left(H\sqrt{-e_1}\right)=1+2e_1K_2{}^2.$$

These three cases are the theoretical counterparts for plane viscous-gravity jets of the profiles of axisymmetric jets discussed in [3].

The axisymmetric jet profiles are easily obtained from equations 8–10 for the case of $n = 4$. These results, previously given in [3] are summarized below for ease of reference:

The jet radius, a is given by

$$a=\cos C_2/\cos\left(\frac{x}{K_3}\cos C_2+C_2\right) \quad \text{if} \quad \frac{H}{K_3}>1$$

where the constant C_2 is the solution of the equation

$$\frac{H}{K_3}\cos C_2+C_2=\pi/2 (C_2\neq\pi/2)$$

or

$$a=\sinh C_1/\sinh\left(C_1-\frac{x}{K_3}\sinh C_1\right) \quad \text{if} \quad \frac{H}{K_3}<1$$

with C_1 given by

$$C_1-\frac{H}{K_3}\sinh C_1=0 (C_1\neq 0)$$

and if $\frac{H}{K_3}=1$, then $a=1/\left(1-\frac{x}{K_3}\right)$.

$K_3{}^2=6\nu U_0/ga_0{}^2$ in all these equations.

It is interesting to note that the magnitude of the parameter n is a direct consequence of the area relationships for the given profiles. Thus, in the derivation of the governing equations, the cross-sectional area of the plane jet, being proportional to t the jet thickness, leads to the case $n = 3$ while for the axisymmetric jet, this area is proportional to a^2 and leads to $n = 4$. Clearly, one may speculate about the possible existence of flows that arise from cases $n > 4$ or $n < 3$, but such flows would have no apparent physical relevance in our three-dimensional world.

References

1 Trouton, F. T., "On the Coefficient of Viscous Traction and Its Relation to That of Viscosity." *Proc. Roy. Soc.*, Series A77, No. A519, May 1906, pp. 426–440.

2 Matovich, M. A., and Pearson, J. R. A., "Spinning of a Molten Threadline," *Ind. Eng. Chem.* (Fund), Aug. 1969, pp. 512–519.

3 Cruickshank, J. O., and Munson, B. R., "The Viscous-Gravity Jet in Stagnation Flow," ASME JOURNAL OF FLUIDS ENGINEERING, Vol. 104, Sept. 1982, pp. 360–362.

4 Brown, D. R., "A Study of the Behavior of a Thin Sheet of a Moving Liquid," *J. Fluid Mech.*, Vol. 10, 1961, pp. 297–305.

5 Taylor, G. I. (in an appendix to reference [4]).

ERRATA

H. Pascal, "Compressibility Effect in Two Phase Flow and its Application to Flow Metering With Orifice Plate and Convergent-Divergent Nozzle," published in JOURNAL OF FLUIDS ENGINEERING, Vol. 105, Dec. 1983, pp. 394–399.

The following correction is to be noted in relation to (5). Instead of

$$\frac{1}{\rho_m} = -\frac{\mu}{(1+\mu)\rho_{g_1}}\left(\frac{p_1}{p}\right)^{1/\lambda} + \frac{1}{(1+\mu)\rho_l}$$

the correct relation is

$$\frac{1}{\rho_m} = \frac{\mu}{(1+\mu)\rho_{g_1}}\left(\frac{p_1}{p}\right)^{1/\lambda} + \frac{1}{(1+\mu)\rho_l}.$$

Potential Flow From a Tapering Nozzle Impinging on a Flat Plate

J. E. Jones
Department of Mathematics,
University of Wales
Institute of Science and Technology,
Cardiff, Wales

A perfect flow from a two-dimensional nozzle is considered discharging against a normally placed flat plate. Particular attention is given to the effect of the angle of the nozzle, and results for angles of 15, 30, 45, and 60 deg are compared with those for a parallel-sided orifice. This model can be regarded as a two-dimensional representation of a plate valve or flapper valve in which the flow does not reattach to the land of the nozzle. The variations of the back pressure and the contraction coefficient with valve aperture have been plotted, and the shape of the free streamlines and the pressure distribution on the plate have been found. By considering the effect of fluctuations far upstream, the flow in a tapering orifice is shown to be inherently more unstable than that in a parallel-sided orifice. It is also shown that the control of the valve aperture over the back pressure is better in parallel-sided orifices than in angled ones.

1 Introduction

An extensive body of literature has been published on the practical and theoretical nature of plate valves, but despite a thorough literature search it appears that the action of the cone-angle of the nozzle on the flow has been ignored. The basic configuration is as shown in Fig. 1, and it is clear that the inward taper of the nozzle must have a prominent effect. The lack of any attempt to quantify this has prompted the present work which uses the hodograph and conformal transformations in a two-dimensional model of such an angled orifice.

Valves fall into two basic categories: the "sharp-edged" and "flat-faced" types [1]. These correspond to large and small ratios of the valve aperture h to the length of the land l (the land being the outer edge of the nozzle parallel to the plate). In flat-faced types the flow emerging from the nozzle frequently reattaches to the land forming a separation zone or bubble. Numerical solutions for various valve geometries have been given by Hayashi, Matsui, and Ito [2], and potential theory has been applied to this type of flow in a parallel-sided valve by Duggins [3]. For tapering valves the conformal transformations that have to be used for the flat-faced type are far more complicated than those for the sharp-edged type, so that in this study only the latter sort of valve has been considered.

The results for a tapering orifice are compared with those for a parallel-sided orifice, and it will be shown that instabilities of the flow are more likely for tapering nozzles. The theory for a parallel-sided orifice is well-known and easy to derive [4, 5, 6, 7]. It is the basis of the work of several authors e.g. Lichtarowicz and Markland [8] give a development of the theory of separated flows from an idea suggested by Birkhoff [9] and developed by Roshko [10, 11] and others.

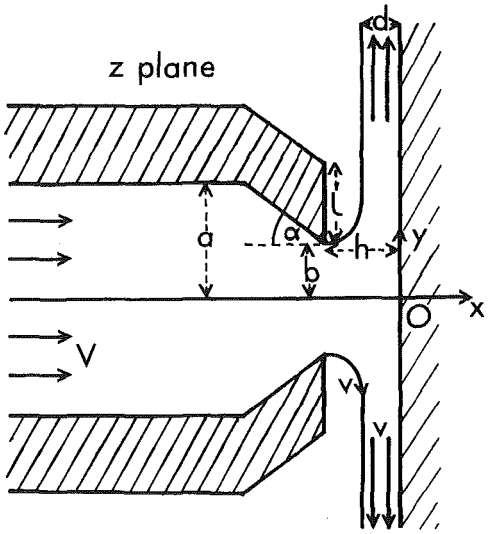

Fig. 1 Diagram and notation for a tapering valve

Important developments in potential theory have been made by Erich [12] and McNown and Hsu [13]. Other significant contributions to the theory of free streamlines are given by Whiteman [14] and in the early works of Mitchell [15] and Cissotti [16].

The behavior of the flow with increasing Reynolds' number has been the subject of much experimental work, and details of these measurements are given by Duggins [17]. A theoretical analysis of axisymmetric flat-faced valves has been given by Ishizawa [18, 19]. There is particular interest in the discharge coefficient and the force on the plate or flapper. Details of how these vary with the angle of the nozzle are given in the later sections and the figures.

Contributed by the Fluids Engineering Division for publication in the JOURNAL OF FLUIDS ENGINEERING. Manuscript received by the Fluids Engineering Division, December 3, 1981.

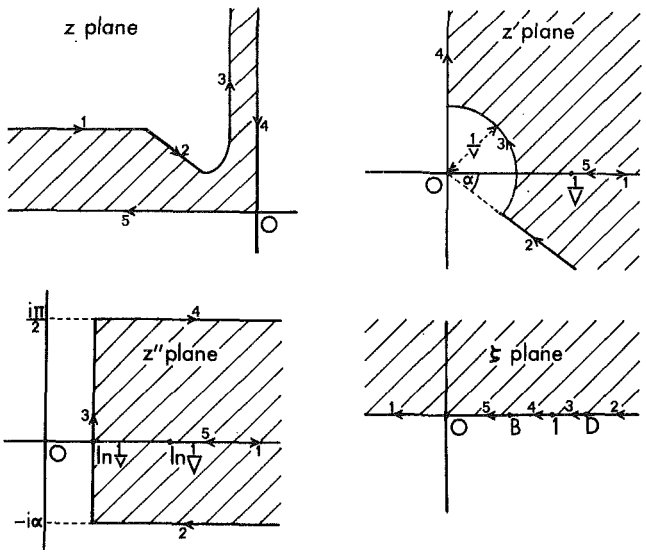

Fig. 2 Two-dimensional transformations for a tapering valve. The numbered arrows indicate the positions and directions of the edges of the transformed area.

2 Potential Flow in an Angled Orifice

Consider the ideal two-dimensional flow in a symmetric jet as shown in Fig. 1. As well as the quantities defined in this diagram the constant density of the fluid is ρ, and far upstream in the orifice ($x \to -\infty$) the pressure is P and the fluid-speed V. If v is the constant speed on the free streamline where the external pressure is Π, the total static pressure p is given by

$$p = P + \frac{1}{2}\rho V^2 = \Pi + \frac{1}{2}\rho v^2 \tag{1}$$

using Bernoulli's equation and ignoring gravitational and time-dependent effects. There is also the continuity relation

$$Va = vd \tag{2}$$

and if the limiting downstream width d can be found in terms of the flow parameters, then V and P can be easily calculated by giving values to p and Π. To do this, and to determine the other flow characteristics, the flow area of the z-plane must be transformed into the upper half of the ζ-plane.

The relevant transformations are demonstrated in Fig. 2: if ω is the complex velocity potential then

$$\frac{d\omega}{dz} = u - iv = q\exp(-i\theta') \tag{3}$$

in the usual notation, and

$$z' = \frac{dz}{d\omega} \tag{4}$$

overcomes the difficulty of the free streamline. Putting

$$z'' = \ln z' \tag{5}$$

makes all the boundaries straight lines, and the upper half plane is achieved by using a Schwartz-Christoffel transformation. The relevant form of this is given by

$$\frac{dz''}{d\zeta} = K\frac{(\zeta - A)}{(\zeta - B)(\zeta - C)^{1/2}(\zeta - D)^{1/2}} \tag{6}$$

where K is a complex constant, and $A < B < C < D$ are real numbers, two of which may be given arbitrary values. It is appropriate to take $A = 0$ and $C = 1$, and by integrating (6) the required transformation can be shown to be

$$z'' = \frac{2\alpha}{\pi}\ln(\sqrt{\zeta - 1} + \sqrt{\zeta - D}) + \ln(\sqrt{(D-B)(1-\zeta)} + \sqrt{(1-B)(D-\zeta)}) - \frac{1}{2}\ln(\zeta - B) - \frac{(2\alpha + \pi)}{2\pi}\ln(D-1) - \ln v + i(\pi - 2\alpha)/2. \tag{7}$$

Here the principal branches of the roots and logarithms are taken, and the constants B and D are related by

$$D = B + \left(\frac{2B\alpha}{\pi}\right)^2/(1-B) \tag{8}$$

and

$$\ln\frac{d}{a} = \frac{\alpha}{\pi}\ln\frac{\sqrt{D}-1}{\sqrt{D}+1} + \frac{1}{2}\ln\frac{\sqrt{D-B} - \sqrt{D(1-B)}}{\sqrt{D-B} + \sqrt{D(1-B)}}. \tag{9}$$

The relationship between z and ζ can be expressed by considering $\omega(\zeta)$ the complex velocity potential in the ζ-plane. A source at $\zeta = 0$ with a volume input $Va = vd$ into the upper

Nomenclature

A, B, C, D = real parameters of the Schwartz-Christoffel transformation
C_c = the contraction coefficient
C_d = the discharge coefficient
C_p = the pressure coefficient
$C_{p'}$ = local pressure coefficient on the flapper
K = complex parameter of the Schwartz-Christoffel transformation
P = upstream pressure
V = upstream fluid-speed
a = upstream half-width of the nozzle
b = stream half-width at the outlet of the nozzle
c = integration constant
d = downstream width
h = valve opening
l = length of the land
p = stagnation pressure
p' = local pressure on the flapper
q = fluid-speed
u = real part of the complex fluid-velocity
v = the imaginary part of the complex fluid-velocity
v = downstream fluid-speed
x = real coordinate in the z-plane
u = imaginary coordinate in the z-plane
z = complex variable representing the geometry of the two-dimensional valve
z', z'' = complex variables of intermediate stages of the transformation from the z-plane to the ζ-plane
Π = atmospheric pressure
α = inward angle of taper of the nozzle
ζ = complex variable of Schwartz-Christoffel transformation
ζ' = complex variable of final transformation for the parallel-sided valve
η = dimensionless real parameter of the ζ' transformation
θ = complex function of ζ
θ' = argument of the complex fluid-velocity
ξ = substitution used in the integration of C_c in terms of ζ
ρ = fluid density
ϕ = complex function of ζ'
χ = real parameter in the transformation for the parallel-sided orifice
ψ = real function of ξ
ω = complex velocity potential

half plane represents the oncoming jet in the z plane, and a similar sink at $\zeta=1$ represents the flow as $z\to i\infty$. Hence the form of $\omega(\zeta)$ is

$$\omega(\zeta)=\frac{Va}{\pi}\ln\frac{\zeta}{\zeta-1}. \tag{10}$$

This is used with the equations (3) – (9) in the relation

$$z=\int\frac{d\omega}{d\zeta}\frac{dz}{d\omega}d\zeta+c \tag{11}$$

to give z as a function of ζ. The integrand can be seen to be

$$-i\frac{Va}{v\pi}e^{-i\alpha}\cdot$$

$$\frac{(\sqrt{\zeta-1}+\sqrt{\zeta-D})^{2\alpha/\pi}(\sqrt{(D-B)(1-\zeta)}+\sqrt{(1-B)(D-\zeta)})}{\zeta(\zeta-1)\sqrt{\zeta-B}(D-1)^{(2\alpha+\pi)/2\pi}} \tag{12}$$

where principal values are taken, and c is a complex constant of integration which depends on the path of integration.

The form of the free streamline and the relationship between z and ζ on the imaginary z-axis can be found from (11) and (12). (The latter is needed to find the pressure distribution on the flapper.) The free streamline corresponds to $1\le\zeta\le D$ and its shape is given by

$$z=-\frac{d}{\pi}ie^{-i\alpha}\int_D^\zeta\frac{e^{i\theta}}{\zeta(\zeta-1)}d\zeta-h+ib \tag{13}$$

where

$$\theta=\frac{\alpha}{\pi}\cos^{-1}\frac{2\zeta-D-1}{D-1}$$

$$-\frac{1}{2}\cos^{-1}\frac{2(D-B)(1-B)-(D+1-2B)(\zeta-B)}{(\zeta-B)(D-1)} \tag{14}$$

and on the imaginary z-axis $B\le\zeta\le1$ so that

$$z=i\frac{d}{\pi}\int_B^\zeta$$

$$\frac{(\sqrt{1-\zeta}+\sqrt{D-\zeta})^{2\alpha/\pi}(\sqrt{(D-B)(1-\zeta)}+\sqrt{(1-B)(D-\zeta)})}{\zeta(1-\zeta)\sqrt{\zeta-B}(D-1)^{(2\alpha+\pi)/2\pi}}d\zeta \tag{15}$$

The limiting form of (13) gives

$$\frac{d}{a}=\frac{h}{a}+\frac{d}{\pi a}\int_1^D\frac{\sin(\theta-\alpha)}{\zeta(\zeta-1)}d\zeta \tag{16}$$

which with (8) and (9) form a set of nested implicit equations for d/a, D and B in terms of h/a and α.

The theory for a parallel-sided orifice is well-known [4, 5, 7]. It might be expected that allowing $\alpha\to0$ in the preceding would give the appropriate results. However a careful appraisal of the mappings will show that this is not the case. A limiting form of the Schwartz-Christoffel transformation has to be used and this limiting process is not interchangeable with $\alpha\to0$. More precisely, the point at infinity below the real axis of the z'' and z' planes cannot be removed by allowing $\alpha\to0$.

In a consistent notation with the preceding, the shape of the free streamline when $\alpha=0$ is given by

$$z=\frac{d}{\pi}\int_{\zeta'}^{2/v^2}\left(\frac{v^4V^2}{v^4V^2\zeta'-v^4-V^4}-\frac{v^2}{v^2\zeta'+2}\right)e^{i\phi/2}d\zeta'-h+ia \tag{17}$$

where

$$\phi=\cos^{-1}\zeta'v^2/2 \tag{18}$$

and $-2\le\zeta'v^2\le2$, so that the coordinates are

$$x=-\frac{d(v^2+V^2)}{2\pi vV}\ln\left[\frac{(v-V)^2(v^2+V^2+vV\sqrt{\zeta'v^2+2})}{(v+V)^2(v^2+V^2-vV\sqrt{\zeta'v^2+2})}\right]-h \tag{19}$$

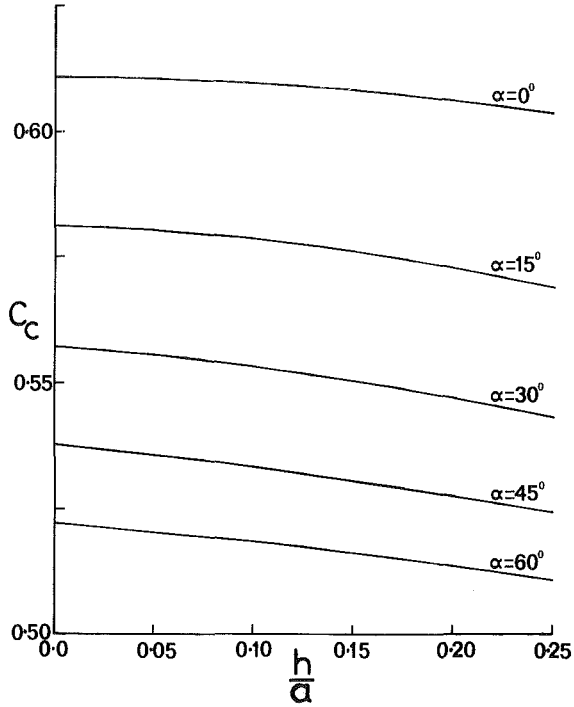

Fig. 3 Variation of C_c with h/a when $\alpha=0$, 15, 30, 45, and 60 deg

$$y=\frac{d}{\pi}\left[\ln\left(\frac{2+\sqrt{2-\zeta'v^2}}{2-\sqrt{2-\zeta'v^2}}\right)\right.$$

$$\left.-\frac{v^2-V^2}{2vV}\tan^{-1}\left(\frac{vV\sqrt{2-\zeta'v^2}}{v^2-V^2}\right)\right]+a \tag{20}$$

The form of d is given by (19) with $\zeta'v^2=-2$, namely

$$h/a=d/a+\frac{1+(d/a)^2}{\pi}\ln\left(\frac{1+d/a}{1-d/a}\right) \tag{21}$$

Also when $\alpha=0$, the imaginary z-axis (the flapper) is given by

$$z=\frac{2id}{\pi}\left[\ln\left(\frac{\chi+1}{\chi-1}\right)+\frac{d}{a}\left(\frac{\pi}{2}-\tan^{-1}\frac{a\chi}{d}\right)\right.$$

$$\left.+\frac{a}{d}\left(\frac{\pi}{2}-\tan^{-1}\frac{d\chi}{a}\right)\right] \tag{22}$$

where

$$\chi=\sqrt{-\frac{\zeta'v^2}{2}-\sqrt{\frac{\zeta'^2v^4}{4}-1}} \tag{23}$$

and $$-\infty<\zeta'v^2\le-2.$$

3 Numerical Calculation of the Contraction and Pressure Coefficients

The variation of the downstream width d with the other flow variables is of primary interest. A dimensionless version of this variable is the contraction coefficient defined by

$$C_d=d/h=(d/a)/(h/a) \tag{24}$$

and consideration of equations (8), (9), (14), (16) and (21) will show that this only depends on the geometric variables α and the dimensionless valve opening h/a. As a perfect flow has been assumed C_c does not depend on the pressure drop across the valve, moreover it is equal to the discharge coefficient C_D which appears frequently in the literature. Energy losses in a real flow will make the downstream width greater than d. In

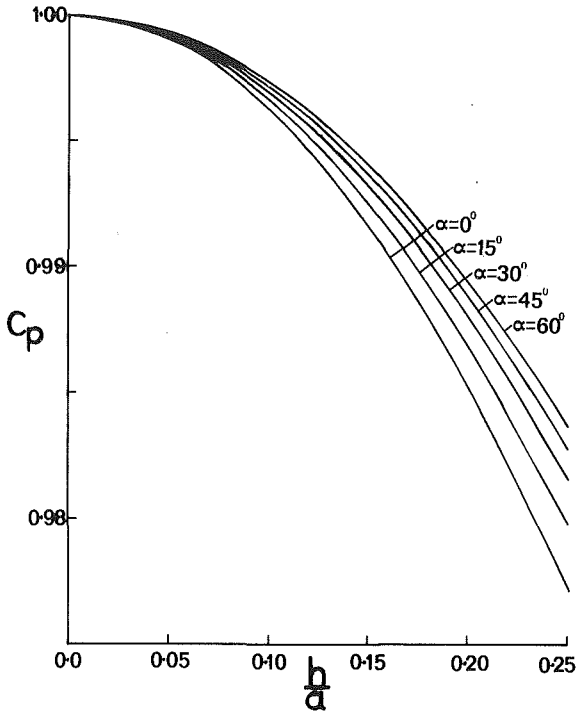

Fig. 4 Variation of C_p with h/a when $\alpha = 0$, 15, 30, 45, and 60 deg

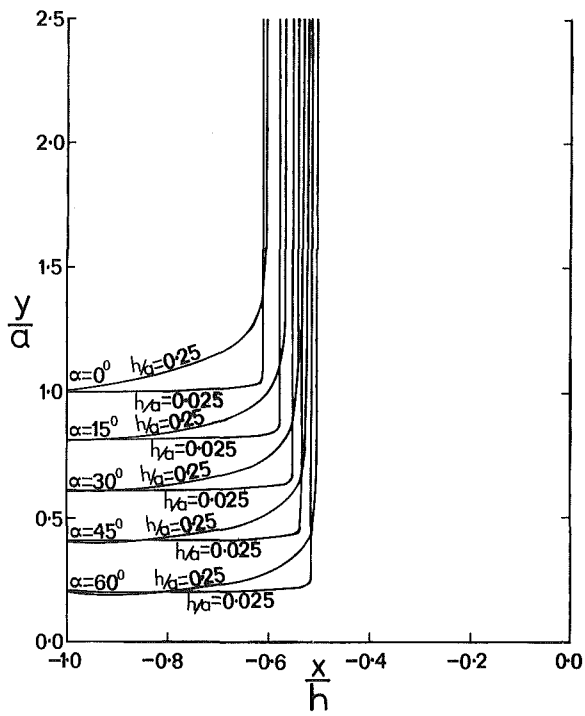

Fig. 5 Shapes of the free streamlines with $h/a = 0.025$ and 0.250 for $\alpha = 0$, 15, 30, 45, and 60 deg

general d/h is a function of Reynolds' number and other dimensionless flow variables.

To find d/a and hence C_c as a function of α and h/a the equations (8), (9), (14) and (16) have to be solved simultaneously. The transformation parameter D is given explicitly in terms of B and α by equation (8), so that (9) and (16) are a pair of nested implicit equations for d/a and the parameter B.

The integral in (16) is difficult to evaluate numerically because $D \searrow 1$ as $h \to 0$ and the range of integration tends to zero. To overcome this difficulty the transformation

$$\xi = \frac{2\zeta - D - 1}{D - 1} \tag{25}$$

enables the integral to be written

$$\int_{-1}^{1} \frac{2\sin(\psi - \alpha)}{(\xi + 1)[\xi(D-1) + D + 1]}\, d\xi \tag{26}$$

where

$$\psi = \frac{\alpha}{\pi}\cos^{-1}\xi - \frac{1}{2}\cos^{-1}\left[\frac{-\xi(D+1-2B) - D + 1}{\xi(D-1) + D + 1 - 2B}\right] \tag{27}$$

and the integral can now be evaluated by Gaussian quadrature.

A secant method was used for the implicit equations with the iteration for B nested in the iteration for d/a. The results of these numerical processes are given in Fig. 3 where C_c is plotted against h/a for $\alpha = 15$, 30, 45, and 60 deg. As the aperture is considerably smaller than the nozzle diameter in operating valves, the range chosen for h/a is $0 \le h/a \le 1/4$. (When $h/a > 1/2$ in three-dimensional valves, the area of the aperture is greater than the flow area upstream. At these openings there is a loss of sensitivity to the aperture setting and the valve characteristics will depend on the flow pattern in the nozzle.)

As $h \to 0$, $D \searrow 1$ and it can be deduced that $B \to 1/(1 + 2\alpha/\pi)$ so that the limiting values of the contraction coefficient are given by

$$C_c = 1\Big/\left[1 + \frac{1}{\pi}\int_{-1}^{1} \frac{\cos\left[\left(\frac{\alpha}{\pi} + \frac{1}{2}\right)\cos^{-1}\xi - \alpha\right]}{\xi + 1}\, d\xi\right] \tag{28}$$

and the numerical values of this are given by the intercepts on the C_c axis of Fig. 3.

The values of C_c for $\alpha = 0$ are also given for comparison in Fig. 3. From (21) the variation of C_c with h/a is given by the implicit equation

$$(1 - C_c)h/a = (1 + C_c h/a)\ln\left[\frac{1 + C_c h/a}{1 - C_c h/a}\right] \tag{29}$$

which was again solved by a secant technique. The intercept of this curve on the C_c axis is found by allowing $h \to 0$ which gives

$$C_c = \frac{\pi}{2 + \pi} - = 0.6110. \tag{30}$$

A check of the form of C_c for $\alpha > 0$ can be made by showing that the limiting values of C_c given by (28) correspond to the above form. Putting $\alpha = 0$ in (28) gives

$$C_c = 1\Big/\left[1 + \frac{1}{\pi}\int_{-1}^{1} \frac{d\xi}{\sqrt{2(\xi + 1)}}\right] = \frac{\pi}{2 + \pi} \tag{31}$$

as required. The results for nonzero α have also been checked numerically by showing that the curves of C_c against h/a approach the curve for $\alpha = 0$ as α gets smaller.

The curve of C_c against h/a for a parallel-sided orifice has also been obtained by Lichtarowicz and Markland [8]. This is given in their Fig. 3, and corresponds to $k = 1$ in their notation. Their k is a measure of the proportional increase in the discharge velocity v along the free streamline. It is worth noting that increasing α and increasing their k have opposite effects, so that experimental results with a tapered orifice may be close to the theoretical values of a straight orifice due to error cancellation.

Clearly C_c decreases as α increases, and it can also be seen that d is nearly proportional to h for operating values of h

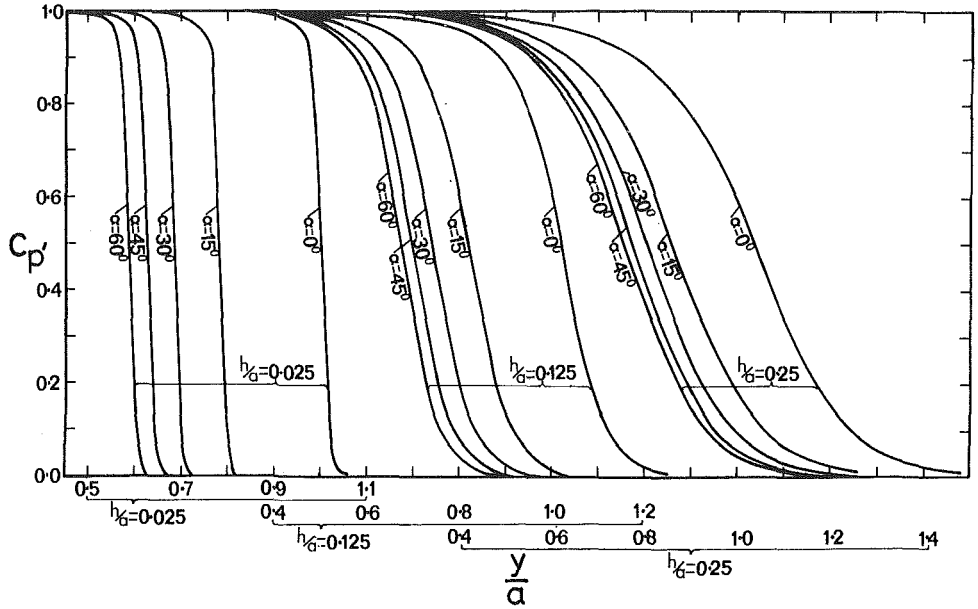

Fig. 6 Variation of $C_{p'}$ with y/a when $h/a = 0.025$, 0.125, and 0.25 for $\alpha = 0$, 15, 30, 45, and 60 deg

(this becoming less true as α increases). An implication of this is that the pressure coefficient

$$C_p = \frac{P-\Pi}{\frac{1}{2}\rho v^2} = 1-(d/a)^2 \tag{32}$$

is roughly parabolic in h/a as can be seen in Fig. 4. This relationship between C_p and h/a gives the sensitivity of the pressure control to the value opening. These results imply that as α increases a given change in the value aperture gives a progressively smaller change in back pressure. More will be said about this in Section 5.

4 The Free Streamlines and the Pressure Distribution on the Flapper

The shapes of the free streamlines are given by using the previously calculated values of d/a in (13), (14), (19) and (20), and are shown in Fig. 5. The values of h/a have been chosen to be 0.025 and 0.25; only two values are illustrated to avoid making the diagram too confused. As a perfect flow has been assumed, the shape does not depend on the pressure drop $p-\Pi$ or the orifice diameter b, but only on the aperture h and the taper α. In the figure the values of b are chosen to be evenly spaced for the sake of clarity. When h is small, the change in direction of the flow is very abrupt, but as the aperture widens the curvature of the free streamline at the elbow decreases.

The pressure distribution along the flapper is shown in Fig. 6 where the local pressure coefficient

$$C_{p'} = \frac{p'-\Pi}{\frac{1}{2}\rho v^2} = 1-(q/v)^2 \tag{33}$$

is drawn against y/a. Here p' is the pressure at the point iy where the fluid speed is q. For $\alpha>0$, $C_{p'}$ and y/a are both expressed parametrically in terms of ξ. The form of y/a is given by (15) and this was evaluated using Gaussian quadrature. Using (3) – (9) it can be seen that

$$C_{p'} = \frac{(D-1)^{(2\alpha+\pi)/\pi}(\zeta-B)}{[\sqrt{(D-B)(1-\zeta)}+\sqrt{(1-B)(D-\zeta)}]^2[\sqrt{1-\zeta}+\sqrt{D-\zeta}]^{4\alpha/\pi}} \tag{34}$$

where $B \le \zeta \le 1$.

The shape of $C_{p'}$ when $\alpha=0$ is required for completeness. The form of y/a is given by (22) and (23); also if $\eta=\zeta' v^2$ where ζ' is the transformation variable for the parallel sided orifice, it can be deduced that

$$C_{p'} = 1+\frac{1}{2}(\eta+\sqrt{\eta^2-4}) \tag{35}$$

where $-\infty<\eta\le -2$. The variation of this form of $C_{p'}$ with y/a is also given in Fig. 6 where the values given to h/a are 0.025, 0.125, and 0.25. This curve has previously been obtained by Lichtarowicz and Markland [8], but they take $h/a = 0.1$ and 1.0.

5 Conclusions

The curves of Fig. 4 indicate that the sensitivity of the pressure control decreases with increasing α. Changes in the valve opening h/a give progressively smaller changes in back pressure as α increases. This loss of control implies that fluctuations in the flow which inevitably occur in practice have a greater effect in tapered orifices than in untapered ones. In a perfect flow the relationships between P, h, and d lie on the curves of Figs. 3 and 4. Consequently a fluctuation in back pressure is equivalent to a change in valve aperture, which promotes a variation in downstream width. It can be seen that the amplitude of the variation in d increases rapidly with α. For example, a comparison of valves running at a pressure corresponding to $C_p = 0.985$ shows that a pressure fluctuating gives rise to a variation in d nearly twice as big for $\alpha=60$ deg as for $\alpha=0$ deg. Hence the likelihood of reattachment of the free streamline to the land increases with the angle of taper. In a real fluid the speed in the elbow of the flow also increases with α, and there is a risk of transition from laminar flow. The combined effect is to make flow in a tapered orifice more unstable than in a parallel-sided one, reattachment is more likely to occur with the associated change in the flow characteristics.

The very rapid acceleration of the fluid at the elbow is illustrated by the rapid spatial change of the local pressure coefficient $C_{p'}$ shown in Fig. 6. At small valve openings the transition from the stagnation pressure p to the downstream pressure Π is very sharp, but this becomes more gradual as the aperture increases and the pressure force is spread over a

greater area of the flapper. This is in accordance with the early observations of Schrenk [20]. These characteristics are also implied by the forms of the free-streamlines given in Fig. 5. The position of the transition does not depend on the orifice diameter b, since a perfect flow has been assumed $C_{p'}$ is a function of α and h/a only. As the angle of the taper increases from zero, there is at first a considerable shift in the position of the transition, as α increases further, however, this effect diminishes rapidly, e.g., there is little difference between the curves for $\alpha = 45$ and 60 deg.

The ideal orifice seems to be one which interrupts the flow of a jet on to a flat plate as little as possible; abrupt changes in the direction of the flow with their associated rapid accelerations and risk of transition should be avoided. There seems to be a good case for the experimental investigation of trumpet-shaped valves, as these orifices should give more stable characteristics than ones with parallel sides or an inward taper. The use of valves with an outward taper is a poor alternative to bell-shaped nozzles, as this arrangement has several inherent faults. It must be noted that giving α negative values in the present work does not represent a potential flow model for such a chamfered orifice, as separation would take place at the inner corner. There might or might not be reattachment on the sloping edge of the nozzle giving the possibility of more than one separation zone. The manufacture of these valves with chamfered edges has been criticized by Lichtarowicz [1] because of manufacturing difficulties and the possibility of dirt-blockage due to the smaller operating apertures.

Acknowledgment

Dr. K. F. Martin of the Department of Mechanical Engineering and Engineering Production at UWIST suggested this problem to the author, and has given encouragement and advice during the research.

References

1 Lichtarowicz, A., "Flow and Force Characteristics of Flapper Valves", Third International Fluid Power Symposium, Turin, 1973.

2 Hayashi, S., Matsui, T., and Ito, T., "Study of Flow and Thrust in Nozzle-Flapper Valves", ASME JOURNAL OF FLUIDS ENGINEERING, Vol. 97, 1975, pp. 39-50.

3 Duggins, R. K., "A Potential Flow Model for a Closed Separation Region", Thermodynamics and Fluid Mechanics Convention, Bristol, 1968.

4 Milne-Thomson, L. M., *Theoretical Hydrodynamics*, 5th ed., Macmillan, 1974, p. 349.

5 Robertson, J. M., *Hydrodynamics in Theory and Application*, Prentice Hall, 1965.

6 Birkhoff, G., and Zarantonello, E. H., *Jets, Wakes and Cavities*, Academic Press Inc., New York, 1957.

7 Gurevitch, M. I., *The Theory of Jets in an Ideal Fluid*, Academic Press, New York, 1965.

8 Lichtarowicz, A., and Markland, E., "Calculations of Potential Flow with Separation in a Right-Angled Elbow with Unequal Branches", *J. of Fluid Mechanics*, Vol. 17, Part 4, 1963, pp. 596-606.

9 Birkhoff, G., *Hydrodynamics*, Dover, New York, 1950.

10 Roshko, A., "A New Hodograph for Free-Streamline Theory", N.A.C.A. Tech. Note No. 3168, 1953.

11 Roshko, A., "On the Drag and Shedding Frequency of Two-Dimensional Bluff Bodies", N.A.C.A. Tech. Note No. 3169, 1953.

12 Ehrich, F. F., "The Hydrodynamics of Flow Regulation", DSc. thesis, Massachusetts Institute of Technology, 1951.

13 McNown, J. S., and Hsu, E., "Application of Conformal Mapping to Divided Flow", *Proc. of the Mid-Western Conference on Fluid Dynamics*, State University of Iowa, Reprint No. 96, 1951, p. 143.

14 Whiteman, K. J., "Free Streamline Theory and its Application to Flow Through Orifices", British Hydromechanics Research Association, Technical Note 539, 1956.

15 Mitchell, J. N., "On the Theory of Free Streamlines", *Phil. Trans. Royal Society*, London, Vol. A181, 1890, p. 389.

16 Cissotti, U., *I Dromeccanica Piana*, Vols. I and II, C. Tamburini, Milano, 1921 and 1922.

17 Duggins, R. K., "Further Studies of Flow in a Flapper Valve", Third International Fluid Power Symposium, Turin, 1973.

18 Ishizawa, S., "The Axi-symmetric Laminar Flow in an Arbitrarily Shaped Narrow Gap (1st Report, Theoretical Analysis for the Inlet Region)", *Bulletin of JSME*, Vol. 8, No. 31, 1965.

19 Ishizawa, S., "The Axi-symmetric Laminar Flow in an Arbitrarily Shaped Narrow Gap (2nd Report, Theoretical Analysis for the Downstream Region)", *Bulletin of JSME*, Vol. 9, No. 33, 1966.

20 Schrenk, E., "Disc Valves, Flow Patterns, Resistance and Loading", *Forschungsarbeiten auf dem Ingen.*, 272, 1957, BHRA T.547, 1925.

A Re-Evaluation of Schlichting's Surface Roughness Experiment

H. W. Coleman

B. K. Hodge

R. P. Taylor

Mechanical and Nuclear Engineering Department,
Mississippi State University,
Mississippi State, Miss. 39762

A re-evaluation of the skin friction coefficient and equivalent sand roughness data reported by Schlichting in 1936 on fourteen rough surfaces is presented. Several assumptions made during the original data reduction are shown to have significant effects on the final results. Additional data and analytical results published since 1936 allow the use of more precise assumptions and enable a re-evaluation of the original data. Corrected results are presented for seventy-nine runs reported by Schlichting on the fourteen surfaces containing spherical, spherical segment and conical roughness elements with various spacings. The original skin friction coefficients are shown to be higher than the corrected values by amounts ranging from 0.5 to 73 percent, while the original equivalent sand roughness values are higher than the corrected ones by 26 to 555 percent. Roughness Reynolds numbers determined using the corrected data indicate that sixteen of the runs on three surfaces were probably in the transitionally rough regime, not the fully rough regime as originally reported.

Introduction

To analytically determine the skin friction in a turbulent flow over a rough surface, experimental results must be used as an input at some stage of the procedure. While the classic sandgrain-roughened pipe flow experiment of Nikuradse [1] is the most well-known experimental effort, the results and analyses reported by Schlichting [2] have probably been the ones most widely used by later workers in the area. Schlichting determined the skin friction for a number of surfaces which were roughened with elements of various shapes, sizes and spacings. He also proposed the concept of "equivalent sand roughness", k_s, which is the size of sand grain in Nikuradse's experiment which would give the same resistance as the particular roughness being investigated, and determined the value of k_s for each of the surfaces in his experiment.

One of the primary approaches later workers have taken in attempts to calculate the skin friction (and heat transfer) in turbulent flows influenced by roughness is to formulate the turbulence models they use as a function of k_s. Some recent examples are Healzer [3], Cebeci and Chang [4], Ligrani [5], Lin and Bywater [6], and Christoph [7]. This approach, of course, requires some means of determining k_s for a particular surface, and various correlations of k_s as a function of the characteristics of a rough surface have been proposed (Dvorak [8], Dirling [9], Simpson [10], and Denman [11]). All of these correlations rely heavily on the Schlichting [2] results, since that experiment is still the most comprehensive in terms of the number of roughness element shape and spacing variations investigated.

Another approach to the problem of modeling roughness effects on turbulent flow is the discrete element method, in which the form drag and other influences of the roughness elements are taken into account in the governing equations. Some investigators have used this method coupled with k_s influences on the turbulence model (Adams and Hodge [12], Lin and Bywater [6], and Christoph [13]). Others (Finson and Wu [14] and Finson [15]) have used the discrete element approach in a manner so that there is no dependence on the equivalent sand roughness concept. The Schlichting skin friction results were used as the basic calibration data for a discrete element model by Finson and are being used by the present authors in a similar manner.

In the course of working with the Schlichting data, the present authors were led to question several of the assumptions used by Schlichting in his data reduction. This is not to say that Schlichting made errors in his analysis in 1936—that this work has been so widely used by so many researchers in the past forty-plus years argues for the basic soundness and importance of the work. Rather, additional data and analytical results published since 1936 now allow the use of more precise assumptions and enable a re-evaluation of the original data. The present availability of the digital computer also facilitates the analysis of large data sets and allows more options to be considered than were reasonable with hand calculations.

In this article, the authors present results of the re-evaluation of Schlichting's original data for the surfaces roughened with spheres, spherical segments and cones. It is shown that the original skin friction coefficients are higher than the corrected values by amounts ranging from 0.5 to 73 percent. Although the k_s concept is not used in the discrete element approach, the equivalent sand roughness values were re-evaluated for the same set of surfaces. These values are also presented, and it is shown that the original values are higher than the corrected values by amounts ranging from 26 to 555 percent.

Schlichting's Experiment

The experiment utilized a water tunnel with a test section of

Contributed by the Fluids Engineering Division for publication in the JOURNAL OF FLUIDS ENGINEERING. Manuscript received by the Fluids Engineering Division, June 13, 1983.

40 mm height and 170 mm width. A 3.2 m long section with four smooth walls preceded the 3.2 m long section in which the upper wall was rough and the side and lower walls were smooth. Fully developed channel flow thus existed in the section containing the rough wall. The 14 rough walls with spherical, spherical segment and conical roughness elements were those of interest in this analysis. The geometry and nomenclature for the channel and roughness elements are shown in Fig. 1, and the values of the parameters for the rough surfaces are given in Table 1.

The effective wall location for a rough wall was defined by Schlichting as the location of a "smooth wall that replaces the rough wall in such a manner as to keep the fluid volume the same." Thus, if V is the volume of all the roughness elements on a surface of dimensions L by W, then $\Delta y = V/LW$ is the distance of the effective wall location from the smooth wall on which the roughness elements occur. This is illustrated in Fig. 2. The mean channel height, b, was then taken to be the original distance between smooth upper and lower walls (40 mm) minus Δy.

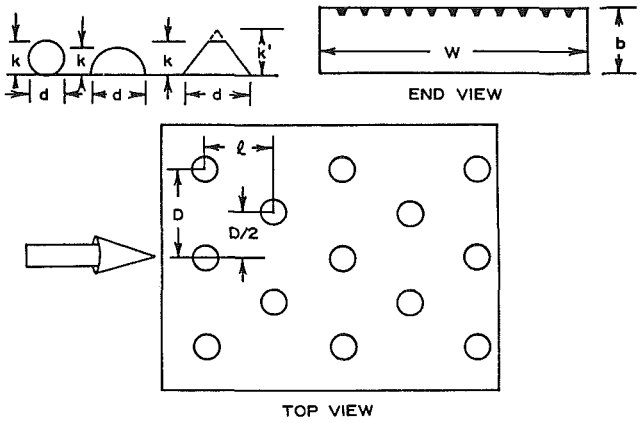

Fig. 1 Nomenclature for Schlichting's experiment

For each of the rough surfaces used, either 5 or 6 different Reynolds number runs were made. Data taken were the pressure drop in the rough wall test section and the velocity profile at the outlet plane of the rough wall test section. A pitot probe was used for the velocity measurements. The flow rate was not reported, so the reported maximum velocity, u_{max}, is used as the reference velocity in the Reynolds number and skin friction coefficient definitions:

$$\mathrm{Re} = u_{max} b/\nu \tag{1}$$

$$C_f = 2\tau/\rho u^2_{max} = 2u^{*2}/u^2_{max} \tag{2}$$

where τ is the wall shear stress and u^* is the friction velocity.

Actually, for the rough wall τ is considered to be the force on the wall in the mean flow direction divided by the plan area of the wall, since the force on the wall consists of shear and form drag components. In the following, the words "wall shear stress" are used in this sense when referring to values for the rough walls.

Schlichting's Evaluation of C_f

Schlichting determined the skin friction on the rough walls

Table 1

Plate No.	d (cm)	D (cm)	l (cm)	k (cm)	k' (cm)	b (cm)	Schl. k_s/k	Corr. k_s/k
				Spheres				
XII	0.41	4	4	0.41	--	3.99	0.277	0.120
III	0.41	2	2	0.41	--	3.99	0.838	0.410
I	0.41	1	1	0.41	--	3.96	3.07	2.43
II	0.41	0.6	0.6	0.41	--	3.88	3.81	2.59
V	0.41	0.41	0.36	0.41	--	3.68	0.626	0.378
VI	0.21	1	1	0.21	--	3.99	0.819	0.430
IV	0.21	0.5	0.5	0.21	--	3.97	3.61	2.47
				Spherical segments				
XIII	0.8	4	4	0.26	--	3.99	0.118	0.018
XIV	0.8	3	3	0.26	--	3.99	0.186	0.034
XV	0.8	2	2	0.26	--	3.98	0.571	0.278
XIX	0.8	0.8	0.69	0.26	--	3.85	1.40	0.953
				Cones				
XXIII	0.8	4	4	0.375	0.425	3.99	0.159	0.046
XXIV	0.8	3	3	0.375	0.425	3.98	0.437	0.122
XXV	0.8	2	2	0.375	0.425	3.95	0.996	0.471

Nomenclature

b = channel height (Fig. 1)
C_f = skin friction coefficient defined by (2)
d = roughness element base diameter (Fig. 1)
D = transverse element spacing (Fig. 1)
k = roughness element height (Fig. 1)
k_s = equivalent sand roughness
l = stream wise element spacing (Fig. 1)
n = velocity profile slope in log region
dP/dx = pressure drop
Re = Reynolds number
r = radius
u = mean velocity
u^+ = u/u^*
u^* = friction velocity = $\sqrt{\tau/\rho}$
W = channel width (Fig. 1)
y = distance from effective wall (Fig. 2)
y' = distance from the wall (Fig. 2)
z = distance from effective wall (Fig. 2)
z' = distance from wall (Fig. 2)
z_0 = parameter defined by (18)
Δy = location of effective wall (Fig. 2)
Δz = location of effective wall (Fig. 2)
ν = kinematic viscosity
ρ = fluid density
τ = wall shear stress

Subscripts

av = average values
c = corrected values
max = maximum values
meas = measured values
r = rough wall values
s = smooth wall values
1 = values determined from pressure drop measurements
2 = values determined from velocity profile measurements

by two different methods, then reported the average of these values, $C_{f,av}$, as *the* value of skin friction. The first method he used (subscript 1) was based on the pressure drop measurements, while the second method (subscript 2) was based on the measured velocity profiles and a rough surface "law of the wall."

For the first method, an application of the basic momentum theorem to the fully developed flow in the channel yields the equation Schlichting used

$$\tau_{r1} + \tau_s = b|dP/dx| \tag{3}$$

if one assumes the shear stresses on the smooth side walls are negligible. Here, the subscripts r and s refer to the rough and smooth walls, respectively. This can be recast, using the definition of friction velocity, as

$$u^{*2}_{r1} + u^{*2}_{s} = \frac{b}{\rho}\left|\frac{dP}{dx}\right| \tag{4}$$

The smooth wall friction velocity was determined by plotting the measured velocity profile on the smooth wall in u versus log y coordinates, determining the slope n_s graphically, and by comparison with the smooth wall "log law"

$$u/u^*_s = 5.5 + 5.75 \log (yu^*_s/\nu) \tag{5}$$

finding

$$u^*_s = n_s/5.75 \tag{6}$$

This determination, together with the measured pressure drop data, allowed calculation of u^*_{r1} using equation (4). These values are presented in Table 2 in the dimensionless form C_{f1} for the seventy-nine runs made with the rough surfaces of interest in this study.

For the second method, Schlichting used a rough wall "log law"

$$u/u^*_{r2} = 5.75 \log (y/k) + A \tag{7}$$

where y is measured from the effective wall location as described previously and k is roughness height. For Nikuradse's fully rough sand roughness cases, $A = 8.48$ and $k = k_s$, the sand grain size. From the velocity profile measurements on each rough wall, Schlichting knew u versus y' (see Fig. 2). By plotting u versus log $(y' - \Delta y)$, determining the slope n_r graphically, and comparing with equation (7), he was able to calculate

$$u^*_{r2} = n_r/5.75 \tag{8}$$

These values are presented in Table 2 in the dimensionless form C_{f2}.

Also shown in Table 2 are the averages of C_{f1} and C_{f2}, labeled $C_{f,av}$, which were the values reported by Schlichting.

Re-Evaluation of C_f

As described in the previous section, Schlichting determined his C_{f1} values by neglecting the shear on the two smooth side walls. If the side wall shear is included, application of the basic momentum theorem yields

$$\tau_r = b\left|\frac{dP}{dx}\right| - \left(\frac{W+2b}{W}\right)\tau_{s,av} \tag{9}$$

Table 2

Plate No. (l/k)	Re (x10^{-3})	u_{max} (cm/s)	Schlichting C_{f1} (x10^3)	Schlichting C_{f2} (x10^3)	Schlichting $C_{f,av}$ (x10^3)	Corrected C_{fc} (x10^3)	Corrected Re_{k_s}	Corrected Δz (cm)
				Spheres				
XII	110	321	7.60	7.01	7.31	6.29	75	0.12
(9.75)	124	385	7.44	7.21	7.33	6.24	91	0.12
	162	476	7.52	7.13	7.32	6.46	114	0.12
	190	547	7.33	7.31	7.32	6.26	130	0.12
	224	650	6.86	7.85	7.35	5.69	148	0.12
III	107	316	10.22	11.94	11.06	8.66	299	0.12
(4.88)	138	391	10.48	11.70	11.08	9.18	394	0.12
	174	500	10.06	12.13	11.07	8.70	486	0.21
	204	568	10.28	11.83	11.04	9.01	572	0.21
	251	704	10.17	11.94	11.04	8.95	700	0.21
	290	816	10.19	11.76	10.96	8.99	806	0.21
I	107	310	19.34	17.16	18.23	18.13	2556	--
(2.44)	132	384	18.95	17.40	18.17	17.87	3118	0.08
	166	508	17.77	18.70	18.23	16.42	3819	--
	195	566	17.48	18.94	18.20	16.11	4360	0.16
	224	658	17.69	18.75	18.22	16.42	5127	0.16
	263	778	17.60	18.79	18.19	16.37	5944	0.16
II	104	313	16.76	23.80	20.13	15.46	2562	0.41
(1.46)	129	384	17.86	22.92	20.31	16.73	3243	--
	166	500	18.34	22.07	20.16	17.23	4248	--
	186	586	18.36	22.01	20.14	17.17	4774	0.37
	224	646	18.70	21.86	20.25	17.57	5691	0.41
	257	746	19.04	21.43	20.22	18.00	6708	--
V	98	311	9.62	10.77	10.19	8.08	264	--
(0.87)	123	385	9.87	10.54	10.20	8.44	337	--
	162	498	9.81	10.64	10.22	8.37	438	--
	190	585	9.95	10.48	10.21	8.52	525	--
	214	662	9.94	10.49	10.21	8.56	589	0.41
	263	809	10.17	10.25	10.21	8.86	739	0.37
VI	110	316	8.44	8.90	8.67	7.12	147	0.11
(4.86)	135	390	8.20	9.18	8.68	6.82	177	--
	170	491	8.70	8.72	8.71	7.55	234	--
	200	566	8.71	8.66	8.69	7.61	276	--
	234	664	8.39	9.02	8.70	7.21	315	0.11
	275	806	8.47	8.96	8.71	7.32	373	--
IV	107	325	14.69	14.37	14.53	13.50	1154	--
(2.43)	129	396	13.44	15.74	14.57	12.02	1316	--
	186	572	13.96	15.16	14.56	12.90	1953	--
	204	646	13.68	15.45	14.55	12.59	2126	--
	245	751	13.62	15.55	14.57	12.53	2548	0.13

Table 2 (continued)

Plate No. (l/k)	Re (x10^{-3})	u_{max} (cm/s)	Schlichting C_{f1} (x10^3)	Schlichting C_{f2} (x10^3)	Schlichting $C_{f,av}$ (x10^3)	Corrected C_{fc} (x10^3)	Corrected Re_{k_s}	Corrected Δz (cm)
				Spherical segments				
XIII	115	314	5.77	5.15	5.46	4.32	6	--
(15.4)	141	389	5.15	5.76	5.45	3.72	7	0.16
	178	495	5.56	5.40	5.48	4.37	10	--
	204	574	5.54	5.39	5.46	4.40	11	--
	229	648	4.99	5.91	5.44	3.70	12	0.16
	302	830	4.69	6.25	5.44	3.33	14	0.16
XIV	135	380	5.61	6.50	6.05	4.12	14	--
(11.5)	174	497	5.85	6.22	6.03	4.57	18	0.23
	195	572	6.05	6.08	6.07	4.87	22	--
	245	700	5.10	7.08	6.05	3.68	23	--
	295	834	4.94	7.29	6.06	3.50	27	0.23
XV	135	382	8.43	8.70	8.57	7.16	146	--
(7.69)	170	502	8.54	8.53	8.54	7.42	187	0.18
	190	564	8.25	8.88	8.56	7.04	205	--
	234	687	7.83	9.37	8.58	6.51	242	--
	288	817	8.02	9.08	8.54	6.79	302	0.13
XIX	107	316	11.29	11.40	11.35	9.93	484	--
(2.65)	132	386	11.13	11.76	11.45	9.75	590	--
	158	480	11.49	11.26	11.38	10.27	734	--
	186	563	10.60	12.23	11.40	9.08	803	--
	224	671	11.44	11.31	11.37	10.21	1033	0.26
	282	818	11.46	11.37	11.42	10.25	1296	--
				Cones				
XXIII	117	321	6.04	6.83	6.43	4.67	24	--
(10.7)	141	386	6.16	6.72	6.44	4.89	30	--
	178	488	5.98	6.93	6.44	4.69	37	0.30
	214	574	6.09	6.83	6.45	4.84	45	--
	251	668	6.28	6.67	6.47	5.12	55	0.30
XXIV	112	307	8.60	8.54	8.57	7.31	79	--
(8.00)	141	384	8.12	9.12	8.61	6.88	95	--
	186	495	7.94	9.33	8.62	6.77	123	--
	209	567	7.61	9.67	8.61	6.39	136	--
	251	662	7.41	9.87	8.60	6.19	159	0.38
	324	890	7.50	9.79	8.61	6.38	211	0.38
XXV	115	310	11.37	11.42	11.40	10.32	375	--
(5.33)	145	388	10.22	12.50	11.33	8.93	428	--
	178	476	10.20	12.62	11.38	8.91	530	--
	209	564	10.54	12.20	11.39	9.38	638	--
	251	668	10.51	12.29	11.39	9.34	761	0.30
	295	787	10.55	12.19	11.36	9.42	909	0.34

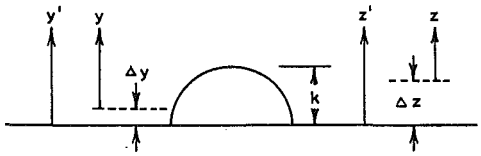

Fig. 2 Rough wall coordinate system definitions

where $\tau_{s,av}$ is the average shear stress on the three smooth walls. The value of smooth wall shear was determined as described previously from a smooth bottom wall velocity profile measured in a plane parallel to and midway between the side walls.

Examination of the data of Leutheusser [16] for the shear distribution around the walls of a smooth channel of aspect ratio 3:1 for turbulent fully developed flow shows that the wall shear stress in the center plane is larger than the average shear stress over the channel perimeter by 10 to 20 percent, depending on Reynolds number. The present authors have used the following relationship between the average shear stress and $\tau_{s,meas}$, the smooth wall value at the centerplane determined by Schlichting:

$$\tau_{s,meas} = 1.10\,\tau_{s,av} \tag{10}$$

This was chosen with the realization that for the larger aspect ratio used by Schlichting, the influence of the corner flows on the average shear stress should be slightly less than in Leutheusser's case. In addition, of course, Leutheusser had no influence of a rough upper wall on his flows.

Recasting (9) and (10) in terms of friction velocities,

$$u^{*2}_{rc} = \frac{b}{\rho}\left|\frac{dP}{dx}\right| - \left(\frac{W+2b}{1.10\,W}\right)u^{*2}_{s,meas} \tag{11}$$

where the *rc* subscript indicates a corrected rough wall value. All values on the right-hand side of (11) were reported by Schlichting, allowing calculation of u^*_{rc} for each run. These values are reported in Table 2 in the dimensionless form C_{fc}. Comparison of $C_{f,av}$ and C_{fc} shows the originally reported values are larger than the corrected ones by 0.5 to 73 percent, depending on Reynolds number and roughness configuration.

Now consider the velocity profile slope method of determining wall shear. Using the z-coordinate shown in Fig. 2 to avoid confusion with Schlichting's Δy, (7) can be written as

$$u = 5.75\,u^*_{r2}\log(z'-\Delta z) - 5.75\,u^*_{r2}\log k + Au^*_{r2} \tag{12}$$

where Δz is the "wall shift" required to give a velocity profile slope of 5.75 in u^+ versus log z coordinates. For a given velocity profile on a given surface, the final two terms in (12) are constants, so u^*_{r2} can be calculated from a slope determination using the measured data pairs (u,z') *if* Δz *is known a priori.*

In using this approach, Schlichting assumed that his Δy (as defined previously) was equal to the Δz in (12). Although the definition of Schlichting's Δy is a very logical one when considered on physical grounds, it is unrelated to any characteristics (assumed or proven) of the velocity profile.

Unfortunately, for the cases investigated by Schlichting, the

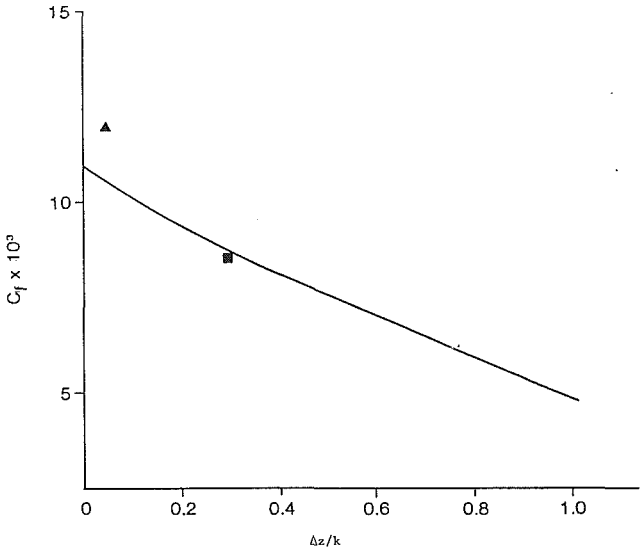

Fig. 3 Demonstration of influence of effective wall location on skin friction calculated from velocity profile slope. (Plate III, Re = 107,000; ▲ $-C_{f2}$, ■ $-C_{fc}$.)

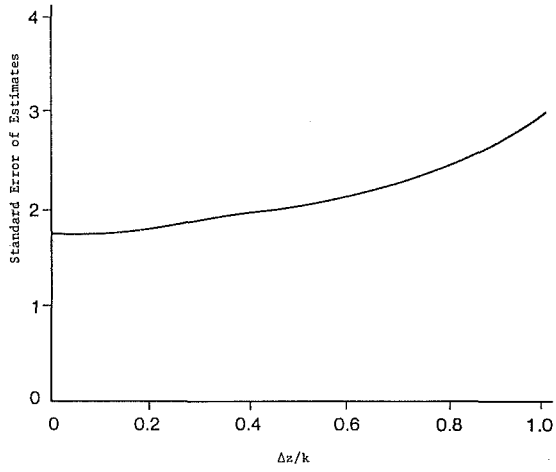

Fig. 4 Standard error of estimates for velocity profile regressions for the effective wall locations in Fig. 3

skin friction determined using this technique is highly sensitive to the value of Δz. This is illustrated in Fig. 3, which shows the results obtained for the value of C_f using this technique and considering a range of Δz values from zero to the roughness element height. The velocity profile data used are for Plate III, Re = 107,000. The slope determinations were made using a linear least squares regression in u versus log $(z' - \Delta z)$ coordinates. Plotted for comparison with the curve are two points. One is Schlichting's C_{f2} (graphical slope determination) plotted using his value of Δy. The other is the corrected value determined from the pressure drop measurements (C_{fc}) plotted at the "optimum" value of Δz (discussed in the following section).

When u^* is not known from an independent measurement, the question of which Δz choice gives the "best" linear regression is generally one which cannot be answered unambiguously when actual velocity profiles are being evaluated. This is illustrated in Fig. 4, which shows the standard error of estimates (Schenck, [17]) versus $\Delta z/k$ for the results which are presented in Fig. 3. For this particular case, there is essentially no difference in the standard error over the range $\Delta z/k$ from 0.0 to 0.2, and the difference for $\Delta z/k$ from 0.0 to 0.5 is only ±5 percent about the average value of standard error in that range.

After considering the sensitivity of the velocity profile slope method to the assumptions required to obtain a value of u^*, it was concluded that for the conditions of the Schlichting experiment this approach produces estimates of u^* for which the uncertainties are much larger than for those estimates based on pressure drop measurements. The present authors therefore recommend the corrected (C_{fc}) values based on the pressure drop measurements as the best estimates of the true values of C_f in Schlichting's experiment.

Re-Evaluation of Equivalent Sand Roughness

For each of the surfaces he tested, Schlichting determined an equivalent sand roughness, k_s. He did this by comparing the rough wall "log law" in the form

$$u/u^*_{r,\text{av}} = 5.75 \log(y/k) + A \tag{13}$$

to the form Nikuradse reported for his velocity profile data in the fully rough regime

$$u/u^* = 5.75 \log(y/k_s) + 8.48 \tag{14}$$

It should be noted that in (13),

$$y = y' - \Delta y \tag{15}$$

while Nikuradse [1] did not explicitly define the origin of his y coordinate used in (14). Schlichting set (13) and (14) equal, assumed all of his data were in the fully rough regime, and obtained

$$5.75 \log(k_s/k) = 8.48 - A \tag{16}$$

By computing an average value of A for each velocity profile using (13) and then calculating a mean value of A from all the profiles on each plate, he was then able to use (16) to solve for a k_s/k value for each of the rough surfaces he tested. These values are listed in Table 1 for the surfaces of interest in the present study.

In view of the discussion in the preceding sections, the use of $u^*_{r,\text{av}}$ and Δy in (13) are open to serious question. It is more appropriate to use the corrected friction velocity and the wall shift Δz such that

$$u/u^*_{rc} = 5.75 \log(z' - \Delta z)/k + A \tag{17}$$

If (17) is used in determining an equivalent sand roughness, then Δz values must be determined before the computation can proceed.

Monin and Yaglom [18] show that, within the logarithmic layer, the quantity

$$z_0 = (z' - \Delta z)\exp(-\kappa u/u^*) \tag{18}$$

is independent of distance from the wall. Thus, if the friction velocity and the data pairs (u,z') in a velocity profile are known, z_0 can be determined as a function of $(z' - \Delta z)$ for various Δz values. The "optimum" Δz value is then the one which gives values of z_0 which are the closest to being constant with $(z' - \Delta z)$. The "optimum" Δz values were determined in this study using the above approach and a criterion of minimum standard error of estimates from a linear least squares regression of z_0 on $(z' - \Delta z)$ with zero slope. The Karman constant, κ, was taken as 0.40 for consistency with the slope in (17).

In using this procedure, the velocity profile points must be read from Schlichting's [2] figures. The symbols for the different profiles are not distinguishable in most cases in the NACA English translation, so the original German version was used. Shown in Table 2 are the calculated "optimum" Δz values for each of the velocity profiles which could be distinguished in the originally published figures.

For each of the profiles for which Δz was calculated, a linear least squares regression of the form of (17) was used to determine a value of A. Then (16) was used to calculate the corresponding k_s/k value. The mean values of k_s/k (shown in Table 2) were then determined for each surface. Comparisons

show that Schlichting's original k_s/k values are higher than the corrected values by 26 to 555 percent.

In using (16) to determine k_s/k, it is assumed that $(z' - \Delta z)$ for Schlichting's data and Nikuradse's y are equivalent. In other words, the origins for the coordinate systems must be those which give a slope of 5.75 in the log regions for both sets of data. It has been shown previously that Δz meets this requirement by its definition. However, since Nikuradse did not explicitly define his origin for y, the sensitivity of his results to a "wall shift" must be considered.

Fortunately, Nikuradse's results are much less sensitive to assumed wall position than are those of Schlichting. Nikuradse tested configurations over a range of r/k from 15 to 507, where r is pipe radius and k the average sand size. The analogous parameter in Schlichting's configurations, b_2/k, ranged from 6.1 to 13.8 for the surfaces considered in this study. Schlichting defined b_2 as the distance from the rough wall to the maximum in the velocity profile across the channel. If it is assumed that the virtual or effective wall location lies between the bottom and the top of the roughness elements, then the points in Nikuradse's velocity profiles are much less affected than are Schlichting's, since as z' becomes much greater than Δz, $\log(z' - \Delta z)$ approaches $\log(z')$.

Using the corrected k_s values for each surface and the corrected friction velocities u^*_{rc}, a roughness Reynolds number

$$\mathrm{Re}_{k_s} = u^*_{rc} k_s/\nu \tag{19}$$

was calculated for each of Schlichting's runs which were considered. These values are recorded in Table 2. It should be noted that for all runs using Plates XIII, XIV, and XXIII, the calculated roughness Reynolds numbers are in the transitionally rough regime, not in the fully rough regime as assumed by Schlichting. Of course, the method by which the k_s values were determined assumes fully rough flow, so the meaning of the k_s values for these three plates is not the same as for those plates on which fully rough flow existed.

Discussion and Summary

The experimental results of Nikuradse [1] and Schlichting [2] remain the most basic and comprehensive data sets yet reported on rough surface effects on turbulent flow. These results have been used to some extent in nearly every effort, analytical or experimental, made in this area since 1936.

During analysis of his data, Schlichting made several assumptions which had significant effects on the final values which he reported. Work reported in the years since 1936 has made the use of these assumptions unnecessary and allows a more accurate analysis of the original data to be made. The present authors have presented the results of such a re-evaluation of Schlichting's data in the preceding sections.

The assumptions which significantly affected the originally reported values of C_f were neglecting the shear stresses on the smooth side walls of the channel and using the definition of wall shift, Δy, which was appealing from a physical standpoint but which bore no relationship to the wall shift, Δz, required to attain the assumed value of slope in the logarithmic region of the velocity profiles. The first of these assumptions led to values C_{f1} which were always too large by an amount which varied with Reynolds number and roughness configuration. The second of these assumptions, coupled with the small values of b_2/k and the slope determination, led to a method which yielded values C_{f2} which were so uncertain as to be unusable, in the opinion of the present authors. The corrected values C_{fc}, which were determined from the pressure drop measurements and with the side wall shear taken into account, are recommended as the best estimates of the true skin friction coefficients.

The values of equivalent sand roughness, k_s, originally reported by Schlichting were influenced by problems arising from all the assumptions mentioned above. Since $C_{f,\mathrm{av}}$ and Δy were used in the calculations, the k_s values contain the inaccuracies due to calculating C_{f1} neglecting the side wall shear stresses, to calculating C_{f2} assuming Δy was the wall shift required to obtain the logarithmic region with the correct slope in the velocity profiles, and to assuming the effective wall location was the same for Nikuradse's data and for Schlichting's data when Δy was used. In addition, Schlichting assumed all the flows in his experiment were in the fully rough regime.

The corrected k_s values are recommended when the equivalent sand roughness concept is used. These corrected values were determined using the corrected friction velocities and the wall shift, Δz, which insures the desired slope in the logarithmic region of the velocity profiles.

Calculation of roughness Reynolds numbers using the corrected friction velocity and corrected k_s for each run reveals that all the runs for plates XIII, XIV, and XXIII were in the transitionally rough, not the fully rough, regime. This violates the assumption of fully rough flow used in determining k_s on these plates. There is some uncertainty, then, as to the true state of these flows. The present authors feel that it is likely that the flows on these three surfaces were in the transitionally rough regime.

This work was supported by the U.S. Air Force Armament Laboratory, Contract F08635-82-K-0062. The authors wish to thank Lt. Bruce Haupt, Dr. Lawrence Lijewski and Dr. Donald Daniel for their support and encouragement.

References

1 Nikuradse, J., "Stromungsgesetze in Rauher Rohen," *VDI-Forschungsheft 361*, 1933. (Also "Laws of Flow in Rough Pipes," NACA TM-1292).

2 Schlichting, H., "Experimentelle Untersuchungen zum Rauhigkeits-problem," *Ingenieur-Archiv VII*, Vol. 1, 1936, pp. 1-34. (Also "Experimental Investigation of the Problem of Surface Roughness," NACA TM-823).

3 Healzer, J. M., "The Turbulent Boundary Layer on a Rough Porous Plate: Experimental Heat Transfer with Uniform Blowing," Ph.D. thesis, Mech. Eng. Dept., Stanford University, 1974.

4 Cebeci, T., and Chang, K. C., "Calculation of Incompressible Rough-Wall Boundary-Layer Flows," *AIAA Journal*, Vol. 16, 1978, pp. 730-735.

5 Ligrani, P. M., "The Thermal and Hydrodynamic Behavior of Thick, Rough-Wall, Turbulent Boundary Layers," Ph.D. thesis, Dept. of Mech. Eng., Stanford University, 1979.

6 Lin, T. C., and Bywater, R. J., "The Evaluation of Selected Turbulence Models for High-Speed Rough-Wall Boundary Layer Calculations," AIAA Paper 80-0132, 1980.

7 Christoph, G. H., "Skin-Friction and Heat-Transfer Calculations on Ablating Axisymmetric Vehicles," AIAA Paper 81-0419, 1981.

8 Dvorak, F. A., "Calculation of Turbulent Boundary Layers on Rough Surfaces in Pressure Gradient," *AIAA Journal*, Vol. 7, 1969, pp. 1752-1759.

9 Dirling, R. B., "A Method for Computing Roughwall Heat Transfer Rates on Reentry Nosetips," AIAA Paper 73-763, 1973.

10 Simpson, R. L., "A Generalized Correlation of Roughness Density Effects on the Turbulent Boundary Layer," *AIAA Journal*, Vol. 11, 1973, pp. 242-244.

11 Denman, G. L., "Turbulent Boundary Layer Rough Surface Heat Transfer on Blunt Bodies at High Heating Rates," Ph.D. thesis, Dept. of Mech. Eng., Ohio State University, 1976.

12 Adams, J. C., and Hodge, B. K., "The Calculation of Compressible, Transitional, Turbulent and Relaminarizational Boundary Layers Over Smooth and Rough Surfaces Using an Extended Mixing Length Hypothesis," AIAA Paper 77-682, 1977.

13 Christoph, G. H., "Law of the Wall Analysis for Turbulent Heating on Rough Surfaces," AIAA Paper 82-0197, 1982.

14 Finson, M. L., and Wu, P. K. S., "Analysis of Rough Wall Turbulent Heating with Application to Blunted Flight Vehicles," AIAA Paper 79-008, 1979.

15 Finson, M. L., "A Model for Rough Wall Turbulent Heating and Skin Friction," AIAA Paper 82-0199, 1982.

16 Leutheusser, H. J., "Turbulent Flow in Rectangular Ducts," *Journal of the Hydraulics Division, Proc. of ASCE*, Vol. 89, No. HY3, 1963, pp. 1-20.

17 Schenck, H., *Theories of Engineering Experimentation*, 3rd Ed., Hemisphere Publishing Co., 1979.

18 Monin, A. S., and Yaglom, A. M., *Statistical Fluid Mechanics*, Vol. 1, MIT Press, 1971.

Wall Confinement Effects for Spheres in the Reynolds Number Range of 30 – 2000

V. J. Modi
Professor.

T. Akutsu
Graduate Research Assistant.

Department of Mechanical Engineering,
The University of British Columbia,
Vancouver, B.C., Canada, V6T 1W5

The paper studies in detail the time history of formation, evolution, and instability of the vortex ring, associated with a family of spheres in the Reynolds number range of 30–2000 and with a blockage ratio of 3–30 percent. The flow visualization results are obtained using the classical dye injection procedure. Simultaneous measurements of pressure distribution on the surface of the sphere help establish correlation between the onset of instability of the vortex ring and the surface loading. The results suggest that the influence of the Reynolds number on the surface pressure distribution is primarily confined to the range $R_n < 1000$. However, for the model with the highest blockage ratio of 30.6 percent, the pressure continues to show Reynolds number dependency for R_n as high as 2300. In general, effect of the Reynolds number is to increase the minimum as well as the wake pressures. On the other hand, the effect of an increase in the blockage ratio is just the opposite. The wall confinement tends to increase the drag coefficient, however, the classical dependence of skin friction on the Reynolds number $C_{d,f} \propto R^{-1/2}$, is maintained. The paper also presents useful information concerning location of the separating shear layers as affected by the Reynolds number and blockage. For comparison, available analytical and experimental results by other investigators are also included. Results show that for a given blockage, separation points may move upstream by as much as 20 deg over a Reynolds number range of 100–600. In general, for a given Reynolds number, the wall confinement tends to move the separation position downstream.

1 Introduction

There are numerous situations of practical importance where bodies of revolution in general and spherical objects in particular operate in fluid fields with relatively low Reynolds number. Towed sonars or stationary hydrophones used in submarine detection systems, oceanographic platforms employed in hydrographic surveys, proposed configurations of underwater habitats, oil-storage tanks, meteorological studies of rain drops and balloons, spray drying in the chemical industry, etc. belong to this class of problems. For laboratory simulation, a model of a given system is usually tested in wind or water tunnel where confined conditions are created either unintentionally, or through choice for geometric similarity.

Interest in the behavior of a sphere moving through a fluid goes back to the days of Newton who is credited with the first recorded measurements on sphere drag. Ever since, theoretical and practical interest in the subject has resulted in a large volume of literature, and the contributions up to 1960 have been cited by Torobin and Gauvin [1] in their comprehensive review of the field. More important contributions [2–16] to the field since this classical study suggest the fact that most efforts to date have been aimed at the determination of the total drag and associated effects of the free stream turbulence, compressibility, and surface roughness. Surprising as it may seem, blockage effects for even a uniform flow past a sphere at low Reynolds numbers remain virtually unexplored. Isolated attempts at the measurements of surface pressure distribution and blockage effects are confined to a relatively higher Reynolds number range of $6\times10^3 - 2\times10^5$ by Maxworthy [7] and $5\times10^4 - 6\times10^6$ by Achenbach [11, 16]. Here again the focus is on the pressure distribution or the drag coefficient and not on the wall confinement effects. In the present study, an effort is made to investigate: (i) formation, development and instability of the vortex ring; (ii) associated pressure distribution; (iii) total and skin friction drag; and (iv) near wake geometry for a family of spheres in the Reynolds number range of 30–2000 and the blockage ratio varying from 3–30 percent. An extensive flow visualization study in conjunction with still and high speed movie photography complemented the test program.

2 Experimental Set-Up and Test Procedures

2.1 Glycerol Tunnel. The tests were conducted in a glycerol-water solution tunnel designed to produce Reynolds

Contributed by the Fluids Engineering Division and presented at the Winter Annual Meeting, Phoenix, Ariz., November, 1982, of THE AMERICAN SOCIETY OF MECHANICAL ENGINEERS. Manuscript received by the Fluids Engineering Division, February 8, 1983.

number in the range 30–4000. The choice of concentration of the working fluid provided a degree of flexibility, but only to a certain extent, as governed by the characteristics of the power unit. The test section is built of four plexiglas walls 2.44 m (8 ft) long, 1.9 cm (0.75 in.) thick and wide enough to produce an inside cross-section of 20.32 cm × 20.32 cm (8 in. × 8 in.). Deflection annular vanes together with several sections of honeycombs, brass screens and nylon wool gave exceptionally flat velocity profiles, recorded using a quartz coated wedge shaped platinum hot film probe (DISA 55A83). The power unit consists of a centrifugal pump (Aurora type GAPB, 200 gal/min, 7.6 m head, 1750 rpm) driven by a three horsepower variable speed d-c motor. The pump impeller and housing are of cast brass to guard against possible corrosion. The motor is energized by a three phase grid, the voltage being adjusted through an autotransformer and rectified by selenium diodes. No further smoothing of the d-c output was required.

It was important to minimize dirt contamination of the tunnel fluid. This was achieved by incorporating a 10 μ filter in a bypass circuit across the pump. The system filters the entire volume at least once in twenty-four hours of operation. The tunnel is shown schematically in Fig. 1.

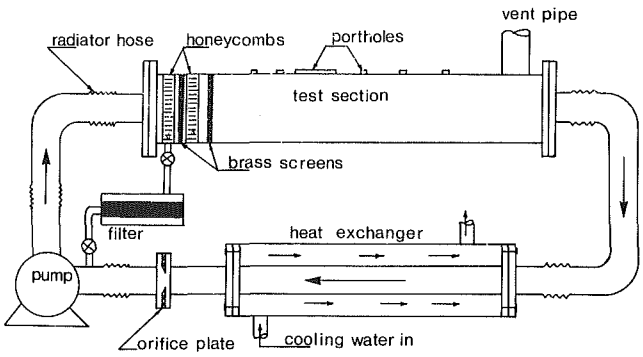

Fig. 1 A schematic diagram of the glycerol tunnel

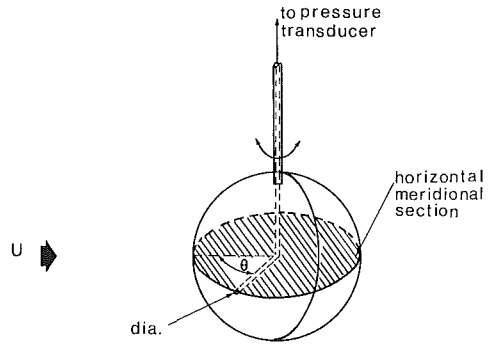

Fig. 2 A schematic diagram showing the spherical model and its support system during pressure measurements

2.2 Models and Pressure Transducer. A set of spheres with diameter in the range of 3.8–12.7 cm was used in the test programme to cover the desired range of blockage. The model was supported by a vertical stainless steel tube, which also served as the pressure conducting line. Its outside diameter was dictated by the relative size of the sphere and the stem's influence on the pressure field. On the other hand, the inside diameter was governed by the time constant to reach the steady state pressure. A series of tests conducted with 5.08 cm diameter sphere showed that the sphere to stem diameter ratio must be at least ten to make the stem interference negligible.

Because of the symmetry, pressure measurements were confined to horizontal meridional section of the model. A 1.5 mm pressure tap connected the stem through a groove (1.5 mm diameter) drilled in the body of the sphere (Fig. 2). The mean static pressure being relatively small demanded a highly sensitive instrumentation for its measurement. This was accomplished using a "Barocel Modular Pressure Transducing System" developed by Datametrics Inc. of Watertown, Mass. Barocel is accurately calibrated for steady pressures and has a sensitivity of 0.07 N/m^2.

2.3 Choice of Reference Velocity and Pressure. For low Reynolds number flows in a tunnel, the fluid velocity and pressure vary significantly along the axis of the test section, even in absence of the model, due to boundary layer growth along the walls. The presence of model and the associated wake only accentuates this problem. Obviously, a choice of suitable reference parameters demands special attention.

After careful consideration of available alternatives it was decided to express pressure coefficient as

$$C_p = \frac{P_\theta - P_r}{P_0 - P_r}$$

where: P_θ = pressure at a given θ;
P_r = pressure at the reference location $\theta = \theta_r$, here $\theta_r = 60$ deg;
P_0 = pressure at $\theta = 0$, i.e., stagnation pressure.

The definition proved to have several advantages. It tends to compensate for pressure gradients in the tunnel, irregularity of the velocity profile, electrical drifts of the pressure measuring system and blockage effects. Furthermore, in conjunction with the Reynolds number (based on average flow velocity and sphere diameter), it promises to assist in

Nomenclature

C = tunnel cross-sectional area
C_d = $F_t/(1/2)\rho U^2 S$
$C_{d,t}$ = total drag coefficient, $C_{d,p} + C_{d,f}$ based on average velocity
$C_{d,f}$ = skin friction component of total drag, based on average velocity
C_p = $(P_\theta - P_r)/(P_0 - P_r)$
C_{p_b} = base pressure coefficient, $(P_b - P_r)/(P_0 - P_r)$
C_{p_m} = minimum pressure coefficient, $(P_m - P_r)/(P_0 - P_r)$
D = sphere diameter
d_s = stem diameter
F_t = total sectional drag
P = static pressure
P_0 = static pressure on the surface of the sphere at stagnation point
P_θ = static pressure on the surface of the sphere at an angle θ from the front stagnation point
P_b = base pressure
P_r = static pressure at reference tap, in the present case $r = 60$ deg
R_n = Reynolds number, UD/ν
S = diametral cross-sectional area
U = average velocity in the test-section based on a flow rate as given by the orifice meter
θ = angular location of a pressure tap with reference to the front stagnation point
θ_r = angular location of the reference pressure location, in the present case, $\theta_r = 60$ deg
θ_s = angular location of the separating shear layer with respect to the rear stagnation point
μ = dynamic viscosity
ν = kinematic viscosity, μ/ρ
ρ = density

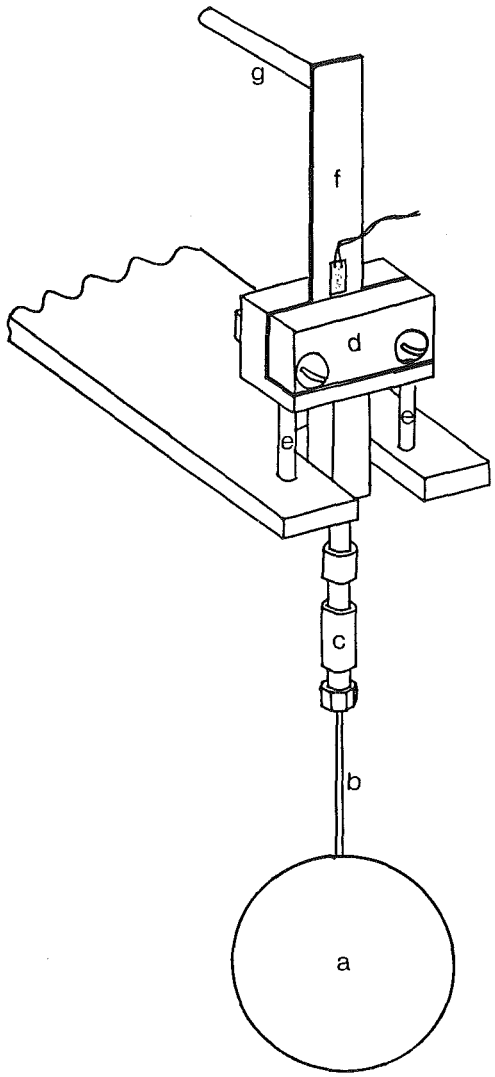

Fig. 3 Drag balance assembly with spherical model: (a) spherical model; (b) supporting stem; (c) intermediate connection; (d) central suspension block; (e) needle bearings supporting the central block; (f) cantilever with strain gages; and (g) stopper

duplication and comparison of similar data by other investigators using different test facilities.

2.4 Drag Measurements. A highly sensitive strain gage balance was designed for drag measurements. Essentially it consists of three components:

(i) removable stem supporting the spherical model;
(ii) central suspension block supported by a pair of needle bearings; and
(iii) interchangeable cantilever type sensing unit with strain gages fixed near its root.

Interchangeable character of the sensing element was purposely introduced to achieve a desired degree of accuracy in a given range of drag force. Several beams of varying flexural rigidity and length were constructed for measurement of drag in the range of 0.1–15 grams with a sensitivity of 0.001 gram. Two strain gages, one on each side of the beam, were used for temperature compensation. The tip of the beam rested against a fixed wedge shaped support. The calibration of the balance was carried out under actual test arrangement with a spherical model located in the tunnel but in the absence of flow. The general arrangement is shown in Fig. 3.

2.5 Flow Visualization. To better appreciate the character of the flow past the model and trends indicated by

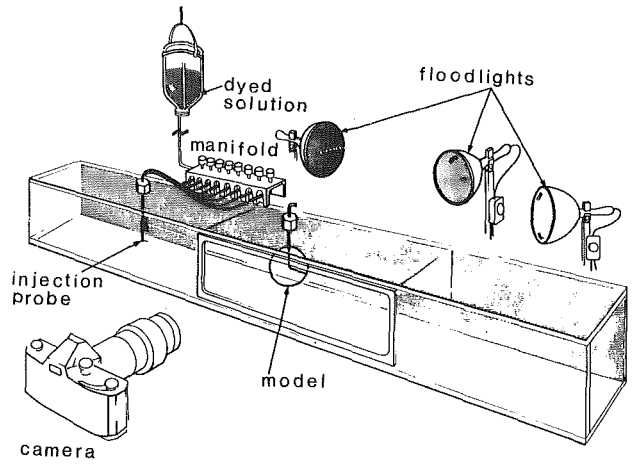

Fig. 4 A sketch showing the equipment layout during flow visualization

the pressure measurements, flow visualization was undertaken. The classical dye injection method with carefully controlled back-lighting at the test section was used to this end.

Appropriate volumes of the dye and pure glycerin were mixed to produce a glycerol-water solution of the same density as that of the test fluid. The dyed glycerol-water solution was injected approximately 25 cm upstream of the model. The dye employed was an imitation cochineal food color.

A dye injecting probe, consisting of seven #23 hypodermic needles (0.38 mm) placed 0.5–1.0 cm apart on a streamlined support, was constructed. "Intramedic" tubings (0.6 mm inside diameter) were used to connect the needles to the manifold. The rate of injection was controlled with brass needle valves. To ensure adequate flow through each needle, i.e., to provide sufficient head, the supply bottle was suspended from the ceiling 4 m above the injection level. At times, the dyed solution was injected directly into the separated region through a long needle or an existing pressure measuring port. Dissipation of the trapped dye solution into the stream was slow enough to permit photographing of the wake.

A combination of three variable intensity photo floods (maximum 500 watts, 3400°K) back-illuminated the test-section. To minimize hot spots, the light beam was evenly diffused by masking the test section wall with a tracing paper. A schematic diagram of the flow visualization set-up is shown in Fig. 4.

3 Results and Discussion

The amount of information obtained by a systematic variation of the Reynolds number and blockage is rather extensive [17]. For conciseness, only a few of the typical results useful in establishing trends are recorded here.

3.1 Effect of Reynolds Number. Figure 5 presents, rather concisely, considerable amount of experimental data pertaining to the surface pressure distribution in the low Reynolds number range ($R_n < 1000$) and at small blockage ratios ($S/C < 5$ percent).

It is apparent that the effect of Reynolds number is essentially confined to the region downstream of the zero pressure point. In general, it tends to increase the minimum as well as the wake pressures. Furthermore, location of the minimum pressure point together with the approximate location of the separation point (as indicated by the beginning of the uniform pressure region of the wake) show a slight tendency to shift upstream with an increase in the Reynolds

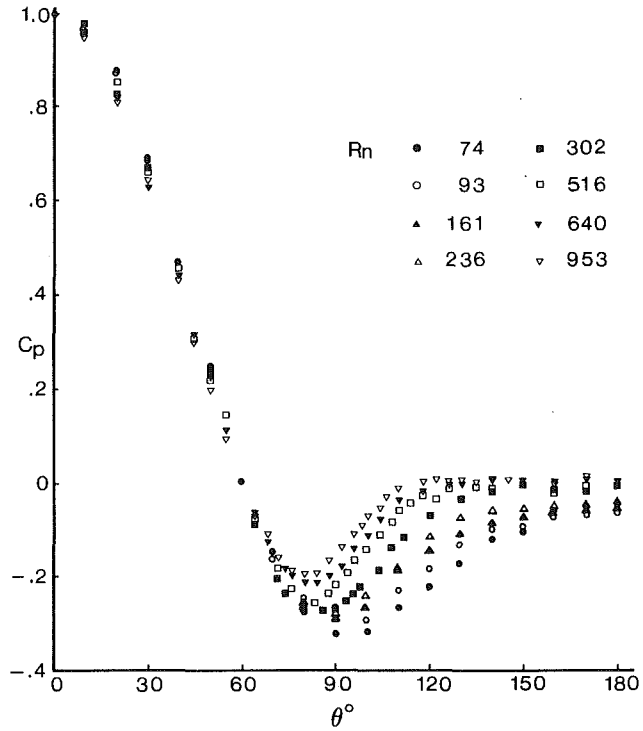

Fig. 5 Surface pressure distribution as affected by Reynolds number at small blockage ratios of less than 5 percent

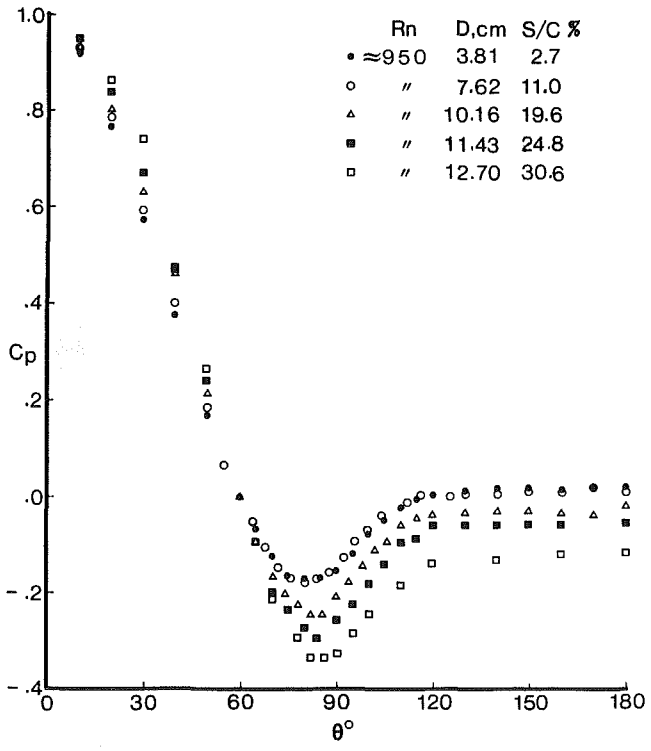

Fig. 6 Pressure plots as affected by higher blockage

number. At higher blockage ratios in the range 11–19.6 percent essentially the same trend was observed. However, for any further increase in the wall confinement the base pressure began to be a little more sensitive to the Reynolds number.

3.2 Wall Confinement Effects. Figure 6 summarizes the results on the influence of blockage offered by the spherical models at an essentially fixed Reynolds number. Note, the

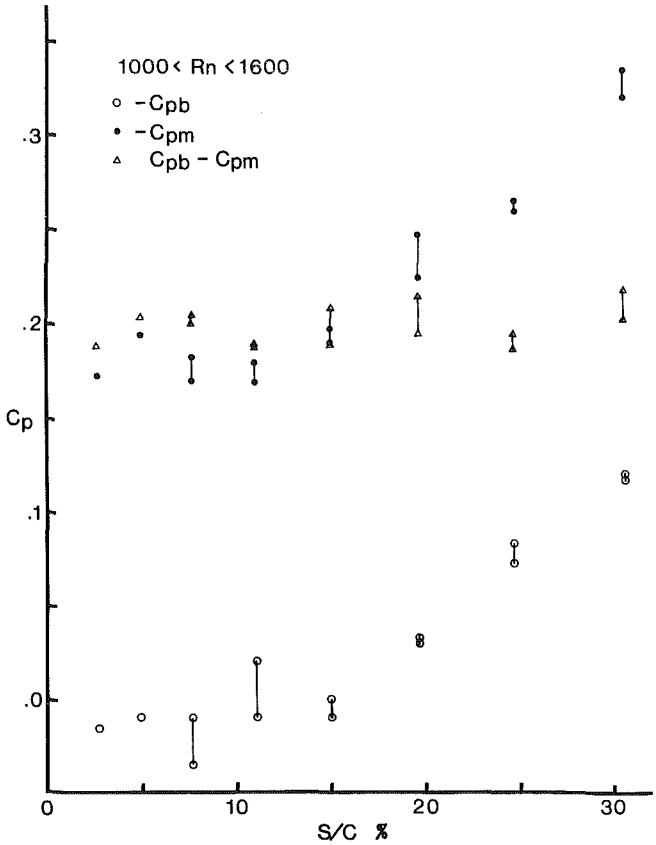

Fig. 7 Effect of wall confinement on the minimum and base pressure, $1000 < R_n < 1600$. Note both C_{pb} and C_{pm} are essentially constant up to the blockage ratio of around 13 percent.

effect of wall confinement is insignificant below the blockage of 11 percent. The blockage has a definite tendency to reduce the minimum as well as the base pressures. The minimum pressure point shows a distinct rearward shift. Similar downstream movement of the separation point can also be discerned although it is not quite distinct. A flow visualization study described later confirmed this trend. As can be expected from the earlier discussion, the blockage effects remain essentially the same for $R_n > 1000$.

Figure 7 shows variation of the average base pressure and the minimum pressure with blockage. Up to S/C of around 12–15 percent the base pressure as well as the minimum pressure remain essentially constant, however, beyond that there is a distinct rise in the pressures with blockage. Thus there appears to be a critical value of the blockage ratio above which the effect of wall confinement appears to become significant.

Interestingly the difference $C_{pb} - C_{pm}$, which is a measure of the pressure rise sustained by the boundary layer prior to separation, remains virtuallly independent of the blockage throughout. The near independence of this quantity from the confinement effects may be attributed to the relative insensitivity of the boundary layer to the local changes in the free stream velocity resulting from blockage. However, at lower Reynolds number, due to dominance of viscous forces, one would expect this trend to change. Measurements conducted at $R_n = 600$ confirmed this. Although the base pressure continued to remain relatively insensitive to blockage, there was a definite drop in the minimum pressure resulting in a clear increase of $C_{pb} - C_{pm}$.

Useful condensation of Reynolds number and blockage effects on base pressure is presented in Fig. 8. The results suggest that Reynolds number effects are confined to the range $R_n < 1000$ for all blockage ratios and $R_n > 1600$ for

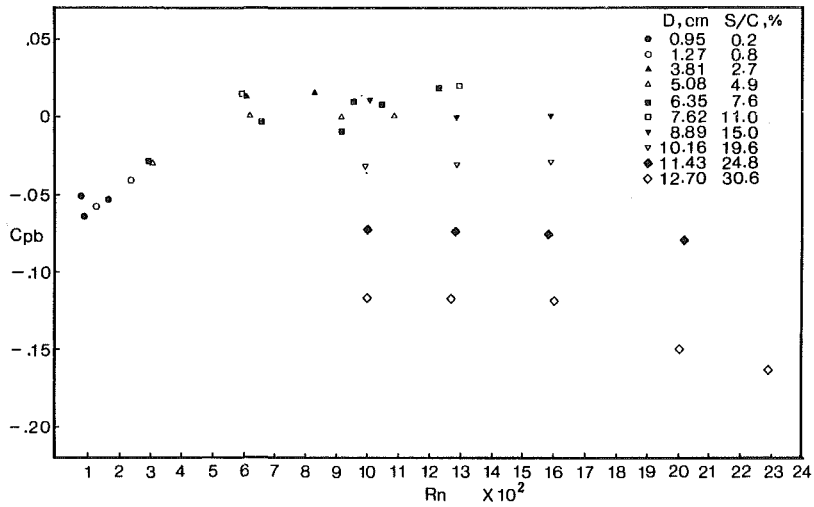

Fig. 8 Condensation of the base pressure data showing the influence of Reynolds number and blockage

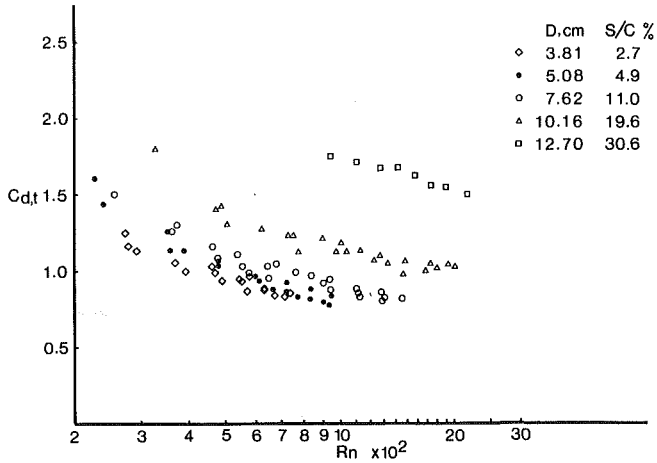

Fig. 9 Total drag coefficient as affected by the Reynolds number and blockage

higher blockage (S/C = 30.6 percent). Thus for a sphere operating in a highly confined condition, there is only a small region of the Reynolds number where the base pressure coefficient remains essentially constant, perhaps due to compensative effects of the blockage and Reynolds number. Hence, in general, considering fluid dynamics of spheres with $S/C > 30$ percent to be independent of R_n may lead to misleading conclusions.

3.4 Drag Coefficient. One would expect the drag coefficient to be primarily governed by magnitude and location of the minimum pressure point, the pressure distribution downstream of it, as well as the skin friction contribution. Since the pressure profiles do not change beyond R_n = 1000, the pressure drag coefficient for a given blockage is expected to remain essentially constant. However, the total drag would show a drop with an increase in the Reynolds number (Fig. 9). As can be expected, the effect of blockage is to increase the drag coefficient because of the local increase in the free stream velocity.

With pressure and total drag information at hand it was convenient to plot variations of skin friction with the Reynolds number and blockage. Corresponding results by Achenbach [11] near critical end of the Reynolds number range and empirical relations as suggested by Rosenhead [18] and White [19] are also included for comparison (Fig. 10). The results tend to confirm the classical dependence of skin friction on the Reynolds number, $C_{d,f} \propto R_n^{-1/2}$, however, the information is not extensive enough to establish any well defined trend for the blockage effect. Achenbach's results near the critical Reynolds number and the present data in a relatively lower Reynolds number range can be fitted quite well along the line $C_{d,f}/C_{d,t} = 6.08\ R_n^{-0.5}$, which corresponds to $C_{d,f} = 2.432/(R_n^{0.5} - 6.08)$ and $C_{d,p} = 0.4$.

3.5 Flow Visualization. To provide better appreciation as well as substantiation of the certain behavior exhibited by the measured data, extensive flow visualization program was undertaken. The main objective was to observe the formation, development and instability of the vortex ring and associated influence on the measured pressure data. It was also hoped that this would provide some indication concerning location of the separation point and its movement. The flow visualization through dye injection showed formation of the vortex ring in a rather spectacular fashion as presented in Fig. 11 (note: Original flow visualization photographs are in color). Numerous photographs were taken at systematic increments of the Reynolds number. Only a few of the typical pictures illustrating formation, symmetric elongation, onset of asymmetry and instability followed by turbulent shedding are presented here.

The existence of an axisymmetric, stable vortex ring for low Reynolds number in a stream essentially free of macroscopic turbulence is shown in Fig. 11(*a*). For the Reynolds number above a critical value (corresponding to the first formation of a stable ring, $10 < R_n < 25$), the streamlines separate from the surface and form a closed region immediately behind the sphere. A single streamline emerges from the vertex of the closed region extending to a long distance behind the sphere. The size of the ring is such as to maintain an equilibrium between the rate at which the vorticity is generated and dissipated into the main stream. As the Reynolds number is increased the vortex ring becomes elongated in the flow direction to maintain this equilibrium, and the separation points move upstream towards the front stagnation point (Fig. 11(*a-d*)). This forward movement of the separation points was also suggested by the pressure plots presented earlier.

For Reynolds number between 230-270 an asymmetry in the circulatory motion within the vortex sheet produces a corresponding asymmetry in the circulatory motion in the sheet itself and a resultant shift from the center line (Fig. 11(*e*)). This wake is followed by two distinctly inclined streamlines which maintain an equilibrium between rates of generation and diffusion of the vorticity. Taneda [20] related

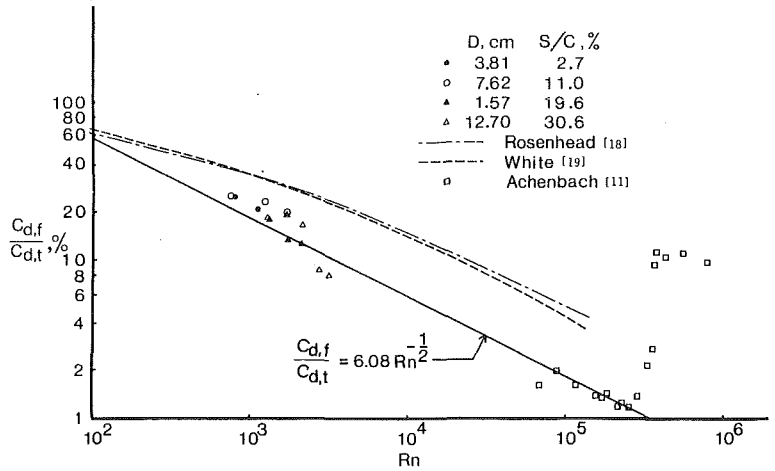

Fig. 10 Friction force as a percentage of the total drag

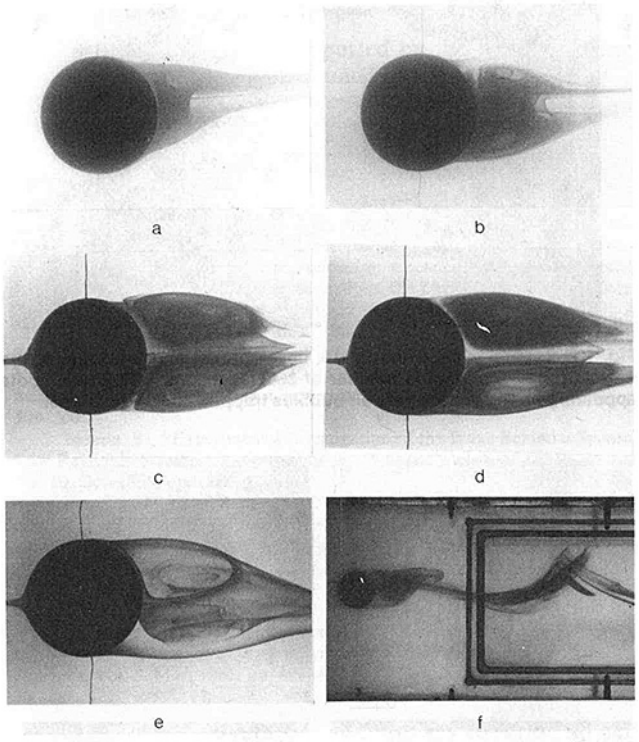

Fig. 11 A flow visualization study showing development and instability of vortex ring with Reynolds number: (*a*) R_n = 22; (*b*) R_n = 60; (*c*) R_n = 190; (*d*) R_n = 221; (*e*) R_n = 265; and (*f*) R_n = 280

the slight asymmetry of the vortex ring to the support effect. However, this could not be so as the asymmetry prevailed regardless of the support diameter

$$d_s\left(\frac{1}{150} < \frac{d_s}{D} < \frac{1}{16}\right).$$

The state of the unsymmetrical but steady wake is disturbed by a further increase in the Reynolds number. The rate at which the vorticity is diffused from the sheet into the main body of the fluid remains practically constant, but the increased rate at which it is transferred to the vortex ring creates unstable conditions within the vortex sheet. Basically, the process is one of build-up and release, but no sizable portion of the ring escapes through an opening in the end of the vortex sheet during the cycle. This in turn causes the oscillation of the asymmetrical wake about the axis of symmetry. When the vortex strength of the ring reaches a critical value, a sudden motion of the ring disturbs the sheet, which in turn is responsible for a release of vorticity and a consequent return of the ring to its original position and shape. This phenomenon appears to happen in the Reynolds number range of about 270-290 (Fig. 11(*f*)).

With further increase in the Reynolds number, the oscillatory motion of the vortex ring assumes higher frequency and the circulation within the sheet ceases to be symmetrical. In the cycle of build-up and release, the vorticity generated in the boundary layer becomes concentrated on diametrically opposite sides of the flow axis within the vortex sheet. The sections in which the vortex strength is greatest are periodically discharged into the main body of the fluid. With each ejection a portion of the sheet is carried away. The vortex element discharged into the stream interacts with the dispersed liquid to form a regular wake pattern.

Evolution of a ring vortex during shedding is captured by a series of rapid sequence photographs taken using a 35 mm motor drive camera. Both side and top views at a given instant are presented which clearly suggest loop formation (Fig. 12). It seems to substantiate Achenbach's [15] observation concerning shedding of the vortices from the same side. This is in contrast to the double helical vortex loop implying alternate shedding from opposite sides as concluded by Pao and Kao [20].

A set of typical photographs of the vortex ring associated with spheres offering different blockage is presented in Fig. 13. For the same Reynolds number, effect of the blockage is to retard evolution of the vortex ring. As the vortex shedding is governed by the vorticity generation, it appears that the blockage tends to diminish the rate at which the vorticity is produced. Note also a downstream movement of the separation position due to the blockage. The analysis of numerous such photographs and 16 mm movies resulted in the information on separation angle, θ_s, as affected by the confinement and Reynolds number (Fig. 14). Note that the separation point moves forward by as much as 20°, for the blockage ratio of 2.7 percent, over the Reynolds number range of 100-600. For comparison, available results by other investigators are also included [21-25]. Here the line attributed to Pruppacher et al. [21] represents an average value based on their own data as well as those by Jensen [23], Hamielec et al. [24], and Rimon and Cheng [25]. In general, for a given Reynolds number, the effect of blockage is to move the separation point downstream. It must be emphasized that the visual determination of separation point is, at best, approximate. Considering this and the unstable character of the process, scatter in the experimental results is surprisingly small.

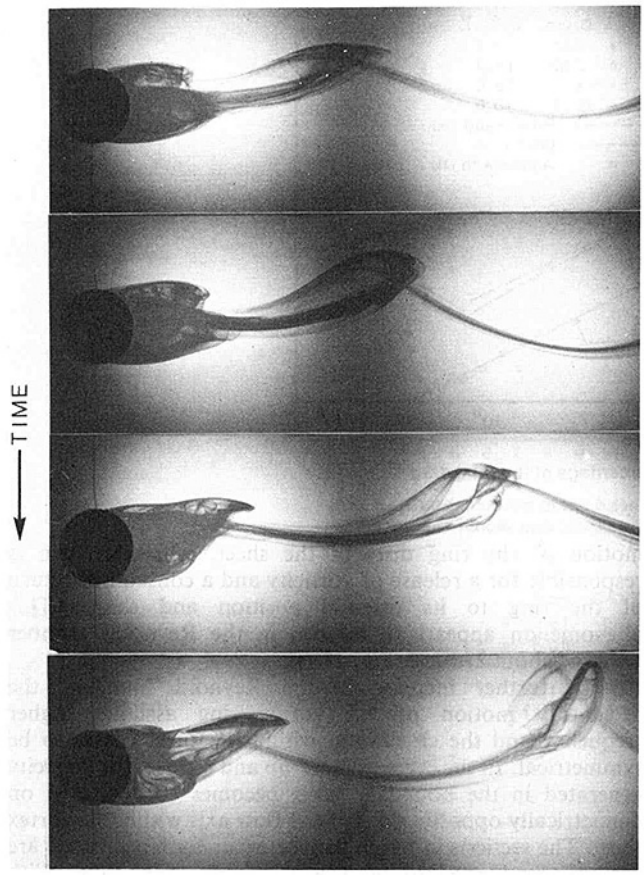

Fig. 12 Typical cycle of initiation, development and shedding of the ring vortex at a Reynolds number of 350: (*a*) side view

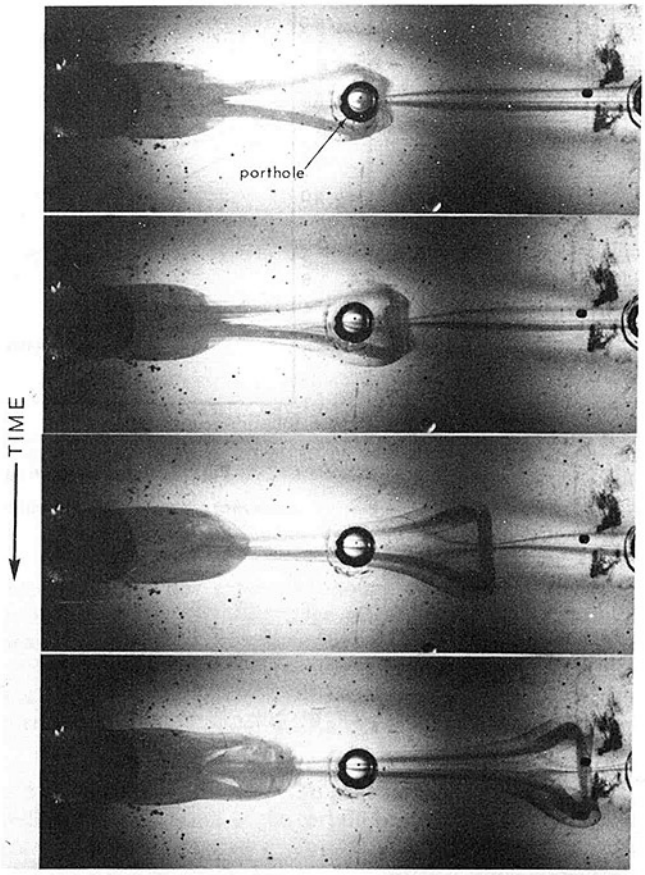

Fig. 12 Typical cycle of initiation, development and shedding of the ring vortex at a Reynolds number of 350: (*b*) top view. The black dots appearing on the pictures are air bubbles trapped inside the tunnel.

Uncertainty estimates

Figure	Abscissa	Ordinate
5	±1 deg	±0.01
6	±1 deg	±0.01
7	0.1 percent	as indicated in diagram
8	±5	±0.01 (maximum)
9	±5	±0.05
10	±5	±0.5 percent
14	±5	±2 deg

4 Concluding Remarks

The important conclusions based on the study can be summarized as follows:

(i) The sphere to stem diameter ratio must be at least ten to make stem interference negligible.

(ii) The effect of Reynolds number is essentially confined to the region downstream of zero pressure point and even here it is limited to $R_n < 1000$, except for the very high blockage ratio of 30.6 percent. In general, it increases the minimum as well as the wake pressures. Furthermore, locations of the minimum pressure and separation points tend to shift a little upstream.

(iii) The confinement effects are essentially negligible up to around 11 percent blockage but beyond that it has a definite tendency to reduce the minimum and base pressures. The minimum pressure point shows a distinct rearward shift with an increase in the blockage.

(iv) In general, the drag coefficient increases with blockage because of the local rise in the velocity. Results show that classical dependence of skin friction on the Reynolds number, $C_d \propto R_n^{-1/2}$, is maintained even in the low Reynolds number range investigated.

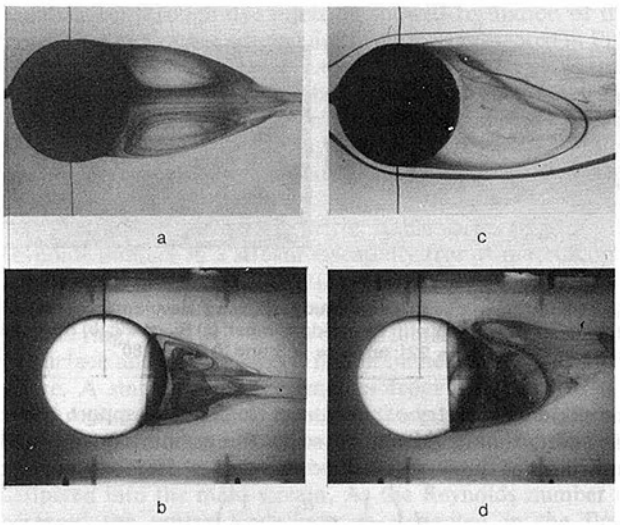

Fig. 13 Typical photographs showing downstream movement of the separation position due to blockage:
(*a*) R_n = 170, *S/C* = 2.7 percent;
(*b*) R_n = 170, *S/C* = 30.6 percent;
(*c*) R_n = 290, *S/C* = 2.7 percent;
(*d*) R_n = 290, *S/C* = 30.6 percent.

(v) Flow visualization provided better appreciation as to the physical character of the flow in terms of formation, evolution and shedding of the vortex ring. It seems the wall confinement tends to retard the generation of vorticity. Obviously this has substantial effect on the associated Strouhal number.

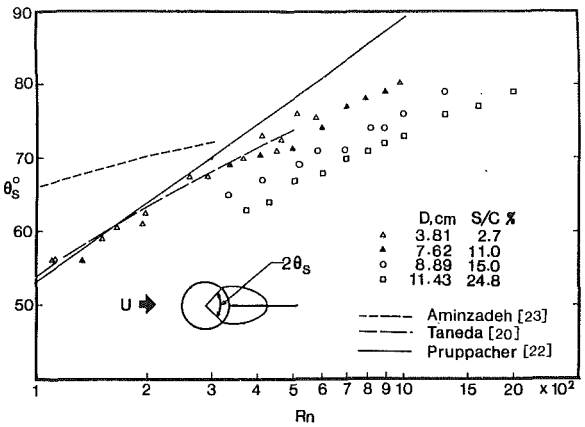

Fig. 14 Position of separation as affected by Reynolds number and wall confinement

Acknowledgment

This investigation was supported by the Natural Sciences and Engineering Research Council of Canada, Grant No. A-2181.

References

1 Torobin, L. B., and Gauvin, W. H., "Fundamental Aspects of Solids-Gas Flow, Part I: Introductory Concepts and Idealized Sphere Motion in Viscous Regime," *The Canadian Journal of Chemical Engineering*, Vol. 37, No. 4, Aug. 1959, pp. 129–141; also "Part II: The Sphere Wake in Steady Laminar Fluids," Vol. 37, No. 5, Oct. 1959, pp. 167–176; "Part III: Accelerated Motion of a Particle in a Fluid," Vol. 37, No. 6, Dec. 1959, pp. 224–236; "Part IV: The Effects of Particle Rotation, Roughness and Shape," Vol. 38, No. 5, Oct. 1960, pp. 142–153; "Part V: The Effects of Fluid Turbulence on the Particle Drag Coefficient," Vol. 38, No. 6, Dec. 1960, pp. 189–200.

2 Taneda, S., "Experimental Investigation of the Wake Behind a Sphere at Low Reynolds Numbers," *Journal of the Physical Society* of Japan, Vol. 11, No. 10, Oct. 1956, pp. 1104–1108.

3 Heinrich, H. G., Niccum, R. J., and Haak, E. L., "The Drag Coefficient of a Sphere Corresponding to a 'One Meter Robin Sphere' Descending from 260,000 ft. Altitude (Reynolds Nos. 789 to 23,448; Mach Nos. 0.056 to 0.90)," *Research and Development of Robin Meteorological Rocket Balloon*, Vol. II, Contract AF 19(604)-8034 AD480309, University of Minnesota, Minneapolis, Minn., May 1963.

4 Lee, K., and Barrow, H., "Some Observations on Transport Processes in the Wake of Sphere in Low Speed Flow," *International J. Heat and Mass Transfer*, Vol. 8, Mar. 1965, pp. 403–409.

5 Sivier, K. R., "Subsonic Sphere Drag Measurements at Intermediate Reynolds Numbers," Ph.D. thesis, 1967, The University of Michigan, Ann Arbor, Mich.

6 Goin, K. L., and Lawrence, W. R., "Subsonic Drag of Spheres at Reynolds numbers from 200 to 10,000," *AIAA Journal*, Vol. 6, No. 5, May 1968, pp. 961–962.

7 Maxworthy, T., "Experiments on the Flow Around a Sphere at High Reynolds Numbers," ASME *Journal of Applied Mechanics*, Vol. 36, No. 3, Sept. 1969, pp. 598–607.

8 Zarin, N. A., "Measurement of Non-Continuum and Turbulence Effects on Subsonic Sphere Drag," Ph.D. thesis, 1969, The University of Michigan, Ann Arbor, Mich.

9 Mujumdar, A. S., and Douglas, W. J. M., "Eddy Shedding from a Sphere in Turbulent Free Stream," *Int. J. Heat and Mass Transfer*, Vol. 13, 1970, pp. 1627–1629.

10 Ross, F. W., and Willmarth, W. W., "Experimental Results on Sphere and Disk Drag," *AIAA Journal*, Vol. 9, No. 2, Feb. 1971, pp. 285–291.

11 Achenbach, E., "Experiments on the Flow Past Spheres at Very High Reynolds Numbers," *J. Fluid Mechanics*, Vol. 54, Part 3, 1972, pp. 565–575.

12 Vlnajinac, M., and Covert, E. E., "Sting-free Measurements of Sphere Drag in Laminar Flow," *J. Fluid Mechanics*, Vol. 54, Part 3, 1972, pp. 385–392.

13 Baily, A. B., and Hiatt, J., "Sphere Drag Coefficients for a Broad Range of Mach and Reynolds Numbers," *AIAA Journal*, Vol. 10, No. 11, Nov. 1972, pp. 1436–1440.

14 Calvert, J. R., "Some Experiments on the Flow Past a Sphere," *Aero. J. Royal Aero. Soc.*, Vol. 76, No. 4, 1972, pp. 248–250.

15 Achenbach, E., "Vortex Shedding from Spheres," *J. Fluid Mechanics*, Vol. 62, Part 2, 1974, pp. 209–221.

16 Achenbach, E., "The Effects of Surface Roughness and Tunnel Blockage on the Flow Past Spheres," *J. Fluid Mechanics*, Vol. 65, Part 1, 1974, pp. 113–125.

17 Akutsu, T., "Wall Confinement Effects for Spheres in the Reynolds Number Range of 30–2000," M.A.Sc. thesis, University of British Columbia, June 1977.

18 Rosenhead, L., *Laminar Boundary Layers*, Oxford University Press, 1963, pp. 102–109.

19 White, F. M., *Viscous Fluid Flow*, McGraw-Hill, New York, 1974, pp. 208–210.

20 Pao, H. P., and Kao, T. W., "Vortex Structure in the Wake of a Sphere," *The Physics of Fluids*, Vol. 20, No. 2, Feb. 1977, pp. 187–191.

21 Pruppacher, H. R., Le Clair, B. P., and Hamielec, A. E., "Some Relation Between Drag and Flow Pattern of Viscous Flow Past a Sphere and a Cylinder at Low and Intermediate Reynolds Numbers," *J. Fluid Mechanics*, Vol. 44, Part 4, 1970, pp. 781–790.

22 Aminzadeh, M., "Hydrodynamic Performance of an Artificial Aortic Valve Implant," Ph.D. thesis, 1975, The University of British Columbia, Vancouver, B.C., Canada.

23 Jensen, V. G., "Viscous Flow Around a Sphere at Low Reynolds Number (<40)," *Proc. Roy. Soc.*, Series A, Vol. 249, No. 1257, Jan. 1959, pp. 346–366.

24 Hamielec, A. E., Hoffman, T. W., and Ross, L. L., "Numerical Solution of the Navier-Stokes Equation for Flow Past Spheres, Part I—Viscous Flow Around Spheres with and without Radial Mass Efflux," *J. of the American Institute of Chemical Engineers*, Vol. 13, No. 2, Mar. 1967, pp. 212–219.

25 Rimon, Y., and Cheng, S. I., "Numerical Solution of a Uniform Flow Over a Sphere at Intermediate Reynolds Numbers," *The Physics of Fluids*, Vol. 12, No. 5, May 1969, pp. 949–959.

Experiments on the Buckling of Thin Fluid Layers Undergoing End-Compression

K. R. Blake

A. Bejan

Department of Mechanical Engineering,
University of Colorado,
Boulder, Colo. 80309

This paper reports a series of experiments concerning the buckling of a slender fluid layer in a state of longitudinal compression. The experiments consist of floating a layer of highly viscous oil on a pool of water and, manually, compressing the layer from the side. Photographs of the buckled layer show conclusively that the buckling wavelength is largely insensitive to either the rate of compression or the viscosity of the fluid layer. The observations suggest that the buckling wavelength is actually a characteristic length scale (a property) of the fluid layer, in contrast with the buckling theory of purely viscous layers (Buckmaster, Nachman, and Ting, [7]) where the buckling wavelength remains to be determined randomly by initial disturbances.

1 Introduction

The concept of "fluid buckling" is relatively new in fluid mechanics research: during the past decade it has been used with increasing frequency to account theoretically for a number of flow phenomena, the explanation of which appears to shed new light on the theoretical origins of turbulence (Cruickshank [1], Bejan [2], Munson [3]). In the present paper, the buckling concept is used to describe a series of experimental observations of how a sheet of viscous fluid wrinkles as it is compressed from one end. As shown in Fig. 1, the fluid buckles and assumes a sinusoidal shape with characteristic wavelength λ. The objective of this experiment is to measure the buckling wavelength and to learn how this wavelength is influenced by the geometry (slenderness) of the fluid layer, the fluid properties and the rate of compression.

The buckling of highly viscous fluids was first studied by Biot [4]. In a series of papers, Biot developed the equations to describe the buckling of a multilayered viscous fluid. The equations were solved and were shown to be unstable when the viscous layers were subjected to an arbitrary finite strain with a small perturbation superimposed on the initial state. Solutions were determined numerically and were found to agree with solutions given by the theory of elasticity and viscoelasticity when the instability was of a significant magnitude. Biot's work was motivated by applications to the problems of tectonic folding of stratified geological structures.

The instability of jets, threads, and sheets of viscous fluids was studied qualitatively by Taylor [5]. In his paper, Taylor argues that the instability created by the compression of viscous fluids is the same as the Euler buckling of solid columns. Of the many experiments he conducts, two are especially relevant to the work presented here. In one, Taylor compresses a thread of an extremely viscous fluid floating on mercury and compares the resultant shape with the shapes of elastica under compression as calculated by Love [6]. The other experiment was designed to determine when a sheet of a viscous fluid under compression would become unstable.

With Taylor's experimental results in mind, Buckmaster, Nachman, and Ting [7] considered theoretically the buckling of a thin viscous layer (the *viscida* problem). The problem was that of a two-dimensional *viscida* immersed in vacuum, whose ends are moved together slowly so that inertia terms could be neglected. Since their analysis was not limited to small deformations, it was a generalization of Biot's work. They derived a *global* equation for the evolution of the slope of the centerline as a function of time and distance from one end, by integrating the momentum equations over the thickness of the viscous layer. This equation was then solved using asymptotic expansions for the case of small centerline deviation. Based on these results the solutions for large centerline deviations were found numerically. The case where surface tension effects cannot be neglected was incorporated into this theory by Buckmaster and Nachman [8] in a subsequent paper.

In a more recent paper, Suleiman and Munson [9] investigated the buckling of a thin viscous fluid layer subjected to linear shear. They found that if the dimensionless shear stress exceeded a critical value, the layer would buckle in a manner similar to the buckling of a thin elastic plate. In another study, Munson [10] examined experimentally the buckling of a falling viscous jet flowing out of a vertical slit orifice onto a horizontal plate. In this experiment Munson observed that the jet sometimes buckles in a manner similar to the buckling of a cantilever beam. Another experimental study was conducted by Cruickshank and Munson [11] on the spontaneous oscillations of a falling viscous jet flowing from a horizontal orifice onto a flat plate. They determined the

Contributed by the Fluids Engineering Division for publication in the JOURNAL OF FLUIDS ENGINEERING. Manuscript received by the Fluids Engineering Division, February 8, 1983.

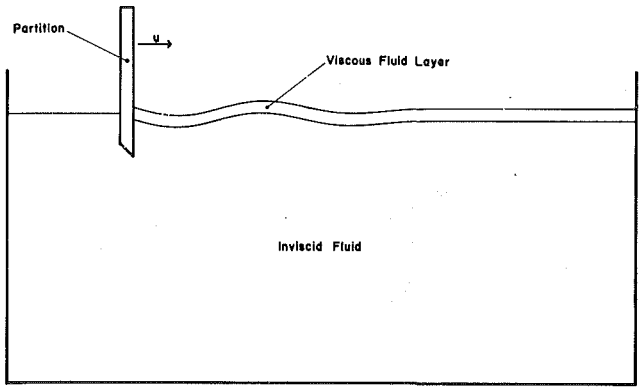

Fig. 1 The buckling of a thin viscous layer floating on top of a heavier inviscid fluid

minimum distance from the jet orifice to the flat plate for which the jet would buckle (termed the "buckling height") as a function of fluid and flow variables. They found that if the flow exceeded a critical Reynolds number, the jet does not buckle. Below this critical Reynolds number, surface tension becomes the dominant factor in influencing the buckling height. The origin of buckling was attributed to the jet flow transition from tension in the falling stage, to compression in the deceleration stage when the jet strikes the plate.

Commenting on Suleiman and Munson's paper, Bejan [2] noted that the buckling phenomenon is not only a property of highly viscous fluids, but also a property of inviscid columns (streams), and, as such, explains the "meander" phenomenon. The process of inviscid stream buckling was treated analytically by Bejan [12] who showed that all inviscid fluid layers buckle so that the wavelength is proportional to the layer thickness only. The proportionality between buckling wavelength and jet diameter was verified recently in two separate experiments, one involving the meandering of air streams driven by falling paper ribbons (Bejan [13]) and the other focusing on the buckled shapes of fast capillary jets (Stockman and Bejan [14]).

At this stage in our understanding of fluid buckling, an important discrepancy exists between the observed buckling behavior of viscous layers and the behavior predicted by the viscida theory [7]. The theoretical wavelength of the buckled shape is indeterminate and, presumably, dictated randomly by the original deformation (disturbance) of the straight layer. Experimental observations, on the other hand, seem to suggest that the buckling wavelength is not random [1, 5, 11]. Thus, the objective of the experimental work described in this paper is to establish whether the buckling wavelength of viscous layers in indeterminate, as in the *viscida* theory, or, in fact, a "characteristic" length. The experiment does not correspond fully to the geometry of Taylor [5] or Buckmaster et al. [7, 8], however, it does shed light on the uniqueness of the observed buckling wavelength.

2 Experiment

The experiment was designed to measure the buckling wavelength of a viscous fluid layer and to determine quantitatively what parameters affect the wavelength. The experiment is shown schematically in Fig. 1. A layer of viscous fluid, floating on a relatively inviscid fluid, is compressed by the partition. The partition extends into the inviscid fluid a distance on the order of the viscous layer's thickness and has a rate of compression u. The geometrical shape of the layer is given by the slenderness ratio L/d where L and d are the length and thickness of the unbuckled layer. The slenderness ratio was varied from about 20 to 70 by changing the thickness of the layer and leaving the length constant.

The experiment was carried out in an aluminum box with

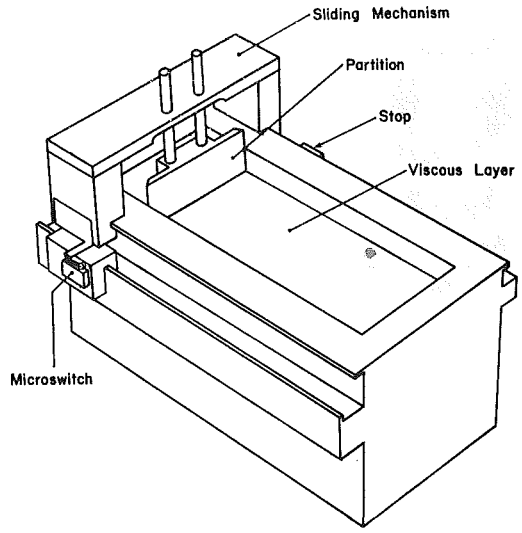

Fig. 2 Construction details of the experimental apparatus

inside dimensions measuring 20.3 cm in length, 7.6 cm in width and 10.2 cm in depth. The sides of the box serve as a track for a sliding mechanism carrying a partition (gate) which can be lowered into the box (see Fig. 2). It is by means of this partition that the layer is compressed. The sliding mechanism was designed to operate without vibrations and to hold the partition perpendicular to the viscous fluid layer and to the walls on each side. It also holds the partition in contact with the side walls preventing the fluid layer from escaping behind the partition as the viscous layer is compressed.

The sliding mechanism was moved by hand; in order to bring uniformity to the results, two stops were positioned to set the initial length L and to control the maximum excursion of the partition. As the sliding mechanism moved between the stops, it passed over a microswitch sending an electrical pulse to a timer and, at the same time, triggering the camera. The duration of the pulse was used to make a time of flight measurement, and with the assumption that the partition undergoes a constant acceleration, it was possible to determine the rate of compression at any instant. The accuracy of the velocity measurement is determined by the constant acceleration assumption. Since the compression stroke is very short (13 to 32 milliseconds) and the force applied by hand during that interval is approximately constant, the acceleration is also approximately constant.

Experiments were run to determine the effects of the excursion length and rate of compression on the buckling wavelength. In varying the excursion length, it was found that there exists an optimum range of lengths for the most accurate portrayal of the buckling phenomenon. This range was from 1 cm to 2 cm. If the excursion length was less, there was no visible buckling, and if it was greater, the buckling became so pronounced that the "waves" would collide. The effect of the rate of compression is discussed in greater detail in the next section.

It is important to note that although the buckled layer has the appearance of a propagating gravity wave, it is not. This is demonstrated by the observation that after the partition has stopped, the buckled shape remains stationary. In time, the amplitude decreases and eventually the layer reaches equilibrium again. In many cases the buckled shape and its wavelength remained visible and could be photographed for up to 30 minutes after the compression stroke. As shown in section 4, the observation that the amplitude of the buckled shape decreases away from the moving partition (Figs. 3, 4) can be explained by the fact that the layer is not uniformly compressed. The nonuniform compression rate can be due to

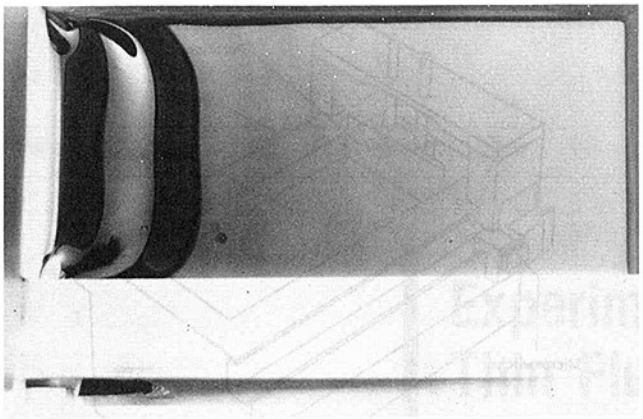

Fig. 3 Photograph showing the buckled layer as seen from above (the partition moves from left to right)

the no-slip condition along the side wall, or to the inertia of the fluid layer itself.

The buckling wavelength was measured photographically using a camera triggered by the trailing edge of the pulse created by the microswitch. Special lighting conditions were needed in order to make the buckling wavelength easy to measure on the photographs (Blake [15]). This system enabled one side of a "wave crest" to be illuminated while leaving the other side in darkness. The photograph then contained a series of light and dark bands where one light and one dark band together account for one wavelength. The sample photograph shown in Fig. 3 has three bands, implying that the buckled region extended one and one half wavelengths into the viscous fluid layer. The other photographs contained between two and five bands (see also Fig. 4).

In all the experiments involving data acquisition, Dow Corning 200 silicone oil was used as the viscous fluid and distilled water as the inviscid substance. The silicone oil has several desirable attributes such as its small variation in viscosity with temperature, its low surface tension, its immiscibility with water, and its availability over a wide range of high viscosities. In addition, any intermediate viscosity can be achieved simply by mixing a higher and lower viscosity in the proper proportions. Since, as shown in the next section, the buckling wavelength is not strongly dependent on viscosity, it was not necessary to know the precise viscosity, therefore, the oil viscosity reported in these experiments is the viscosity calculated based on Dow Corning information. Furthermore, the experiments were run at room temperature, which is within a few degrees of the temperature (75°F) at which the viscosity was measured. The viscosity of the silicone oil used in the experiments ranged from 10^3 to 10^5 centistokes (cSt) where one centistoke is approximately the viscosity of water and the units of stokes are centimeters squared per second. Lastly, the silicone oil was demonstrated to be a Newtonian fluid by Suleiman and Munson [9].

To set up the experiment, a flat, uniform layer of the viscous fluid, of a prescribed thickness, must be placed on the surface of the water. The method used was to put the silicone oil in a standard 100 ml burret with the following modifications: the tapered end of the burret was ground off, and the hole in the valve was drilled out to be the same size as the tube. The burret was held about a centimeter above the surface of the water and the oil was allowed to drain out until the desired thickness was obtained. Depending on the viscosity, it took from one to five hours to drain out the required amount. This extremely slow pouring rate allowed the oil to slowly creep across the surface of the water providing a flat, smooth layer. Knowing the volume of oil and the area of the layer, the thickness d could be calculated to an

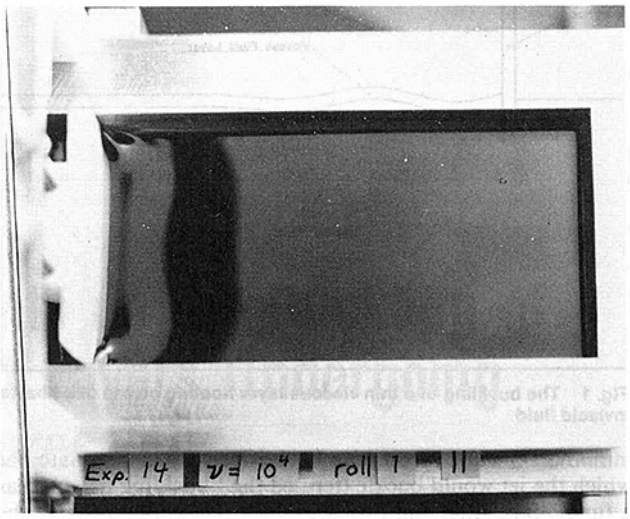

Fig. 4(a) $d = .394 \pm .003$ cm, $L = 16.35 \pm .03$ cm, $u = 42.3 \pm .2$ cm/s, $\nu = 10^4 \pm 400$ cSt

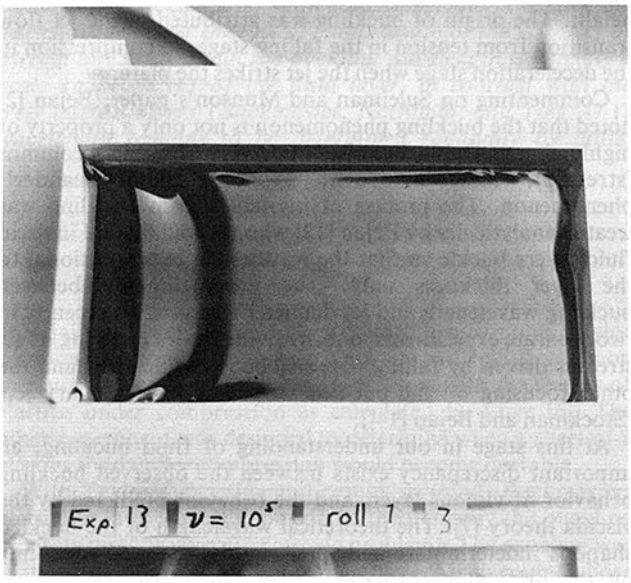

Fig. 4(b) $d = .264 \pm .003$ cm, $L = 16.35 \pm .03$ cm, $u = 32.6 \pm .2$ cm/s, $\nu = 10^5 \pm 4000$ cSt

Fig. 4 Two separate experimental runs:

accuracy of 0.003 cm with most of the error resulting from the meniscus on the edges of the oil layer.

Since the experiment sometimes took days to run, deaerated (distilled) water was needed for the lower fluid. Otherwise bubbles of air would form under the layer of oil creating little bumps in the surface.

4 Results

Despite the fact that in the present experiment the motion of the position is not mechanized, it is important to document the effect of changes in the rate of compression u. It is also important to report the minimum rate of compression necessary for buckling the layer. Referring to buckling in a purely two-dimensional layer geometry, Taylor [5] stated that when

$$-4\mu\epsilon d - T > 0 \tag{1}$$

the viscous sheet is unstable to disturbances of any wavelength, where μ and ϵ are the viscosity and the rate of strain. The total surface tension T is the sum of the oil-air interface T_{0a} and the water-oil interface T_{w0}. For two im-

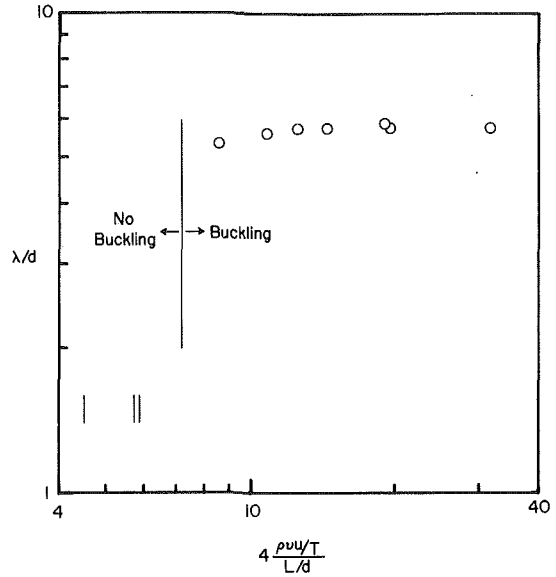

Fig. 5 The weak dependence between buckling wavelength (λ) and rate of compression (*u*). (Uncertainty in $\lambda/d = \pm 0.06$, in $4(\rho\nu u/T)/(L/d) = \pm 0.06$ at 20:1 odds)

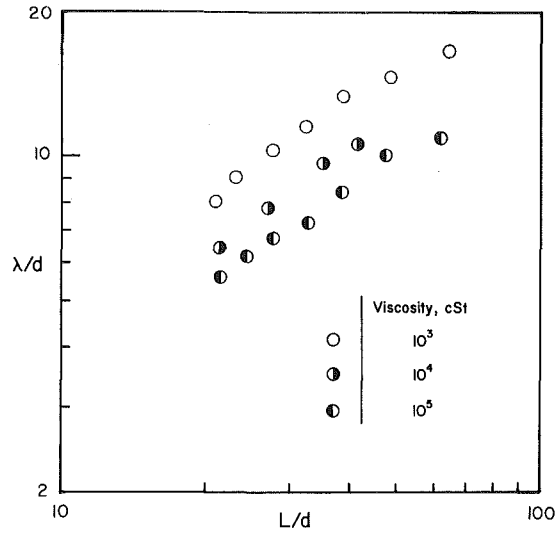

Fig. 6 The relationship between buckling wavelength (λ) and both length to thickness ratio (L/d) and viscosity (ν). (Uncertainty in $\lambda/d = \pm 0.06$, in $L/d = \pm 0.01$, in $\nu = \pm 0.04$ at 20:1 odds.)

miscible liquids, the value of T_{w0} is approximately $T_{wa} - T_{0a}$, where T_{wa} is the surface tension of the water-air interface (Suleiman and Munson [9], Davies and Rideal [16]). Therefore, $T = T_{0a} + (T_{wa} - T_{0a}) = T_{wa}$, that is, the total surface tension T is just the surface tension of the water-air interface. Upon substituting $-u/L$ for ϵ in Taylor's equation and rearranging, it is found that the layer buckles when

$$4(\rho\nu u/T)/(L/d) > 1 \tag{2}$$

It should be noted that Taylor's conclusions do not apply exactly to the present experiment. As shown in Figs. 3 and 4, the no-slip condition along the side walls gives rise to a three-dimensional flow such that only the middle portion of the buckled layer shows parallel waves and can be regarded approximately as two-dimensional. Therefore, the substitution $\epsilon = -u/L$ used to derive equation (2) can only be approximately valid. That $-u/L$ is not the rate of strain everywhere in the layer is demonstrated by the fact that buckling does not occur throughout the layer but only near the compressed end. Figures 3 and 4 show that sufficiently close to the partition, the bands (waves) are relatively constant size, hence, it is reasonable to assume that in that region the rate of strain is relatively constant. In cases where the photographed bands are unequal in size, the reported wavelength was calculated by averaging the first two bands.

For this experiment the viscous fluid layer had a slenderness ratio (L/d) of 25, a viscosity (ν) of 3×10^4 cSt, a density (ρ) of 0.975 g/cm^3, and a surface tension (T) of 72.8 dyne/cm. The results of the experiment are given in terms of the buckling wavelength to thickness ratio λ/d versus $4(\rho\nu u/T)/(L/d)$ and graphed as shown in Fig. 5. The data fall into two categories: points where the fluid buckled and points where the fluid did not. The cases in which buckling did not occur have no λ/d value and are indicated with short vertical lines at the bottom of the graph. The large vertical line indicates the approximate minimum value of $4(\rho\nu u/T)/(L/d)$ that will buckle the layer. This value is approximately 7, i.e., greater than the value 1 appearing in equation (2) derived from Taylor's buckling criterion (1). This discrepancy is not surprising in view of the three-dimensional effects and nonuniform ϵ that distinguish the present experiment from Taylor's two-dimensional geometry.

An important result of the present experiment is the independence of λ/d on the rate of compression, as witnessed by the nearly horizontal distribution of the data on Fig. 5. The data was limited on the right by the inability to compress the layer at a faster rate. This conclusion is further supported by the results given in Fig. 6 where each datum is an average obtained from three different rates of compression. In each set of three, the group $4(\rho\nu u/T)/(L/d)$ varies with an average 55 percent increase from the smallest to the largest value. However, the corresponding values of λ/d only have an average 5 percent increase, as indicated approximately by the size of the circles. Thus for a variety of L/d ratios and viscosities it can be seen that the sizable change in $4(\rho\nu u/T)/(L/d)$ has only a marginal, if any, effect on λ/d.

To determine the relationship between the buckling wavelength and the slenderness ratio, a series of experiments were conducted varying the thickness of the layer and using different viscosity oils. The data were obtained in the following manner. The partition was placed at the maximum distance from the far end so that $L = 16.4$ cm. The box was filled with water and then a thin layer of oil was poured onto the water surface from the burret. To obtain different slenderness ratios more oil was added from the burret, and allowed to reach equilibrium. For each slenderness ratio the layer was usually compressed three times. Between each compression the partition was moved back to its initial position and the oil layer was given enough time to reach equilibrium again. For each change in viscosity, the burret was drained of the previous oil and the new viscosity oil was poured in.

The results of these experiments are graphed as λ/d versus L/d in Fig. 6. The plot contains three sets of points indicated by an open circle and right and left half-filled circles for viscosities of 10^3 cSt, 10^4cSt, and 10^5cSt, respectively. It is clear from Fig. 4 that λ/d is dependent on L/d. For L/d less than 40 the slopes of the curves are almost unity, indicating that λ is proportional to L. Due to the construction of the experimental apparatus, the value of L/d could not be increased beyond 65.

The effect of viscosity on the buckling wavelength can also be interpreted from the data in Fig. 6. The value of λ/d decreases by about one-third when changing the viscosity from 10^3 cSt to 10^5 cSt and keeping L/d constant. This change is fairly consistent throughout the range of values of L/d. Within this range, then, the effect of viscosity on λ/d is seen to be very slight.

The error in the results presented here is governed primarily by the measured value of λ. The variables d, L, and u have all

been calculated to within 1 percent. The other variables influencing the results, although unknown precisely, remain constant throughout each experiment and therefore do not effect the overall trends shown in the graphs.

5 Conclusions

The object of this experimental report has been to present a series of observations concerning the buckling wavelength of a highly viscous fluid layer undergoing end-compression. The motivation for designing and running these experiments stemmed from the unresolved issue of whether the buckling wavelength is arbitrary (as in the *viscida* theory, Buckmaster et al. [7]), or a characteristic length of the layer. Based on the measurement produced by the present study, the following conclusions may be drawn:

1 In a fluid layer of fixed geometry and viscosity, the buckling wavelength is practically independent of the rate of compression, that is, independent of the layer velocity relative to the fluid ambient (Fig. 5).

2 The viscosity of the buckled layer has only a minor impact on the buckling wavelength (Fig. 6).

3 In the range $L/d < 100$ the buckling wavelength λ scales with the length of the compressed layer, L (Fig. 6).

In view of these findings, the wavelength of a buckled viscous layer emerges as a property of the layer (a characteristic length), as opposed to the undetermined length dictated by random initial disturbances assumed in the *viscida* theory.

Acknowledgment

This research was supported by the Office of Naval Research. The experimental apparatus and the instrumentation were constructed by Mr. Karl A. Rupp, Michael Hacker and Mr. Richard C. Cowgill.

References

1 Cruickshank, J. O., "Viscous Fluid Buckling: A Theoretical and Experimental Analysis with Extensions to General Fluid Stability," PhD thesis, Iowa State University, 1980.

2 Bejan, A., "Comments on 'Viscous Buckling of Thin Fluid Layers'," *Phys. Fluids*, Vol. 24, 1981, p. 1764.

3 Munson, B. R., "Reply to the Comment by A. Bejan," *Phys. Fluids*, Vol. 24, 1981, p. 1766.

4 Biot, M. A., "Theory of Viscous Buckling of Multilayered Fluids Undergoing Finite Strain," *Phys. Fluids*, Vol. 7, 1964, p. 855.

5 Taylor, G. I., "Instability of Jets, Threads, and Sheets of Viscous Fluids," *12th Intl. Congr. Appl. Mech.*, Stanford, 1968 (Berlin: Springer-Verlag, 1969), p. 543.

6 Love, A. E. H., *A Treatise on the Mathematical Theory of Elasticity*, 4th Ed., Dover, New York, 1944, p. 404.

7 Buckmaster, J. D., Nachman, A., and Ting, L., "The Buckling and Stretching of a Viscida," *J. Fluid Mech.*, Vol. 69, Part I, 1975, p. 1.

8 Buckmaster, J. D. and Nachman, A., "The Buckling and Stretching of a Viscida," *Q. J. Mech. Appl. Meth.*, Vol. 31, Part II, 1978, p. 157.

9 Suleiman, S. M. and Munson, B. R., "Viscous Buckling of Thin Fluid Layers," *Phys. Fluids*, Vol. 24, 1981, p. 1.

10 Munson, B. R., "Viscous Buckling of Slender Horizontal Jets," *Phys. Fluids*, Vol. 24, 1981, p. 1780.

11 Cruickshank, J. O., and Munson, B. R., "Viscous Fluid Buckling of Plane and Axisymmetric Jets," *J. Fluid Mech.*, Vol. 113, 1981, p. 221.

12 Bejan, A., "On the Buckling Property of Inviscid Jets and the Origin of Turbulence," *Letters in Heat and Mass Transfer*, Vol. 8, 1981, p. 187.

13 Bejan, A., "The Meandering Fall of Paper Ribbons," *Phys. Fluids*, Vol. 25, 1982, p. 741.

14 Stockman, M., and Bejan, A., "The Nonaxisymmetric (Buckling) Flow Regime of Fast Capillary Jets," *Phys. Fluids*, Vol. 24, 1982.

15 Blake, K. R., "Viscous Buckling of Thin Fluid Layers Undergoing End Compression," Master's thesis, University of Colorado, Boulder, 1982.

16 Davies, J. T., and Rideal, E. K., *Interfacial Phenomena*, Academic Press, New York, 1961.

R. C. Strawn
Acurex Corp.,
Aerotherm Division,
Mountain View, Calif. 94039

J. H. Ferziger
Professor.

S. J. Kline
Professor.
Fellow ASME

Thermosciences Division,
Department of Mechanical Engineering,
Stanford University,
Stanford, Calif. 94305

A New Technique for Computing Viscous-Inviscid Interactions in Internal Flows

A new viscous-inviscid interaction technique has been developed for computing separated flow in planar diffusers. The method couples a set of integral equations for the boundary layers to a fully elliptic potential core flow. Rapid convergence of the method is demonstrated for planar diffusers with large regions of transitory stall. For these cases, convergence of the new method is an order of magnitude faster than that obtained using the interaction schemes of Carter and Le Balleur. Good agreement between the prediction method and experimental data is obtained for diffusers that are operating near peak pressure recovery. More importantly, the onset of asymmetric detachment is successfully predicted for these cases.

1 Introduction

In this paper, planar diffuser flows with thin turbulent inlet boundary layers are modeled with separate zones of viscous and inviscid flow. The viscous effects are confined to the boundary layers, and the inviscid core flow is assumed to extend to the end of the diffuser. Matching between the viscous and inviscid solutions takes place at the adjacent zonal boundaries.

The principal objective of this paper is to develop a fast viscous-inviscid interaction procedure for use in predicting planar diffuser flows with large separation regions. This interaction scheme must couple a fully elliptic, two-dimensional solution of the inviscid flow field to a parabolic marching procedure for the boundary layers.

Other authors have used a one-dimensional inviscid core assumption to simplify the matching between the viscous and inviscid zones [1-4]. These methods were developed for diffusers with straight centerlines. The method described in this paper is designed for diffusers with strongly curved centerlines. In these cases, use of a two-dimensional, fully elliptic core model cannot be avoided. These diffusers also require curvature models for the convex and concave boundary layers; these effects will not be considered here, however.

There are several current methods for computing viscous-inviscid interactions with a two-dimensional inviscid flow. Among these are the methods of Carter [5, 6], Le Balleur [7, 8], Wigton [9], Veldman [10], and Moses [11, 12]. All of these schemes couple a system of elliptic equations for the inviscid flow to a set of nonlinear parabolic equations for the boundary layers. None of the existing interaction schemes was found to meet our requirements of a fast-running procedure that can compute internal flows with large regions of boundary layer separation. For this reason, we have developed a new interaction scheme that is designed specifically for internal flows.

2 Quasi-Simultaneous Interaction

The new scheme has an overall structure that Veldman [10] defines as quasi-simultaneous viscous-inviscid interaction. A schematic of this interaction scheme is given in Fig. 1. The subscript V refers to the most recent estimate of a quantity obtained from the viscous flow solution. Similarly, the subscript I refers to quantities obtained from the inviscid solution.

The method begins with an estimate for the location of the displacement surface (δ_I^* in Fig. 1). The inviscid solution is then computed for the displaced body, producing a velocity distribution U_I on the displacement surface. Next, the viscous equations are solved together with a simplified form of the inviscid flow equations. This coupling equation is a perturbation of the two-dimensional inviscid flow equations. Thus, approximations used in this relation will not be present in the converged result. This simplified inviscid flow model provides a strong interaction between the boundary layer and the inviscid flow. The result provides a new estimate for the

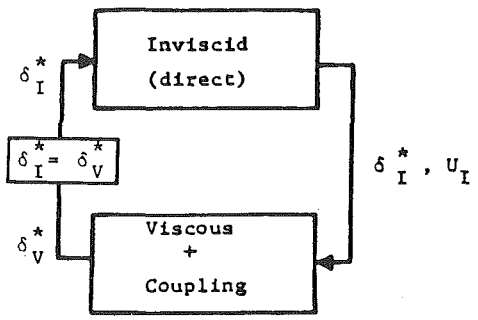

Fig. 1 Quasi-simultaneous interaction

Contributed by the Fluids Engineering Division for publication in the JOURNAL OF FLUIDS ENGINEERING. Manuscript received by the Fluids Engineering Division, April 1, 1983.

inviscid flow displacement surface, δ_v^*. Iteration continues until an appropriate convergence criterion is satisfied for the entire flow field.

The three major components in a quasi-simultaneous scheme for viscous-inviscid interaction can be listed as follows: (i) a model for the viscous flow, (ii) a model for the inviscid flow, and (iii) a simplified inviscid flow relation that can be coupled directly to the boundary layer equations.

3 Models for the Inviscid and Viscous Flow

For the cases described in this paper, the inviscid flow is assumed to be incompressible and irrotational. It is modeled with a boundary integral method developed by Bardina et al. [13]. This method is derived from the Plemelj integral formula and is related to panel methods applied to external flow. Matching between the viscous and inviscid flow occurs at $y = \delta^*$ along the diffuser walls.

The effective channel boundary is discretized with N points denoted by the complex coordinates $z_j = x_j + iy_j$, $j = 1,2, \ldots N$. Bardina et al. [13] show that any analytic function satisfies the following set of equations on the boundary

$$\sum_{j=1}^{N} A_{kj} f(z_j) = 0, \quad k = 1,2, \ldots, N \tag{1}$$

$$A_{kj} = \frac{z_{j+1} - z_k}{z_{j+1} - z_j} \ln \frac{z_k - z_{j+1}}{z_k - z_j} + \frac{z_k - z_{j-1}}{z_j - z_{j-1}} \ln \frac{z_k - z_j}{z_k - z_{j-1}} \tag{2}$$

$$A_{kk} = \ln \frac{z_k - z_{k+1}}{z_k - z_{k-1}}$$

where $f(z_j)$ is analytic inside and on the boundary. Choosing $f(z_j) = \ln |U_j| - i\alpha_j$ where U is the velocity and α the flow angle, the imaginary part of equation (1) can be written

$$\sum_{j=1}^{N} \mathrm{Im}(A_{kj})(\ln |U|)_j = \sum_{j=1}^{N} \mathrm{Re}(A_{kj})\, \alpha_j,$$

$$k = 1, 2, \ldots, N \tag{3}$$

The flow angles are specified as tangent to the displacement surface. In order to have a well-posed problem, we must also set $(\ln |U_1|) = 0$ at one point on the diffuser inlet plane. The set of equation (3) can then be solved to find $\ln |U|$ at every point on the boundary.

The main advantages of this boundary integral method are its speed and flexibility. For a given geometry, the method requires the solution of an $N-1$ by $N-1$ system of linear equations, where N represents the total number of points around the effective channel contour. No coordinate mappings are needed, since the problem is solved in the physical plane and only on its boundaries. Values at interior points are not required, since matching to the viscous flow occurs only at the zonal boundaries.

An integral method has been used to model the viscous flow. Originally, the complete lag entrainment method of East et al. [14] was incorporated into the new viscous-inviscid interaction procedure. Rapid convergence of the method was obtained for both attached and separated flow. However, the converged results did not show good agreement with experimental data in cases with large regions of separated flow. Pressure recovery after detachment was consistently too large for all tested flows. An example of this behavior is discussed in Section 6.

Another boundary layer integral method was found to give the best results of any of the viscous flow models tested. It consists of two ordinary differential equations – the von Kármán momentum integral equation (4) and the definition of boundary layer entrainment given by equation (5).

$$\frac{d\theta}{dx} + (2+H)\frac{\theta}{U}\frac{dU}{dx} = \bar{C}_f/2 \tag{4}$$

$$\frac{1}{U}\frac{d}{dx}[U(\delta - \delta^*)] = E \tag{5}$$

The shape factor correlation used is that of East et al. [14]. For incompressible flow it can be written as:

$$H^* = 3.15 + \frac{1.72}{H-1}, \quad H \le 1.6$$

$$H^* = 4.5455 + 295 \exp(-3.325\, H), \quad H > 1.6 \tag{6}$$

Other algebraic relations used in the boundary layer model are the skin friction correlation of Lyrio et al. [15] (equation (7)) and Head's entrainment correlation (equation (8)) (see reference [16]).

$$V_T = (0.44)(1 - 2\Lambda)^{0.885} \left(\frac{\Lambda}{\mathrm{Re}_{\delta^*}} \right)^{0.115} \tag{7}$$

$$E = 0.0306(0.8234(H-1.1)^{-1.287} + 0.3)^{-0.6169}, \quad H \le 1.6$$

$$E = 0.0306(1.5501(H-0.6778)^{-3.064} + 0.3)^{-0.6169}, \quad H > 1.6 \tag{8}$$

It should be pointed out that the objective of this work is

Nomenclature

a = fluid speed of sound
C_f = friction coefficient = $2\bar{\tau}_w/\rho U^2$
C_p = pressure coefficient = $2(P - P_1)/\rho U^2$
E = nondimensional entrainment rate
H = shape factor = δ^*/θ
H^* = shape factor = $(\delta - \delta^*)/\theta$
M = Mach number
P = pressure
Q = volume flow rate
Re_{δ^*} = displacement thickness Reynolds number = $\rho U \delta^*/\mu$
S = distance along diffuser wall measured from throat
u_τ = shear velocity = $(\mathrm{sign}\ \bar{\tau}_w)\sqrt{|\bar{\tau}_w|/\rho}$
U = boundary layer edge velocity
V_T = nondimensional shear velocity = $u_\tau/\kappa U$
W = passage width
x = distance along the diffuser wall
y = distance normal to diffuser wall
γ = ratio of specific heats
δ = boundary layer thickness
δ^* = boundary layer displacement thickness
η = relaxation parameter
θ = boundary layer momentum thickness
κ = von Kármán constant = 0.41
Λ = shape factor = δ^*/δ
μ = dynamic viscosity
ρ = fluid density
τ_w = wall shear stress
2θ = total included angle for a straight-wall diffuser
$\bar{(\ )}$ = time-averaged quantity

Subscripts

0 = stagnation condition
u = upper-wall boundary layer
l = lower-wall boundary layer
1 = inlet quantity
v = viscous flow quantity
I = inviscid flow quantity

Superscripts

n = iteration number

not to develop new turbulent boundary layer models for separated flow. It is, rather, to use a model that will give reasonably good results for planar diffuser flows. The model described above is satisfactory in this regard.

4 Viscous-Inviscid Coupling Equation

The key element in a quasi-simultaneous interaction scheme is a simple approximation for the inviscid flow that can be coupled directly to the boundary layer model of Section 3. Consider the two-dimensional internal flow sketched in Fig. 2. The upper-wall boundary layer is ignored for now. U_I is obtained from a two-dimensional inviscid flow solution based on an initial guess for δ_I^*. For incompressible flow, we can define an approximate local volume flux using a one-dimensional model.

$$Q = U_I(W - \delta_I^*) \tag{9}$$

Our objective is to generate an equation relating U_v and δ_v^* that can be directly coupled to the boundary layer equations. This allows U_v to be treated as a dependent variable and thus gives the strong coupling effect that prevents singularities in separated flows. We can accomplish this by requiring that δ_v^* and U_v relate to each other in the one-dimensional manner of equation (9), with the volumetric flow rate determined by the inviscid solution and the previous estimate of δ_I^*; i.e.,

$$U_I(W - \delta_I^*) = U_v(W - \delta_v^*) \tag{10}$$

Equation (10) can be differentiated to give

$$\frac{d}{dx}[U_I(W - \delta_I^*)] - U_v\frac{dW}{dx} = (W - \delta_v^*)\frac{dU_v}{dx} - U_v\frac{d\delta_v^*}{dx} \tag{11}$$

Equation (11) can then be directly coupled to the viscous flow equations (4–8). The resulting system of ordinary differential equations is formulated with primary variables H, U_v, and δ_v^*, as shown in equation (12). The coefficients R_{ij} and P_i are given in reference [17].

$$\begin{matrix}\text{momentum}\\ \text{entrainment}\\ \text{coupling}\end{matrix}\begin{bmatrix} R_{11} & R_{12} & R_{13} \\ R_{21} & R_{22} & R_{23} \\ R_{31} & R_{32} & R_{33}\end{bmatrix}\begin{bmatrix} \frac{dH}{dx} \\ \frac{dU_v}{dx} \\ \frac{d\delta_v^*}{dx}\end{bmatrix} = \begin{bmatrix} P_1 \\ P_2 \\ P_3\end{bmatrix} \tag{12}$$

The iteration around the cycle of Fig. 1 is realized as follows. An initial guess is made for δ_I^*, and the two-dimensional inviscid flow is solved for U_I. Next, the viscous flow equations are solved simultaneously with the approximate coupling relation of equation (11). This generates updated values for U_v and δ_v^*. This new distribution of δ_v^* is then used as a boundary condition for the inviscid flow as the second iteration begins. When convergence is achieved, $\delta_I^* = \delta_v^*$ and $U_I = U_v$, and equations (10) and (11) are trivially satisfied. Thus, the one-dimensional approximation for the inviscid flow is no longer present in the converged result.

The coupling equations (10) and (11) are written for a case of an inviscid top wall. When a boundary layer is present on the upper wall of the channel, the diffuser width (W) in equations (10) and (11) must be replaced by $(W - \delta_u^*)$; i.e., the upper-wall displacement thickness is subtracted from the overall width to obtain the effective channel area seen by the lower-wall boundary layer. Note that the viscous-inviscid interaction procedure can solve only one boundary layer at a time. If both boundary layers interact with the inviscid core, the solution to the entire flow field must be obtained by alternating the interaction from one wall to the other.

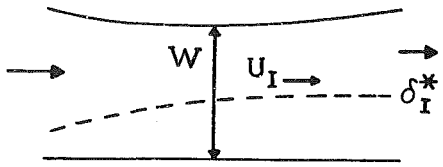

Fig. 2 An idealized internal flow

There are two reasons why the coupling relation of equation (11) has been chosen for this interaction scheme. First, a one-dimensional inviscid flow approximation is an accurate one for internal flow. Thus, the method should converge quickly. Second, the one-dimensional approximate relation allows for a strong interaction between the boundary layer and the inviscid flow. Hence, the overall interaction method should be robust.

For compressible flow, the approximate inviscid relation of equation (11) takes the following form:

$$\frac{d}{dx}[\rho_I U_I(W - \delta_I^*)] = \frac{d}{dx}[\rho_v U_v(W - \delta_v^*)] \tag{13}$$

The isentropic flow relations of equations (14) and (15) can be used to express ρ_I and ρ_v in terms of U_I and U_v, respectively.

$$\frac{U}{a_0} = M\left(1 + \frac{\gamma - 1}{2}M^2\right)^{-1/2} \tag{14}$$

$$\frac{\rho}{\rho_0} = \left(1 + \frac{\gamma - 1}{2}M^2\right)^{1/1-\gamma} \tag{15}$$

The system of equations (13) to (15) can then be coupled directly to the boundary layer model.

By using a linearized stability analysis of the type described by Le Balleur [7] and Wigton [9], one can show that the new interaction scheme for internal flows is inherently stable for both subsonic and supersonic attached flow. Details are given in reference [17]. For the case of separated subsonic flow, there is a possible stability problem for high-frequency disturbances on fine grids. No instabilities were encountered for any of the separated flows tested in this paper or in reference [17]. If stability problems are encountered, underrelaxation can always be used to make the method inherently stable. If underrelaxation is required, the $\delta_I^* = \delta_v^*$ box in Fig. 1 is replaced by $(\delta_I^*)^{n+1} = \eta(\delta_v^*)^n + (1 - \eta)(\delta_I^*)^n$, where η is a relaxation parameter.

Finally, it is shown in reference [17] that unstable behavior of the new viscous-inviscid interaction scheme is expected for the case of supersonic separated flow. This instability cannot be corrected by using underrelaxation.

It is important to point out that the new interaction scheme has been tested only for the case of incompressible flow. The above comments are only our estimates of its expected behavior for compressible flow cases.

5 Test Cases: Iteration Histories

An examination of the convergence history of the new interaction method has been made for two test cases. An additional test case is presented in reference [17]. All of these cases involve incompressible flow in internal passages with large regions of boundary layer separation. The converged results for these flows and their comparisons to experimental data are given in Section 6 of this paper. The first case is the experimental flow of Simpson et al. [18]. The calculation is set up as described in Kline et al. [19]. A separating boundary layer is located on the lower surface of a two-dimensional channel. The upper surface consists of an experimentally measured streamline located near the physical top wall of the

channel. This streamline is assumed to be an inviscid surface. Thus only one boundary layer interacts with the inviscid flow.

For this flow, Fig. 3 compares the convergence rate of the new interaction method to the methods of Carter [5] and Le Balleur [7]. The Carter method is used without overrelaxation, which has been suggested in some cases. All three interaction methods are used with the same models for the inviscid and viscous flow zones. Therefore, all converge to the same solution. Fractional error in δ^* is defined as $((\delta^*)'' - \delta_f^*)/\delta_f^*$, where δ_f^* is the converged result.

Figure 3 shows the convergence at the point $x = 3.21$ meters in the flow field. This point is near the location of incipient detachment. Convergence of the new interaction scheme is very fast – approximately two iterations for <1 percent error in δ^* at every point in the flowfield. This compares to 30+ iterations required by the other two methods.

The second test case is the $2\theta = 10$ deg symmetric diffuser tested by Ashjaee et al. [20]. This is an example of a straightwall diffuser with incompressible flow that is operating at peak pressure recovery. An asymmetric transitory stall is present on the lower surface of the diffuser. In order to avoid the added complication of interacting both the attached and detached boundary layers with the inviscid flow, the displacement surface for the attached boundary layer is specified at the outset and held constant at its experimentally measured value. Thus only the separated boundary layer interacts with the inviscid flow.

For this flow, Fig. 4 presents interaction histories for the three interaction methods. These are plotted at $S/W_1 = 10.8$ along the lower diffuser wall. This point is located just beyond the measured location of zero mean wall skin friction. Once again, the new interaction method shows rapid convergence. Its level of convergence over the entire flow field after just one iteration is equal to that of either of the other two methods after 30+ iterations.

The test cases presented here demonstrate two important characteristics of the new interaction method for internal flows. First, the method converges very rapidly, and second, the method can handle large regions of boundary layer separation.

6 Results

Simpson et al. [18]: Separating Boundary Layer. This flow was described in Section 5. Results for U versus X are presented in Fig. 5. Agreement with experimental results is quite good, particularly in the region of separated flow ($X/X_{ref} > 13.0$). Also presented in Fig. 5 are converged results using the boundary layer model of East et al. [14]. Boundary layer detachment occurs at approximately $X/X_{ref} = 13.2$. Beyond this point, the East et al. boundary layer model predicts values of velocity that are too low.

The corresponding results for δ^* versus X are presented in Fig. 6. Again the agreement is quite good using the new boundary layer model. Note that the initial guess for δ^* is quite far from the converged result. The iteration history for this flow was discussed in Section 5. Convergence to <1 percent error in δ^* for the entire flow is achieved after only two iterations. Sixty node points were evenly spaced around the effective channel contour. Computation time was approximately ten CPU seconds per iteration on a VAX 11-750 computer.

Ashjaee et al. [20]: Symmetric Diffusers. These experimental data are from a study of straight-wall symmetric diffusers with low-speed incompressible flow. These diffusers have moderate inlet blockage ($(2\delta^*/W)_1 = 0.027$), and an aspect ratio of 4. Measurements of C_p versus x were recorded along the upper and lower diffuser walls. Also, boundary layer profiles were measured along the side walls of the $2\theta = 10$ deg diffuser.

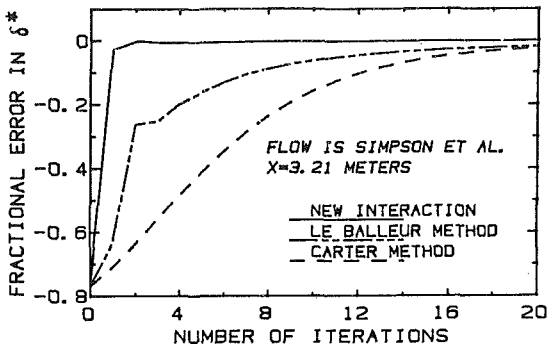

Fig. 3 Comparison of convergence rates for Simpson et al. [18] separating boundary layer flow (x = 3.21 m)

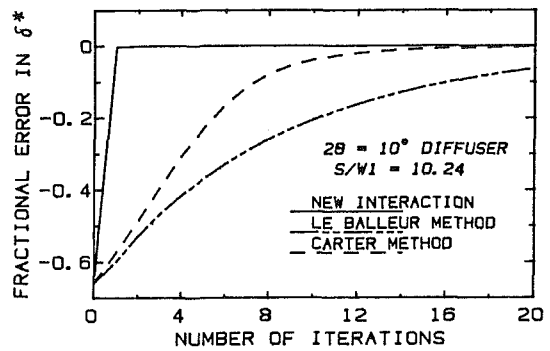

Fig. 4 Comparison of convergence rates for Ashjaee et al. [20], $2\theta = 10$ deg symmetric diffuser

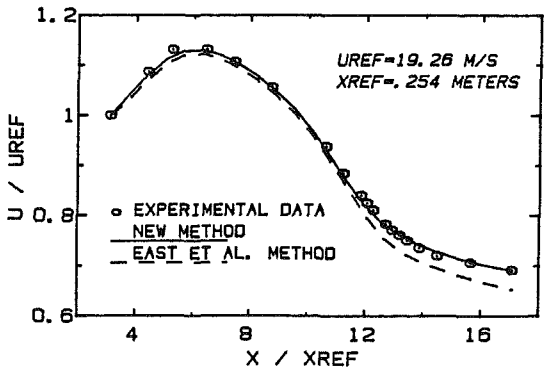

Fig. 5 Predicted and experimental results for U/U_{ref} vesus X/X_{ref}. Flow is that of Simpson et al. [18], separating boundary layer.

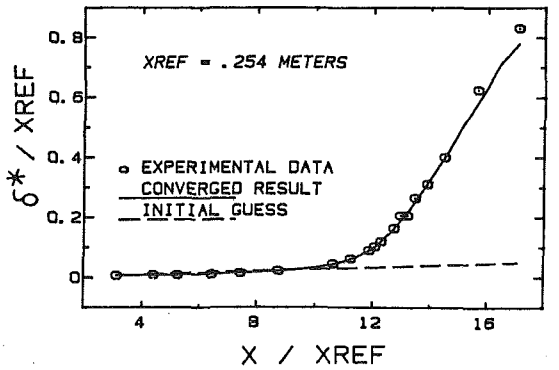

Fig. 6 Predicted and experimental results for δ^*/X_{ref} versus X/X_{ref}. Flow is that of Simpson et al. [18], separating boundary layer.

For a symmetric diffuser, it is easy to show that the solution to the coupled set of elliptic inviscid equations and parabolic boundary layer equations is not unique. For symmetric diffusers with asymmetric stall regions, the boundary layer may separate from either the upper or lower channel walls. Also, there must be a symmetric solution to the problem.

Ashjaee et al. [20] have shown experimentally that asymmetric detachment from either side wall is possible for a symmetric diffuser. The symmetric solution for diffusers with separated flow has been seen experimentally only at very high angles of divergence. For diffusers that operate with transitory stall, the symmetric solution is unstable. This instability is the result of the interaction between the separating boundary layer and the two-dimensional inviscid flow.

This same behavior is found for the numerical model equations. For diffusers that operate in the transitory stall flow regime, the iterative method never converged to a symmetric solution. For attached flow, however, the method yields the symmetric result. Note that the present viscous-inviscid interaction procedure deals with only one boundary layer at a time. The solution procedure alternates from wall to wall until convergence is achieved for the entire flow field. This extra level of iteration can require large amounts of computer time, unless one uses an efficient viscous-inviscid interaction procedure.

For cases with transitory stall, it is possible for the model equations to converge to either of the asymmetric solutions. The structure of the iteration procedure determines which solution is obtained. Assume that initial guesses of attached flow are made for both of the wall boundary layers. If the iteration procedure begins with the lower-wall boundary layer in a symmetric diffuser, this wall will become the stalled wall, and vice versa. Note that this iteration structure does not force the solution to an asymmetric result. In an unstalled diffuser, the method converges to the expected symmetric solution. If more than one asymmetric solution exists for the system of equations, the initial ordering of iterations simply determines which asymmetric solution is obtained.

Figure 7 presents experimental results for pressure recovery in symmetric diffusers with $2\theta = 4$, 6, and 7 deg. The predicted pressure recovery for these diffusers is slightly higher than the experimental data. The prediction method of Lyrio et al. [15] showed similar disagreement at low opening angles. For low aspect ratio diffusers with small opening angles, the end-wall boundary layers may contribute significantly to the channel blockage. In these cases, the pressure recovery will be less than that of a two-dimensional flow.

Figure 8 shows pressure recovery results for $2\theta = 8$, 9, and 10 deg. Agreement between predicted performance and experimental data is good. More importantly, the new viscous-inviscid interaction method correctly predicts the onset of asymmetric detachment. For $2\theta < 8$ deg, the method converges to a symmetric result. For $2\theta > 8$ deg, the method converges to an asymmetric solution with flow detachment on one diffuser wall. This behavior is in excellent agreement with the experimental observations of Ashjaee et al. [20].

For all of these different calculations, 60 node points were evenly spaced around the effective channel area. Convergence to <1 percent error in δ^* was obtained after 20–30 iterations over the entire channel. Reference [17] contains additional comparisons to experimentally tested diffuser flows. These include cases in which the diffusers have mild centerline curvature.

The results presented above show that the combination of the new viscous-inviscid interaction method and the integral boundary layer method of Section 3 is successful in predicting the performance of low-speed planar diffusers. Convergence of the method is extremely fast, and accurate results are obtained.

This represents the first time that planar diffusers with transitory stall have been computed with a fully two-dimensional inviscid core. The key to the prediction method is the new scheme for viscous-inviscid interaction. Its flexibility for incorporating different boundary layer procedures makes it ideal for testing boundary layer turbulence models in separated flow.

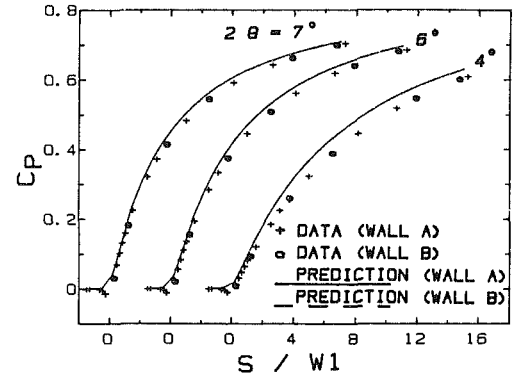

Fig. 7 Predicted results of C_p versus S/W_1. Experimental data are from Ashjaee et al. [20], symmetric diffuser study.

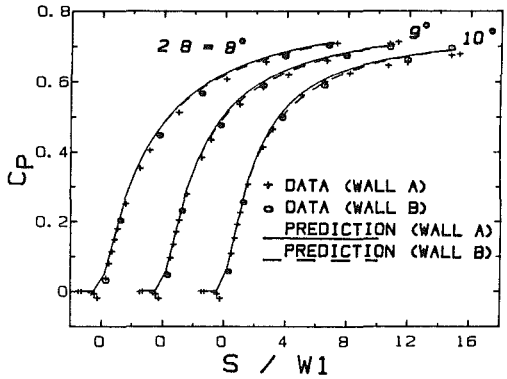

Fig. 8 Predicted results for C_p versus S/W_1. Experimental data are from Ashjaee et al. [20], symmetric diffuser study.

7 Conclusions

- A new viscous-inviscid interaction procedure has been developed for computing planar diffuser flows. The method is applicable to cases with both subsonic and supersonic flow.
- The iterative interaction scheme has been shown to converge very quickly in several incompressible test cases. These test cases contain large regions of separated flow. For these test cases, convergence rates are an order of magnitude faster than those obtained using the Carter [5] and LeBalleur [7] interaction methods. The improvement in speed of computation is achieved by use of an approximate one-dimensional continuity equation at each marching step. The approximation disappears in the converged result.
- The interaction scheme has been used successfully to predict cases of incompressible flow in planar diffusers. These predictions represent the first time that diffusers with asymmetric detachment have been computed with a fully two-dimensional inviscid flow model.
- A boundary layer model has been developed for diffusers with separated flow. Good agreement between the prediction method and experimental data is seen for incompressible symmetric diffusers that are operating near peak pressure recovery ($2\theta = 8$–10 deg). More importantly, the onset of asymmetric detachment is successfully predicted for these cases.

References

1 Moses, H. L., and Chappell, J. R., "Turbulent Boundary Layers in Diffusers Exhibiting Partial Stall," Trans. ASME *Journal of Basic Engineering*, Vol. 89, Sept. 1967, pp. 655–665.

2 Bower, W. W., "Analytical Procedure for Calculation of Attached and Separated Subsonic Diffuser Flows," *J. of Aircraft*, Vol. 13, No. 1, 1976, pp. 49–56.

3 Ghose, S., and Kline, S. J., "Prediction of Transitory Stall in Two-Dimensional Diffusers," Rept. MD-36, Thermosciences Div., Mech. Engrg. Dept., Stanford University, Dec. 1976. See also ASME JOURNAL OF FLUIDS ENGINEERING, Vol. 100, Dec. 1978, pp. 419–426.

4 Bardina, J., Lyrio, A., Kline, S. J., Ferziger, J. H., and Johnston, J. P., "A Prediction Method for Planar Diffuser Flows," ASME JOURNAL OF FLUIDS ENGINEERING, Vol. 103, June 1981, pp. 315–321.

5 Carter, J. E., "A New Boundary Layer Interaction Technique for Separated Flow," NASA-TM-78690, 1978.

6 Carter, J. E., "Viscous-Inviscid Interaction of Transonic Turbulent Separated Flow," AIAA 81-1241, presented at AIAA 14th Fluid and Plasma Dynamics Conference, Palo Alto, CA, June 1981.

7 Le Balleur, J. C., "Couplage Visqueux Non Visqueux: Methode Numerique et Applications Aux Ecoulements Bidimensionals Transoniques et Supersoniques," La Recherche Aerospatial, No. 1978-2, Mar.–Apr. 1978, pp. 67–76.

8 Le Balleur, J. C., "Calcul des Ecoulements a Forte Interaction Visqueuse au Moyen de Methodes de Couplage," Paper No. 1, AGARD Conference Proceedings No. 291, Feb. 1981.

9 Wigton, L. B., "Viscous-Inviscid Interaction in Transonic Flow," Ph.D. thesis, Dept. of Applied Mathematics, University of California, Berkeley, CA, May 1981.

10 Veldman, A. E. P., "Calculation of Incompressible Boundary Layers with Strong Viscous-Inviscid Interaction," Paper No. 12, AGARD Conference Proceedings No. 291, Feb. 1981.

11 Moses, H. L., Jones, R. R., O'Brien, W. F., and Peterson, R. S., "Simultaneous Solution of the Boundary Layer and Freestream with Separated Flow," *AIAA Journal*, Vol. 16, No. 1, Jan. 1978, pp. 61–66.

12 Moses, H. L., Thomason, S. B., and Jones, R. R., "Simultaneous Solution of the Inviscid Flow and Boundary Layers for Compressor Cascades," *AIAA Journal*, Vol. 20, No. 10, Oct. 1982, pp. 1466–1468.

13 Bardina, J., Kline, S. J., and Ferziger, J. H., "Computation of Straight Diffusers at Low Mach Number Incorporating an Improved Correlation for Turbulent Detachment and Reattachment," Rept. PD-22, Thermosciences Div., Dept. of Mech. Engrg., Stanford University, Feb. 1982.

14 East, L. F., Smith, P. D., and Merryman, P. J., "Prediction of the Development of Separated Turbulent Boundary Layers by the Lag-Entrainment Method," Tech. Rept. 77046, British Royal Aircraft Establishment, 1977.

15 Lyrio, A., Ferziger, J. H., and Kline, S. J., "An Integral Method for the Computation of Steady and Unsteady Turbulent Boundary Layer Flows, Including the Transitory Stall Regime in Diffusers," Rept. PD-23, Thermosciences Div., Dept. of Mech. Engrg., Stanford University, Mar. 1981. See also Ferziger, J. H., Lyrio, A., and Bardina, J. G., "New Skin Friction and Entrainment Correlations for Turbulent Boundary Layers," ASME JOURNAL OF FLUIDS ENGINEERING, Vol. 104, No. 4, Dec. 1982, pp. 537–540.

16 Cebeci, T., and Bradshaw, P., *Momentum Transfer in Boundary Layers*, McGraw-Hill, New York, 1977, p. 193.

17 Strawn, R. C., Kline, S. J., and Ferziger, J. H., "Flowfield Prediction and Design of Internal Passages with Strong Viscous-Inviscid Interaction," Rept. PD-27, Thermosciences Div., Dept. of Mech. Engrg., Stanford University, Feb. 1983.

18 Simpson, F. A., Chew, Y. T., and Shivaprasad, B. G., "Measurement of a Separating Turbulent Boundary Layer," Tech. Rept. SMU-4-PU, Apr. 1980.

19 Kline, S. J., Cantwell, B. J., and Lilley, G. M. (eds.), *Proceedings of 1980–81 AFOSR-HTTM-Stanford Conference on Complex Turbulent Flows, Vol. II*, Thermosciences Div., Dept. of Mech. Engrg., Stanford University.

20 Ashjaee, J., Johnston, J. P., and Kline, S. J., "Subsonic Turbulent Flow in Plane Wall Diffusers: Peak Pressure Recovery and Transitory Stall," Rept. PD-21, Thermosciences Div., Dept. of Mech. Engrg., Stanford University, July, 1980. See also ASME JOURNAL OF FLUIDS ENGINEERING, Vol. 102, Sept. 1980, pp. 275–282.

Theoretical Study on the Flow About Savonius Rotor

Takenori Ogawa
Associate Professor,
Hyogo University of Teacher Education,
Department of Practical Life Studies,
Yashiro, Hyogo, 673-14 Japan

A method for the two-dimensional analysis of the separated flow about Savonius rotors is presented. Calculations are performed by combining the singularity method and the discrete vortex method. The method is applied to the simulation of flows about a stationary rotor and a rotating rotor. Moreover, torque and power coefficients are computed and compared with the experimental results presented by Sheldahl et al. Theoretical and experimental results agree well qualitatively.

Introduction

In comparison with efficiencies of propeller-type and Darrieus wind turbines, the efficiency of the Savonius-type wind turbine is generally not high. However, the starting torque of the Savonius rotor which is one of the low-speed wind turbines, is large and the rotor starts to rotate by itself, as soon as wind begins to blow from any direction. On the other hand, it is not easy for the high-speed wind turbines like propeller-type and Darrieus wind turbines to start by themselves. On account of the above-mentioned advantage and also of the simple structure, Savonius rotors may find applications for small-scale household wind turbines and for a starter of the large-scale vertical-axis high-speed wind turbine.

Since Savonius [1] published his work in 1931, the Savonius rotor has been investigated experimentally by Bach [2], Khan [3], Charwat [4], Sheldahl et al. [5], Sivasegaram [6] and others. Theoretical studies are not many. Though the momentum theory can also be applied to Savonius rotors as an analytical method, it is not possible to represent the difference between performances of various types of wind turbines by this method, much less to clarify the effects of each parameter of the Savonius rotor on its performance. Other theories for wind turbines are the blade element theory [7], and vortex theory [8, 9]. These methods are, however, those for the high-speed wind turbines like propeller-type and Darrieus turbines, and are not suitable for the wind turbine like the Savonius type in which the flow separates from the blade surface. As for the Savonius rotor, an analytical model has been developed for the performance analysis by Wilson et al. [10], and then Van Dusen and Kirchhoff [11] have presented a vortex sheet model. Though these models contribute to the development of Savonius rotors as the first two theoretical analyses, they include an assumption to ignore the flow separation from bucket tips of the rotor. As shown in the flow field investigation presented by Wilson et al. [11], the actual flow about the Savonius rotor is complex, that is, it separates somewhere at all bucket angular positions. This is easily seen from the shape of buckets and their configuration. Lately, the discrete vortex method attracts attention as a method to analyze such a separated flow theoretically. This method has been applied to separated flows about an inclined flat plate [12–14], a circular cylinder [15, 16], an airfoil [17] and the flow behind the square-based body [18, 19] in the uniform flow.

This work is an attempt to analyze the flows about the rotating and stationary Savonius rotors with the aid of the discrete vortex method. One of the advantages of the discrete vortex method is, that the separated viscid flow at large Reynolds number can be analyzed as a potential flow by employing discrete vortices. However, as shown in earlier studies, the results obtained by this method are not accurate quantitatively, though the method contributes to the flow simulation and then, to qualitative explanation of the flow.

In the present work, fundamental equations to analyze the flow in the physical-plane directly without conformal mapping are presented. Then, influences of bucket angular positions on the static torque of the rotor are investigated, and power coefficients of the rotating rotor are calculated.

The flow patterns about stationary and rotating rotors are also presented and above-mentioned computed results are compared with the experimental results presented by Sheldahl et al. [5].

Discrete Vortex Method

In the present study, the Savonius rotor consists of two thin semicircle buckets as shown in Fig. 1. The rotor is placed in the uniform flow, which is parallel to the x-axis. The center of revolution agrees with the origin of the coordinate system.

In analyses performed by the use of the discrete vortex method, a flat plate and an ellipse are mapped conformally into a circle and in general, analyzed in the mapped plane. However, in the case that the shape is complex and moreover it rotates, it is not easy to find the mapping function, and advantages of the mapping are few. Accordingly, the analysis is developed in the physical plane with the aid of the singularity method which has been applied to the cascade theory [20]. To satisfy the boundary condition that the bucket contours agree with stream lines in the relative flow system,

Contributed by the Fluids Engineering Division of THE AMERICAN SOCIETY OF MECHANICAL ENGINEERS and presented at the 7th Annual Energy Sources Technology Conference and Exhibition, New Orleans, La., February 11–17, 1984. Manuscript received by the Fluids Engineering Division, October 5, 1982. Paper No. 84-FE-12.

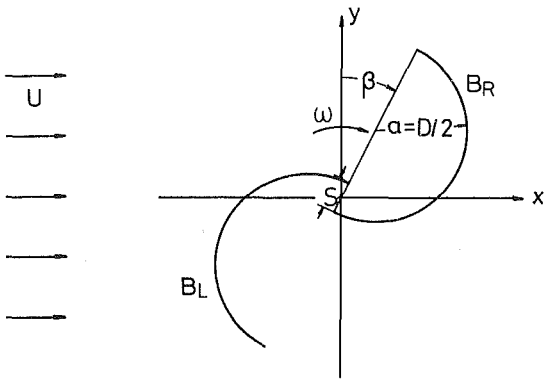

Fig. 1 Configuration of the Savonius rotor

bound vortices $d\Gamma_{Ri}$ and $d\Gamma_{Li}$ are distributed on each bucket surface. Free vortices shed from the nascent point, which are s_d distant from the bucket edges (Fig. 2). There are two methods to introduce the first free vortex. One is the method to fix the position of the first nascent vortex and make the strength of the first free vortex unknown [12, 14]. The other is the method to give the strength of the vortex and to make its position unknown [13]. In this study the former is used.

As shown in Fig. 2, each of bucket contours B_R and B_L is divided into m equal line segments, and bound vortices $d\Gamma_{Ri}$ and $d\Gamma_{Li}(i=1, \ldots, m)$ are distributed on the midpoints of each segment. The boundary condition that the bucket contour agrees with one of the relative stream lines is expressed as

$$\mathrm{Im}\{\bar{w}e^{i\gamma}\} = r\omega\cos(\gamma-\theta) \tag{1}$$

where $\bar{w}$ is the complex velocity induced by bound vortices $d\Gamma_{Ri}$, $d\Gamma_{Li}$, free vortices Γ^j_{Rfk}, Γ^j_{Lfk} $(k=1, 2; j=1, \ldots, n)$ and U.

Let all dividing points including bucket edges be control points, then $2(m+1)$ equations are obtained from equation (1). Since the number of bound vortices is $2m$ and the number of nascent vortices is four, the number of unknowns becomes $2m+4$. Accordingly, as more two conditions, Kelvin's theorem is used. That is, the sum of strengths of all bound vortices and all free vortices reduces to zero for each bucket:

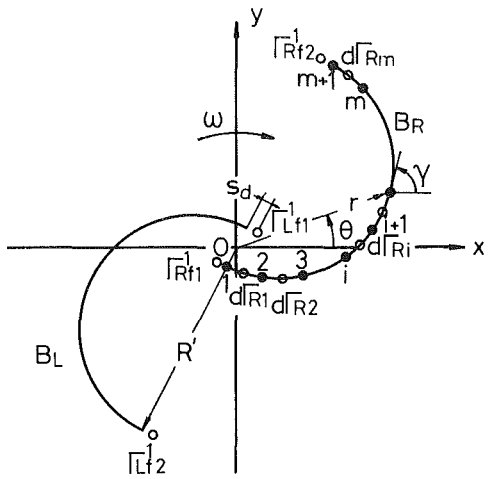

Fig. 2 Schematic description of the vortex distribution

$$\left.\begin{aligned}\sum_{i=1}^{m} d\Gamma_{Ri} + \sum_{j=1}^{n}\sum_{k=1}^{2}\Gamma^j_{Rfk} = 0\\ \sum_{i=1}^{m} d\Gamma_{Li} + \sum_{j=1}^{n}\sum_{k=1}^{2}\Gamma^j_{Lfk} = 0\end{aligned}\right\} \tag{2}$$

By solving equations (1) and (2), strengths of $2m$ bound vortices and four nascent vortices are determined. During a time interval Δt, the free vortices shed with the velocity induced by another vortices and uniform flow, and the rotor rotates in angle $\omega\Delta t$. At the next moment strengths of the bound and free vortices are determined newly by solving the $2(m+2)$ simultaneous linear equations again.

The complex potential W of the flow after n steps is given by

$$W = \frac{i}{2\pi}\sum_{i=1}^{m}\{d\Gamma_{Ri}\log(z-z_{Ri}) + d\Gamma_{Li}\log(z-z_{Li})\}$$

Nomenclature

a = radius of a bucket
As = rotor projected area
c_p = power coefficient
c_t = torque coefficient
D = $2a$
$d\Gamma_{Ri}, d\Gamma_{Li}$ = strengths of bound vortices
H = rotor height
Im{ } = imaginary part
JS = number of time steps
m = number of bound vortices on a bucket surface
(r,θ) = components of the cylindrical coordinate at a point on the bucket surface
R' = maximum radius of rotor
Re = Reynolds number ($= 2R'U/\nu$)
Re{ } = real part
S = spacing between two buckets, see Fig. 1
s_d = spacing between the first nascent vortex and a bucket edge
Δt = time interval
T = rotor torque
U = wind velocity
$\bar{w}$ = conjugate complex velocity
W = complex potential
z = complex coordinates ($= x + iy$)
$\bar{z}$ = conjugate complex value of z
β = azimuthal angle measured from y-axis, see Fig. 1
γ = angle between a tangent to the bucket surface and x-axis
$\Gamma^j_{Rfk}, \Gamma^j_{Lfk}$ = strengths of the jth free vortices
μ = tip speed ratio
ν = kinematic viscosity
ω = angular velocity of the rotor
ρ = fluid mass density
σ = limit spacing between two free vortices
$\oint_c$ = integration along the arbitrary path except singular points
$\oint_B$ = integration along the contour line

Subscripts

ex = experiment
f = free vortex
L = left bucket in Fig. 1
R = right bucket in Fig. 1
th = theory
0 = value at a point on the bucket surface

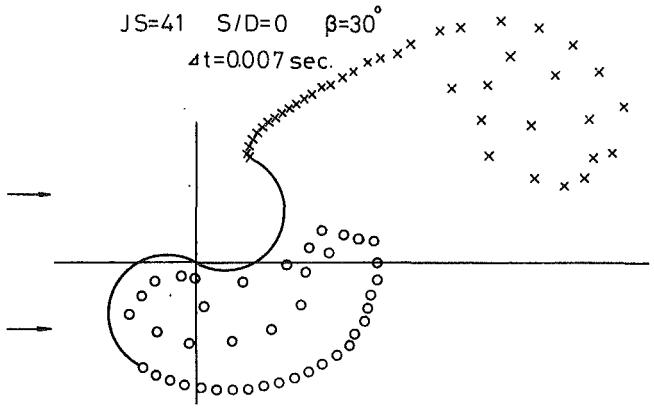

Fig. 3(a)

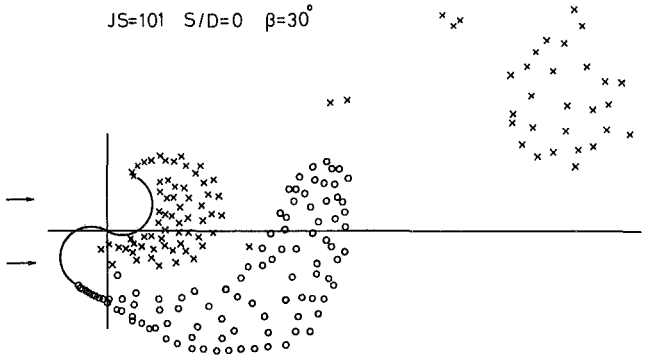

Fig. 3(b)

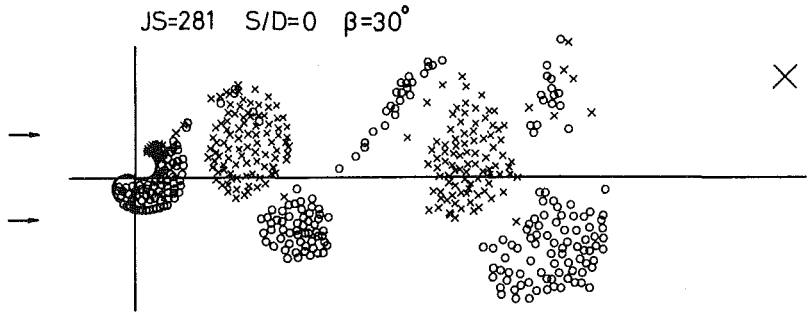

Fig. 3(c)

Fig. 3 Time variation of the vortex shedding behind a stationary rotor ($S/D = 0, \beta = 30$ deg)

$$+\frac{i}{2\pi}\sum_{j=1}^{n}\sum_{k=1}^{2}\{\Gamma^j_{Rfk}\log(z-z^j_{Rfk}) + \Gamma^j_{Lfk}\log(z-z^j_{Lfk})\} + Uz \tag{3}$$

Then, $\bar{w}$ reduces to

$$\bar{w} = \frac{i}{2\pi}\sum_{i=1}^{m}\left(\frac{d\Gamma_{Ri}}{z-z_{Ri}} + \frac{d\Gamma_{Li}}{z-z_{Li}}\right) + \frac{i}{2\pi}\sum_{j=1}^{n}\sum_{k=1}^{2}\left(\frac{\Gamma^j_{Rfk}}{z-z^j_{Rfk}} + \frac{\Gamma^j_{Lfk}}{z-z^j_{Lfk}}\right) + U \tag{4}$$

Torque and Power Coefficients

The rotor torque T can be calculated from the Blasius equation

$$T = -\frac{\rho}{2}\mathrm{Re}\left\{\oint_c \bar{w}^2 z dz\right\} + \frac{\rho}{2}\mathrm{Re}\left\{\frac{d}{dt}\oint_B \bar{w} z \bar{z} dz\right\} \tag{5}$$

From equation (4) the velocity on the bucket surface is given by

$$\bar{w}(z_0) = \frac{i}{2\pi}\sum_{i=1}^{m}\left(\frac{d\Gamma_{Ri}}{z_o - z_{Ri}} + \frac{d\Gamma_{Li}}{z_0 - z_{Li}}\right) \pm \frac{1}{2}\frac{d\Gamma_{R,L}}{ds}e^{-ir}\Big|_{z=z_0} + \frac{i}{2\pi}\sum_{j=1}^{n}\sum_{k=1}^{2}\left(\frac{\Gamma^j_{Rfk}}{z_0 - z^j_{Rfk}} + \frac{\Gamma^j_{Lfk}}{z_0 - z^j_{Lfk}}\right) + U \tag{6}$$

where ds is the length of the line segment and + of the double sign denotes the inner surface of the bucket and − outer surface.

Tip speed ratio μ, torque coefficient c_t and power coefficient c_p are defined as

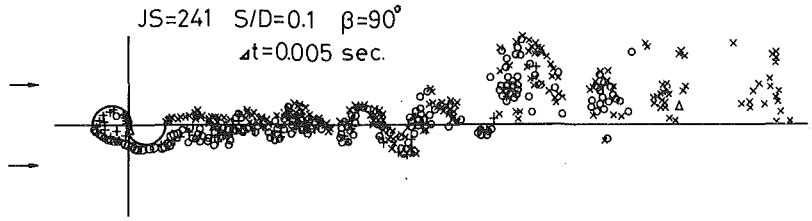

Fig. 4 Vortex shedding behind a stationary rotor ($S/D = 0.1$, $\beta = 90$ deg)

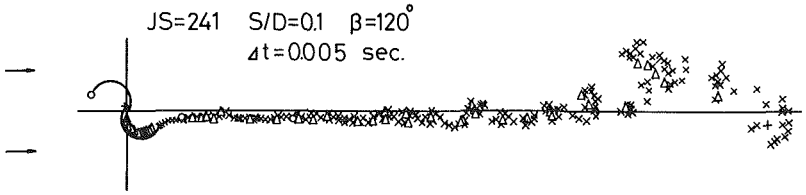

Fig. 5 Vortex shedding behind a stationary rotor ($S/D = 0.1$, $\beta = 120$ deg)

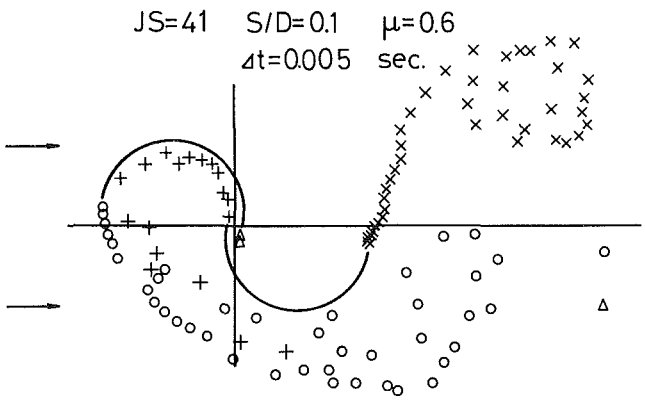

Fig. 6(*a*)

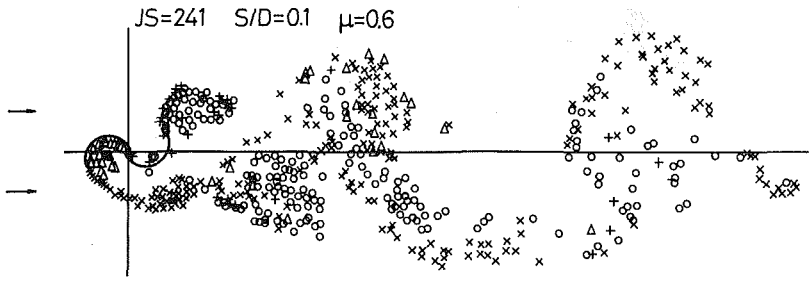

Fig. 6(*b*)

Fig. 6 Time variation of the vortex shedding behind a rotating rotor ($S/D = 0.1$, $\mu = 0.8$)

$$\left.\begin{aligned} \mu &= R'\omega/U, c_t = T\Big/\frac{1}{2}\rho U^2 R' A_s, \\ c_p &= T\omega\Big/\frac{1}{2}\rho U^3 A_s, A_s = 2R'H \end{aligned}\right\} \quad (7)$$

Numerical Calculation

Calculation was run for $U = 7$m/s, $a = 0.25$m, $S/D = 0$, 0.1, and 0.2. The Reynolds number becomes $\mathrm{Re} = 4.32 \times 10^5$, and is equal to that of the experimental work [5].

One bucket contour is divided into 20 equal line segments ($m = 20$), and the number of unknowns of the simultaneous linear equations, which are solved at each time step, becomes 44. When the bucket shape is continuous "S" shape, the number of unknowns is 42.

Time interval which has great influence upon the results computed by the use of the discrete vortex method, was determined in the range $\Delta t = 0.042 \sim 0.098 \times (2a/U)$ ($0.003 \sim 0.007$s). For large μ, smaller value of Δt should be chosen, since rotational angle of the rotor during Δt becomes too large.

In the case that a shedding vortex gets too near to the bucket surface, the assumption that the vortex is cancelled on account of the effect of viscosity is used. In this work the limit spacing between a vortex and the bucket surface is $0.05(2a)$.

If the spacing between two adjacent vortices is too small, the induced velocity becomes unrealistically large. Therefore, the calculation was performed with assumption that the

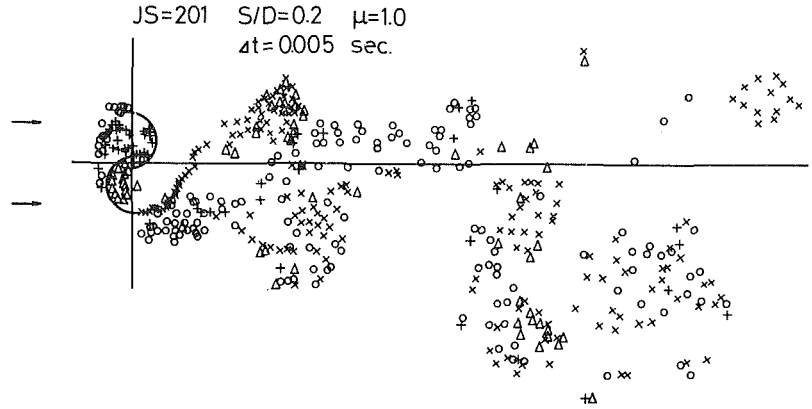

Fig. 7 Vortex shedding behind a stationary rotor ($S/D = 0.2$, $\mu = 1.0$)

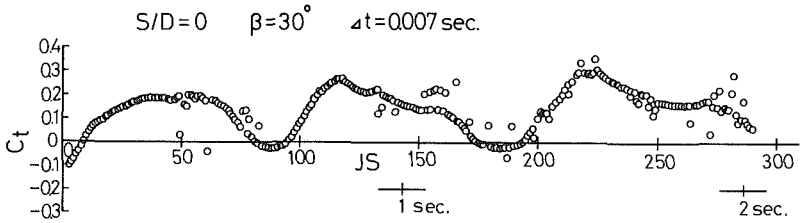

Fig. 8 Time-dependent fluctuation of c_t ($S/D = 0$, $\beta = 30$ deg)

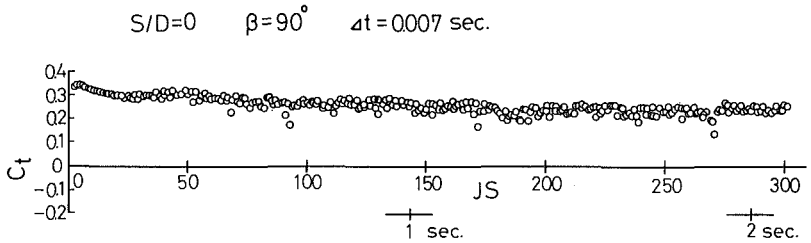

Fig. 9 Time-dependent fluctuation of c_t ($S/D = 0$, $\beta = 90$ deg)

velocity induced at each vortex position becomes constant ($= \Gamma/2\pi\sigma$), if the spacing between two vortices is smaller than the limit value $\sigma = 0.05(2a)$. The spacing s_d between the bucket edge and the nascent point of the free vortex was chosen as $1.1 \times 0.05(2a)$.

As described above, there are many parameters in the discrete vortex method and it is necessary to input the values of all parameters at the execution of the calculation. However, such values ought to vary in accordance with the subject of the analysis, and it requires vast calculation to find out the optimum values for each subject. In this work, with reference to the values of parameters presented for the inclined flat plate [14] and by varying them, the appropriate values for the present case are found. For instance, for the case of the inclined flat plate, $0.02(2a^*/U)$s [18] or $0.08(2a^*/U)$s [14] ($4a^*$ = full length of the plate) has been used as Δt. Hence, Δt in the present work was chosen with reference to above-described values in consideration with the following matter. Smaller value of Δt should be chosen so that the free vortex might not shed across the bucket contour after one time step procedure. Especially, in the case of large μ, smaller Δt is better, because rotational angle $\omega\Delta t$ of rotor becomes large. On the other hand, if small Δt is employed, the number of steps, that is, calculating time which is necessary till free vortices shed down in the sufficient distance, increases.

As the limit spacing from the bucket surface to cancel the vortex, $0.05(2a)$ which is one of the values presented in the earlier study [14] was used. As the value of s_d, the value $1.1 \times 0.05(2a)$ was employed, which was a little larger than the limit spacing of vortex cancelling. It can be presumed, that there exists an optimum vortex nascent position, to simulate the flow exactly, and that its location varies with bucket position and μ. In this study, however, the vortex nascent position was fixed on the extension line of the bucket contour for simplification.

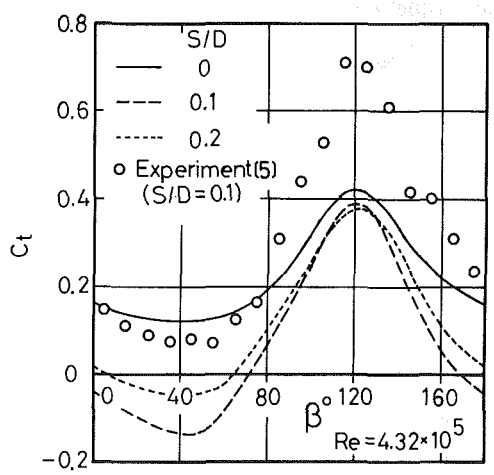

Fig. 10 Comparison of c_t with experimental data [5]

Damping effect of the strengths of shedding vortices is not considered in the calculation.

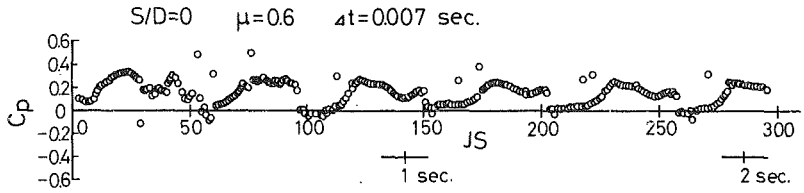

Fig. 11 Time-dependent fluctuation of c_p ($S/D = 0$, $\mu = 0.6$)

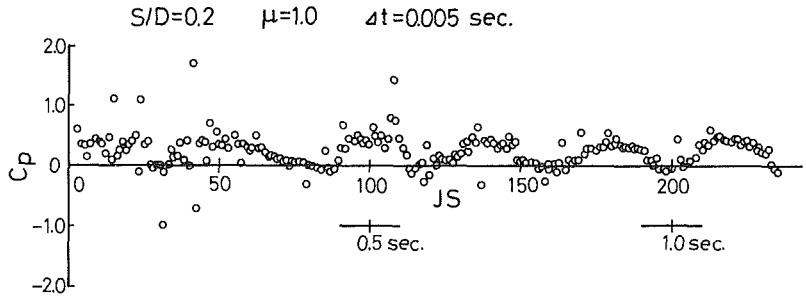

Fig. 12 Time-dependent fluctuation of c_p ($S/D = 0.2$, $\mu = 1.0$)

Results of Calculation

Flow Simulation. In Figs. 3, 4, and 5, simulations of the flow past the stationary rotor are presented. The time variation of the growth and shedding of vortices is shown in Fig. 3. In the case of $\beta = 30$ deg, vortices shed down periodically as Karman vortex sheet. The flow pattern varies with the value of β.

As shown in Figs. 4 and 5, vortices behind the rotor with the angular positions $\beta = 90$ deg and 120 deg shed down continuously in a straight line.

Figures 6 and 7 present the flow simulations about the rotor rotating with $\mu = 0.6$ and $\mu = 1.0$, respectively. The vortex locations after the first 41 steps are shown in Fig. 6(*a*), and fully growth flows are presented in Figs. 6(*b*) and 7.

Torque Coefficient. The time-dependent fluctuations of the static torque which operates upon the stationary rotor with the overlap ratio $S/D = 0$ are presented in Figs. 8 and 9. Apparently, the bucket angular position, that is, the value of β has great influence on the fluctuating pattern. In cases that the vortices shed down continuously in a straight line, that is, in cases of $\beta = 90$ deg and 120 deg, c_t fluctuates scarcely.

The comparison with the experimental data measured by Sheldahl et al. [5] is presented in Fig. 10. As discussed above, results obtained by the discrete vortex method do not agree with the experimental data quantitatively, but agree well in tendency.

Power Coefficient. The time dependent fluctuations of the power coefficient c_p are presented in Fig. 11 ($\mu = 0.6$) and Fig. 12 ($\mu = 1.0$). Power coefficient c_p varies periodically and its period agrees with a half period of one revolution of the rotor. Figure 13 shows the comparison with the experimental data [5]. The theoretical and experimental values of μ at which c_p becomes maximum do not agree.

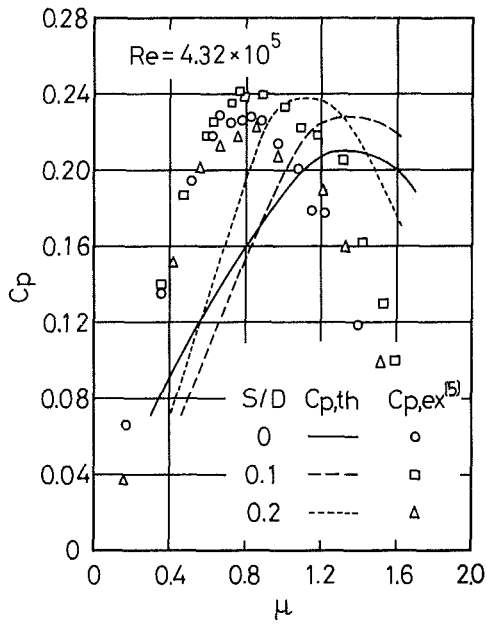

Fig. 13 Comparison of c_p with experimental data [5]

Concluding Remarks

It has been presented that the flow about the Savonius rotor can be analyzed numerically by the use of the discrete vortex method. As described in the foregoing, the analysis with the aid of the discrete vortex method includes many kinds of parameters, and it is not easy to find the optimum values of parameters according to each subject of studies. Therefore, in the present work, effects of the parameters on the results of the calculation have not been investigated in detail, since this work aims to present the first method to analyze the separated flow about the Savonius rotor theoretically.

The quantitative discrepancy between the results by the discrete vortex method and the experimental results can be found also in the results even for the simple shapes, that is, an inclined flat plate [13] and a cylinder [16].

Furthermore, the assumption that the flow about the Savonius rotor separates only at the bucket tips is not always adequate. The flow may separate on the bucket surface. If it is possible to analyze such a case, for example, if the method, which Wilson et al. [21] have presented for the analysis of a Darrieus rotor, can be applied, we will be able to expect exacter results than those in this study.

References

1 Savonius, S. J., "The S-Rotor and Its Applications," *Mechanical Engineering*, Vol. 53, No. 5, 1931, pp. 333–338.

2 Bach, G., "Untersuchungen über Savonius-Rotoren und verwandte Strömungsmaschinen," *Forschung*, 2. Bd./Heft 6, 1931, pp. 218–231.

3 Khan, M. H., "Model and Prototype Performance Characteristics of Savonius Rotor Windmill," *Wind Engineering*, Vol. 2, No. 2, 1978, pp. 75–85.

4 Charwat, A. F., "Performance of Counter- and Corotating Arrays of Savonius Turbines," *Journal of Energy*, Vol. 2, No. 1, 1978, pp. 61–63.

5 Sheldahl, R. E., Blackwell, B. F. and Feltz, L. V., "Wind Tunnel Performance data for Two- and Three-Bucket Savonius Rotors," *Journal of Energy*, Vol. 2, No. 3, 1978, pp. 160–164.

6 Sivasegaram, S., "Concentration Augmentation of Power in a Savonius-Type Wind Rotor," *Wind Engineering*, Vol. 3, No. 1, 1979, pp. 52–61.

7 Shankar, N. P., "On the Aerodynamic Performance of a Class of Vertical Shaft Windmills," *Proceedings Royal Society of London*, A349, 1976, pp. 35–51.

8 Strickland, J. H., Webster, B. T., and Nguyen, T., "A Vortex Model of the Darrieus Turbine: An Analytical and Experimental Study," ASME JOURNAL OF FLUIDS ENGINEERING, Vol. 101, 1979, pp. 500–505.

9 Murata, S., Miyake, Y., Qgawa, T., Nakano, H., and Kitano, Y., "Vortex Theory of High-Speed Vertical-Axis Wind Turbine," *Technology Reports of the Osaka University*, Vol. 30, No. 1576, 1980, pp. 527–536.

10 Wilson, R. E., Lissaman, P. B. S. and Walker, S. N., "Aerodynamic Performance of Wind Turbines," ERDA/NSF/04014-76/1, 1976, pp. 111–164.

11 Van Dusen, E. S., and Kirchhoff, R. H., "A Two Dimensional Vortex Sheet Model of a Savonius Rotor," *Fluids Engineering in Advanced Energy Systems*, ASME, 1978, pp. 15–31.

12 Kuwahara, K., "Numerical Study of Flow past an Inclined Flat Plate," *Journal of the Physical Society of Japan*, Vol. 35, No. 5, 1973, pp. 1545–1551.

13 Sarpkaya, T., "An Inviscid Model of Two-Dimensional Vortex Shedding for Transient and Asymptotically Steady Separated Flow Over an Inclined Flat Plate," *Journal of Fluid Mechanics*, Vol. 68, Part 1, 1975, pp. 109–128.

14 Kiya, M., and Arie, M., "A Contribution to an Inviscid Vortex-Shedding Model of an Inclined Flat Plate in Uniform Flow," *Journal of Fluid Mechanics*, Vol. 82, Part 2, 1977, pp. 223–240.

15 Sarpkaya, T., and Shoaff, R. L., "Inviscid Model of Two-Dimensional Vortex Shedding by a Circular Cylinder," *AIAA Journal*, Vol. 17, No. 11, 1979, pp. 1193–1200.

16 Stansby, P. K., "A Numerical Study of Vortex Shedding from one and two Circular Cylinders," *The Aeronautical Quarterly*, Vol. 32, Part 1, 1981, pp. 48–71.

17 Katz, J., "A Discretevortex Method for the Non-Steady Separated Flow Over an Airfoil," *Journal of Fluid Mechanics*, Vol. 102, 1981, pp. 315–328.

18 Clements, R. R., "An Inviscid Model of Two-Dimensional Vortex Shedding," *Journal of Fluid Mechanics*, Vol. 57, Part 2, 1973, pp. 321–336.

19 Clements, R. R. and Maull, D. J., "The Representation of Sheets of Vorticity by Discrete Vortices," *Progress in Aerospace Sciences*, Vol. 16, No. 2, 1975, pp. 129–146.

20 Ogawa, T. and Murata, S., "On the Flow in the Centrifugal Impeller with Arbitrary Aerofoil Blades (1st Report Impeller with Constant Width)," *Bulletin of the JSME*, Vol. 17, No. 108, 1974, pp. 713–722.,

21 Wilson, R. E., Lissaman, P. B. S., James M. and McKie, W. R., "Aerodynamic Loads on a Darrieus Rotor Blades," ASME JOURNAL OF FLUIDS ENGINEERING, Vol. 105, Mar. 1983, pp. 53–58.

Tan Yuecan
Associate Professor of Huazhong University of Science and Technology, Wuhan, China; Formerly visiting scholar at The Ohio State University, Columbus, Ohio 43210

H. R. Velkoff
Professor, The Ohio State University, Columbus, Ohio 43210

A Study of the Measurement of Cavitation Inception Using an Electrostatic Technique

A new concept for detecting cavitation inception has been studied experimentally. In this exploratory study, cavitation is generated by varying the flow velocity and pressure around a circular cylinder. Cavitation inception has been detected by sensing the natural charges and electrification generated during cavitation. The agreement between visual determination and detection using electrostatic probes was quite good. The background and possible mechanisms are reviewed and discussed.

Introduction

Cavitation, as a dynamic phenomenon concerned with the formation, growth and disruption of vapor and gas cavities in a liquid, has been the subject of extensive research. One of the inherent problems in both the study of the nature of cavitation and the design of machines in which it occurs is the difficulty which arises when attempting to measure the inception and disappearance of cavitation [1-8]. Some of the existing methods for detecting the presence of cavitation can be summarized as follows [1, 5]:

(1) Indirect observation by determining the effect of cavitation on the performance of a piece of equipment;

(2) Indirect observation by measuring the effect of cavitation on the distribution of pressure over the boundary at which cavitation occurs;

(3) Indirect observation by sensing the noise emitted by cavitation;

(4) Indirect observation by allowing cavitation to scatter laser beam light into a photocell;

(5) Indirect observation by light-beam interruption;

(6) Direct observation by visual and photographic means.

Each of the above methods has its proper usage and limitation. It is believed that if a measurement method could be developed which would essentially be non-intrusive and useful in existing hardware, that such a technique could be useful in both research and applied fields related to cavitation.

The use of electrostatic probes is believed to offer such a technique. The approach considered depends upon the charge formation and decay which accompanies droplet or bubble formation and decay in liquids, and the use of simple probes to detect the charge effects. Electrical effects related to cavitation have been observed in the past. Some literature on cavitation have indicated: weak emission of light (or sonoluminescence) and sparks (usually in oils) have been seen during the cavitation process [1, 2]; significant effects of magnetic fields and electrostatic fields on cavitation damage and cavity growth have also been observed [9-12]. Nevertheless, the measurement of cavitation using the electrical charges and electrification in the flow has not been accomplished as far as the present authors are aware of.

Because of the need for non-intrusive cavitation measurement and because of the possible use of electrostatic phenomena as a base for detection, a program to study the electrostatic actions and their detection was undertaken and is reported in this paper.

Background

"Waterfall Electrification" or "Spray Electrification." The existence of an electrical double layer at phase interfaces is well recognized [13-16]. The surface charges in these double layers can lead to significant static electrification effects. Spraying of liquids has been found to lead to high potentials. The breakup of water droplets in certain waterfalls, such as in the Austrian Alps, leading to intense electrification and static sparks has been investigated [13].

Prior Use of Electrostatics in the Study of Fluid Flow. Some prior research work using electrostatic effects in measuring techniques for studying fluid behavior offer very interesting possibilities [17, 18].

M. Deluca and H. R. Velkoff conducted an analytical and experimental investigation of injected ion technique. Gas flow around a cylinder and an airfoil has been studied. In one case, ions were generated electrostatically by means of a corona discharge from a suitable point or line source. In the second case, the charges were obtained either from the natural dust or water particles in the air. The charges were collected as currents by strips located over the aerodynamic shape being studied. The measured ion currents followed vortex shedding that is characteristic of flow about a circular cylinder. The

Contributed by the Fluids Engineering Division of THE AMERICAN SOCIETY OF MECHANICAL ENGINEERS and presented at the 7th Annual/Energy-Sources Technology Conference and Exhibition, New Orleans, La., February 11-17, 1984. Manuscript received by the Fluids Engineering Division, July 16, 1982. Paper No. 84-FE-11.

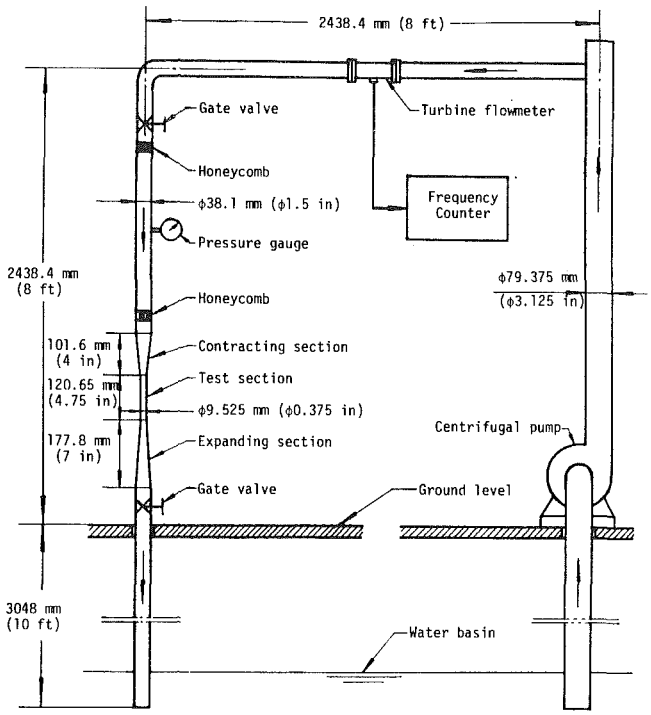

Fig. 1 Schematic of the open-circuit tunnel

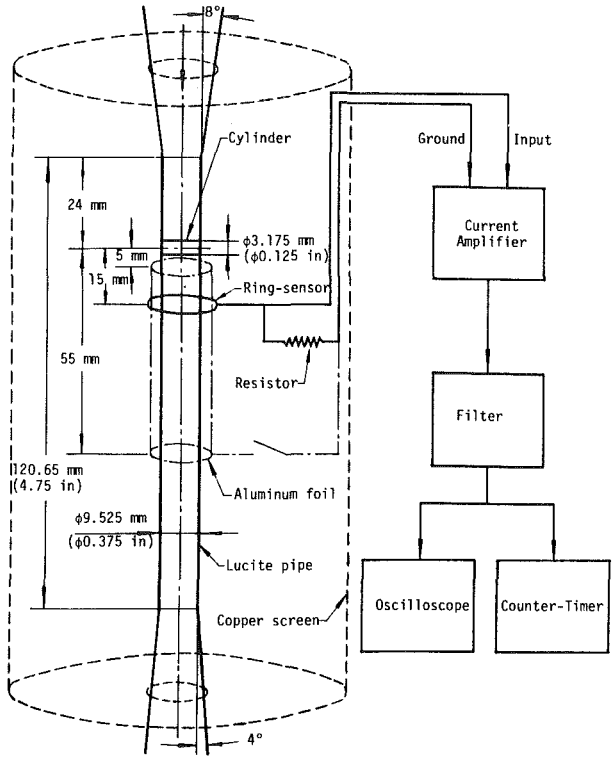

Fig. 2 Schematic of the test section and measurement system for detecting cavitation

experimental results indicated that the ion measurement method responded properly to the characteristics of the flow field.

Measurement of fluid surface velocity using the electrical properties of the double layer has been conducted by Melcher [19]. A use of electrostatic effects to measure air velocity has been studied by Durbin [20].

Charge Measurement of Droplets and Bubbles in Motion. In order to determine the basic difficulties of measuring charge formation and motions in liquid systems, the present authors conducted a series of experiments to measure the natural charges and electrification of droplets and bubbles in motion. Tap water, distilled water, freon and natural air were tested. The measurement system was the same as that used for later detecting cavitation inception and will be described at the next section of this paper (see Fig. 1).

These revealed that the existence and behavior of charges and electrification on droplets and bubbles in motion could be measured in a repeatable fashion.

Experimental Equipment. The purpose of this study was to investigate any electrical effects in cavitation that could be of use to detect cavitation. In order to make the experiments comparable with some recent results, a hydraulic system for producing controlled cavitation was selected based upon the approach used by Shalobasov and Shal'nev [10].

Experiments were carried out using an open-circuit tunnel (Figs. 1, 2). Tap water was driven by a centrifugal pump from the basin through the test section and back to the basin. The volume of the basin was large enough to keep the water temperature and air content relatively steady. During the test period the water temperature was 61 ± 1 °F (15 °C to 16.11 °C). The rotation of the pump was controlled by a DC motor and the pressure of the pump was controlled at selected values up to 50 psi (3.45 Kg/cm^2).

The test section was made of lucite pipe with ϕ 0.375 in. (ϕ 9.525 mm) inner diameter and 4.75 in. (120.65 mm) length. A stainless steel cylinder with diameter ϕ 0.125 in (ϕ 3.175 mm) was placed in the center of the channel across the flow. Increasing the flow velocity and (or) reducing the pressure controlled the cavitation produced. By means of the two gate valves (one in front of and the other behind the test section) the pressure, velocity and hence the cavitation were controlled.

The flow to the test section passed through a honeycomb section, a settling section, a second honeycomb section and then through a 16 to 1 contraction rated entry. This arrangement was used to provide for a relatively flat velocity profile at the test section with reduced turbulence. No tur-

Nomenclature

C = average counts of the electrical pulses
Ci = average counts of the electrical pulses of cavitation inception
Cd = average counts of the electrical pulses of cavitation desinence
K = cavitation number = $(P-Pv)/(\rho U^2/2)$
Ki = incipient cavitation number
Kd = desinent cavitation number
P = static pressure at the test section
$= Pg - \frac{1}{2}\rho(U_t^2 - U_g^2) + \gamma \cdot \Delta Z$
Pv = vapor pressure
Pg = reference static pressure from the pressure gauge (see Fig. 1)
U = free stream velocity at the cylinder section (see Figs. 1 and 3)
Ui = U of cavitation inception
Ud = U of cavitation desinence
Ug = free stream velocity at the pressure gauge section
Ut = free stream velocity at the test section
ΔZ = vertical distance between the pressure gauge and the test section
γ = specific gravity of water
ρ = density of water

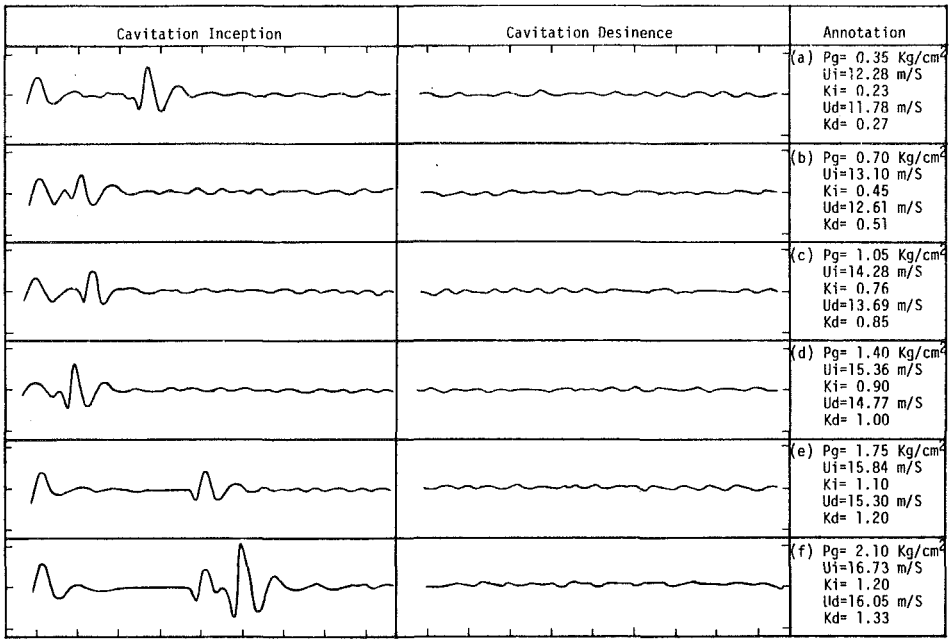

Fig. 3 Typical oscillograms present a striking contrast between cavitation inception and desinence [horizontal ordinate 20 μS/div.; vertical ordinate 1×10^{-8} mA/div. except 1×10^{-7} mA/div. for the left of (e), (f)]. Uncertainty in *Ki* and Kd = ± 0.05.

bulence measurements were made. Because of the short length of channel from the last honeycomb and the high contraction, the boundary layer thickness at the test section could be expected to be quite small. The settling section and the honeycomb should eliminate any secondary flows in the test section prior to the test cylinder. Due to the interaction of the cylinder pressure distribution with the existent boundary layers, secondary flow could be initiated in these regions. Visual observation of cavitation inception did not reveal specific localized points of cavitation but rather a more general initiation aft and along the length of the cylinder.

The flow velocity was measured by a turbine flowmeter and a frequency counter with an accuracy of 0.5 percent. The reference static pressure Pg was measured by a pressure gauge with an accuracy of 1 psi (0.07 Kg/cm^2) when the pressure was fluctuating. The testing range of the reference static pressure Pg was 5 to 30 psi (0.35 to 2.10 Kg/cm^2); while the testing range of the free stream velocity at the cylinder section was 36 to 75 ft/s (11 to 23 m/s).

Through the transparent wall of the test section, the flow and the appearance of cavitation could be observed visually or recorded by photography. When cavitation inception and desinence were detected visually, the accuracies relied on the judgement of the observer.

A schematic of the test section and measurement system is shown in Fig. 2. The copper screen around the test section was used for shielding the cavitation zone and the sensor from outside electrical noise. The sensor was simply made of common insulated copper wire in the shape of a single ring which was set around the test section. The electrical charges and electrification of the cavitation induced a potential and hence a current passed from the sensor through the "Amplifier-Filter-Oscilloscope and Counter-Timer" system. The amplifier and oscilloscope were employed to amplify the received signal and make them readable, their accuracies were 4 percent and 3 percent respectively. The filter was used to filter out the unwanted signals from the cavitation signals. The counter-timer was used to continuously record the counts of the pulse-signals from cavitation. Its accuracy was 1 count. The trigger level of the counter-timer was adjusted to zero when there was no cavitation. When cavitation occurred, because of the random and transient nature of the signal, only an average reading could be taken.

To ascertain the source and nature of the signals received by the sensor and the whole system, a cylinder made of aluminum foil was set between the test section and the ring-sensor. When the aluminum foil cylinder was grounded, the electrical signals from inside (cavitation zone) should be shielded out, and the measurement should show no response. If not, any signals measured would have been from an extraneous source, but not from the electrical sources inside the channel. On the other hand, when the aluminum foil cylinder was not grounded, it worked like an electrode and the gain of the measurements recorded was enhanced.

Test Procedure and Results

(1) Detecting Cavitation Inception and Desinence With the Ring-Sensor. The cavitation inception was obtained by holding the pressure fixed and gradually increasing the flow velocity until the continuous cavitation was observed. Then, the cavitation desinence was obtained by holding the pressure fixed and gradually reducing the flow velocity until no cavitation was observed. Between cavitation inception and desinence, intermittent cavitation was observed.

Using the gauge pressure Pg (lb/in^2) as reference static pressure, the following six pressure points were selected:

5; 10; 15; 20; 25; 30.

The following experiments were run five times independently:

No. 1: Detecting cavitation inception and desinence visually with magnifying glasses.

No. 2: Detecting cavitation inception and desinence by oscilloscope and the ring-sensor.

No. 3: Detecting cavitation inception and desinence by oscilloscope and the ring-sensor. The aluminum foil cylinder (ungrounded) was put between the test section and the ring-sensor.

No. 4: Detecting cavitation inception and desinence by

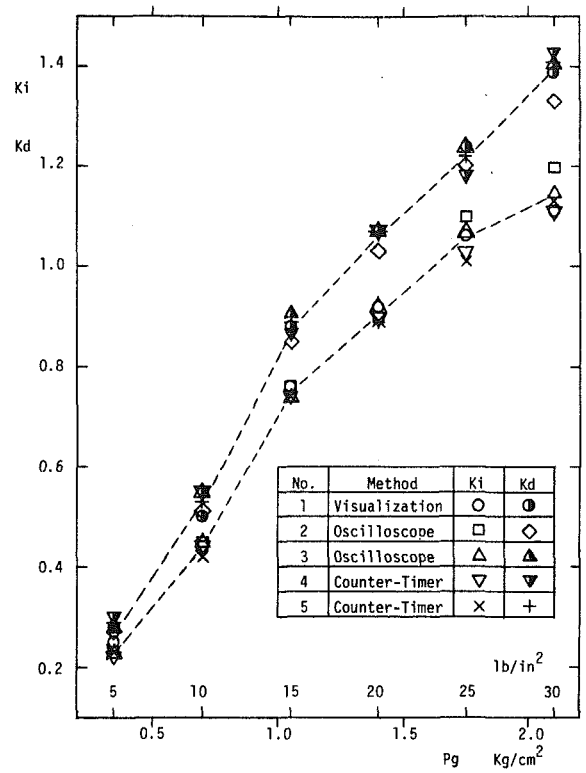

Fig. 4 Incipient and desinent cavitation number *Ki* and *Kd* versus reference static pressure Pg. Uncertainty in *Ki* and *Kd* = ±0.05.

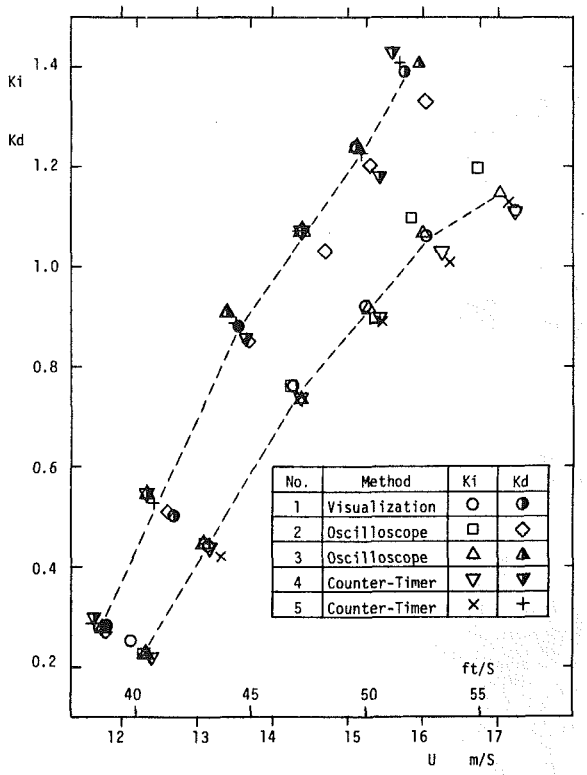

Fig. 5 Incipient and desinent cavitation number *Ki* and *Kd* versus cylinder section velocity U. Uncertainty in *Ki* and *Kd* = ±0.05.

Table 1 Average counts of detecting cavitation inception and desinence by counter-timer. Uncertainty in *Ki* and *Kd* = ±0.05.

Data / Reference Pressure Pg / Run No.	lb/in²	5	10	15	20	25	30
	Kg/cm²	0.35	0.70	1.05	1.40	1.75	2.10
Run No. 4	Ki	0.22	0.44	0.74	0.90	1.03	1.11
	Kd	0.30	0.55	0.86	1.07	1.18	1.43
(Data of 2-10-1982)	Ci,Kc	0.65	1.25	2.00	3.00	5.55	7.05
Run No. 5	Ki	0.23	0.42	0.74	0.89	1.01	1.13
	Kd	0.29	0.53	0.89	1.07	1.23	1.41
(Data of 2-12-1982)	Ci,Kc	0.016	0.057	0.200	0.530	1.500	2.100

counter-timer and the ring-sensor. The aluminum foil cylinder was the same as No. 3.

No. 5: Repeat of run No. 4.

Figure 3 presents a striking contrast of typical oscillograms between cavitation inception and desinence.

Figure 4 shows that the agreement of the results of different runs is quite acceptable. Figure 5 indicates the correlation between the incipient cavitation number *Ki*, desinent cavitation number *Kd* and the free stream velocity at the cylinder section U. Intermittent cavitation occurred in the region between *Ki* and *Kd*. Cavitation number *K*, *Ki* and *Kd* are defined at the "Nomenclature" of this paper. The average counts of detecting cavitation inception are shown in Table 1.

(2) Ascertaining the Source and Nature of the Measured Signals. The question may rise of what kind of signals were measured: were they due to mechanical vibration or something else but not electrical signals associated with cavitation? were they some kind of electrical signals from other sources but not from cavitation?

In order to answer these questions, the experiments using the aluminum foil cylinder were conducted. The cylinder was set between the test section and the ring-sensor.

In experiments No. 4 and No. 5, when the counts of the

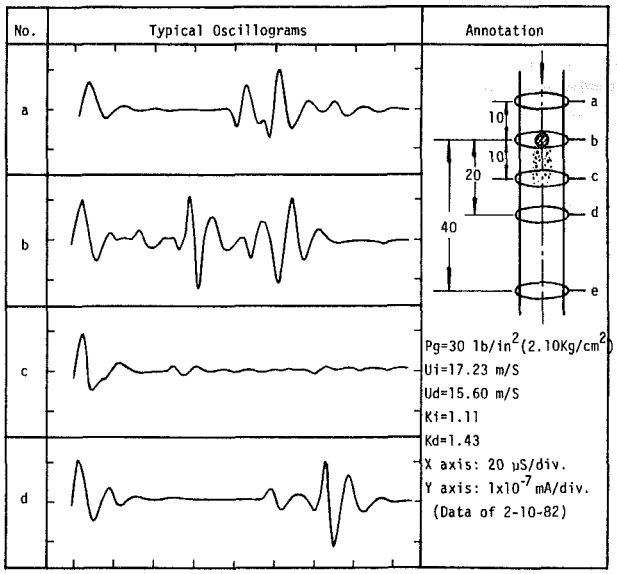

No.	Counts of Pulses (Kc)			
	Data of 2-10-1982		Data of 2-11-1982	
	Inception	Desinence	Inception	Desinence
a	13.56	0.06	1.30	0.00
b	15.62	0.06	0.74	0.00
c	19.41	0.06	2.39	0.00
d	15.48	0.06	1.45	0.00
e	0.66	0.06	0.26	0.00

Fig. 6 Comparison of detecting cavitation inception with different sensor locations (the response of the oscilloscope was too weak for "e" to take a picture). Dimensions in mm. Uncertainty in *Ki* and *Kd* = ±0.05.

counter-timer for cavitation inception were 0.65 to 7.05 Kc (No. 4) and 0.016 to 2.100 Kc (No. 5), while the counts for cavitation desinence were close to zero.

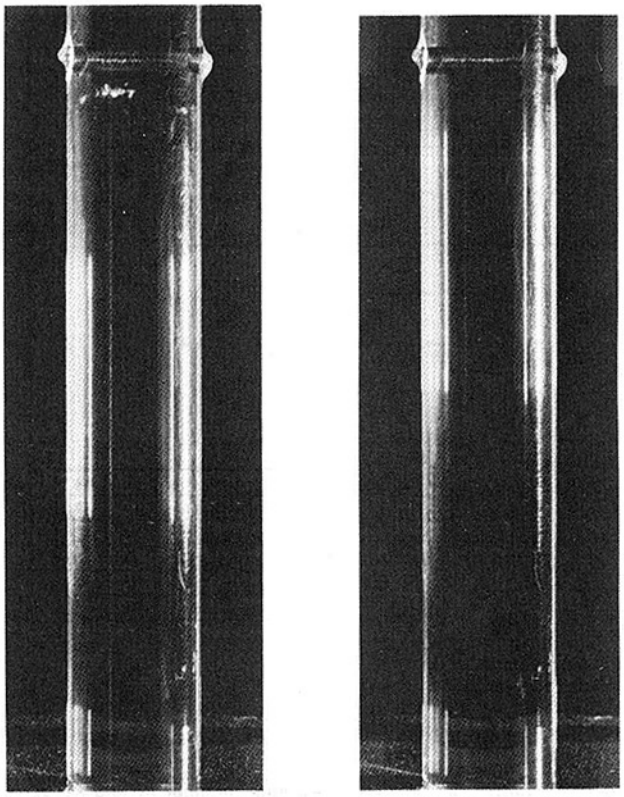

Fig. 7 Photographs of cavitation inception and desinence (flow downwards). Uncertainty in $Ki = \pm 0.05$.

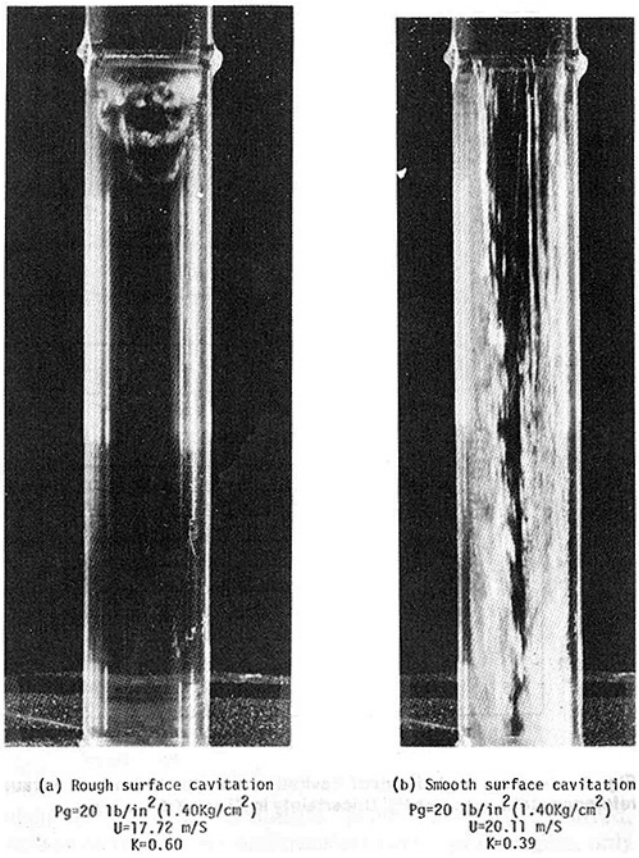

Fig. 8 Photographs of developed cavitation (flow downwards). Uncertainty in $K = \pm 0.05$.

For each of the selected experimental points (six points of inception and six points of desinence in one run), tests were then run holding all the conditions fixed except for grounding the aluminum foil cylinder. In these cases, counts of the counter-timer were close to zero as if there were no cavitation. The oscilloscope was also used to check the effect. When the aluminum foil cylinder was grounded, the oscilloscope also had no response when cavitation was seen. Afterward, the aluminum foil cylinder was ungrounded, and both the counter-timer and the oscilloscope responded to the presence of cavitation again.

If the measured signals were mechanical vibration or something else associated with cavitation, or electrical signals from other outside sources, grounding the aluminum foil should not influence the measured results. Therefore, it is believed that this experiment indicated that the measured signals are definitely the result of the electrical effects associated with cavitation.

(3) Comparison of Detecting Cavitation Inception With Different Sensor Locations. The cavitation appeared near or downstream of the cylinder. Tests were run to determine the effect of the sensor location relative to the cylinder on the measurement results.

As shown in Fig. 6, five locations were selected. Using the counter-timer, the cavitation inception could be detected when the sensor was set at the locations from upstream 10 mm to downstream 40 mm relative to the cylinder centerline. Using the oscilloscope, the cavitation inception could be detected when the sensor was set at the locations from upstream 10 mm to downstream 20 mm relative to the cylinder centerline. When the sensor was set at 40 mm downstream from the centerline of the cylinder, the response of the oscilloscope was too weak for the cavitation inception to be identified.

Among these five sensor locations, the largest pulse was obtained when the sensor was set 10 mm downstream from the cylinder centerline. This was the location closest to the cavity collapsing zone at that test regime. The farther the sensor was set from the cavity collapsing zone, the weaker were the signals detected.

(4) Comparison of Detecting Developed Cavitation of Different Intensities With the Same Sensor Location. Another way to ascertain whether or not the measured signals were associated with cavitation in nature was to determine whether or not a reasonable correlation between the measured signals and the cavitation intensity existed.

The typical appearances of the cavitation produced by the cylinder used in this study are shown by the photographs of Fig. 7 and Fig. 8. Figure 7 shows the typical photographs of cavitation inception and desinence. Cavitation inception and desinence are the critical conditions of the very onset of continuous cavitation and no cavitation respectively. When cavitation was more fully developed, the appearance could be divided into two types. One type is typically shown as Fig. 8(*a*). Here the cavitation zone is full of fine cavities and has a "rough surface." Another type is typically shown as Fig. 8(*b*), the cavitation zone has a "smooth surface" initiating from the cylinder and extending in the downstream direction. The front portion of the cavitation zone is full of relatively large and steady cavities, while the tail is full of fine and unsteady cavities.

Figure 9 shows a comparison of detecting developed cavitation of different intensity with the same sensor location. The ring-sensor was set 15 mm downstream from the cen-

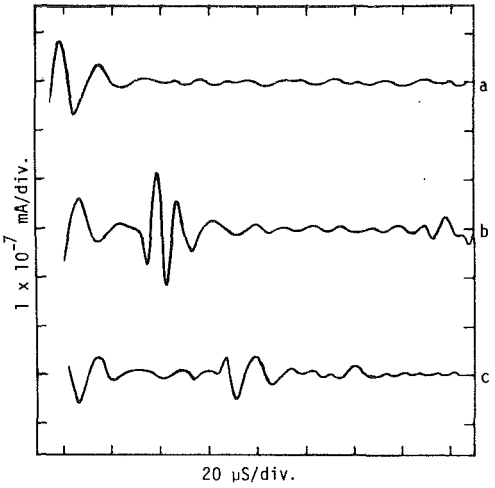

No.	a	b	c
Schematic	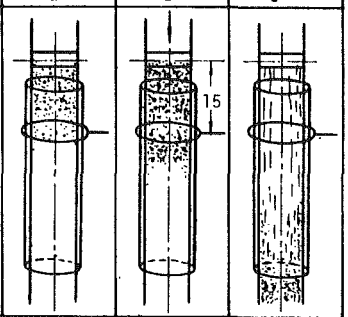		
U m/S	17.72	19.09	20.11
K	0.60	0.47	0.39
C (Kc)	6.91	13.93	8.10
Pg	20 lb/in^2 (1.40 Kg/cm^2)		

(Data of 2-10-82)

Fig. 9 Comparison of detecting developed cavitation of different intensities with the same sensor location (the measurement system, see Fig. 3). Dimension in mm. Uncertainty in $K = \pm 0.05$.

terline of the cylinder, the whole measurement system was the same as Fig. 3. Three cases were compared. Cases (*a*) and (*b*) were "rough surface cavitation" [see Fig. 8(*a*)]. The intensity of (*b*) was higher than the intensity of (*a*); the amplitude and frequency of the oscillogram of (*b*) were higher than those of (*a*); the count of the pulses of (*b*) was also higher than that of (*a*). Case (*c*) was "smooth surface cavitation" [see Fig. 8 (*b*)]; its intensity was higher than that of (*b*), but the amplitude of the oscilloscope and the counts of the pulses were smaller than those of (*b*).

These results are reasonable, because the steady cavities with smooth surfaces produce less electrical charges while the fine cavities with rough surfaces are the main sources of electrical charges.

(5) Comparison of Detecting Developed Cavitation With Different Sensor Locations. Knowing that the steady cavities of the "smooth surface cavitation" are basically not responsible for producing electrical charges and electrification, another question is the effect of the sensor location relative to the tail of the cavitation zone on the measurement results. In other words, the question is: what part of the tail of the "smooth surface cavitation" is the main source of the electrical charges and electrification?

To answer this question, an experiment was conducted to compare three different sensor locations (Fig. 10). Two runs of the experiment presented somewhat different tendencies.

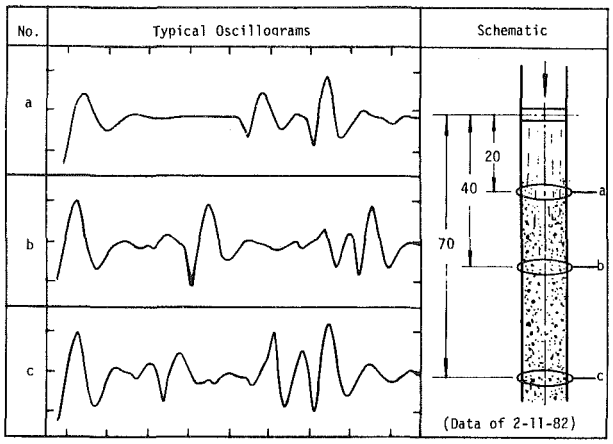

No.	Counts of Pulses (Kc)	
	Data of 2-10-82	Data of 2-11-82
a	32.00	4.87
b	29.00	6.74
c	17.00	14.24

Pg = 30 lb/in^2(2.10 Kg/cm^2)
U = 22.58 m/S
K = 0.51
X axis: 20 μS/div.
Y axis: 1 x 10^{-7} mA/div.

Fig. 10 Comparison of detecting developed cavitation with different sensor locations. Dimensions in mm. Uncertainty in $K = \pm 0.05$.

Since this kind of cavitation was very unsteady and sensitive, the measurement results also had the same properties. Nevertheless, clear readings from both the oscilloscope and the counter-timer were obtained for all three sensor locations. The amplitude of the oscillograms and the counts of the pulses were much higher than those measured in the cavitation inception regime. Therefore, it is reasonable to say that the whole tail of the "smooth surface cavitation" is capable of producing electrical charges and electrification.

Discussion and Conclusions

The main conclusions to be drawn from this study can be discussed and summarized as follows:

(1) Properties of Cavitation Inception and Desinence on a Circular Cylinder. The cavitation observed in this study is one example of vortex cavitation [1, 5]. The cavities are found in the cores of vortices which form in zones of high shear. It may appear as traveling cavities or as a fixed cavity. Figures 7 and 8 show that the cavitation occurs not on or adjacent to the cylinder but on the surface of the separation zone. Since the flow is very unsteady, the vortices and hence the cavities are not regular but are random and transient in nature. From Figs. 4 and 5 we can see the difference between incipient cavitation number *Ki* and desinent cavitation number *Kd*; the scatter of the points of the data are increased as the velocity and hence the inlet pressure are increased. This is due to the existence of random and transient effects which are increased as the velocity is increased. Also, once the vortex is formed the angular momentum of the liquid in it tends to prolong the life of the cavity even if the liquid mass travels into a higher-pressure region. This may be the reason of the existence of the intermittent cavitaiton between *Ki* and *Kd*, especially when the velocity is higher.

(2) Mechanism of Cavitation Electrification. The measured pulses of induced electrical current appear or disappear precisely in accordance with the cavitation inception or desinence respectively. This observation gives

strong support to the hypothesis that cavitation is a source of electrification.

According to Loeb's summarization of the mechanism of spray electrification [13], whenever the gas-liquid interfaces containing electrical double layers are disrupted to create fine droplets involving various thickness of the double layer, electrification should occur. During the cavitation process, vapor and gas cavities form and grow in the lower pressure zone, move downstream, and then collapse in the higher pressure zone. The formation of the electrical double layers are associated with the formation of the cavities, therefore, an electrical field is created in accordance with the cavitation inception. The formation process of the cavities are random and transient in nature, and thus the electrical field should be also random and transient in nature. When the cavities move downstream, the electrical effects should move with them. When the cavities are disrupted, the electrical double layers are also disrupted. Therefore, cavitation process has a mechanism similar to spray electrification in many ways and it may be called "cavitation electrification."

The experimental data of this study have depicted a general feature of cavitation electrification. The frequency of individual pulses of the current induced by cavitation electrification are in range 50 Kc to 100 Kc. The peak-to-peak amplitude of the impulses are in range 0.4×10^{-8} mA to 2.5×10^{-7} mA for the sensors used. The counts of the pulses are in range 0.016 Kc to 7.05 Kc for cavitation inception, up to 32 Kc for developed cavitation. Generally speaking, the amplitude and counts of the pulses increased according to the increase of flow velocity and cavitation intensity. Due to the random and transient nature of cavitation, the measured data are also random and transient.

Cavitation type has a significant influence on the electrification. When cavitation is developed to a certain extent under a given test condition, the front portion of the cavitation zone becomes relatively steady and is filled with macroscopic cavities. The electrification intensity in this portion is decreased, while at the tail of the cavitation zone there is intensive electrification.

The frequency range of cavitation electrification, the corresponding flow velocity, cavitation intensity and cavitation type are somewhat similar to those of the ultrasonic sound properties emitted from cavitation [1, 2]. This similarity may imply that cavitation electrification and cavitation sound occur synchronously.

(3) The Measurement Technique. The measurement method used in this study is simply based on the principle of electrical induction. In order to get useful measurements, the signals from cavitation electrification need to be sensed and amplified, and the background noise must be shielded and unrelated signals filtered out.

It is important to select a suitable shape and location of the sensor. The sensor should be close to or cover the region of the formation or (and) disruption of cavities without disturbing the flow. The high- and low-pass range of the filter is suggested to be set over about 50 Kc to 150 Kc.

In conclusion, the concept and the method of using electrostatic techniques appears to offer promise as a useful technique in the study of the existence of cavitation in fluid flow.

Acknowledgments

The authors wish to express their thanks to Messrs. J. W. Barker, H. K. Carpenter, and R. A. Frank for their assistance in setting up the water tunnel, to Mr. C. L. Rhodes for his assistance in making the electronic measurement system available, and to Mr. H. Byrd for his aid in the initial experiments with droplets and bubbles. Furthermore, they would like to thank Mr. J. W. Barker for his help in the photography.

References

1 Knapp, R. T., Daily, J. W., and Hammitt, F. G., *Cavitation*, McGraw-Hill, New York, 1970.

2 Pearsall, I. S., *Cavitation*, Mills & Boon Limited, London, 1972.

3 *Cavitation Research Facilities and Techniques*, Presented at The ASME Fluids Engineering Division Conference, Edited by Holl, J. W. and Wood, G. M., May 1964.

4 Robertson, J. M., "Cavitation Today—an Introduction," *Cavitation State of Knowledge*, Presented at The ASME Fluids Engineering and Applied Mechanics Conference, Edited by Robertson, J. M. and Wislicenus, G. F., June 1969, pp. 1-9.

5 Acousta, A. J., and Parkin, B. R., "Cavitation Inception—A Selection Review," *J. Ship Res.*, Vol. 19, No. 4, Dec. 1975, pp. 193-205.

6 Arakeri, V. H., and Acosta, A. J., "Cavitation Inception Observations on Axisymmetric Bodies at Supercritical Reynolds Numbers," *J. Ship Res.*, Vol. 20, No. 1, Mar. 1976, pp. 40-50.

7 Holl, J. W., "Limited Cavitation," *Cavitation State of Knowledge*, Presented at the ASME Fluids Engineering and Applied Mechanics Conference, Edited by Robertson, J. M. and Wislicenus, G. F., June 1969, pp. 26-63.

8 Murai, H., and Ihara, A., "Effects of Free Stream Turbulence and Free Stream Velocity on Cavitation Inception on Axisymmetric Bodies," *Rep. Inst. High Speed Mech.*, Tohoku Univ., Vol. 42, Sendai, Japan, 1980, pp. 79-100.

9 Hammitt, F. G., *Cavitation and Multiphase Flow Phenomena*, McGraw-Hill, New York, 1980.

10 Shalobasov, I. A., and Shalnev, K. K., "Effect of an External Magnetic Field on Cavitation and Erosion Damage," *Heat Transfer-Soviet Res.*, Vol. 3, No. 6, 1971, pp. 141-147.

11 Hammitt, F. G., et al., "Effects of Magnetic and Electric Fields Upon Cavitation in Conducting and Non-Conducting Liquids," *Cavitation and Polyphase Flow Forum*, Presented at Joint Meeting of Fluids Engg. Division and Lubrication Division of the ASME, Minneapolis, Minnesota, May 1975, pp. 26-28.

12 Wong, C. P. C., Vliet, G. C., and Schmidt, P. S., "Magnetic Field Effects on Bubble Growth in Boiling Liquid Metals," *Proc. Second Topical Conf. on Tech. of Nucl. Fusion*, Sept. 1976, Vol. 2, pp. 407-419.

13 Loeb, L. B., *Static Electrification*, Springer-Verlag, Berlin, 1958, pp. 58-124.

14 Butler, J. A. V., *Electrical Phenomena at Interfaces*, MacMillan, New York, 1951, pp. 30-74.

15 Klinkenberg, A., "Static Electricity in Liquids," *Static Electrification*, Proceedings of the Conference Organized by The Institute of Physics and The Physical Society Static Electrification Group, London, May 1967, pp. 63-68.

16 Adamson, A. W., *A Textbook of Physical Chemistry*, Academic Press, New York and London, 1973, p. 1015.

17 Deluca, Michael, and Velkoff, H. R., "Use of Electrostatics in the Study of Fluid Flow," *IEEE-IAS Conference*, Philadelphia, Pa., Oct. 1974.

18 Velkoff, H. R., "Evaluating the Interactions of Electrostatic Fields with Fluid Flows," an ASME publication, 71-DE-41, Apr. 1971.

19 Melcher, J. R., "Charge Relaxation of a Moving Liquid Interface," *The Physics of Fluids*, Vol. 10, No. 2, Feb. 1967, pp. 325-332.

20 Durbin, E. J., and Vause, C. R., Unpublished Studies at the U.S. Army Aeronautical Research Laboratory, Ames Research Center, Moffett Field, Calif., 1968.

21 Murai, H., and Ihara, A., "Effects of Free Stream Velocity and Free Stream Turbulence on Developed Cavitation and Ultrasonic Sound Properties Emitted from Developed Cavitation," *Rep. Inst. High Speed Mech.*, Tohoku Univ., Vol. 42, Sendai, Japan, 1980, pp. 101-127.

APPENDIX

A Yellow Springs conductivity meter was used to determine the electrical conductivity of the water used in the cavitation tests. The conductivity was measured as 360 micromhos. A measure of the amount of dissolved gases in the water was obtained with a Yellow Springs D.O. meter. The dissolved oxygen was determined to be 3 p.p.m. The pH of the water was 6.3.

L. A. Crum
Professor of Physics.

J. E. Brosey
Graduate Assistant.

Department of Physics,
The University of Mississippi,
Oxford, Miss. 38677

Effect of Dilute Polymer Additives on the Acoustic Cavitation Threshold of Water

Measurements are presented of the variation of the acoustic cavitation threshold of water with concentration of the polymer additives polyethylene oxide and guar gum. It was found that small amounts of these additives could significantly increase the cavitation threshold. A theoretical model, based upon nucleation of a gas bubble from a Harvey-type crevice in a mote or solid particle, is developed that gives good agreement with the measurements. The applicability of this approach to an explanation of cavitation index reduction in flow-generated or confined jet cavitation, when polymer additives are introduced, is discussed.

Introduction

It is now rather well known that dilute aqueous solutions of long chain polymers cannot only cause a significant drag reduction when compared with pure water, but also can induce a marked decrease in the cavitation index for both submerged jets and flow-generated cavitation. Ellis et al. [1] were able to measure a reduction of the incipient cavitation index for flow-induced cavitation to 30 percent of its value for tap water when polymer additives such as guar gum and polyox (WSR 301) were added. Hoyt [2] observed a reduction to about one half of the pure-water value in the incipient cavitation index for a submerged water jet when a few parts-per-million of polyethylene oxide was added to the water. Baker et al. [3] measured the desinent cavitation indices for a confined jet nozzle. They observed significant cavitation inhibition when polyox was added to the water. In the Baker et al. [3] study the cavitation reduction was also measured as a function of dissolved gas content. They observed a significant dependence of the cavitation index on the dissolved gas concentration and concluded that the cavitation inhibition was related to the effect of the polymer additives upon the cavitation nuclei. Other explanations for the mechanisms whereby the polymer additives reduce the cavitation index have been proposed by Lumley [4]—due to change in the pressure field as a result of viscoelastic effects in the irrotational strain field, and by Arndt et al. [5]—due to a reorientation of the flow field at the point of laminar separation.

In this paper we present measurements of the effect of polymer additives on the *acoustic* cavitation threshold of water as a function of dissolved gas concentration, liquid viscosity, liquid surface tension and polymer concentration. Further, we show that our experimental measurements can be explained nicely in terms of a Harvey-type model of cavitation nucleation, appropriately modified for the particulars of the experimental conditions.

Experimental Apparatus and Procedure

The incipient acoustic cavitation threshold was measured in distilled water for various concentrations of polymer additives and dissolved gas. To induce the cavitation, a hollow piezoelectric cylindrical transducer was used that was open at one end and closed at the other with a thin glass window, thickness 1×10^{-4} m. The liquid surface was unrestrained at the top and the thin glass window provided a second pressure-release interface at the bottom. The cylinder was driven in a $(N_r, N_\theta, N_z) = (3, 0, 1)$ resonant mode at 78.0 kHz with a Q of about 2000. Cavitation occurred only along the axis of the cylinder and only near the innermost radial antinode. The cavitation event was always a transient event and generated a sufficient shock wave on cavity collapse to be heard normally with the unaided ear. The detection criterion, however, was the observation on an oscilloscope of a burst of cavitation noise and a detuning of the resonant mode that was picked up by a small piezoelectric transducer mounted to the bottom window. A typical procedure for a cavitation inception measurement was to increase the driving voltage to the transducer in small increments, with pauses between increments, until a sharp detuning of the cavitation cell was observed. Figure 1 shows a photograph of the cavitation cell used for the measurements. The dimensions of the cell were 0.075 m in height by 0.075 m in o.d.

To prepare a liquid sample for testing, the following procedure was followed. Doubly distilled, deionized water was degassed by a vacuum system to a desired level and its gas content determined by a dissolved oxygen meter. (We assumed that if a sample of liquid was brought to equilibrium at a given pressure that was less than atmospheric, then the ratio of dissolved oxygen concentration to saturation concentration, at that temperature, was equal to the ratio of dissolved gas concentration to saturation concentration.)

Contributed by the Fluids Engineering Division of THE AMERICAN SOCIETY OF MECHANICAL ENGINEERS and presented at the 7th Annual/Energy-Sources Technology Conference and Exhibition, New Orleans, La., February 11-17, 1984. Manuscript received by the Fluids Engineering Division, March 30, 1982. Paper No. 84-FE-2.

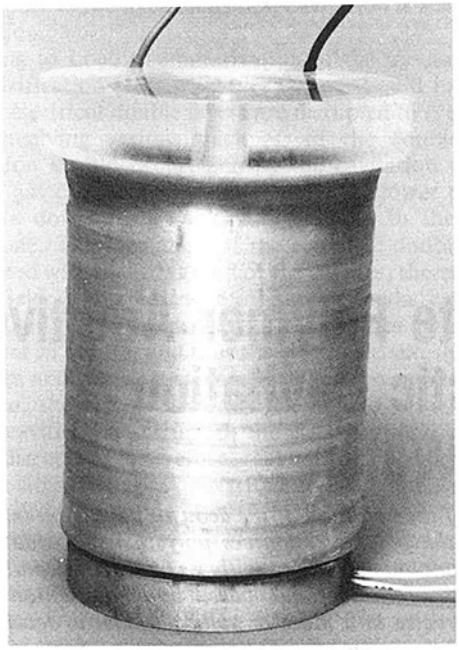

Fig. 1 Photograph of cavitation cell

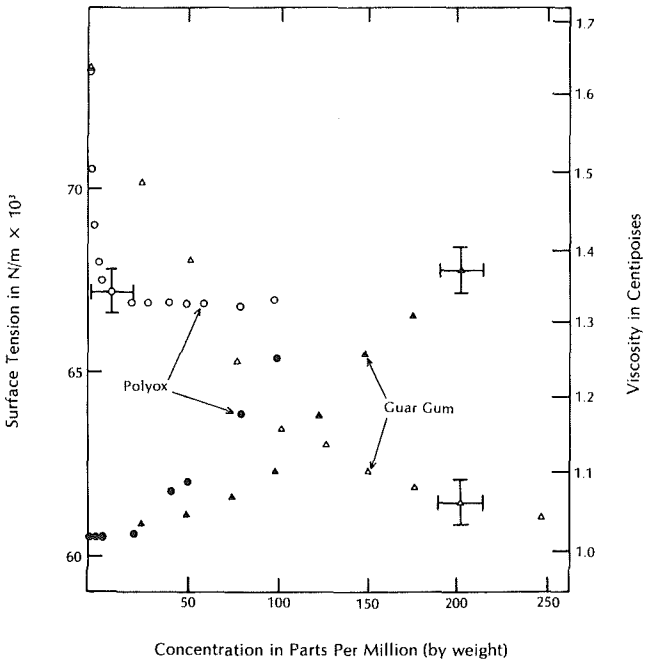

Fig. 2 Variation of the liquid-vapor surface tension and the liquid viscosity for aqueous solutions of polyox and guar gum

Predetermined amounts of powdered polymer were added to the sample to obtain a desired concentration of polymer additive. The sample was then divided into equal parts, one was then transferred to the cell, and the other part was set aside in a similar-shaped container for continuous monitoring of the dissolved gas concentration with the oxygen meter. The liquid was allowed to stand in the cavitation cell for 30 minutes so that weak nuclei such as large pieces of particulate matter and air bubbles could settle out (or rise to the surface) of the sample. At the end of the waiting period, a measurement of the surface tension was made of the liquid sample in the cell by a du Nouy ring tensiometer, and a second measurement of the dissolved gas concentration determined from the set-aside sample. The threshold measurement was then performed within a few minutes. The sample temperature was read and the liquid transferred to a modified Ostwald viscometer in order to determine the liquid viscosity. Thus, within a period of approximately 10 minutes, measurements of the dissolved gas concentration, liquid viscosity, surface tension, temperature, dissolved concentration of polymer additive, and incipient cavitation threshold were all determined. This procedure was then repeated for a different value of a desired parameter until the data set was complete. Figure 2 shows the variation of the liquid-vapor surface tension and the liquid viscosity with concentration of polymer additive (the polymers polyethelene oxide and guar gum were used) for typical concentrations of additives.

Theoretical Model For Cavitation Nucleation

Since the theoretical threshold for liquid rupture is several orders of magnitude larger than measured values, it is commonly accepted that some form of pre-existing nucleus must be the site of cavitation inception. This nucleus, which probably contains significant amounts of the gas phase, acts as a preferential site for liquid rupture. Several models for these nuclei and a review of their relative merits can be found easily in the literature. The authors recommend references [6, 7, and 8].

In this paper we shall use a model originally introduced by Harvey [9], and subsequently modified by Strasberg [10], Apfel [11], and Crum [12–13]. We shall briefly sketch the model here for completeness. Consider a particle of solid impurity containing a pocket of gas entrained in a crevice within the particle as shown in Fig. 3. If this quantity of gas is to survive, the interface must be concave toward the liquid so that the surface tension can prevent the gas from dissolving.

Thus, for the figure, $\alpha_A > \pi/2 + \beta$, where α_A is the advancing contact angle and 2β is the angle of the crevice. For the cavity shown in Fig. 3 the condition of stability is

$$P_h = P_v + P_g + \frac{2\sigma}{R}, \tag{1}$$

where P_h is the hydrostatic pressure, P_v is the vapor pressure, P_g is the equilibrium gas pressure of the gas dissolved in the

Nomenclature

a = half-width of crevice, m
P_A = Acoustic Cavitation Threshold, this study, Pa
P_b = Acoustic Cavitation Threshold, Blake, Pa
P_g = dissolved gas pressure, Pa
P_h = hydrostatic pressure, Pa
P_v = vapor pressure, Pa
Q = quality factor
R = radius of curvature of interface, m
R_b = radius of free bubble in Blake's theory, m
α_A = advancing contact angle
α_E = equilibrium contact angle
α_h = hysteresis angle
α_R = receding contact angle
β = half-angle of conical crevice
δ = $|\cos(\alpha_A - \beta)|$
ϕ = $\alpha_h + \beta$
σ = surface tension, N/m

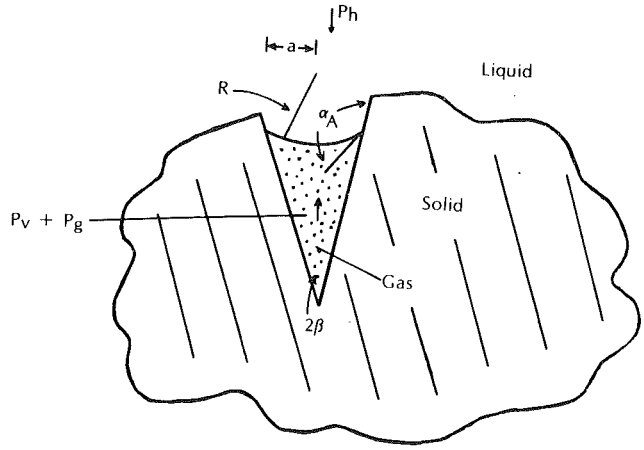

Fig. 3 Model portraying gas-pocket stabilization in a conical crevice in a solid particle

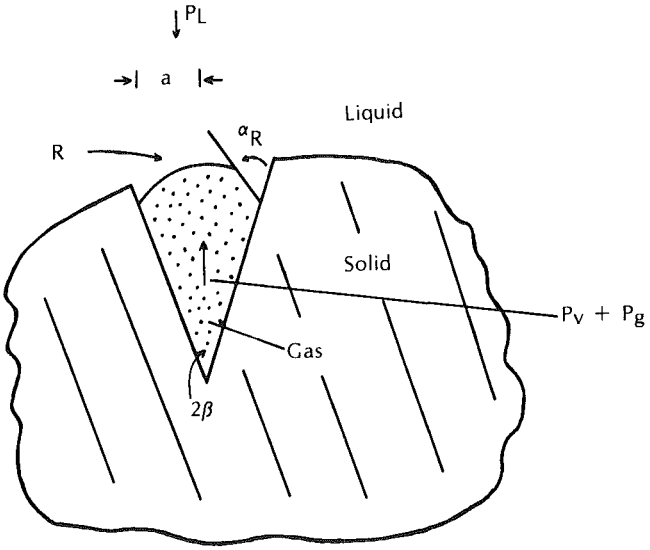

Fig. 4 Model portraying nucleation of a gas bubble from a crevice in a solid particle

liquid, σ is the liquid-vapor surface tension and R is the radius of curvature of the interface. In order for the interface to be concave toward the liquid, there must be some hysteresis in the advancing and receding contact angles for water against the surface of the solid. Otherwise, the interface will be convex toward the liquid, the stabilization condition in equation (1) cannot be met and the gas will dissolve. The hysteresis angle will be discussed later. It is to be noted that even if the liquid is saturated with gas, due to the liquid-vapor surface tension a pocket of gas will slowly dissolve unless the interface bows in. If the liquid is degassed, or if hydrostatic pressure is applied, then the interface will advance, once the advancing contact angle is reached, until the equilibrium condition is reestablished. (Apfel [11] makes a distinction between crevices of larger than or smaller than critical size. For smaller-than-critical size crevices, the interface does not move. Since we deal here with rather "weak" cavitation, the larger crevice model is probably sufficient.) After the interface has advanced, the half-width, a, of the crevice can then be given by

$$a = \frac{2\sigma}{P_h - P_v - P_g} |\cos(\alpha_A - \beta)|. \tag{2}$$

Suppose next that the pressure in the liquid outside the crevice suddenly becomes quite small. The gas will then expand, and the interface will bow out as shown in Fig. 4. If the pressure reduction is sufficiently small, the receding contact angle will be reached and the interface will recede and nucleate a microbubble. Since the radius of curvature of the receding interface is growing, the microbubble nucleated will grow without bound and cavitation will be induced. The acoustic pressure amplitude required to cause the interface to recede is given [1] by

$$P_A = (P_h - P_v - P_g) + (P_h - P_v - P_g)\left|\frac{\cos(\alpha_R - \beta)}{\cos(\alpha_A - \beta)}\right|. \tag{3}$$

Contained in this equation, however, are receding and advancing contact angles that are difficult to determine. We [12–13] have removed much of this difficulty by finding a relationship [14] between equilibrium contact angles and surface tension, viz.

$$\cos\alpha_E = -1 + c/\sigma. \tag{4}$$

Here α_E is the equilibrium contact angle, c is a constant that depends upon the surface properties of the solids, and is approximately 0.050 N/m for a wide variety of nonpolar solids such as paraffin and beeswax. If we combine equations (3) and (4), and redefine some quantities, we have an expression for the cavitation threshold that is primarily a function of surface tension and dissolved gas concentration, viz.

$$P_A = (P_h - P_v - P_g) + \frac{P_h - P_v - P_g}{\delta}\{(c/\sigma - 1)\cos\phi + [1 - (c/\sigma - 1)^2]^{1/2}\sin\phi\}, \tag{5}$$

where $\phi = \alpha_h + \beta$, $\delta = |\cos(\alpha_A - \beta)|$, and α_h is the hysteresis angle. Likely candidates for particulate matter are organic waxes, paraffins and a variety of organic nonpolar solids that are hydrophobic and possess significant hysteresis angles for water. For the conditions of this study we have used $c = 0.050$ N/m, $\alpha_A = 106$ deg, $\beta = 14$ deg and $\alpha_h = 20$ deg. We selected these constants for the following reasons. $c = 0.050$ N/m was selected because this value was suggested by Bargeman and Van Voorst Vader [14] to apply to the paraffins. We have selected $\alpha_A = 106$ deg because this is also the value recommended [14] for the paraffins. We demanded that β be small and used $\delta = |\cos(\alpha_A - \beta)|$ to adjust the amplitude of the threshold to best fit the data; $\beta = 14$ deg was a best choice for this value. Values of the hysteresis angle in the literature for nonpolar solids vary from 14 to 44 deg for water plus surfactants on the paraffins and white beeswax [15]. Our selection of an intermediate angle of 20 deg gave us a best fit to the data.

Although we have not run a sensitivity study to determine how critical the selection of the coefficients was in obtaining a best fit, an independent set of data [12] was fit with the identical coefficients, except that $\alpha_h = 18$ deg in the previous study.

In this study, the range of surface tension was relatively small; the lower limit of surface tension data was approximately 0.060 N/m. However, earlier applications of the equations utilized here gave good agreement in the range 0.030 to 0.070 N/m. Note that in equation (4), α_E becomes undefined for $\sigma \leq .025$ N/m.

In order to compare the predictions of this theory with others, we add in this section also the equation of Blake [16], which assumes that the cavitation nucleus is a free bubble of radius R_b. His equation is

$$P_b = P_h\left(1 + \frac{4}{9}X_b\left[\frac{3X_b}{4(1+X_b)}\right]^{1/2}\right), \tag{6}$$

where P_b is the cavitation threshold and $X_b = 2\sigma/P_h R_b$.

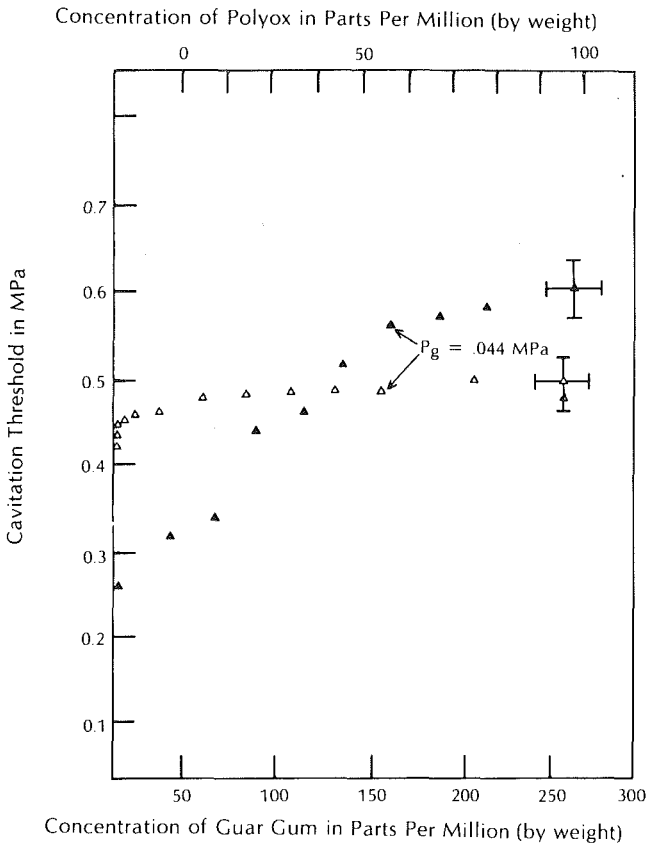

Fig. 5 Variation of the acoustic cavitation threshold with concentration for aqueous solutions of polyox and guar gum. The measurements are for a dissolved gas pressure of 0.044 MPa, a temperature of 23°C and a driving frequency of 78 kHz.

Results

It is seen from equation (5) that a strong dependence of the threshold on liquid-vapor surface tension is expected whereas there should be little dependence on the liquid viscosity. These results are generally confirmed in Fig. 5 which shows the variation of the cavitation threshold with polymer concentration for two additives, polyox and guar gum. Note from Fig. 2 that for both polymers there is a saturation in the surface tension while the viscosity continues to increase (with concentration)—at least for the range of concentrations studied here. In Fig. 5 it is seen that there is a similar saturation or leveling-off of the cavitation threshold with concentration, the plateaus in the threshold occurring at approximately the same concentrations as the plateaus in the surface tension. Note also that guar gum, which has a much larger surface tension variation, shows also a much larger threshold variation. (We found that measurements with polyox were difficult to perform because there was such a sharp dependence on concentration; guar gum on the other hand appears to mimic polyox in its physical effects except that it does not have such a strong dependence on concentration and thus allowed us better control of our measurements.)

The variation of the threshold with surface tension is shown explicitly in Figs. 6 and 7 which are for polyox and guar gum, respectively. Note that as the surface tension is *reduced*, the cavitation threshold *increases*. This behavior is unexpected, as the Blake theory predicts a gradual reduction in threshold with reduced surface tension. The solid curves on Figs. 6 and 7 are the predictions of equation (5) with the constants given in the text. Note that the inhomogeneous nucleation model presented here gives much better agreement than the free-bubble model of Blake.

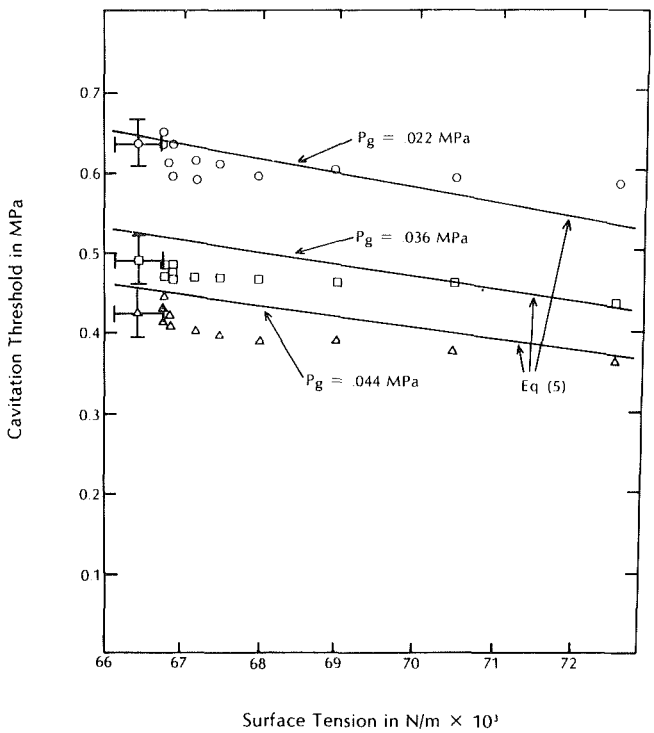

Fig. 6 Variation of the acoustic cavitation threshold with surface tension for aqueous solutions of polyox. The measurements are for a temperature of 23°C and a driving frequency of 78 kHz. The solid lines are the predictions of equation (5) with the indicated values of the dissolved gas pressure.

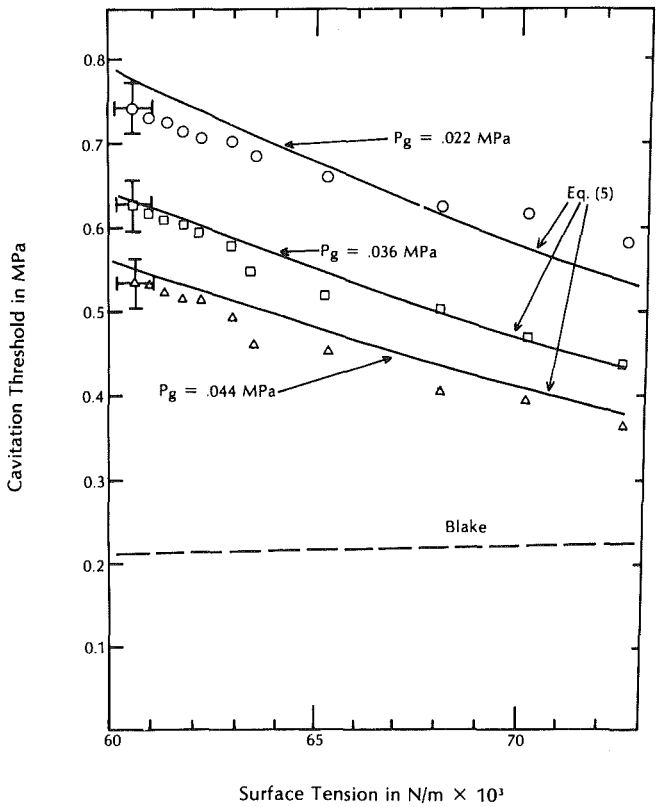

Fig. 7 Variation of the acoustic cavitation threshold with surface tension for aqueous solutions of guar gum. The measurements are for a temperature of 23°C and a driving frequency of 78 kHz. The solid lines are the predictions of equation (5) with the indicated values of the dissolved gas pressure. The dashed line is for the theory of Blake, equation (6), for a free bubble radius of 0.5 × 10^{-6}m and an atmospheric pressure of 0.1 MPa.

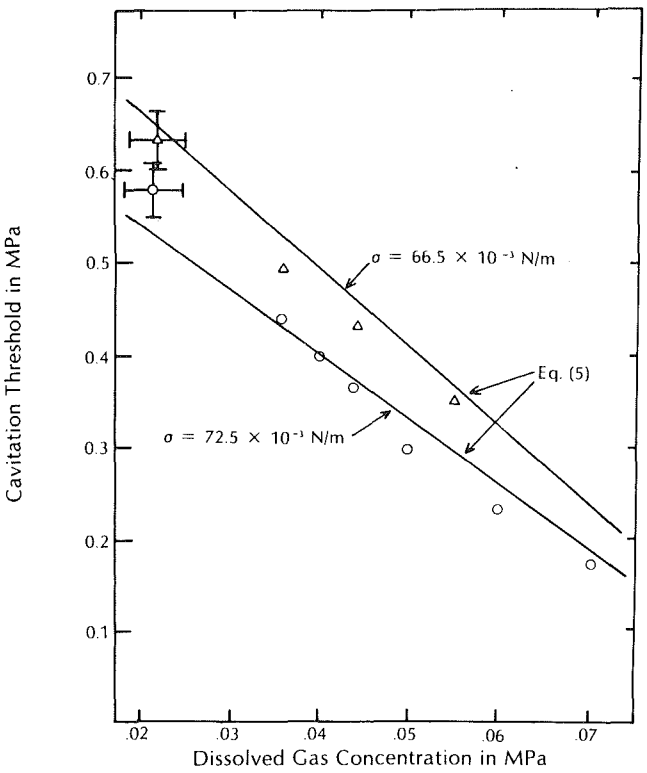

Fig. 8 Variation of the acoustic cavitation threshold with dissolved gas concentration for aqueous solutions of polyox. The measurements are for a temperature of 23°C and a driving frequency of 78 kHz. The solid lines are the predictions of equation (5) with the indicated values of the surface tension.

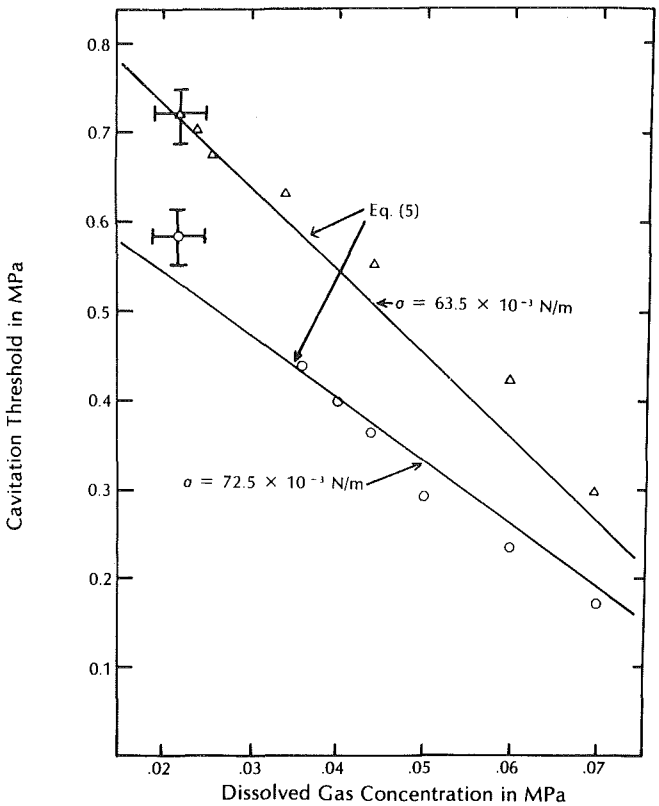

Fig. 9 Variation of the acoustic cavitation threshold with dissolved gas concentration for aqueous solutions of guar gum. The measurements are for a temperature of 23°C and a driving frequency of 78 kHz. The solid lines are the predictions of equation (5) with the indicated values of the surface tension.

It is possible to be given an explanation for the mechanism whereby the reduced surface tension causes an increase in the cavitation threshold. When the surface tension is relatively large, the equilibrium contact angle (see equation (4)) is also relatively large and the interface that recedes up the crevice is relatively flat. When the interface nucleates a gas bubble, the bubble will also be relatively large. When a free bubble is nucleated, the acoustic pressure required to cause this bubble to grow is related to the Laplace pressure ($2\sigma/R$). Thus, large surface tensions nucleate large bubbles that give low thresholds, and vice versa for low surface tensions. We have made movies [17] of gas bubble nucleation from macroscopic conical crevices as a function of surface tension and these movies demonstrate this effect.

Note from these figures that lower values of the dissolved gas concentration also give higher values of the threshold. In applying the Blake theory we arbitrarily selected a value of the free bubble radius to be 0.5×10^{-6} m. A smaller choice for the radius would raise the line, and one could improve the fit. In order to compare the variation with surface tension, and to not clutter the graph, we have selected this higher value.

The explicit dependence on dissolved gas concentration is shown in more detail in Figs. 8 and 9. In these figures, the variation of the cavitation threshold with dissolved gas content is shown for two values of the liquid-vapor surface tension. Note the strong dependence on gas concentration, even for the polyox case. It is seen that the theoretical model predicts this variation rather well, however.

Discussion

The discovery that polymer additives can both reduce drag and cavitation index is a rare event in that two good things happen at once. The explanation for these effects, particularly the latter one, is still being sought and it is hoped that the information presented here can be useful. The suggestion by Baker et al. [3] that the polymer additives may be influencing the nuclei is confirmed to a certain extent with the data presented here. There are several caveats that must be considered, however, before one can arrive at firm conclusions concerning the influence of the nuclei.

1. In many flow-generated or jet-generated cavitation experiments, the liquid is often saturated with gas and the nuclei are very likely free air bubbles that have been introduced into the system by a variety of means. These nuclei are very "weak" and cannot be modeled by the approach presented here. It is only in those situations where the liquid has been strengthened by degassing (to remove the free air bubbles) and filtration (to remove the large particles) that the approach outlined here should give correct predictions. Recall that in this experiment the liquid was carefully handled to permit only inhomogeneous nucleation type cavitation. In the experiments of Ellis et al. [1] and Hoyt [2] nearly a factor of two change in the cavitation index was observed when polyox of a few ppm was added to water. In the experiments performed here, addition of large amounts of polyox changed the cavitation threshold by at most 20 percent. Obviously, there are effects other than changes in the nuclei.

2. The Harvey model has been shown by this experiment and others [12, 13] to be rather versatile in explaining the results of certain experiments. However, other models, such as the surfactant skin model of Yount [7] and ionic charge model of Aculichev [8, 18] have also had some success in explaining experimental results. It is likely that the nuclei present in ordinary tap water are not so simple as our models but rather complex creatures with several special features.

3. The treatment in this paper that the principal effect of the polymer additives is merely to reduce the surface tension, although probably a good first-order effect, is rather oversimplified. Complex things will happen at the air-water in-

terface of a pocket of gas in a solid particle, and simplified approaches as those considered here can be expected to apply only to special cases under controlled conditions.

Experimental Uncertainty

There is a wide variation in the cavitation threshold measurements that exist in the published literature due to the many parameters that affect the threshold. Our results can be seen to compare within a few percent of those of Strasberg [10], whose conditions closely match our own. Our measurements of the surface tension, liquid viscosity, and the dissolved gas concentration are probably good to within 1 percent. Values for additive concentration and density, due to the nature of the measurements, are significantly better than 1 percent.

Conclusions

It is seen that a Harvey-type model of cavitation nucleation can explain some limited measurements of the effect of polymer additives on acoustic cavitation inception. These results are presented to point out that in hydrodynamic experiments involving polymer additives, some effect of the additives on the nuclei may have to be taken into account.

Acknowledgments

The authors wish to gratefully acknowledge the financial support of the National Science Foundation and the Office of Naval Research.

References

1 Ellis, A. T., Waugh, J. G., and Ting, R. Y., "Cavitation Suppression and High-Speed Flows of Water with Dilute Macromolecule Additives," ASME *Journal of Basic Engineering*, Vol. 92, 1970, p. 459.

2 Hoyt, J. W., "Effect of Polymer Additives on Jet Cavitation," ASME JOURNAL OF FLUIDS ENGINEERING, Vol. 98, 1976, p. 106.

3 Baker, C. B., Holl, J. W., and Arndt, R. E. A., "Influence of Gas Content and Polyethylene Oxide Additive upon Confined Jet Cavitation in Water," ASME 1976 Cavitation and Polyphase Flow Forum, ASME, New Orleans, 1976, p. 6.

4 Lumley, J. L., "Drag Reduction by Additives," *Annual Rev. Fluid Mech.*, Vol. 1, 1969.

5 Arndt, R. E. A., Billet, M. L., Holl, J. W., and Baker, C. B., "A Note on the Inhibition of Cavitation in Dilute Polymer Solutions," ASME 1976 Cavitation and Polyphase Flow Forum, ASME, New Orleans, 1976, p. 1.

6 Holl, J. W., "Nuclei and Cavitation," ASME *Journal of Basic Engineering*, Vol. 92, 1970, p. 681.

7 Yount, D. E., "Skins of Varying Permeability: a Stabilization Mechanism for Gas Cavitation Nuclei," *Journal of Acoustical Society of America*, Vol. 65, 1978, p. 1429.

8 Crum, L. A., "Nucleation and Stabilization of Microbubbles in Liquids," *Applied Scientific Research*, Vol. 38, 1982, p. 101.

9 Harvey, E. N., Barnes, K. K., McElroy, W. D., Whitely, A. H., Pease, D. C., and Cooper, K. W., "Bubble Formation in Animals, I. Physical Factors," *Journal of Cellular and Comparative Physiology*, Vol. 24, 1944, p. 1.

10 Strasberg, M., "Onset of Ultrasonic Cavitation in Tap Water," *Journal of the Acoustical Society of America*, Vol. 31, 1959, p. 163.

11 Apfel, R. E., "The Role of Impurities in Cavitation Threshold Determination," *Journal of Acoustical Society of America*, Vol. 48, 1970, p. 1179.

12 Crum, L. A., "Tensile Strength of Water," *Nature*, Vol. 278, 1979, p. 148.

13 Crum, L. A., "Acoustic Cavitation Thresholds in Water," *Cavitation and Inhomogeneities in Underwater Acoustics*, W. Lauterborn, ed., New York: Springer-Verlag, 1980.

14 Bargeman, D., and Van Voorst Vader, F., "Effect of Surfactants on Contact Angles at Nonpolar Solids," *J. Colloid and Interface Science*, Vol. 42, 1973, p. 467.

15 Furmidge, C. G. L., "Studies at Phase Interfaces, I. The Sliding of Liquid Drops on Solid Surfaces and a Theory for Spray Retention," *Journal of Colloid Science*, Vol. 17, 1962, p. 309.

16 Blake, F. G., Jr., "The Onset of Cavitation in Liquids," Technical Memo No. 12, Acoustics Research Laboratory, Harvard University, 1949.

17 Crum, L. A., "Acoustic Cavitation Inception in Water," *Naval Research Reviews*, Vol. 26, 1973, p. 19.

18 Winterton, R. H. S., "Nucleation of Boiling and Cavitation," *Journal of Physics*, D: Applied Physics, Vol. 10, 1977, p. 2041.

19 Aculichev, V. A., "Hydration of Ions and the Cavitation Resistance of Water," *Soviet Physics Acoustics*, Vol. 12, 1966, p. 144.

On the Mechanism of Flashing Injection of Initially Subcooled Fuels

R. D. Oza
Senior Research Engineer,
Engine Research Department,
General Motors Research Laboratories,
Warren, Mich. 48090

The mechanisms responsible for flash-boiling injection were investigated. Using an electromagnetic injector developed for this study, propane, methanol and Indolene were heated and injected into a constant-volume vessel. Two regimes of flash-boiling injection were identified. In the first regime, flash-boiling occurs within the injector nozzle without an increase in spray-cone angle. In the second regime, the nozzle exit pressure is sufficiently low that the two-phase compressible mixture created by flash-boiling within the injector nozzle is underexpanded at the nozzle exit and expands externally to increase the spray-cone angle.

Introduction

In engines with direct cylinder injection of fuel, mixing of the fuel spray with surrounding air is of critical importance in determining the combustion characteristics of the engine. Flash-boiling injection offers a way of improving fuel-air mixing, reducing wall wetting by shortening spray-tip penetration and by improving atomization. This was demonstrated by Kim et al. [1] in their report on the engine run with flash-boiling injection of alcohol. In the present study, the fundamental mechanisms responsible for flash-boiling injection were investigated to obtain the understanding necessary for application of this technique.

Investigations of the flash-boiling injections have been carried out by a number of investigators. Wu et al. [2] and Lienhard et al. [3, 4] investigated the breakup of a superheated jet by homogeneous bubble growth. Sher and Elata [5] studied flashing sprays from a can filled with a mixture of spray liquid and volatile propellant. Suzuki et al. [6] studied the breakup of a superheated water jet ejected into a vacuum chamber. Brown and York [7] studied effect of shapes and surface conditions of nozzles on the flash-boiling sprays of Freon, water and water with carbon dioxide dissolved in it. Recently, Soloman et al. [8] used fuel with dissolved air in experiments with flash-boiling injection. An expansion chamber was incorporated in the injector to promote bubble growth during these experiments. The experiments by the above-mentioned authors have been confined to low degree of superheat. As shown by Plesset and Zwick [9], for a bubble with low degree of superheat, the idle time is longer and the growth rate is smaller than those for a bubble with high degree of superheat. As a result, the liquid jet with a low degree of superheat emerging from an orifice remains intact up to some distance from the orifice, after which it is shattered due to a rapid bubble growth at the end of the idle time. The explanation of mechanism of jet shattering due to such a bubble growth together with empirical models relating the important spray properties such as the spray-cone angle, the breakup length, and the drop diameter with the parameters associated with the flash-boiling processes have been given by various authors [2, 4, 5, 8]. Such a flash-boiling spray with low degree of superheat, however, is unsuitable for

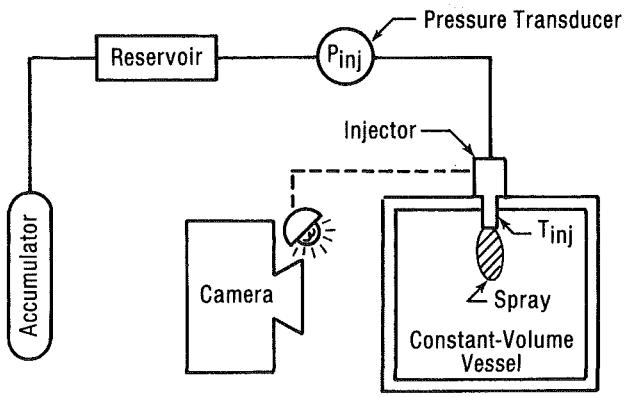

Fig. 1 Experimental apparatus

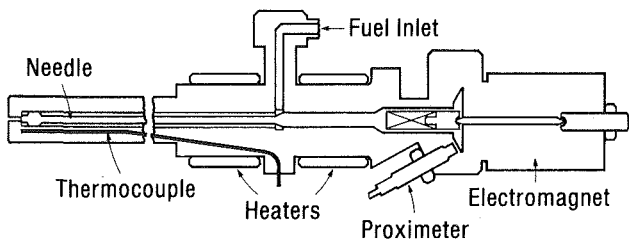

Fig. 2 Injector design

Contributed by the Fluids Engineering Division of THE AMERICAN SOCIETY OF MECHANICAL ENGINEERS and presented at the 7th Annual/Energy-Sources Technology Conference and Exhibition, New Orleans, La., February 11–17, 1984. Manuscript received by the Fluids Engineering Division, September 22, 1982. Paper No. 84-FE-4.

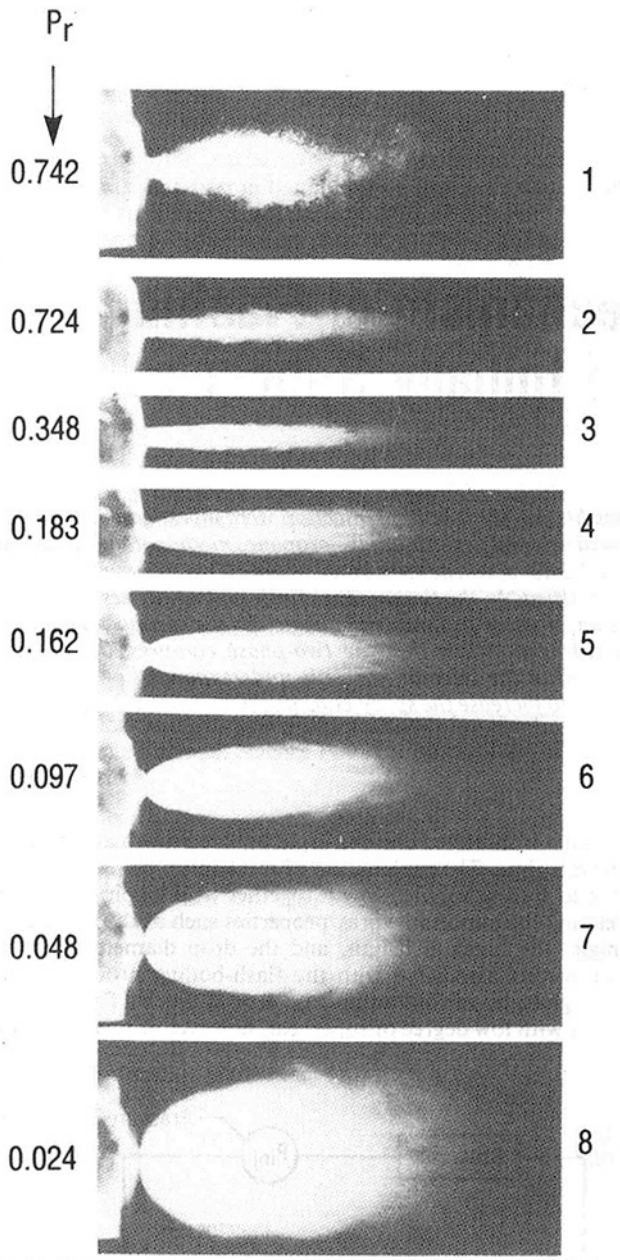

Fig. 3 Propane spray at P_{inj} = 2000 kPa, and T_{inj} = 300 K (uncertainty in P_{inj} = 20 kPa, in T_{inj} = 0.5 K)

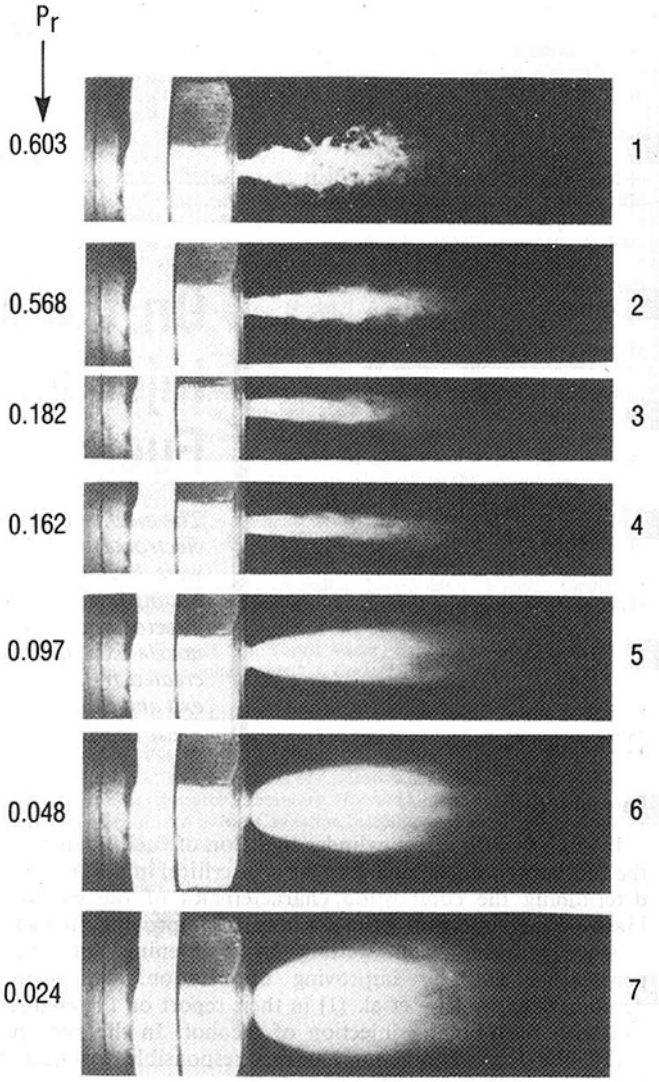

Fig. 4 Methanol spray at P_{inj} = 2000 kPa and T = 380 K (uncertainty in P_{inj} = 20 kPa, in T_{inj} = 0.5 K)

a use in a practical engine. This is because for such sprays, the degree of superheat will be difficult to control with required accuracy in a practical engine. In addition, the swift air motion in the engine is likely to destroy the intact jet before it has a chance to undergo flash boiling.

On the other hand, flash-boiling injection with high degree of superheat has been tried successfully by Kim et al. [1] to improve the engine performance. Although the spray characteristics such as reduced spray penetration, improved atomization and increased spray-cone angle for the spray with high degree of superheat were linked to the improvement in engine performance [1], the basic understanding about what leads to such a favorable spray configuration is completely lacking. The present study contributes to the understanding of the mechanism responsible for flash-boiling injection at high degree of superheat.

In the present study, the flash-boiling injection of three different fuels of practical importance, superheated to conditions promoting large bubble-growth rates, was investigated. Of the three spray characteristics mentioned in the preceding paragraph, the spray-cone angle was studied in detail and its variation as a function of injection pressure, chamber pressure, fuel temperature and injector-needle lift was examined. Also, different regimes of flash-boiling injection were identified and a mechanism to explain these regimes was proposed.

Experimental Apparatus and Procedure. The experimental setup is shown schematically in Fig. 1. Fuel was pressurized using an accumulator and was injected into a constant-volume vessel with an electromagnetic injector (Fig. 2). The use of the accumulator-type injection system with the electromagnetic injector allows accurate adjustment of injection pressure. The electromagnetic injector has an orifice of 1.25 mm and a nozzle length of 5 mm. It can be operated at a maximum injection pressure of 2.86 mPa and a maximum tip temperature of 383 K. It is designed such that needle lift is adjustable and can be measured by monitoring the proximeter output on an oscilloscope. The maximum value of the needle lift was held constant at 0.125 mm for all the experiments for which the needle lift was not an experimental variable to be studied. The time for the needle to open from the zero lift to the maximum lift and the injection-duration time were found to be 0.8 ms and 8.5 ms, respectively, as measured from the oscilloscope trace for the needle lift; and both of them were

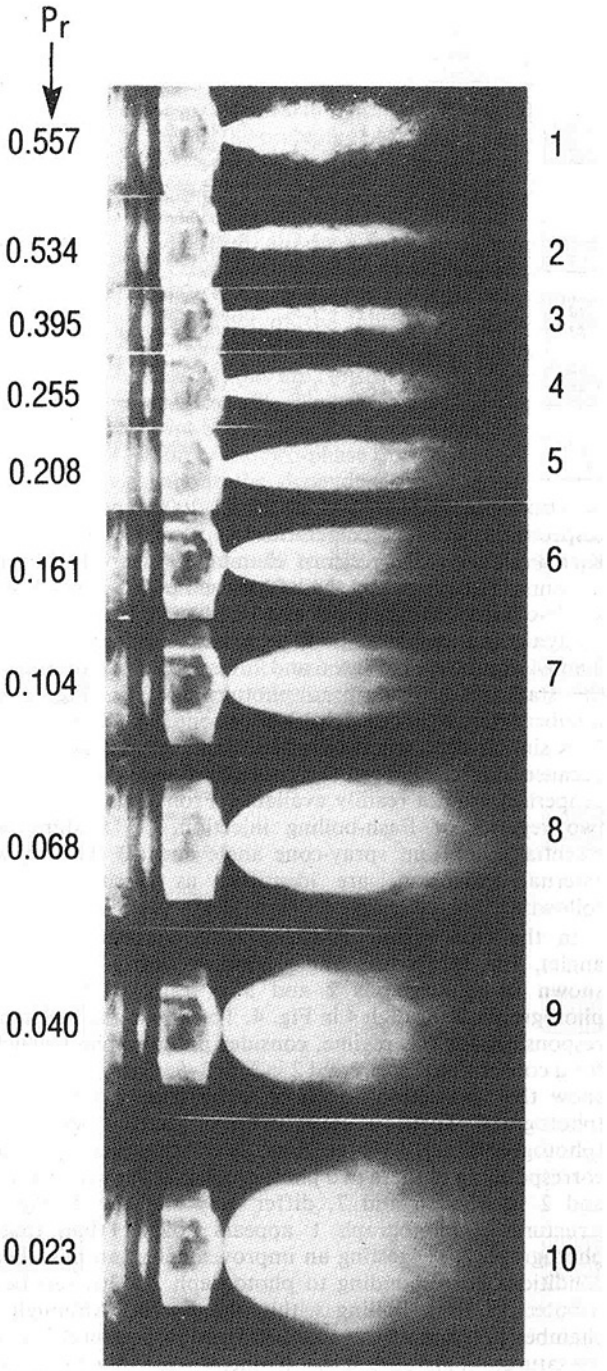

Fig. 5 Indolene spray at P_{inj} = 1480 kPa and T_{inj} = 380 K (uncertainty in P_{inj} = 15 kPa, T_{inj} = 0.5 K)

found to be repeatable. The needle lift remained constant once it reached its maximum value.

During the study, the constant-volume vessel was filled with nitrogen to provide an inert environment at absolute pressures ranging from 35 kPa to 2.1 mPa. A photographic study was conducted using a stroboscopic light source. The signal employed in triggering the electromagnetic injector was also used to trigger the strobe in a single-pulse mode after a predetermined time delay which was determined as follows. A study was made in which the injection conditions were held constant while the time delay after which the strobe was triggered was varied between 1.0 to 8.0 ms. The spray profiles obtained in this study were virtually identical, meaning that the spray remained steady during this period. Consequently, a time delay of 6 ms to trigger the strobe was chosen for all the experiments.

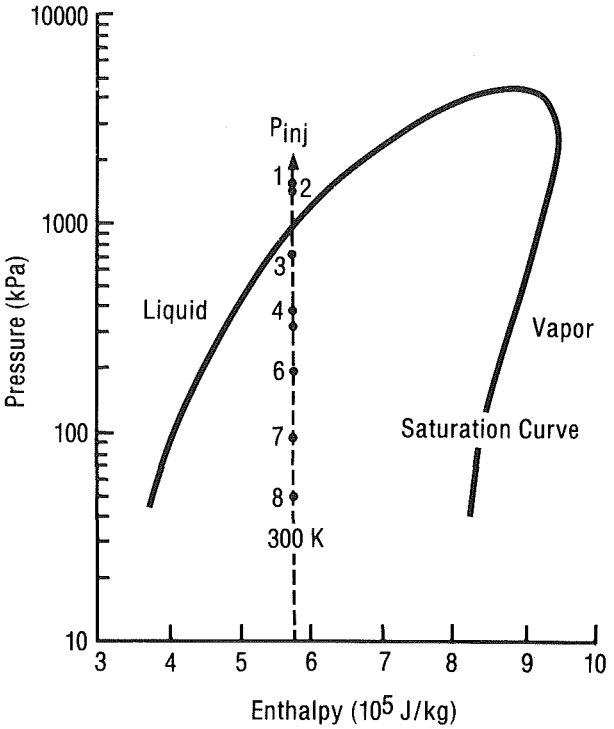

Fig. 6 Thermodynamic representation of propane states at P_{inj} = 2000 kPa (uncertainty in P_{inj} = 20 kPa)

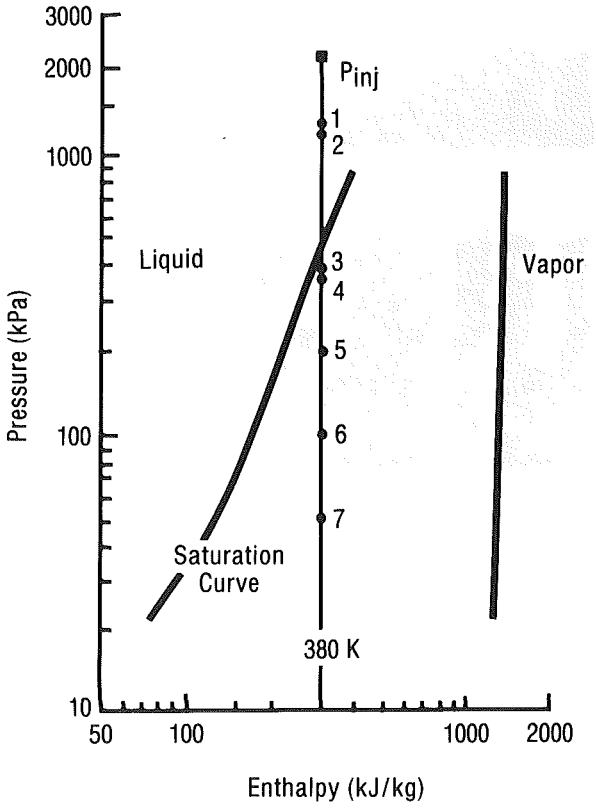

Fig. 7 Thermodynamic representation of alcohol states at P_{inj} = 2000 kPa (uncertainty in P_{inj} = 20 kPa)

During the study of injection at high temperatures, the injector was heated with two band heaters (100 watts each), and the fuel was preheated in the reservoir with a heating

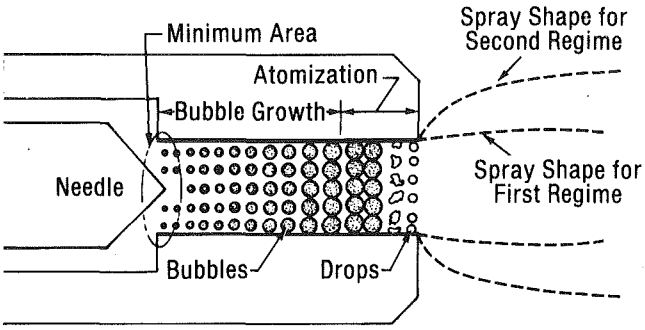

Fig. 8 Expansion of the underexpanded two-phase flow created by flashing within the nozzle

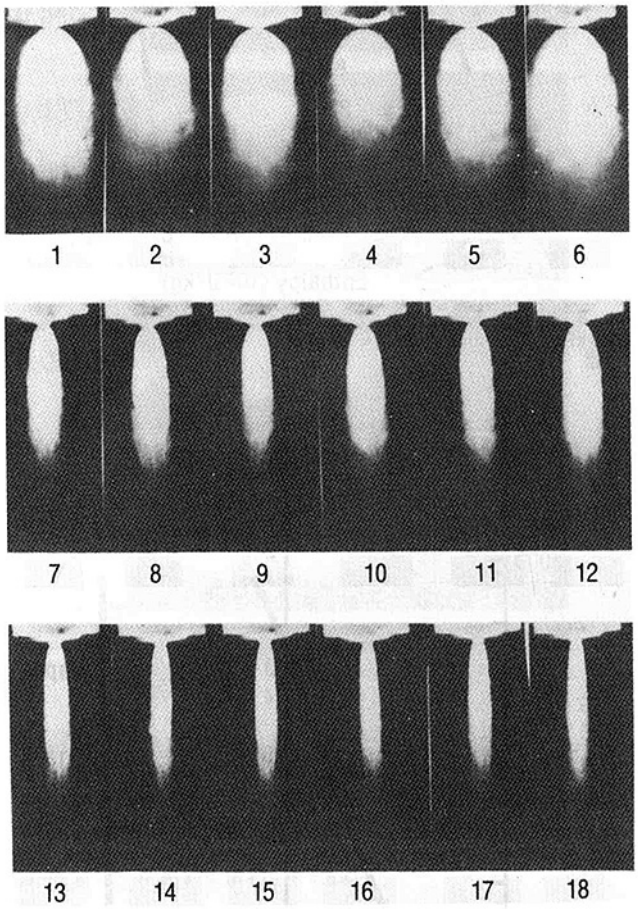

Fig. 9 Dependence of spray-cone angle of propane spray on pressure ratio

ribbon. The fuel temperature was monitored with thermocouples at three different locations: (1) at the injector tip near the orifice, (2) near the fuel-entrance port of the injector, and (3) at the center of the fuel reservoir.

The three fuels tested in this study were: (1) propane, which has a high vapor pressure and is easy to vaporize, (2) methanol, which has a low vapor pressure and is difficult to vaporize, and (3) Indolene, which, unlike the first two, is a multi-component fuel and resembles gasoline in composition.

Reproducibility of the spray shape was found satisfactory when the experiments were repeated.

Results

Figures 3, 4, and 5 contain photographic sequences of propane, methanol and Indolene sprays, respectively, at

Table 1

Picture Number	Injection Pressure (kPa)	Chamber Pressure (kPa)	Pressure Ratio (P_r)	Temperature (K)
1	2862 ± 29	69 ± 0.3	0.024 ± 0.0003	317 ± 0.5
2	2862 ± 29	69 ± 0.3	0.024 ± 0.0003	300 ± 0.5
3	2345 ± 23	55 ± 0.3	0.024 ± 0.0004	317 ± 0.5
4	2345 ± 23	55 ± 0.3	0.024 ± 0.0004	300 ± 0.5
5	2000 ± 20	48 ± 0.3	0.024 ± 0.0004	317 ± 0.5
6	2000 ± 20	48 ± 0.3	0.024 ± 0.0004	300 ± 0.5
7	2862 ± 29	276 ± 3.5	0.097 ± 0.002	317 ± 0.5
8	2862 ± 29	276 ± 3.5	0.097 ± 0.002	300 ± 0.5
9	2345 ± 23	228 ± 3.5	0.097 ± 0.002	317 ± 0.5
10	2345 ± 23	228 ± 3.5	0.097 ± 0.002	300 ± 0.5
11	2000 ± 23	193 ± 3.5	0.097 ± 0.003	317 ± 0.5
12	2000 ± 23	193 ± 3.5	0.097 ± 0.003	300 ± 0.5
13	2862 ± 29	524 ± 3.5	0.183 ± 0.003	317 ± 0.5
14	2862 ± 29	524 ± 3.5	0.183 ± 0.003	300 ± 0.5
15	2345 ± 23	428 ± 3.5	0.183 ± 0.003	317 ± 0.5
16	2345 ± 23	428 ± 3.5	0.183 ± 0.003	300 ± 0.5
17	2000 ± 20	366 ± 3.5	0.183 ± 0.007	317 ± 0.5
18	2000 ± 20	366 ± 3.5	0.183 ± 0.007	300 ± 0.5

injection pressures (P_{inj}) of 2000, 2000 and 1480 kPa, respectively, and fuel temperatures (T_{inj}) of 300, 380, and 380 K, respectively. The ratio of chamber pressure to injection pressure, P_r, is listed on the left of each photograph. For the single-component propane and methanol fuels, the thermodynamic states corresponding to each photograph in Figs. 3 and 4 are shown in Figs. 6 and 7, respectively. For example, the state corresponding to photograph 7 in Fig. 4 (the numbers shown on the right) is represented by State 7 in Fig. 7. A similar representation of Indolene spray is not possible because Indolene is a multi-component fuel and its saturation properties are not readily available. From Figs. 3, 4, and 5, two regimes of flash-boiling injection, (1) flashing with essentially constant spray-cone angle and (2) flashing with external expansion, are identified as discussed in the following.

In the first regime (flashing with constant spray-cone angle), the spray-cone angle remains nearly constant, as shown in photographs 2 and 3 in Figs. 3 and 5, and photographs 2 through 4 in Fig. 4. To explain the mechanism responsible for this regime, consider photographs 1 which is for a conventional spray and 2 in Fig. 3–5. These photographs show the "transition" from a spray with a fluffy plume (photograph 1) to a spray with a pencil-shaped flume (photograph 2). Note that the chamber pressures corresponding to these two photographs, as shown by States 1 and 2 in Figs. 6 and 7, differ only slightly. The plume structure in photograph 1 appears coarser than that in photograph 2, suggesting an improvement in atomization at conditions corresponding to photograph 2. This can be attributed to flash boiling within the nozzle. Although the chamber pressure at transition (transition pressure) is above the saturation pressure at that temperature, as shown by point 2 in Fig. 6 and 7, the local pressure near the location of minimum area within the injector (Fig. 8) falls below the saturation pressure, triggering the bubble growth that creates a two-phase mixture. The ratio of the minimum area measured at the maximum needle lift to the orifice area at the injector exit is 0.14. The location of the minimum area, shown in Fig. 8, is near the injector seat because the flow around the corner at the seat has a contraction. As shown in Fig. 8, when a sufficient number of bubbles grow sufficiently fast during their passage through the nozzle, they coalesce to create a two-phase flow consisting of vapor and crops. Thus, for chamber pressures lower than the transition pressure, it is logical to conclude that two-phase flow exists at the injector exit. Due to small dimensions of the orifice, a direct verification of the two-phase flow, either by pressure measurement or photographic, is virtually impossible.

In the second regime (flashing with external expansion), as shown in photographs 4 to 8 in Fig. 3, photographs 5 to 7 in

Fig. 4 and photographs 4 to 10 in Fig. 5, the spray-cone angle increases as the pressure ratio, P_r, decreases. This suggests an external expansion of a two-phase flow as shown in Fig. 8. Two-phase flow is created because the chamber pressure in this regime is below the transition pressure, and thus the mechanism described in the preceding paragraph is valid.

External expansion of a two-phase mixture is further supported by Fig. 9. The experimental conditions for this figure are listed in Table 1. In this figure, the pressure ratio for each row remains fixed, although the individual values of injection pressure, chamber pressure and fuel temperature vary. As shown in Fig. 9, the spray cone is a function only of the pressure ratio and not of the individual values of the injection pressure, the chamber pressure and the fuel temperature. These observations are consistent with those for an underexpanded gas flow [6]. Thus it is concluded that the increase in spray-cone angle observed in this regime is a result of external expansion of the two-phase flow.

The statement about the dependence of the spray-cone angle on the pressure ratio should not be generalized beyond the range of conditions considered in the present experiments. In the present experiments, the temperature for methanol and Indolene was maintained at 380 K, while the temperatures for propane were at 300 and 317 K. The needle lift was varied in the range 0.04 mm to 0.18 mm. However, if varying either the needle lift or the fuel temperature beyond the range considered here affects vapor fraction, it will change both the compressibility and the sound speed and thus may become an additional variable affecting the spray-cone angle.

In summary, flash-boiling creating a two-phase flow within the nozzle is the mechanism common to both regimes of flash-boiling injection demonstrated. External expansion, on the other hand, occurs only in the second regime and is the mechanism which leads to the increase in spray-cone angle observed in this regime.

References

1 Kim, Y. K., Twai, N., Suto, H., and Tsuruga, T., "Improvement of Alcohol Engine Performance by Flash Boiling Injection," *JSAE Review*, 1980, pp. 81–86.

2 Wu, K. J., Steinberger, R. L., and Bracco, F. V., "On the Mechanism of Breakup of Highly Superheated Liquid Jets," 1981 Spring Meeting, Central State Section, The Combustion Institute, Warren, MI, Mar. 23–24, 1981.

3 Lienhard, J. H., and Stephenson, J. M., "Temperature and Scale Effects Upon Cavitation and Flashing in Free and Submerged Jets," ASME *Journal of Basic Engineering*, Vol. 84, 1966, pp. 525–532.

4 Lienhard, J. H., and Day, J. B., "The Breakup of Superheated Liquid Jets," ASME *Journal of Basic Engineering*, Vol. 88, 1970, pp. 515–522.

5 Sher, E., and Elata, C., "Spray Formation from Pressure Cans by Flashing," *Industrial Engineering and Process Design and Development*, Vol. 16, No. 2, 1977, pp. 237–242.

6 Suzuki, M., Yamamoto, T., Futagami, N., and Maeda, S., "Atomization of Superheated Liquid Jets," First International Conference on Liquid Atomization and Spray Systems," Tokyo, Japan, Aug. 1978.

7 Brown, R., and York, J. L., "Sprays Formed by Flashing Liquid Jets," *A.I.Ch.E. Journal*, May 1962, pp. 149–153.

8 Soloman, A. S. P., Rupprecht, S. D., Chen, L. D., and Faeth, G. M., "Atomization and Combustion Properties of Flashing Injectors," Paper No. 82-0300, 20th Aerospace Sciences Meeting, American Institute of Aeronautics and Astronautics, Orlando, Fla., Jan. 11–14, 1982.

9 Plesset, M. S., and Zwick, S. A., "The Growth of Vapor Bubbles in Superheated Liquids," *Journal of Applied Physics*, Vol. 25, No. 4, 1954, pp. 492–500.

Journal of Fluids Engineering

Discussion

Appraisal of Universal Wake Numbers From Data for Roughened Circular Cylinders[1]

P. W. Bearman.[2] I am pleased to see Professor Buresti returning us to the problem of universal Strouhal numbers. The derivation of the three numbers he has chosen to study all imply a unique relation between SC_D (the product of Strouhal number and drag coefficient) and the base pressure parameter K. The accompanying figure indicates that available experimental data confirms this dependence. In addition I have plotted the functional relationships given by constancy of the three wake Strouhal numbers. Using free streamline theory to link C_D and C_{pb} ($C_D d = -C_{pb} d'$) and assuming $S_r = 0.164$, the Roshko number gives rise to the relation $S.C_D = 0.164\,K(K^2 - 1)$. This can be seen to overestimate the data at high K. My formulation (given in Bearman [2]) is invalid for large values of K. It is based on an interesting idea by Kronauer that vortex streets composed of point vortices arrange themselves into a configuration giving minimum drag. This appears now to have been a too simplistic approach to the real vortex street stability problem. Use of the number suggested by Griffin gives the best overall fit to the data although it overestimates $S.C_D$ for bodies of low bluffness.

The correlation between $S.C_D$ and K suggests that regular vortex shedding is a result of an instability mechanism which is primarily inviscid. The success of the discrete vortex method in predicting Strouhal numbers of bluff bodies is a further indication of the unimportance of viscosity. Results presented in this paper, however, show the interesting result that wake Strouhal numbers depend on a roughness Reynolds number. An alternative parameter is the ratio of roughness height to cylinder diameter, does this also collapse the data?

When referring to different Reynolds number regimes for flow around a circular cylinder I would urge that the nomenclature used by Roshko [10] be followed. However I would endorse the author's use of the term postcritical rather than transcritical to describe the highest Reynolds number range. The regimes then become subcritical supercritical and postcritical. Roshko describes how each is separated by a transition regime. Regular vortex shedding can be detected through the sub and supercritical regimes but disappears in the upper transition range. Separation bubbles form on the cylinder in the supercritical regime and they break down at the commencement of the upper transition region. Professor Buresti calls the lower transition regime the critical regime and states that it is typified by the absence of vortex shedding. Other authors, including most recently Schewe [11], have measured a distinct shedding frequency and hence the author's statement is puzzling.

[1] By G. Buresti published in the December 1983 issue of the JOURNAL OF FLUIDS ENGINEERING, Vol. 105, No. 4, pp. 464-468.

[2] Department of Aeronautics, Imperial College, London, SW7 2BY England.

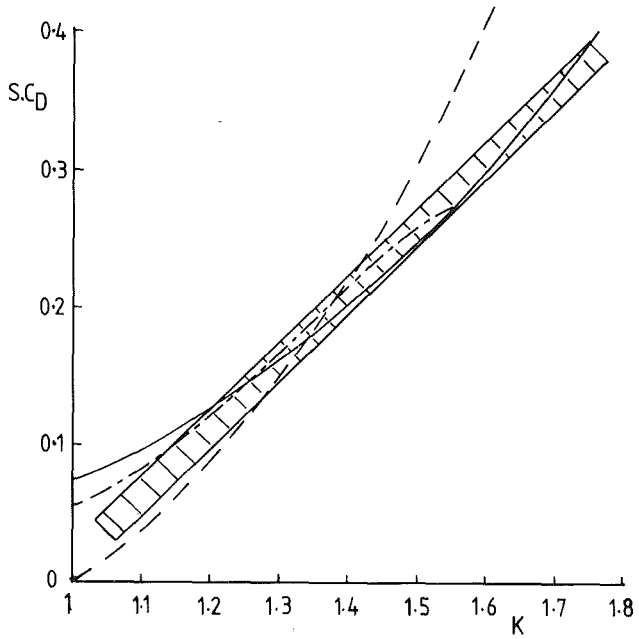

Fig. 5 Variation of $S.C_D$ with K. □□□□□ Range of experimental results; ————, Roshko [1]; -·-·-·-, Bearman [2]; —— Griffin [3]

Additional References

10 Roshko, A., "Experiments on the Flow Past a Circular Cylinder at Very High Reynolds Number," *J. Fluid Mech.*, Vol. 10, 1961.

11 Schewe, G., "On the Force Fluctuations Acting on a Circular Cylinder in Crossflow from Subcritical up to Transcritical Reynolds Numbers," *J. Fluid Mech.*, Vol. 133, 1983.

Author's Closure

I am grateful to Dr. Bearman for his discussion and particularly for his additional data which substantiate the results given in the paper about the possibility of describing the experimentally observed relation between SC_D and K by means of the three universal numbers considered.

As regards the points raised by Dr. Bearman, I would like to start from the problem of the definition of the flow regimes. Indeed, it is certainly true that time has come for researchers to find an agreement on the nomenclature to be used for the flow regimes around circular cylinders. Therefore, I will accept and support Dr. Bearman's proposal of calling the regimes, in order of increasing Reynolds number, subcritical, lower transition, supercritical, upper transition and postcritical. However, it is also important that we all agree on the phenomenological description of the transitional regimes. On this respect, I would like to remark

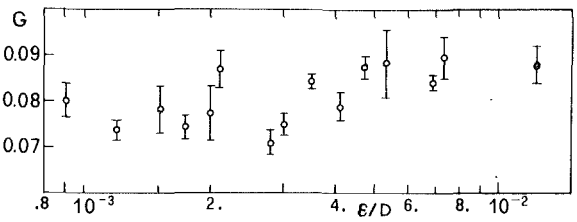

Fig. 6 Variation of Griffin's number with relative roughness

that the curves of C_D and S as a function of Re given by Roshko [10], Bearman [12] and Schewe [11], all refer to very smooth cylinders. The variations induced on these curves by even small quantities of surface roughness are dramatic and well documented (see [5] and [13]). Now, the definition of the flow regimes given in my paper applies to rough cylinders and its correspondence with the nomenclature proposed by Dr. Bearman is as follows: my critical regime corresponds to his lower transition, my supercritical to his upper transition, while the subcritical and postcritical regimes coincide. Dr. Bearman's supercritical regime, which corresponds to a low-C_D, high-S plateau, is practically absent for rough cylinders. The puzzle of the "missing vortex shedding" in the lower transition is easily explained if we recall that, as reported by Schewe [11], vortex shedding in this regime corresponds to a single bubble appearing on one side of the cylinder, a situation which is hardly possible unless the cylinder is smooth and the turbulence level of the wind tunnel low. I would also like to stress the fact that the peaks in the spectra of the lift force reported in [11] and [12] for this regime and for the supercritical one, are normally two orders of magnitude lower than those for the subcritical and postcritical regimes, and thus in the tests described in [5] they could have been masked by turbulence-induced fluctuations. In conclusion, I think that, as suggested by Berger and Wille [14], regular vortex shedding may take place only provided the separation of the boundary layer occurs along a straight line; now, in the transitional regimes of a very smooth cylinder in a low turbulence flow the separation bubbles are extremely unstable, and thus a long range of weak vortex shedding is observed. On the contrary, for a rough cylinder the transition range is much shorter and the bubbles, when they exist, are smaller and have a reduced range of existence. A quicker return to regular vortex shedding, corresponding to a stable separation of the turbulent boundary layer, is then possible, and this explains the absence of the instability phenomena in the upper transition regime which were found in [10] and [11].

I perfectly agree with Dr. Bearman on the observation that all evidence now available suggests that regular vortex shedding can appropriately be described with reference to fundamentally inviscid mechanisms, and I do not think that a moderate dependence of the wake numbers on the roughness Reynolds number contradicts this point. In fact, when we say that the phenomenon is mainly inviscid we mean that the vorticity is concentrated in thin sheets emanating from the separation points of the body. However, the resulting flow and pressure fields are very sensitive to the actual distribution of this vorticity, and therefore it is not unreasonable that slightly different parameters be found for different conditions (and in particular different momentum thicknesses) of the separating boundary layers. The accompanying figure shows that the ratio of the roughness height to the cylinder diameter ϵ/D does not give as good a collapse of the data as was given by R_ϵ. This is not unexpected because ϵ/D is not sufficient to describe the effect of roughness on the transition between the flow regimes; in other words, the regime can be subcritical even for high values of the surface roughness if the Reynolds number is sufficiently low. Conversely, as shown in Fig. 4 of my paper, two distinct values of Griffin's number seem to apply to the subcritical and to the roughness-induced post-critical regimes; it might be interesting to check if a further increase in Reynolds number for a rough cylinder does not give rise to a decrease of G back to its subcritical value.

Additional References

12 Bearman, P. W., "On Vortex Shedding From a Circular Cylinder in the Critical Reynolds Number Regime," *J. Fluid Mech.*, Vol. 37, 1969, pp. 577–585.

13 Achenbach, E., and Heinecke, E., "On Vortex Shedding From Smooth and Rough Cylinders in the Range of Reynolds Numbers 6×10^3 to 5×10^6," *J. Fluid Mech.*, Vol. 109, 1981, pp. 239–251.

14 Berger, E., and Wille, R., "Periodic Flow Phenomena," *Ann. Rev. Fluid Mech.*, Vol. 4, 1972, pp. 313–340.

The Flow Past a Surface-Mounted Obstacle[1]

I. P. Castro.[2] The basic conclusion of this paper is that the flow around a two-dimensional rectangular section surface mounted obstacle is strongly dependent on the axial length/height ratio. This is not a startling conclusion and, despite the authors' statement that to their knowledge "the flow field past a surface mounted obstacle for various width-to-height ratios has not been previously investigated" there is, in fact, an increasing body of literature covering this whole field. Hosker [12] has recently given a very extensive review and cites a number of papers which discuss precisely this point (e.g., Arie et al. [9]). Incidentally, most authors use "width" to mean the spanwise dimension of the body, so the present authors' use of the term to mean the axial length could be confusing.

While it is becoming increasingly apparent that the body geometry is often the dominant factor governing the behavior of the surrounding flow field, particularly of course in the near wake, there is no doubt that the characteristics of the upstream boundary layer and, in wind tunnel experiments, the blockage ratio, can have important effects. The authors' data certainly show again the importance of body geometry and they do specify the blockage ratio and state that the boundary layer velocity profile, in the absence of the body, obeys a 1/6.9 power law and is 0.48H in thickness. However, they do not discuss the likely influences of the upstream flow characteristics and it must be emphasized that their results are specific to their particular flow. Presumably, as other authors have shown, increasing δ/H (i.e., increasing the turbulent energy at, say, the body height) would lead to a reduction in the reattachment length, L_R, and a reduction in the value of W/H at which the separated shear layer permanently reattaches onto the top surface of the body. The authors' technique of "defining" the reattachment point as the location where the mean ouptut from a linearized (near-wall) single hot wire is a minimum has little to justify it and could possibly not be good enough to determine even the trends in L_R as δ/H varied.

Considerable use of flow visualization was made in the work, but the authors do not state how they defined the "trajectory of the shear layer" (Fig. 2). Perhaps it was a certain looseness in this concept (admittedly often inevitable in trying to use flow visualization to obtain quantitative data) which led to their statement "that the angle of separation is much smaller" (for $W/H = 5$) "compared to that of a square section obstacle." This must surely be incorrect? If the Reynolds number is high enough separation at the leading

[1] By G. Bergeles and N. Athanassiadis, published in the December, 1983 issue of the JOURNAL OF FLUIDS ENGINEERING, Vol. 105, No. 4, pp. 461–463.

[2] University of Surrey, Guildford, United Kingdom.

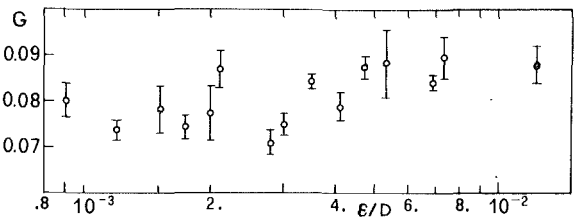

Fig. 6 Variation of Griffin's number with relative roughness

that the curves of C_D and S as a function of Re given by Roshko [10], Bearman [12] and Schewe [11], all refer to very smooth cylinders. The variations induced on these curves by even small quantities of surface roughness are dramatic and well documented (see [5] and [13]). Now, the definition of the flow regimes given in my paper applies to rough cylinders and its correspondence with the nomenclature proposed by Dr. Bearman is as follows: my critical regime corresponds to his lower transition, my supercritical to his upper transition, while the subcritical and postcritical regimes coincide. Dr. Bearman's supercritical regime, which corresponds to a low-C_D, high-S plateau, is practically absent for rough cylinders. The puzzle of the "missing vortex shedding" in the lower transition is easily explained if we recall that, as reported by Schewe [11], vortex shedding in this regime corresponds to a single bubble appearing on one side of the cylinder, a situation which is hardly possible unless the cylinder is smooth and the turbulence level of the wind tunnel low. I would also like to stress the fact that the peaks in the spectra of the lift force reported in [11] and [12] for this regime and for the supercritical one, are normally two orders of magnitude lower than those for the subcritical and postcritical regimes, and thus in the tests described in [5] they could have been masked by turbulence-induced fluctuations. In conclusion, I think that, as suggested by Berger and Wille [14], regular vortex shedding may take place only provided the separation of the boundary layer occurs along a straight line; now, in the transitional regimes of a very smooth cylinder in a low turbulence flow the separation bubbles are extremely unstable, and thus a long range of weak vortex shedding is observed. On the contrary, for a rough cylinder the transition range is much shorter and the bubbles, when they exist, are smaller and have a reduced range of existence. A quicker return to regular vortex shedding, corresponding to a stable separation of the turbulent boundary layer, is then possible, and this explains the absence of the instability phenomena in the upper transition regime which were found in [10] and [11].

I perfectly agree with Dr. Bearman on the observation that all evidence now available suggests that regular vortex shedding can appropriately be described with reference to fundamentally inviscid mechanisms, and I do not think that a moderate dependence of the wake numbers on the roughness Reynolds number contradicts this point. In fact, when we say that the phenomenon is mainly inviscid we mean that the vorticity is concentrated in thin sheets emanating from the separation points of the body. However, the resulting flow and pressure fields are very sensitive to the actual distribution of this vorticity, and therefore it is not unreasonable that slightly different parameters be found for different conditions (and in particular different momentum thicknesses) of the separating boundary layers. The accompanying figure shows that the ratio of the roughness height to the cylinder diameter ϵ/D does not give as good a collapse of the data as was given by R_ϵ. This is not unexpected because ϵ/D is not sufficient to describe the effect of roughness on the transition between the flow regimes; in other words, the regime can be subcritical even for high values of the surface roughness if the Reynolds number is sufficiently low. Conversely, as shown in Fig. 4 of my paper, two distinct values of Griffin's number seem to apply to the subcritical and to the roughness-induced postcritical regimes; it might be interesting to check if a further increase in Reynolds number for a rough cylinder does not give rise to a decrease of G back to its subcritical value.

Additional References

12 Bearman, P. W., "On Vortex Shedding From a Circular Cylinder in the Critical Reynolds Number Regime," *J. Fluid Mech.*, Vol. 37, 1969, pp. 577–585.

13 Achenbach, E., and Heinecke, E., "On Vortex Shedding From Smooth and Rough Cylinders in the Range of Reynolds Numbers 6×10^3 to 5×10^6," *J. Fluid Mech.*, Vol. 109, 1981, pp. 239–251.

14 Berger, E., and Wille, R., "Periodic Flow Phenomena," *Ann. Rev. Fluid Mech.*, Vol. 4, 1972, pp. 313–340.

The Flow Past a Surface-Mounted Obstacle[1]

I. P. Castro.[2] The basic conclusion of this paper is that the flow around a two-dimensional rectangular section surface mounted obstacle is strongly dependent on the axial length/height ratio. This is not a startling conclusion and, despite the authors' statement that to their knowledge "the flow field past a surface mounted obstacle for various width-to-height ratios has not been previously investigated" there is, in fact, an increasing body of literature covering this whole field. Hosker [12] has recently given a very extensive review and cites a number of papers which discuss precisely this point (e.g., Arie et al. [9]). Incidentally, most authors use "width" to mean the spanwise dimension of the body, so the present authors' use of the term to mean the axial length could be confusing.

While it is becoming increasingly apparent that the body geometry is often the dominant factor governing the behavior of the surrounding flow field, particularly of course in the near wake, there is no doubt that the characteristics of the upstream boundary layer and, in wind tunnel experiments, the blockage ratio, can have important effects. The authors' data certainly show again the importance of body geometry and they do specify the blockage ratio and state that the boundary layer velocity profile, in the absence of the body, obeys a 1/6.9 power law and is 0.48H in thickness. However, they do not discuss the likely influences of the upstream flow characteristics and it must be emphasized that their results are specific to their particular flow. Presumably, as other authors have shown, increasing δ/H (i.e., increasing the turbulent energy at, say, the body height) would lead to a reduction in the reattachment length, L_R, and a reduction in the value of W/H at which the separated shear layer permanently reattaches onto the top surface of the body. The authors' technique of "defining" the reattachment point as the location where the mean ouptut from a linearized (near-wall) single hot wire is a minimum has little to justify it and could possibly not be good enough to determine even the trends in L_R as δ/H varied.

Considerable use of flow visualization was made in the work, but the authors do not state how they defined the "trajectory of the shear layer" (Fig. 2). Perhaps it was a certain looseness in this concept (admittedly often inevitable in trying to use flow visualization to obtain quantitative data) which led to their statement "that the angle of separation is much smaller" (for $W/H = 5$) "compared to that of a square section obstacle." This must surely be incorrect? If the Reynolds number is high enough separation at the leading

[1] By G. Bergeles and N. Athanassiadis, published in the December, 1983 issue of the JOURNAL OF FLUIDS ENGINEERING, Vol. 105, No. 4, pp. 461–463.

[2] University of Surrey, Guildford, United Kingdom.

edge must occur tangential to the front face, irrespective of the body geometry elsewhere. The flow behavior near the leading edge is complex (see, for example, some recent work of our own—Castro and Dianant [10]) and may, in detail, depend on the flow elsewhere, certainly as far as the unsteady behavior is concerned, but the mean streamline outside the viscous region will presumably always be virtually parallel to the front face—provided the corner is sufficiently sharp.

A final point concerns the two-dimensionality of the flow. The authors have rightly sought to ensure that their flow is reasonably two-dimensional but it is exceedingly difficult to maintain two-dimensionality in cases, like this one, where the length of the separated region is of the same order as its width. The inevitable vortex structures at the juction between the side walls and the obstacle itself can have a dominant influence right across the flow. Recent work by Ruderich and Fernholz [11] and shows this clearly. The authors might have found it revealing to investigate the spanwise distribution of L_R! They should anyway be cautious regarding the apparent two-dimensionality of their flow, although the *trends* in their data are unlikely to be greatly changed by such effects.

Additional References

9 Arie, Kiya, Tamura, Kosugi and Takaoka, "Flow Over Rectangular Cylinders Immersed in a Turbulent Boundary Layer, Part 2, Flow Patterns and Pressure Distributions, *Bulletin of J.S.M.E.*, Vol. 18, 1975, pp. 1269-1276.

10 Castro and Dianat, "Surface Flow Patterns on Rectangular Bodies in Thick Turbulent Boundary Layers," 1983.

11 Ruderich and Fernholz, "An Experimental Investigation of the Turbulent Shear Flow Downstream of a Normal Flat Plate With a Long Splitter Plate," Paper presented at 4th Turbulent Shear Flow Symposium, Karlsruhe, Sept. 1983.

12 Hosker, "Flow and Dispersion Near Obstacles," Chapter 7 in *Atmospheric Science and Power Production*, ed. D. Anderson, 1982.

D. J. Cockrell.[3] In adequately demonstrating that reattachment length downstream of a surface-mounted obstacle depends on the width to height ratio of the obstacle the authors have made a useful contribution to our appreciation of separated flows which have engineering significance. However, the prime concern of the engineer is with gross effects which these flow phenomena will cause, such as the drag of the obstacles in isolation and the resultant drag of the surfaces on which they are mounted. Various authors, e.g., Wieghardt [14], have measured the drag of ridges having varying width to height ratios. Some relationship of this work with the author's conclusions would be useful.

Eaton and Johnston [15] have clearly indicated that obstacle width to height ratio is not the only significant parameter which determines the flow reattachment length. Since they considered a backward-facing step, i.e., the rear part only of the authors' obstacles, they could not include width to height ratio but listed instead: (i) momentum thickness Reynolds number at the location of the obstacle; (ii) boundary layer thickness to obstacle height at this location; (iii) freestream turbulence intensity; (iv) streamwise freestream pressure gradient and (v) the ratio of the channel height in which the experiment was performed to the obstacle height. Consider the possible influence of these five parameters to the present Bergeles and Athanassiadis study.

(i) *Momentum thickness Reynolds number.* Using the authors' power law velocity profile the momentum thickness Reynolds number of the undisturbed flow at the obstacle's location is about 1250. The Eaton and Johnston reattachment length of some 8 obstacle heights is within the range which the authors quote. By implication, the reattachment length ratio given in Fig. 3 will slowly decrease with increasing momentum thickness Reynolds number.

(ii) *Boundary layer thickness to obstacle height.* Bradshaw and Wong discuss the effects downstream of the obstacle when this parameter is varied. For both the authors' ridges and Bradshaw and Wong's backward-facing step, $h/\delta_0 > 1$. This promotes overwhelming perturbations to the downstream flow, as the authors indeed established. However, their results will not be applicable to situations in which $h/\delta_0 = 0(1)$ or in which $h/\delta_0 < 1$. There is, as yet, insufficient evidence to show if Tani's results, obtained by examination of the separated flow behind a step of 3.5 boundary layer thickness heights, can be directly compared with those obtained by the authors behind relatively larger obstructions of approximately 2.0 boundary layer thicknesses.

(iii) *Freestream turbulence.* Eaton and Johnston's tabular summary consists of twenty three flow separation experiments behind backward-facing steps. The turbulence level at which the Authors worked was about mid range. Limited evidence indicates that higher levels of freestream turbulence result in decreased reattachment lengths.

(iv) *Streamwise pressure gradient.* Keuhn [16] shows that if the adversity of the freestream pressure gradient is increased the reattachment length behind the surface-mounted obstacle can also increase. But this effect is strongly dependent on the relative size of the obstacle, i.e., parameter (ii). Where $h/\delta_0 << 1$, Nigim [17] has shown that the reattachment length is independent of the streamwise pressure gradient.

(v) *Channel width to obstacle height.* In the authors' experiments this ratio was 11.2. It has been shown by de Brederode and Bradshaw [5] that if the ratio exceeds 10:1 the effect of this parameter on reattachment length is not significant.

It would be interesting to know exactly how the authors used their hot wire to establish the flow reattachment point. Did their method require the sensor to be lined up with the local direction of the flow?

More precise methods of establishing flow two-dimensionality exist than that described by the authors. Coles and Hirst [6] describe the streamwise integration of the momentum equation technique which was effectively used at the 1968 Stanford boundary layer conference. A much simpler but very precise technique is to establish the degree of downstream divergence or convergence of wakes which are set up behind two needles, mounted normal to the surface and transverse to the flow.

I found that $w/H = 0$, used in Fig. 5 to describe a fence was confusing. I would have preferred $w/H \to 0$.

Additional References

14 Wieghardt, K., "Increase of Turbulent Skin Friction Caused by Surface Irregularities," MAP R & T No. 103, Translation of FB 1563, ZWB 1942.

15 Eaton, J. K., and Johnston, J. P., "A Review of Research on Subsonic Flow Reattachment," *AIAA Journal*, Vol. 19, No. 9, Sept. 1981, pp. 1093-1100.

16 Keuhn, D. M., "Effects of Adverse Pressure Gradient on the Incompressible Reattaching Flow over a Rearward-Facing Step," *AIAA Journal*, Vol. 18, No. 3, Mar. 1980, pp. 323-344.

17 Nigim, H., "Effects of Small Isolated Roughness Elements on Turbulent Boundary Layers," Ph.D. thesis, University of Leicester, England, 1981.

18 de Brederode, V., and Bradshaw, P., "Three-Dimensional Flow in Nominally Two-Dimensional Separation Bubbles, I Flow Behind a Rearward-Facing Step," Imperial College London Aeronautical Report 72-19, 1972.

19 Coles, D. E., and Hirst, E. A., "Proceedings Computation of Turbulent Boundary Layers," AFOSR-IFP-Stanford Conference, Vol. II, Stanford University, 1968.

[3] Engineering Department, University of Leicester, Leicester, LE1 7RH, England.

Authors' Closure

I would like to thank Professors Cockrell and Castro for the additional information they have supplied concerning the influence of various parameters, additional to the geometry of the obstacle, on the length of the recirculating region behind the obstacle; the information supplements the present work and makes even more clear that the main parameters are the geometry of the obstacle and the status of the boundary layer before separation. As regards Professor Castro's comment that the angle of separation at the leading corner of the obstacle must be 90 deg, this is the case over the front face of the obstacle but this does not hold in the limit as the flow approaches the upstream corner. This argument comes out apart from the present study (based mainly on flow visualization) and from velocity measurements at the upstream corner of the obstacle {1}, Ackeret, J. "Anwendungen der Aerodynamik im Bauwesen. Zeitschr für Flugwissenschaften, Braunschweig, Vol. 13, Apr. 1965, Heft 4."

Boundary Layer Effects on Particle Impaction and Capture[1]

D. E. Rosner[2] and **J. Fernandez de la Mora.**[3] Our comments on the MGMS manuscript[4] fall naturally into the following four sections:

1. Boundary Layer (BL) Effects on Inertial Impaction/Capture of Small Particles.

We are pleased that MGMS have focused attention on the "cushion" effects of a BL on small particle inertial impaction, since, previously, N. Fuchs [14] drew attention only to the (numerically less important) "displacement" effect of the viscous BL in modifying the external inviscid flow about a target. In extending a useful correlation of inertial capture efficiencies [15], we recently estimated both contributions to the BL effect on the *critical Stokes number*, $\mathrm{Stk}_{\mathrm{crit}}$ (for the "onset" of inertial impaction on a cylinder). By representing the viscous BL as a quiescent "cushion" adjacent to the target, we find [16] that the BL effect is to increase $\mathrm{Stk}_{\mathrm{crit}}$ by nearly 10 percent even at a Reynolds number as high as 10^6. At this Re-value the displacement effect, if acting "alone," would be to increase $\mathrm{Stk}_{\mathrm{crit}}$ from its inviscid value (1/8) by less than 0.2 percent. Have MGMS also included the "displacement" effect in their combustion turbine numerical example (*i.e.* evaluated the particle "initial conditions" using the BL-perturbed inviscid flow), or is the prevailing Re high enough to render it negligible?

2. Relevant Dimensionless Groups.

MGMS report that the BL effect on particle impaction is important for particles in the nominal diameter range 3-6 μm. *in a particular numerical example* [1-3]. Of course, this conclusion is specific to the conditions of the example, and it is therefore helpful to consider a *general* criterion for the importance of such BL "cushion" effects. It is not difficult to conclude that such effects will be important whenever the characteristic particle "stopping time," t_p, is the same order of magnitude as the characteristic momentum BL "crossing time" $\delta/(V_{p,n})_e$, where $(V_{p,n})_e$ is the normal component of the particle velocity (relative to the surface) evaluated at the BL outer edge. Clearly, particles for which this time ratio, or "BL-Stokes number," is $<<1$ will never reach the surface (except by diffusion), whereas particles for which this BL-Stokes number is $>>1$ will impact without appreciable deceleration (and an associated change in angle-of-incidence). On this basis the BL-"cushion" effect will inevitably be most important for particle sizes which depend not only on Re and relative position on the target, but also on *particle* density and gas viscosity. While, for numerical convenience, MGMS's calculations have been cast in *dimensional* terms, for purposes of generalization and understanding it would be helpful if the corresponding *dimensionless* parameters were computed, stated, and systematically varied. Indeed, we have found that by introducing a Stokes number, $\mathrm{Stk}_{\mathrm{eff}}$, based on *relevant* characteristic times (or lengths) the correlation of inertial impaction phenomena is dramatically simplified [15, 17; see also, Section 4 below], and the same philosophy allows correlations of *diffusional* particle capture [17, 18] even simpler than those based, say, on formal dimensional analysis (see, e.g., [19]).

3. Analogous Effects of Particle/Gas Energy and Mass Exchange Within BLs.

Whereas MGMS focus attention on particle/gas *momentum* exchange during particle transit of the *momentum* defect BL, there are important and completely analogous *energy* and *species* exchange processes that occur when particles traverse the enthalpy defect and species defect BLs. For example, we are currently investigating the effects of (*a*) BL droplet freezing on particle capture by targets cooled below the droplet freezing temperature, and (b) chaperon vapor uptake by particles impacting on targets cooled below the vapor dew-point. However, as the number and complexity of such phenomena increases, the need for clever, rational simplifications clearly becomes more pressing. Only if our theoretical methods and correlations focus on the essential features, display the important functional dependencies, and lend themselves to design/optimization studies, are they likely to have a real impact on present or future engineering practice.

4. Combined Effects of Particle Inertia and Diffusion.

MGMS report that in their numerical illustration diffusive and inertial mechanisms "act together" for particles in the diameter range 0.5 μm-3 μm, in which case the assumptions underlying existing predictive models become questionable.

For *laminar* BLs the consequences of the "onset" of inertial effects on diffusional capture are not difficult to understand and calculate, since the dominant effect of non-negligible particle inertia (even at *sub-critical* Strokes numbers) is to alter the effective "local" particle mass fraction at the outer edge of the particle diffusion boundary layer. This "inertial enrichment" (or depletion) is investigated for high Re-flows in [20], and for low Re-flows in [21], using an approach which is asymptotically exact in the limit of high Schmidt number (low particle diffusivity cf. fluid momentum diffusivity).

In contrast, the diffusion-like behavior of inertial particles inside a *turbulent* boundary layer (TBL) raises more difficult questions [22], as yet unanswered. MGMS also report "deposition velocities" in that problematic regime, evidently by making use of a variant of [5] (e.g., that in [3]). For reasons presented elsewhere [22], we are skeptical about the quantitative reliability of such methods, especially as applied in the combustion turbine context. Nonetheless, it is interesting to observe (Fig. 14) the "merging" of the two different "branches" (diffusion-dominated and inertia-dominated). Paradoxically, the same BL that reduces im-

[1] By M. Mengüturk, D. Gunes, H. K. Mimaroglu, and E. F. Sverdrup (hereafter referred to as MGMS), published in the September 1983 issue of the JOURNAL OF FLUIDS ENGINEERING, Vol. 105, No. 3.

[2] Professor of Chemical Engineering and Applied Science, Yale University, New Haven, Conn. 06520.

[3] Assistant Professor of Mechanical Engineering, Yale University.

[4] Based on research at Yale University-High Temperature Chemical Reaction Engineering Laboratory; supported in part by AFOSR (Contract F49620-82K-0020) and NASA-Lewis Research Center (Grant NAG 3-201).

Authors' Closure

I would like to thank Professors Cockrell and Castro for the additional information they have supplied concerning the influence of various parameters, additional to the geometry of the obstacle, on the length of the recirculating region behind the obstacle; the information supplements the present work and makes even more clear that the main parameters are the geometry of the obstacle and the status of the boundary layer before separation. As regards Professor Castro's comment that the angle of separation at the leading corner of the obstacle must be 90 deg, this is the case over the front face of the obstacle but this does not hold in the limit as the flow approaches the upstream corner. This argument comes out apart from the present study (based mainly on flow visualization) and from velocity measurements at the upstream corner of the obstacle {1}, Ackeret, J. "Anwendungen der Aerodynamik im Bauwesen. Zeitschr für Flugwissenschaften, Braunschweig, Vol. 13, Apr. 1965, Heft 4."

Boundary Layer Effects on Particle Impaction and Capture[1]

D. E. Rosner[2] and **J. Fernandez de la Mora.**[3] Our comments on the MGMS manuscript[4] fall naturally into the following four sections:

1. Boundary Layer (BL) Effects on Inertial Impaction/Capture of Small Particles.

We are pleased that MGMS have focused attention on the "cushion" effects of a BL on small particle inertial impaction, since, previously, N. Fuchs [14] drew attention only to the (numerically less important) "displacement" effect of the viscous BL in modifying the external inviscid flow about a target. In extending a useful correlation of inertial capture efficiencies [15], we recently estimated both contributions to the BL effect on the *critical Stokes number*, $\mathrm{Stk}_{\mathrm{crit}}$ (for the "onset" of inertial impaction on a cylinder). By representing the viscous BL as a quiescent "cushion" adjacent to the target, we find [16] that the BL effect is to increase $\mathrm{Stk}_{\mathrm{crit}}$ by nearly 10 percent even at a Reynolds number as high as 10^6. At this Re-value the displacement effect, if acting "alone," would be to increase $\mathrm{Stk}_{\mathrm{crit}}$ from its inviscid value (1/8) by less than 0.2 percent. Have MGMS also included the "displacement" effect in their combustion turbine numerical example (*i.e.* evaluated the particle "initial conditions" using the BL-perturbed inviscid flow), or is the prevailing Re high enough to render it negligible?

2. Relevant Dimensionless Groups.

MGMS report that the BL effect on particle impaction is important for particles in the nominal diameter range 3-6 μm. *in a particular numerical example* [1-3]. Of course, this conclusion is specific to the conditions of the example, and it is therefore helpful to consider a *general* criterion for the importance of such BL "cushion" effects. It is not difficult to conclude that such effects will be important whenever the characteristic particle "stopping time," t_p, is the same order of magnitude as the characteristic momentum BL "crossing time" $\delta/(V_{p,n})_e$, where $(V_{p,n})_e$ is the normal component of the particle velocity (relative to the surface) evaluated at the BL outer edge. Clearly, particles for which this time ratio, or "BL-Stokes number," is $<<1$ will never reach the surface (except by diffusion), whereas particles for which this BL-Stokes number is $>>1$ will impact without appreciable deceleration (and an associated change in angle-of-incidence). On this basis the BL-"cushion" effect will inevitably be most important for particle sizes which depend not only on Re and relative position on the target, but also on *particle* density and gas viscosity. While, for numerical convenience, MGMS's calculations have been cast in *dimensional* terms, for purposes of generalization and understanding it would be helpful if the corresponding *dimensionless* parameters were computed, stated, and systematically varied. Indeed, we have found that by introducing a Stokes number, $\mathrm{Stk}_{\mathrm{eff}}$, based on *relevant* characteristic times (or lengths) the correlation of inertial impaction phenomena is dramatically simplified [15, 17; see also, Section 4 below], and the same philosophy allows correlations of *diffusional* particle capture [17, 18] even simpler than those based, say, on formal dimensional analysis (see, e.g., [19]).

3. Analogous Effects of Particle/Gas Energy and Mass Exchange Within BLs.

Whereas MGMS focus attention on particle/gas *momentum* exchange during particle transit of the *momentum* defect BL, there are important and completely analogous *energy* and *species* exchange processes that occur when particles traverse the enthalpy defect and species defect BLs. For example, we are currently investigating the effects of (*a*) BL droplet freezing on particle capture by targets cooled below the droplet freezing temperature, and (b) chaperon vapor uptake by particles impacting on targets cooled below the vapor dew-point. However, as the number and complexity of such phenomena increases, the need for clever, rational simplifications clearly becomes more pressing. Only if our theoretical methods and correlations focus on the essential features, display the important functional dependencies, and lend themselves to design/optimization studies, are they likely to have a real impact on present or future engineering practice.

4. Combined Effects of Particle Inertia and Diffusion.

MGMS report that in their numerical illustration diffusive and inertial mechanisms "act together" for particles in the diameter range 0.5 μm-3 μm, in which case the assumptions underlying existing predictive models become questionable.

For *laminar* BLs the consequences of the "onset" of inertial effects on diffusional capture are not difficult to understand and calculate, since the dominant effect of non-negligible particle inertia (even at *sub-critical* Strokes numbers) is to alter the effective "local" particle mass fraction at the outer edge of the particle diffusion boundary layer. This "inertial enrichment" (or depletion) is investigated for high Re-flows in [20], and for low Re-flows in [21], using an approach which is asymptotically exact in the limit of high Schmidt number (low particle diffusivity cf. fluid momentum diffusivity).

In contrast, the diffusion-like behavior of inertial particles inside a *turbulent* boundary layer (TBL) raises more difficult questions [22], as yet unanswered. MGMS also report "deposition velocities" in that problematic regime, evidently by making use of a variant of [5] (e.g., that in [3]). For reasons presented elsewhere [22], we are skeptical about the quantitative reliability of such methods, especially as applied in the combustion turbine context. Nonetheless, it is interesting to observe (Fig. 14) the "merging" of the two different "branches" (diffusion-dominated and inertia-dominated). Paradoxically, the same BL that reduces im-

[1] By M. Mengütürk, D. Gunes, H. K. Mimaroglu, and E. F. Sverdrup (hereafter referred to as MGMS), published in the September 1983 issue of the JOURNAL OF FLUIDS ENGINEERING, Vol. 105, No. 3.

[2] Professor of Chemical Engineering and Applied Science, Yale University, New Haven, Conn. 06520.

[3] Assistant Professor of Mechanical Engineering, Yale University.

[4] Based on research at Yale University-High Temperature Chemical Reaction Engineering Laboratory; supported in part by AFOSR (Contract F49620-82K-0020) and NASA-Lewis Research Center (Grant NAG 3-201).

paction rates (*via* the abovementioned "cushion" mechanism) in part "compensates" for this impediment by the action of its shear-generated turbulence! In view of the discussion of Section 2 above, it is worth recalling that the latter "eddy-impaction" mechanism begins to dominate eddy & Brownian diffusional delivery to a (fluid-dynamically) smooth wall when $t_p > \delta_m/u_*$ [23], where δ_m is the (slope) thickness of the Brownian diffusion mass transfer BL, and u_* is the prevailing time-averaged "friction velocity," $(\tau_w/\rho)^{1/2}$. Put another way, eddy-impaction sets in when t_p exceeds the time it would take a particle to traverse δ_m if traveling at about the rms (turbulence) velocity in the outer region of the TBL. Combining all of the abovementioned observations, we arrive at the following conclusion (perhaps not surprising, in retrospect): *the importance of each of the "inertial" effects of concern in particle impaction/deposition can be delineated in terms of an appropriate Stokes number, i.e. the ratio of the characteristic particle stopping time, t_p to an appropriate characteristic "flow time" for either the body, BL or a sublayer.* This observation should prove useful in "scaling" (to other systems and/or conditions) the interesting phenomena predicted and displayed by MGMS for a particular turbine application [1–3].

Additional References

14 Fuchs, N. A., *The Mechanics of Aerosols*, Pergamon Press, Oxford, 1964, Section 34, pp. 165, 166.

15 Israel, R., and Rosner, D. E., "Use of a Generalized Stokes Number to Correlate the Aerodynamic Capture Efficiency of Non-Stokesian Particles from a Compressible Gas Flow to Collectors of Different Geometry," *J. Aerosol Sci. & Technology*, Vol. 2, 1983, pp. 45–51.

16 Israel, R., and Rosner, D. E., "Increase of the Critical Stokes Number (for Particle Impaction) Due to the Presence of a Viscous Boundary Layer Adjacent to a Bluff Body at High Reynolds Number—Consequences of a Simple Flow Model, and Implications for the Correlation of Inertial Capture Efficiencies" (in preparation, spring 1983).

17 Rosner, D. E., Gokoglu, S., and Israel, R., "Rational Engineering Correlations of Diffusional and Inertial Particle Deposition Behavior in Non-Isothermal Forced Convection Environments," *Proc. Engrg. Foundatoin Int. Conf. on the Fouling of Heat Exchanger Surface*, 1983, pp. 235–256.

18 Gokoglu, S., and Rosner, D. E., "Correlations of Thermophoretically-Modified Small Particle Deposition Rates in Forced Convection Systems with Variable Properties, Transpiration Cooling and/or Viscous Dissipation," *Int. J. Heat and Mass Transfer*, Vol. 27, No. 5, pp. 693–645.

19 Becker, H. A., *Dimensionless Parameters—Theory and Methodology*, Wiley, Halstead Press, New York, 1976.

20 Fernandez de la Mora, J., and Rosner, D. E., "Inertial Deposition of Particles Revisited and Extended: Eulerian Approach to a Traditionally Lagrangian Problem," J. PhysicoChemical Hydrodynamics, Vol. 2, 1981, pp. 1–21.

21 Fernandez de la Mora, J. and Rosner, D. E., "Effects of Inertia on the Diffusional Deposition of Small Particles to Spheres and Cylinders at Low Reynolds Number," *J. Fluid Mechanics*, Vol. 125, 1982, pp. 379–395.

22 Rosner, D. E., and Fernandez de la Mora, J., "Correlation and Prediction of Thermophoretic and Inertial Effects on Particle Deposition from Non-Isothermal Turbulent Boundary Layers," *Particulate-Laden Flows in Turbomachinery*, ASME, New York, 1982, pp. 85–94.

23 Rosner, D. E., and Fernandez de la Mora, J., "Small Particle Transport Across Turbulent Non-Isothermal Boundary Layers," ASME *Engineering for Power*, Vol. 104, 1982, pp. 885–894.

Author's Closure

We would like to thank Prof. D. E. Rosner and Prof. J. F. de la Mora for their interesting discussion.

Our intent in this study has been to determine the effect of blade boundary layer on location, frequency, angle and velocity of particle impacts with turbine blade surfaces, and thereby, to enable accurate calculation of particle erosion and/or deposition rates by combining these results with information regarding the erosion response of the blade material and the sticking probability of particles to the surfaces. In this context, our blade boundary layer particle trajectory model is a supplement to a long cortegè of numerical models that we presented previously [1, 2, 3, 24]. These models treat, in sequence, the inviscid gas flow through turbine blade passages, the boundary layer flow around blades, the inertial motion of particles in the inviscid main flow, and their diffusive and, with the addition of the present model, inertial motions inside the blade boundary layer. Our most recent work in this subject includes detailed modelling of blade leading edge zones [25] and an application of our predictive capability to all the stages of a multistage electric-utility gas turbine [26]. In view of the multitude of phenomena involved, a rigorous and comprehensive generalization of the problem under consideration is extremely difficult, if not hopeless. In addition to the well-known dynamic parameters, inviscid and boundary layer flows in turbine passages are strongly dependent on the detailed geometry of the machine (especially blade profiles) which varies considerably with the manufacturer and the area of application. The design philosophy of turbine geometry cannot be associated with a universal standard, and further, it is subject to continuous change and modification through research and development. In contrast to the problem of fluid-particle flows in geometries characterized by a fixed shape, such as flows about spherical objects, that are amenable to generalization through a set of appropriate nondimensional dynamic parameters (e.g. see [27]), this feature of variable geometry constitutes a major drawback that prohibits universal description of turbine flows, and thereby, motions of suspended particles. We wholeheartedly join Rosner and de la Mora in their wish to obtain simple yet rational correlations to these phenomena. However, such simplified correlations tend to be limited in their usefulness, because they can only reveal some general features and trends rather than the details necessary for an acceptably accurate assessment of turbine erorsion/deposition. For example, in a recent study [26] we have suggested that the capture efficiency of a turbine blade (defined as the ratio of the amount of particles impacting the blade to the total amount entering the respective blade passage) can be approximately related, in the absence of boundary layer effect, to a blade average Stokes number, $\mathrm{ST}_{\mathrm{avg}} = \rho_p d_p^2 V_{\mathrm{avg}}/\mu b$ where V_{avg} is the average gas velocity in the passage and b the blade chord, the angle through which the flow is turned, α, the space-chord ratio, s, and deviation of particles from the gas flow at the passage inlet that may be expressed by the angle $\delta = \beta_p - \beta_g$ where β_p and β_g denote the inlet angles of particles and gas, respectively. Such a correlation indicates the parametric effects of various factors on the amount of particles impacting blades but does not give the local frequency, angle and velocity of impacts which must be known for the calculation of the distribution of erosion/deposition rates along blade surfaces.

Concerning the correlation of the boundary layer effect on particle trajectories in terms of a boundary layer entry Stokes number defined as $t_p(V_{p,n})_e/\delta$, where $(V_{p,n})_e$ is the normal component of the particle velocity evaluated at the boundary layer edge and δ the local boundary layer thickness, as suggested by Rosner and de la Mora, it is not clear to us what practical purpose this would serve, because afterall $(V_{p,n})_e$ is dependent on particle's previous history in the inviscid main flow, the general description of which is not available due to the reasons discussed above. Besides, we do not believe that this parameter is a good measure of the blade boundary layer effect. The proposed formation of the Stokes number implies that the dominant direction of particle motion is normal to the surface. However, in the turbine application particles approach blade surfaces usually at small angles, and therefore, the streamwise component of their motion becomes very important. The actual location and conditions with which a particle lands on the surface not only depends on its boundary layer entry location but also on, among other things, the magnitude and direction of the surface curvature.

To state extremes, a particle having a large boundary layer entry Stokes number may be missing the convex surface of the blade entirely, while a particle having a small boundary layer entry Stokes number may very well be hitting the concave side.

Strictly speaking, in the range of particle diameters for which diffusive and inertial mechanisms act together the existing models that treat these mechanisms separately lose their validity. Our current studies include development of a mixed Lagrangian-Eulerian approach for application to this mixed particle transport regime.

The displacement effect described by Rosner and de la Mora was not considered in our analysis, because the prevailing Reynolds number is very high (Re based on the blade chord and the average velocity across the first stage stator is of the order of 10^6).

Additional References

24 Wenglarz, R. A., and Menguturk, M., "Use of Cascade and Small Turbine Tests to Determine Erosion of Utility Turbines," ASME *Journal of Engineering Power*, Jan. 1982, pp. 58–63.

25 Gunes, D., and Menguturk, M., "Improved Particle Trajectory Calculations Around Blade Leading Edge," Sixth International Conference on Erosion by Liquid and Solid Impact (ELSI VI) Cambridge, Sept. 1983. (Paper No. 52).

26 Menguturk, M., Gunes, D., Erten, M. and Sverdrup, E. F., "Multistage Turbine Erosion," To be Presented at the 29th ASME Gas Turbine Conference, Amsterdam, June 1984.

27 Menguturk, M., and Gunes, D., "Investigation of Particle Collection Mechanisms in Granular Bed Filters," *Proc. of Conf. on Gas Borne Particles*, I. Mech. E., C81/81, June 1981.